

Investigation into the potential of MgSO_4 for
interseasonal domestic thermochemical energy
storage

By

Daniel Mahon

Doctoral Thesis

Submitted in partial fulfillment of the requirements

for the award of

Doctor of Philosophy of Loughborough University

June 2018

© by Daniel Mahon 2018

I. Abstract

Approximately 26% of the UK's primary energy consumption is used specifically for Domestic Space Heating (DSH) and Domestic Hot Water (DHW) production [1]. The majority of this, 88%, comes directly from gas and oil with only 2% coming from renewable energy sources [1]. Decarbonising DSH and DHW represents a huge challenge for the UK's government which is targeting a reduction of CO₂ emissions of 80% by 2050 [2].

The amount of energy utilised from renewable sources can be increased by effective Thermal Energy Storage (TES). In a domestic environment thermal energy is typically required when the energy supplied from renewable sources is low (i.e. thermal energy demand is high in the winter and low in the summer), interseasonal Thermochemical Energy Storage (TCES) offers a solution to this problem. TCES has the ability to store thermal energy from the summer months within chemical bonds and release the stored heat when required with heat losses of only around 15%.

Magnesium sulphate heptahydrate (MgSO₄·7H₂O) has the potential to store 2.8GJ/m³ of energy, is a low cost, non-toxic, safe material that can be dehydrated to MgSO₄·0.1H₂O (fully charged) at 150°C making it suitable for domestic integration. Research has shown that when MgSO₄ is used for TCES it suffers from problematic issues such as agglomeration. However, more research is needed to understand the characteristics of MgSO₄ further, develop high energy density TCES materials containing MgSO₄ and to understand if MgSO₄ should be used within a domestic interseasonal TCES system on a large scale, which is the aim of this research.

Throughout this research several thermal analysis devices were used to characterise TCES materials. The devices used include a Differential Scanning Calorimeter (DSC), Thermogravimetric Analyser (TGA), Residual Gas Analyser (RGA), Scanning Electron Microscope (SEM), Energy Dispersive X-ray Spectrometer (EDX) and several custom built laboratory experimental rigs.

MgSO₄ and novel composite materials containing MgSO₄ were characterised at a small (10mg) scale to investigate their energy density and what impact the dehydration heating rate and particle size had on the charging of MgSO₄. The results have shown that MgSO₄ has a dehydration enthalpy of 1118J/g that is not impacted by the heating rate used.

MgSO₄ was dehydrated and hydrated at a larger (100g+) scale and it was shown to have significant agglomeration and permeability problems. To solve the problems caused when using pure MgSO₄ a novel sample preparation method to create TCES pellets from powdered materials was developed. The novel pellet preparation methodology was optimised and the results showed that the initial dehydration heating rate and preparation methodology used (mix or impregnation) did have an impact on the TCES potential of the synthesised pellets.

A high energy density novel TCES material (ZMK) was synthesised and experimentally tested. The ZMK had a dehydration enthalpy of 715J/g and a performance of 85%. The dehydration enthalpy and TCES performance of 13X absorbent pellets were improved through an ion exchange process.

A large scale (40kg) modular TCES experimental test rig was designed and built to test TCES materials at a larger scale for experimental investigations into optimisation of efficient charge and discharge cycles.

This research shows the future potential of interseasonal domestic TCES through experimental results. Novel composite energy dense TCES materials containing MgSO₄ have been shown to have potential for larger scale testing. Future work is required to optimise the novel ZMK material developed and also test TCES materials at a larger scale to understand the associated scaling losses of TCES materials and understand better their role in future domestic TES systems.

II. Table of contents

I.	Abstract	II
II.	Table of contents	IV
III.	List of tables	XI
IV.	List of figures.....	XIII
V.	Nomenclature	XXIII
VI.	List of symbols	XXV
VII.	Acknowledgements	XXVI
1	Chapter 1 - Introduction	1
2	Chapter 2 - Literature Review	6
2.1	Introduction to the literature review	6
2.1.1	Social cost of CO ₂	6
2.1.2	Flooding due to increased atmospheric Green House Gases (GHG).....	6
2.1.3	Energy sources and energy linked problems.....	11
2.1.4	Thermal energy storage.....	14
2.1.5	Sorption and chemical energy storage terminology.....	15
2.2	The reason TCES has potential for domestic interseasonal thermal energy storage	18
2.3	Possible domestic TCES material candidates	20
2.3.1	Summary of possible TCES material candidates	22
2.4	The characteristics of MgSO ₄ for TES	22

2.4.1	The dehydration of MgSO_4	22
2.4.2	The hydration of MgSO_4	27
2.4.3	Summary of MgSO_4 characteristics section.....	34
2.5	Promising host materials for TCES	34
2.5.1	Zeolites	35
2.5.2	The structure of zeolites	35
2.5.3	Attapulgite and vermiculite for use as TCES materials	44
2.5.4	Carbon fibres and activated carbons for use as TCES materials.....	45
2.5.5	Silica gel for use as a TCES material	45
2.5.6	Summary of promising host materials for TCES	48
2.6	Sample preparation methodologies for creating TCES materials.....	49
2.6.1	Monoliths and bricks for TCES	49
2.6.2	Beads for TCES.....	49
2.6.3	Honeycombs for TCES	52
2.7	Possible ways to create composite materials	54
2.7.1	Simple mixture for creating TCES composite materials.....	54
2.7.2	Impregnation for creating TCES composite materials.....	54
2.7.3	Mixture or impregnation and consolidation for creating TCES composite materials	54
2.7.4	Summary of the different preparation methodologies discussed	55
2.8	Reactor designs and theory for TCES.....	55
2.8.1	Reactor design theory for TCES	55

2.8.2	Reactor designs for TCES	59
2.8.3	Summary of discussed potential reactor designs for TCES	62
2.9	Larger scale experimental results of TCES systems.....	63
2.9.1	Summary of the large scale experimental results of TCES systems	64
2.10	Conclusions of this literature review	65
3	Chapter 3 - Methodology	66
3.1	Introduction to the methodology.....	66
3.2	Methodology used for the ~10mg scale tests of the TCES materials	67
3.2.1	Small hydration chamber – Hydration of DSC, TGA + RGA and SEM+EDX samples	67
3.2.2	DSC dehydration enthalpy analysis methodology	71
3.2.3	TGA (+ RGA) mass loss methodology	75
3.2.4	SEM + EDX analysis methodology	81
3.2.5	Nitrogen vapour sorption testing methodology.....	85
3.3	200g Scale testing of the TCES materials.....	89
3.3.1	Custom built 200g dehydration hydration chamber.....	89
3.3.2	Bulk density measurements.....	92
3.4	Sample preparation methodology	94
3.4.1	Introduction to the sample preparation methodology	94
3.4.2	Incipient wetness impregnation method.....	94
3.4.3	Modified wetness impregnation method	95
3.4.4	Ion exchange methodology for the 13x pellets	96

3.4.5	Pellet creation from powders using the pellet press	97
3.5	Summary of methodology chapter	99
4	Chapter 4 – Characterization of MgSO ₄ , zeolite-Y and composite materials.....	100
4.1	Initial DSC, TGA and RGA characterization of MgSO ₄ .7H ₂ O.....	100
4.2	MgSO ₄ .7H ₂ O heating rate effects and cycle stability investigations.....	101
4.2.1	Sudden dehydration peaks from MgSO ₄ .xH ₂ O with high heating rates	101
4.2.2	Using lower temperatures for the dehydration of MgSO ₄	103
4.2.3	Structural changes of MgSO ₄ following de/hydration cycles	104
4.2.4	High hydration levels of MgSO ₄ using 1.3kPa pH ₂ O	105
4.2.5	Heating rate effect on the cycle stability and dehydration enthalpy of MgSO ₄ 106	
4.2.6	Slow kinetics of MgSO ₄	110
4.3	Zeolite cycle stability investigations.....	110
4.3.1	Thermal storage potential of zeolite-Y.....	111
4.4	Composite TCES materials analysis	112
4.4.1	Composite TCES materials enthalpy analysis	112
4.4.2	Composite TCES materials dehydration heating rate effects.....	115
4.5	Nitrogen vapour sorption measurements	117
4.6	Introduction to further slow kinetics tests.....	120
4.6.1	MgSO ₄ -90°C slow kinetics analysis.....	122
4.6.2	MgSO ₄ -150°C-75%RH slow kinetics measurements	126
4.6.3	MgSO ₄ dehydration enthalpy analysis without an isothermal period	127

4.6.4	MgSO ₄ particle size effect on slow kinetics.....	130
4.7	Conclusions from chapter 4	136
4.7.1	Slow kinetics section conclusions	137
5	Chapter 5 – Understanding the larger scale (100g+) characteristics of MgSO ₄ and investigating sample preparation methods for MgSO ₄ for use as a TCES material.	139
5.1	Introduction to chapter 5	139
5.2	Issues using MgSO ₄ and zeolite as TCES materials	139
5.2.1	MgSO ₄ agglomeration issues	139
5.2.2	MgSO ₄ permeability issues	141
5.2.3	Zeolite permeability issues.....	145
5.3	Initial investigations into sample preparation methodologies	146
5.3.1	Investigation into the potential of using a pelletizing disc for TCES sample preparation	146
5.3.2	Investigation into the potential of hand rolling beads for TCES sample preparation	149
5.3.3	Investigation into the potential of using a pellet press for TCES sample preparation	150
5.4	Conclusions of chapter 5.....	162
6	Chapter 6 - Investigation into potential host materials for impregnating with MgSO ₄	163
6.1	Introduction to chapter 6.....	163
6.2	13x pellet investigation results.....	164

6.2.1	Comparison of 13x powder, 13x pellets and zeolite-Y powder absorbents.	164
6.2.2	Comparison of 13x materials with different absorbed quantities of MgSO ₄ prepared using the wetness impregnation method.....	166
6.2.3	Analysis of DSC plots for composite 13x + MgSO ₄ materials to determine cause of lower than expected dehydration enthalpies	167
6.2.4	200g dehydration/hydration cycle testing results of the 13x materials and ZMK	169
6.2.5	Comparison of dehydration/hydration cycle results from theory, DSC measurements and 200g sample size measurements	170
6.2.6	Theoretical dehydration enthalpy, excluding MgSO ₄ .xH ₂ O enthalpy, compared to DSC and 200g sample measured tests	171
6.3	13x Mg ²⁺ ion exchange pellet testing results	172
6.3.1	SEM and EDX analysis of 13x ion exchanged pellets.....	174
6.4	Additional potential host materials for MgSO ₄	177
6.4.1	Activated Alumina measurements	178
6.4.2	Activated Carbon measurements.....	183
6.5	Conclusions of chapter 6.....	187
7	Large scale testing of TCES materials	189
7.1	Introduction and purpose of the custom built modular 40kg rig	189
7.2	Custom built modular 40kg rig system design	190
7.2.1	Arduino microcontroller control of the custom built modular 40kg rig	191

7.3	Experimental operating procedure for the custom built modular 40kg rig methodology.....	192
7.3.1	Default microcontroller data logger program of the custom built modular 40kg rig	193
7.3.2	Data collection for the custom built modular 40kg rig	193
7.4	Conclusions from the custom built 40kg reactor design.....	194
8	Thesis conclusions.....	195
8.1	Conclusions from Chapter 4 – Characterisation of MgSO ₄ , zeolite-Y and composite materials.....	195
8.2	Conclusions from chapter 5 - Understanding the larger scale (100g+) characteristics of MgSO ₄ and investigation of sample preparation methods for MgSO ₄ for use as a TCES material.....	196
8.3	Conclusions from chapter 6 - Investigation into potential host materials for impregnating with MgSO ₄	197
8.4	Conclusions from chapter 7 - Large scale testing of TCES materials	198
9	Recommendations for future work.....	199
9.1	Identified future work from chapter 4.....	200
9.2	Identified future work from chapter 5.....	200
9.3	Identified future work from chapter 6.....	200
9.4	Identified future work from chapter 7.....	201
10	Research	202
11	References	203

III. List of tables

Table 2-1 Comparison of different TES mechanisms based on various performance factors [22].....	19
Table 2-2 Promising materials for thermochemical energy storage [22]	20
Table 2-3 Important thermodynamic characteristics of candidate salt hydrates after dehydration under a water partial vapour pressure ($p_{H_2O} = 21\text{mbar}$, 105°C) (references in table refer to references within the paper by N'Tsoukpoe et al. [45]).	21
Table 2-4 Energy densities and prices of selected salt hydrates for use as TCES materials [24].....	22
Table 2-5 Variables used and delta T achieved in 6 hydration experiments of MgSO_4 monohydrate [54].....	31
Table 2-6 Comparison of the specific heat storage density of absorbent materials compared to the heat capacity of water at different temperatures [92].....	46
Table 2-7 Advantages and disadvantages of absorbent host materials	48
Table 2-8 Comparison of the desorption capacities in g/g of binderless and ordinary zeolite types A and X [77]	49
Table 2-9 Advantages and disadvantages of the different composite preparation methods	55
Table 3-1 Example EDX data showing elemental analysis of 13x pellets	84
Table 3-2 Normalised Mg and Na EDX example for 13x pellets.....	84
Table 3-3 Numerical values used for heat output calculations	91
Table 3-4 The amounts of MgSO_4 added in each impregnated 13x pellet.	95
Table 4-1 Average dehydration enthalpy compared to the maximum dehydration temperature for $\text{MgSO}_4 \cdot x\text{H}_2\text{O}$	104

Table 4-2 Enthalpy data showing dehydration enthalpy (after a 150°C dehydration) and cycle stability of MgSO ₄	106
Table 4-3 Description of the different particles of MgSO ₄ .7H ₂ O used	130
Table 6-1 DSC determined averaged enthalpies of absorbent zeolite materials over the temperature range of 20 - 150°C	165
Table 6-2 Calculated theoretical dehydration enthalpies for samples, not accounting for the MgSO ₄ .xH ₂ O dehydration enthalpy, compared to the measured DSC and 200g enthalpy results over the temperature range 20-150°C.....	172
Table 6-3 DSC and TGA Energy output of AA samples.....	182
Table 6-4 200g Energy output of AA samples	183
Table 6-5 A summary of the results from the AC and AC+MgSO ₄ DSC and TGA analysis	186

IV. List of figures

Figure 2-1 Topographic map of London [6]	7
Figure 2-2 Temperature predictions for SRES scenarios and the RCP's [10].....	9
Figure 2-3 Diagram showing sources of energy for production and storage [14]	11
Figure 2-4 Final energy consumption (EU-28), 2015 [15].....	13
Figure 2-5 Energy consumption in EU households for 2016 [16].....	13
Figure 2-6 Energy density with temperature of different energy storage materials [29]...	15
Figure 2-7 Chemical and sorption energy storage classification [29]	17
Figure 2-8 An indication of volume of storage material needed to store 6.7GJ/year of thermal energy for an average household [24]	18
Figure 2-9 The screening process used for the salt hydrates assessed by N'Tsoukpoe et al. [45].....	21
Figure 2-10 TGA mass loss data and DSC enthalpy measurements for the dehydration of MgSO ₄ .7H ₂ O [50].....	23
Figure 2-11 TGA mass loss measurements for the dehydration of MgSO ₄ .7H ₂ O [23].....	23
Figure 2-12 The changing XRD diffraction patterns of MgSO ₄ .7H ₂ O as it is dehydrated [51].....	24
Figure 2-13 TGA measurements showing the mass loss of a zeolite and three zeolite + MgSO ₄ composite materials [23].....	25
Figure 2-14 SEM images of MgSO ₄ .7H ₂ O before (a) after dehydration (b) and after rehydration (C) [50]	25
Figure 2-15 DSC dehydration measurements of MgSO ₄ .7H ₂ O. Squares and triangles represent particles of size (20-38µm) and (200-500µm) respectively [50]	27
Figure 2-16 TGA & DSC hydration measurements of MgSO ₄ with varying particle sizes [50].....	28

Figure 2-17 Micrographs of the hydration of NaSO ₄ at 92% RH and 23°C after 2 hours (a), 3 hours (b) and 6 hours (c). Red arrows point to NaSO ₄ green arrows to NaSO ₄ .10H ₂ O and blue arrows to Na ₂ SO ₂ (aq) [46]	29
Figure 2-18 Simultaneous Thermal Analysis (STA) measurements showing the water uptake of MgSO ₄ as it is hydrated under different conditions [50]	30
Figure 2-19 Equilibrium curves for the hydration of MgSO ₄ [54]	30
Figure 2-20 Water uptake hydration curves for MgSO ₄ against time with different hydration humidity's (Red lines = below DRH of MgSO ₄ .H ₂ O, Blue lines = above DRH of MgSO ₄ .H ₂ O, green lines = above DRH of MgSO ₄ .6H ₂ O, light blue lines = above DRH of MgSO ₄ .7H ₂ O) [46].	32
Figure 2-21 TGA & exothermic DSC hydration measurements for MgSO ₄ showing the heat output with varying layer thickness [50]	33
Figure 2-22 Experimental hydration measurements of zeolite/MgSO ₄ [23].....	34
Figure 2-23 Zeolite Structures - Image 1 shows the sodalite cage (β-cage), image 2 shows the unit cell of zeolite A, image 3 the unit cell of zeolite X and Y, image 4 the ion exchange sites on zeolite A and image 5 the ion exchange sites on zeolite X and Y [71]	36
Figure 2-24 Diagram showing the building blocks of different zeolite structures [68].....	37
Figure 2-25 3-D representation of zeolite A (left) and Zeolite X and Y (right) showing their cage structure [73]	38
Figure 2-26 DSC-TGA measurements of various tested zeolite impregnated composites (H-Y, Na-Y, MOR and Na-X from top left to bottom right) [48].	39
Figure 2-27 Pore size against amount of water uptake in porous glass impregnated with MgSO ₄ [46].....	40
Figure 2-28 Temperature lift measurements of the hydration of various composite materials- SM16 = silica gel/MgSO ₄ , ZM15 – zeolite/MgSO ₄ [23].....	41

Figure 2-29 Amount of water absorbed vs. Mg ion exchange degree for Zeolite NaA and NaA.....	42
Figure 2-30 Measurements showing how salt content affects the heat of sorption of the impregnated material [49].....	44
Figure 2-31 Effects of CaCl ₂ concentration on the dynamic sorption characteristics of water on composite sorbents showing the absorbed amounts [42].....	46
Figure 2-32 Moisture vapour sorption isotherms for the selective materials studied SIM-2a = silica gel + CaCl ₂ , SIM-3a = Vermiculite + CaCl ₂ . [36]	47
Figure 2-33 An example pelletizing disc (letters A, B, C and D represent locations of where nozzles are located on this specific pelletizing disc). [101].....	52
Figure 2-34 Inlet and outlet change in temperature with time for different honeycomb filters [103].....	53
Figure 2-35 The trends in pressure drop and bed height with superficial velocity for a fluidised bed reactor (A = part of the curve where the Ergun equation can be used to describe the increasing pressure drop with increasing velocity, B = bed starts to expand while pressure drop remains constant. The force on the particles balances the net weight of the particles and separation of the particles begins, C = bed expands further but pressure drop remains constant, D = bed decreases with velocity but pressure drop remains constant, E = after the velocity is decreased below the superficial velocity the bed height remains constant but the pressure drop decreases with velocity. The bed height is higher than the original bed height after fluidization due to the particles becoming less packed, if left alone, over time the particles will return to the packed bed height.) [107]	57
Figure 2-36 The different types of fluidisation [108]	58
Figure 2-37 Powder classification diagram for fluidization by air [109]	59
Figure 2-38 Charging and discharging diagrams of a zeolite system, respectively [110].60	

Figure 2-39 Integrated reactor design(left), Closed separate reactor design (right) [86] .61	.61
Figure 2-40 Three possible reactor designs for the use of powdered TCESM (screw reactor, fluidized bed reactor, gravity assisted bulkflow reactor) [86].	61
Figure 2-41 Reactor size against four constraints: dehydration time, hydration time, power output (of a screw reactor) and heat transfer (of a screw reactor) [86].	62
Figure 2-42 Modular thermochemical reactor design (left) Central reactor with vessel design (right) [112]	62
Figure 2-43 Novel salt hydrate tray reactor system [113]	63
Figure 2-44 Open sorption drum reactor [114].	64
Figure 3-1 A schematic diagram of the small hydration chamber system.	69
Figure 3-2 Example DSC temperature profile program	73
Figure 3-3 TA instruments discovery TGA balance [122]	76
Figure 3-4 TGA Temperature Profile	79
Figure 3-5 An example overlay of DSC, RGA and TGA data, showing the dehydration of $MgSO_4 \cdot 7H_2O$	80
Figure 3-6 Image 1: Example EDX dot analysis, Image 2: Composition from dot analysis, Image 3: Example of an EDX atomic spectrum from the dot analysis.	83
Figure 3-7 Types of adsorption isotherms [129].	87
Figure 3-8 200g dehydration hydration setup	90
Figure 4-1 $MgSO_4 \cdot 7H_2O$ dehydration to 300°C overlay showing measurements from TGA, RGA and DSC showing the dehydration process.	101
Figure 4-2 DSC measurements for several heating rates, showing volatile behaviour with increasing heating rates.	102
Figure 4-3 Ion current as a function of temperature for $MgSO_4 \cdot 7H_2O$ at 4 different heating rates	102

Figure 4-4 TGA dehydration measurements for $\text{MgSO}_4 \cdot x\text{H}_2\text{O}$ dehydrated with several heating rates and isothermal periods, showing little difference in mass loss between dehydration temperatures of 110°C and 150°C.....	103
Figure 4-5 SEM Images of MgSO_4 after dehydration with different heating rates and images of MgSO_4 after rehydration	105
Figure 4-6 TGA measurements showing cycle stability of MgSO_4 using a 1°C/min heating rate.....	107
Figure 4-7 TGA measurements showing cycle stability of MgSO_4 using a 5°C/min heating rate.....	108
Figure 4-8 TGA measurements showing cycle stability of MgSO_4 using a 10°C/min heating rate.....	108
Figure 4-9 DSC measurements showing cycle stability of MgSO_4 using a 1°C/min heating rate.....	109
Figure 4-10 DSC measurements showing cycle stability of MgSO_4 using a 5°C/min heating rate.....	109
Figure 4-11 DSC measurements showing cycle stability of MgSO_4 using a 10°C/min heating rate.....	110
Figure 4-12 DSC measurements used for evaluating the dehydration enthalpy of hydrated zeolite-Y.....	112
Figure 4-13 DSC dehydration measurements for the hydrated composite materials	113
Figure 4-14 Achieved dehydration enthalpy for each composite material.	113
Figure 4-15 Dehydration enthalpy and performance of composite materials and zeolite-Y	114
Figure 4-16 TGA dehydration measurements for the composite materials.....	115
Figure 4-17 DSC dehydration measurements for the 35wt% composite sample	116

Figure 4-18 Differential TGA dehydration data for 35wt% composite sample	116
Figure 4-19 Comparison of slow kinetics of each composite sample.	117
Figure 4-20 Cumulative pore volume of each composite sample, zeolite-Y and MgSO ₄	119
Figure 4-21 BET surface area and average pore diameter of each composite sample, zeolite-Y and MgSO ₄	119
Figure 4-22 Cumulative pore volume against pore diameter of MgSO ₄ , zeolite-Y and the composite materials	120
Figure 4-23 Illustration of an example isotherm enthalpy analysis conducted on a sample dehydrated to 90°C	122
Figure 4-24 Enthalpy analysis for each of the heating rates tested.....	123
Figure 4-25 Isotherm enthalpy for each of the MgSO ₄ .xH ₂ O samples when dehydrated to 90°C at different heating rates	123
Figure 4-26 Mass loss of MgSO ₄ .xH ₂ O against cycle number with different dehydration heating rates	124
Figure 4-27 Enthalpy per mass loss for each MgSO ₄ .xH ₂ O sample dehydrated with different heating rates	124
Figure 4-28 Isothermal mass loss % of the MgSO ₄ .xH ₂ O samples dehydrated with different heating rates	125
Figure 4-29 Total average enthalpy values for MgSO ₄ .xH ₂ O dehydrated with different heating rates	126
Figure 4-30 Percentage isothermal enthalpy is of total dehydration enthalpy for MgSO ₄ samples dehydrated to 150°C within the DSC.....	127
Figure 4-31 Dehydration of MgSO ₄ .7H ₂ O to 90°C with a heating rate of 1°C/min and 5 minute isothermal period	128

Figure 4-32 Dehydration of $\text{MgSO}_4 \cdot 7\text{H}_2\text{O}$ to 90°C with a heating rate of $5^\circ\text{C}/\text{min}$ and 5 minute isothermal period	129
Figure 4-33 Dehydration of $\text{MgSO}_4 \cdot 7\text{H}_2\text{O}$ to 90°C with a heating rate of $10^\circ\text{C}/\text{min}$ and 5 minute isothermal period	129
Figure 4-34 Samples used for particle size tests – Images show each of the samples used. Large, medium and small from left to right (see Table 4-3 for details of particles).....	130
Figure 4-35 DSC plots for the three different grain sizes dehydrated to 90°C with a heating rate of $5^\circ\text{C}/\text{min}$	131
Figure 4-36 Average DSC enthalpy measurements for each grain size	132
Figure 4-37 Average TGA mass loss data for the different grain sizes.....	132
Figure 4-38 Enthalpy per % mass loss for each of the grain sizes (J/%).....	133
Figure 4-39 Isothermal enthalpy for each grain size	134
Figure 4-40 Isothermal mass loss and isothermal mass loss % for small and medium/large grain sizes.....	134
Figure 4-41 TGA plots for small grain sizes showing the similar dehydration cycles for all samples and runs	135
Figure 4-42 TGA plots for larger grain sizes showing the similar dehydration cycles for all samples except for the first dehydration cycle.....	135
Figure 5-1 Image of $\text{MgSO}_4 \cdot 7\text{H}_2\text{O}$ in a beaker after a heating to 150°C , with a 3h isotherm, showing the solid structure which was formed.....	140
Figure 5-2 Ground $\text{MgSO}_4 \cdot x\text{H}_2\text{O}$ in the reaction chamber after being heated to 150°C . 141	141
Figure 5-3 $\text{MgSO}_4 \cdot x\text{H}_2\text{O}$ after hydration in reactor showing agglomeration	141
Figure 5-4 Image of empty plunger hydration chamber	142
Figure 5-5 Delta T vs. time for the hydration of MgSO_4	144

Figure 5-6 Stills from a video of MgSO ₄ hydration showing the fluidisation effect caused.	145
Figure 5-7 Image of material in pelletizing disc showing the anticlockwise agglomerating motion of particles into beads	147
Figure 5-8 Image of pellets created with the pelletizing disc	148
Figure 5-9 Image of beads created with pelletizing disc after an oven bake at 150°C....	148
Figure 5-10 Image of sausage rolling table (left) and sausage gun (right)	149
Figure 5-11 Three SEM images of the mix 1°C/min pellets.....	152
Figure 5-12 Three SEM images of the mix 5°C/min pellets.....	153
Figure 5-13 Three SEM images of the impreg 1°C/min pellets.....	153
Figure 5-14 Three SEM images of the impreg 5°C/min pellets.....	154
Figure 5-15 EDX elemental data for each of the different sample preparation methods	155
Figure 5-16 Total cumulative pore volume for each of the different preparation methods	156
Figure 5-17 BET surface area and average pore diameter for each of the different preparation methods.....	156
Figure 5-18 DSC dehydration enthalpy and performance ratio for each sample preparation method.....	158
Figure 5-19 DSC dehydration enthalpy and average pore size for each sample preparation method.....	159
Figure 5-20 DSC dehydration enthalpy and 200g hydration enthalpy for each sample preparation method	160
Figure 5-21 DSC dehydration enthalpy and scaling losses for each sample preparation method.....	161

Figure 5-22 200g hydration enthalpy and energy density for each sample preparation method.....	161
Figure 6-1 DSC dehydration plots of zeolite-Y, 13x powder and 13x pellets showing the dehydration enthalpy and sensible enthalpy.	165
Figure 6-2 Graph showing average dehydration enthalpy, mass loss and predicted dehydration enthalpy for 13x samples with different wt% of MgSO ₄ created using the wetness impregnation method.....	167
Figure 6-3 DSC plots showing the endothermic dehydration heat flow for 13x samples, ZMK, 13xMK and MgSO ₄	168
Figure 6-4 200g hydration tests Delta T (outlet air – inlet air temperature) output cycle results for 13x pellets, 13xMK, 13x+MgSO ₄ (12.9wt%) and ZMK.....	170
Figure 6-5 Comparison of loss in performance percentage between tested samples at different tested mass.	171
Figure 6-6 DSC dehydration enthalpy and TGA dehydration mass loss results of 13x ion exchanged pellets.....	173
Figure 6-7 Sensible enthalpy and performance (dehydration enthalpy / total enthalpy) of 13x ion exchanged pellets.....	174
Figure 6-8 EDX analysis of normalised Mg vs Na content of the internal structure of the 13x ion exchanged pellets.....	175
Figure 6-9 EDX external surface analysis of normalised Mg vs Na content of the 13x ion exchanged pellets.....	176
Figure 6-10 SEM images of the 24 hour ion exchanged 13x pellets.....	177
Figure 6-11 DSC dehydration measurements of hydrated activated alumina.....	178
Figure 6-12 Activated alumina DSC results when dehydrated to different temperatures.....	179

Figure 6-13 DSC dehydration results of activated alumina and activated alumina impregnated with MgSO ₄	180
Figure 6-14 Comparison of AA and AA+MgSO ₄ dehydration enthalpy	181
Figure 6-15 TGA dehydration of AA showing differential weight with temperature	181
Figure 6-16 24h 200g hydration results of AA	182
Figure 6-17 DSC dehydration measurements of activated carbon	183
Figure 6-18 TGA differential weight loss showing the dehydration of activated carbon	184
Figure 6-19 TGA differential weight loss showing the dehydration of activated carbon over the temperature range of 30-67.5°C	185
Figure 6-20 DSC dehydration plots of activated carbon and activated carbon with 6.9wt% of impregnated MgSO ₄	186
Figure 7-1 Image of the 40kg modular reactor	191
Figure 7-2 Microcontroller data logger.....	192

V. Nomenclature

AA	Activated Alumina
AC	Activated Carbon
BET	Brunauer Emmett Teller
DHW	Domestic Hot Water
DI	Deionised
DRH	Deliquescence Relative Humidity
DSC	Differential Scanning Calorimeter
DSH	Domestic Space Heating
EDX	Energy Dispersive X-ray Spectrometer
FCC	Fluid Catalytic Cracking
GHG	Green House Gases
GMSLR	Global Mean Sea Level Rise
IPCC	Inter-governmental Panel on Climate Change
JRC	Joint Research Centre
LTES	Latent Thermal Energy Storage
MAC	Marginal Abatement Cost
MET	Meteorological office
PM	Particulate Matter
RCP	Representative Concentration Pathways

RGA	Residual Gas Analyser
RH	Relative Humidity
RPM	Revolutions Per Minute
SCC	Social Cost of Carbon
SEM	Scanning Electron Microscope
SSA	Specific Surface Area
STC	Solar Thermal Collector
STES	Sensible Thermal Energy Storage
TCES	Thermochemical Energy Storage
TCESM	Thermochemical Energy Storage Materials
TES	Thermal Energy Storage
TGA	Thermogravimetric Analyser
VFPC	Vacuum Flat Plate Collector
WHO	World Health Organization
WSS	Wakkanai Siliceous Shale
XRD	X-ray Diffraction

VI. *List of symbols*

Q	Heat
m	Mass
C_p	Specific heat capacity
Δ	Delta
L	Latent heat
H	Enthalpy
T	Temperature
S	Entropy
G	Gibbs free energy
K	Permeability
n	Porosity
d	Diameter of grains
n_{cr}	Critical revolutions per minute
D	Disc diameter
ΔH_T	Total dehydration enthalpy
ΔH_D	Dehydration enthalpy
ΔH_S	Sensible enthalpy
q_m	Monolayer capacity of the sample
σ	Surface area occupied by one molecule at analysis temperature
N_a	Avogadro's number
E_{out}	Energy out
P	Power
\dot{m}	Mass flow rate
ρ	Density
t_0	Start time
v	Volume

VII. Acknowledgements

I would like to acknowledge both of my PhD supervisors Professor Philip Eames and Dr Gianfranco Claudio for their continuous support of my PhD studies, guidance, motivation and knowledge.

This work was supported in full by the UK Engineering and Physical Sciences Research Council (EPSRC) (grant number: EP/K011847/1), i-STUTE and a Loughborough University PhD studentship.

1 Chapter 1 - Introduction

Almost half of the UK's energy consumption is used for heating purposes and 26% used for Domestic Hot Water (DHW) and Domestic Space Heating (DSH). The issue with DHW and DSH in the UK is currently almost all of the energy comes from fossil fuels (88% from gas and oil) [1]. For this reason DSH and DHW energy sources need to be sourced from cleaner and ideally renewable energy sources if the UK is to meet its 2050 goal of an 80% reduction of CO₂ emissions [2].

The sun delivers enough energy to the earth in one hour than the whole of humanity uses in an entire year. The energy the sun delivers to the earth is referred to as solar energy. An issue in the UK, and most of the world, is typically solar irradiance is high when demand for DSH and DHW is low. For example, in the summer times the UK's demand for DSH and DHW is low however; the incoming solar irradiance is typically at its highest. Currently, this results in a lot of unutilized solar thermal energy from the incoming day time solar irradiance.

To bridge the offset between supply and demand a Thermal Energy Storage (TES) mechanism should be utilized. The large amount of unutilized day time solar thermal energy should be stored ready for use when demand is high and supply is low (i.e. evening times). If done successfully this would reduce the need for the current typical energy sources used (i.e. fossil fuels) to supply thermal energy in times of demand. Storing thermal energy from the sun ready for later use offers a solution to help decarbonise DSH and DHW. In the UK the demand for DSH and DHW is highest in the winter months and lowest in the summer months.

TES has the potential to store the unutilized day time solar irradiance as thermal energy and then release the thermal energy when required on demand. Using this method there is no need to convert and store the solar thermal energy as a different energy source (i.e. electrical or mechanical) for it to be used later as thermal energy thus, reducing the energy losses through conversion.

There are three main types of thermal energy storage, Sensible Thermal Energy Storage (STES), Latent Thermal Energy Storage (LTES) and Thermochemical Energy Storage (TCES). STES stores heat by increasing the temperature of a material (i.e. rocks). This TES

method suffers from large thermal losses making it suitable for short term TES and not suitable for long term TES (i.e. interseasonal TES).

LTES stores thermal energy within a material but also takes advantage of the large amounts of energy required for phase transitions of materials (i.e. the melting of a wax). LTES keeps the material in a phase-changed state while storing the thermal energy. When the thermal energy is required the LTES material reduces in temperature causing a phase transition which releases the stored latent heat. LTES typically has a higher energy density than STES however, it suffers from heat losses making this technology short term and again not suitable for interseasonal thermal energy storage.

TCES stores thermal energy as chemical potential energy. A material is heated to a temperature causing it to break into working reactants. These reactants are stored separate from one another to store the thermal energy. When the thermal energy is required the reactants are recombined causing a chemical reaction, which releases the stored thermal energy. As the thermal energy is stored in chemical bonds TCES only suffers from sensible enthalpy losses when the energy is stored, which typically accounts for 10-15% of the total energy input to the TCES material (i.e. assuming a domestic interseasonal storage system where all of the sensible heat is lost). Once the thermal energy is stored and the sensible enthalpy is lost there are no further energy losses, meaning this technology is suitable for interseasonal TES.

TCES materials can be classified as physisorption or chemisorption materials. Physisorption refers to a process where a sorbate bonds to the surface of or within the bulk of a sorbent. This process typically involves Van der Waals forces and as a result this process typically has the weakest formed bonds with the lowest energy density. Chemisorption involves the process of a sorbate bonding with the bulk of a sorbent and involves stronger bonds such as covalent and ionic bonding. The stronger bonds result in a higher energy density material. These classifications are explained in more detail in Chapter 2 – Literature Review.

Within composite TCES materials there are typically several different physical processes taking place including adsorption and absorption meaning throughout this work the materials are all referred to as TCES materials.

If a TCES material is to be used in a domestic environment for DSH and DHW it needs to meet specific requirements. First the TCES material is required to have a reversible chemical reaction making it suitable for multiple energy storage cycles. The materials need to be safe and non-toxic to humans as they are to be integrated into a domestic environment. It is assumed that the TCES materials will be charged using a Solar Thermal Collector (STC) and hence, the maximum charging temperature for the TCES materials is required to be around 150°C. Also, the materials used need to be energy dense and cost effective to ensure they are an attractive technology and competitive with current energy sources for DSH and DHW.

There are two types of TCES reactor systems, open and closed. Each of these two systems can be further classified as integrated or separate making a total of four different reactor types. Each type of reactor has advantages and disadvantages which make them suitable for different applications. Separate and integrated reactors refer to where the TCES materials are stored and reacted. For an integrated reactor the materials are stored within the same location to where the reaction takes place (i.e. no transportation of chemicals is required). A separate reactor stores the chemicals in a location different to where the reaction takes place (i.e. the chemicals have to be transported to enable the reaction to take place). A closed system does not involve any materials entering or leaving the system where as an open system does involve chemicals leaving and entering the system. An example of an open integrated system would involve using outside humid air pumped into an absorbent packed bed of material causing a hydration reaction to take place.

There are advantages and disadvantages with each type of reactor configuration, which will be explained in more detail in Chapter 2 – Literature Review of this thesis. However, the research conducted in this thesis uses an open integrated reactor system due to the simplicity of the reactor and the suitability for the domestic environment.

A chemical, which meets the specifications required of a domestic TCES material, is $\text{MgSO}_4 \cdot x\text{H}_2\text{O}$. $\text{MgSO}_4 \cdot x\text{H}_2\text{O}$ is a salt hydrate and is used for many different purposes including bath salts. This material is non-toxic, cost effective (£61/ton), can be charged at 150°C and reacts with water resulting in a theoretical energy output of 2.8GJ/m³. However, recent research has shown that there are some practical problems when using MgSO_4 for domestic TCES. These problems include i) agglomeration upon rehydration (discharging) which results in a low vapour transportation throughout the material, reduced energy and power output ii) cycle stability issues.

Recently there have been studies which attempt to take advantage of the high energy density of MgSO_4 while alleviating its issues. Research conducted has looked at the impregnation of MgSO_4 into porous host materials. This impregnation is done to spread the MgSO_4 over a thin surface within a porous host material to reduce agglomeration and increase vapour transportation. For example, zeolites have recently been used as host materials for salt hydrates. Zeolites are crystalline materials which have large surface areas and are typically very porous.

There has been recent research which investigates the potential of MgSO_4 composite TCES materials. However, no material has been developed which meets all of the required specifications and has an energy density large enough to be an economically feasible option for integration into a domestic system. Therefore, more research is needed in the development of MgSO_4 composite TCES materials.

The aim of this thesis was to research the potential of MgSO_4 and develop a composite material which could take advantage of the high energy density of MgSO_4 and have a final energy density large enough to be competitive with current energy sources used for DSH and DHW.

This research investigated novel host materials and novel methods to develop composite TCES materials. The potential of improving host materials ready for MgSO_4 impregnation was investigated.

The thesis was structured so that the following chapter builds upon the questions or issues raised by the previous one.

Chapter 2 presents a review of the current literature concerning domestic TCES, presenting the potential of using MgSO_4 for domestic TCES but also the issues and areas that need to be researched further.

Chapter 3 presents the methodology used throughout this thesis for conducting all of the experimental and analytical work.

Chapter 4 presents experimental research carried out on a small scale (10mg) with MgSO_4 zeolite-Y and composite materials consisting of zeolite-Y and MgSO_4 . This research used many thermal analysis devices including a Differential Scanning Calorimeter (DSC),

Thermogravimetric Analyser (TGA), Residual Gas Analyser (RGA), Scanning Electron Microscope (SEM) and Energy Dispersive X-ray spectrometer (EDX). The research in this chapter was important for identifying some of the issues while also highlighting the potential of both pure MgSO_4 and composite materials comprised of MgSO_4 and zeolite-Y.

Chapter 5 investigated the potential of TCES materials being utilized at a scale larger than 10mg. If TCES + STC systems are to be realized TCES materials need to be tested on a larger more practical scale as the issues on a larger (100g+) scale may be completely different and new relative to the issues on a small (10mg) scale. Chapter 5 first presents the problems when using pure MgSO_4 at a larger scale (on the order of 10's of grams). Once it was established that the application of pure MgSO_4 within an open integrated TCES reactor system for domestic use was problematic sample preparation investigations were conducted. The investigations highlighted one potential method of producing composite TCES pellets. Next this chapter carried out experiments to optimise the methodology for producing these novel pellets.

Chapter 6 explored the possibility of using the developed methodology in chapter 5 to produce high energy density TCES materials with the use of zeolite-Y and 13X molecular sieves. The results from 13x molecular sieve composite materials were unexpected. These results lead to the investigations of modifying 13x molecular sieves using an ion exchange process to increase the energy density of 13x molecular sieves for domestic TCES. This chapter also considered other methods to create large scale batches of TCES composite materials with the use of activated alumina beads and activated carbon pellets as host materials for MgSO_4 .

Chapter 7 describes a designed and built large scale custom 40kg modular TCES test rig. This test rig should experimental enable work to be conducted into the optimisation of efficient charge and discharging of a TCES material store at a large scale using a novel reactor.

Chapter 8 presents the conclusions from the research presented within this thesis.

Chapter 9 presents recommendations for future work.

2 Chapter 2 - Literature Review

2.1 Introduction to the literature review

Throughout this chapter key concepts and literature for the field of domestic thermochemical energy storage are explored and explained. The purpose of this chapter is to give sufficient background knowledge as well as highlight the key research in the field and highlight areas for future research.

2.1.1 Social cost of CO₂

The social cost of CO₂ is the societal cost of each additional ton of CO₂ which is emitted into the environment [3]. The cost is the sum of all the damage caused by the CO₂ over its lifetime in the atmosphere [4]. This cost is not localized to a region or country because the impact or damage to the climate from CO₂ emissions has a worldwide impact.

2.1.2 Flooding due to increased atmospheric Green House Gases (GHG)

Increased CO₂ emissions will lead to a Global Mean Sea Level Rise (GMSLR). According to the Inter-governmental Panel on Climate Change (IPCC) a likely range of GMSLR for 2081-2100 is 0.4m (0.26-0.55) and 0.63m (0.45-0.82) for RCP2.6 and RCP8.5, respectively (i.e. RCP's are Representative Concentration Pathways which, are possible according to the IPCC, and are used for modelling climate changes due to greenhouse gas emissions (see Figure 2-2). Due to the elevation of London being very low in some areas (see Figure 2-1), flooding is a real problem for the city. If a GMSLR of 0.5m is seen then it is predicted that London's sea defences and the Thames barrier would be breached on average once every 100 years [5]. If a GMSLR of 1.0m is seen then the flood protection in London would be breached on average once every 10 years [5].

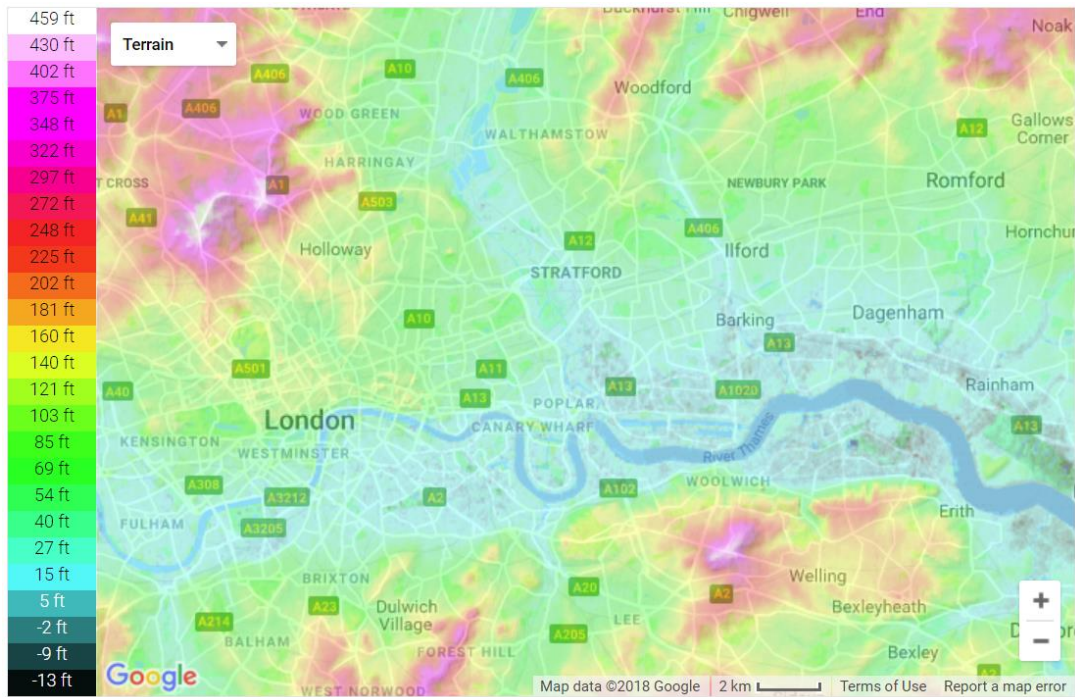


Figure 2-1 Topographic map of London [6]

The UK climate change risk assessment published in 2012 states that the annual cost of flooding in England and Wales is projected to increase from the current value of £1.2 billion to £1.6-£6.8 billion by the 2050s and £2.1-£12 billion by 2080s [7]. The purpose of that report, published in 2012, was to examine the potential changes to flooding and coastal erosion risk as a result of climate change [7]. Flooding is one potential issue and associated social cost of increased CO₂ emissions.

2.1.2.1 Uncertainty in the Social Cost of Carbon (SCC)

The Social Cost of Carbon (SCC) is a relatively new consideration in the global move to reduce CO₂ emissions. The SCC is used to allow governments to evaluate the benefits and drawbacks of implementing different energy technologies which reduce or emit GHG's.

The cost of carbon to the end user typically does not include the cost of damage that carbon has on the environment which ultimately has to be paid by the government (i.e. no carbon tax). If the cost of carbon included the SCC it would likely result in a reduction in the consumption of carbon fuel sources [3]. If there is a reduction in carbon emissions the damage caused by carbon emissions would be reduced meaning the UK government would save money. If a carbon tax was put in place the revenue created could be used to prevent the damage caused from increased GHG emissions, such as improved flood defences for the UK.

However, the SCC varies significantly with different sources, due to uncertainty in the methods used to calculate an SCC. There are two common methodologies used to estimate the SCC.

1. Attempting to value all of the damage caused by the emissions of GHG's
2. Setting a threshold of warming and using economics to value the cost of GHG emissions.

The first methodology at first appears to be the most logical method to put a price on the cost of carbon. However, this methodology requires consideration of all the damage caused by each t/CO₂ emitted, which is very difficult to value. As the carbon emitted today will be in the atmosphere for thousands of years many different considerations need to be taken into account to calculate the SCC this way. The variables include, but are not limited to, population growth, future CO₂ emission, economic growth, the rate of sea level rise (which has been discussed above and has a significant uncertainty within the next 100 years), prediction of extreme weather incidents and the economic impact they will have, the cost of wildlife damage and extinction. Predicting these future events is very difficult and some issues (e.g. wildlife damage and extinction) will be valued differently depending upon opinion, which causes uncertainty in the SCC when calculated in this way.

The SCC, calculated with method 1, is said to not account for all of the damage caused from increases in CO₂ outputs [8]. For example ocean acidification, which increases with increased amounts of absorbed CO₂ and causes damage to sea life and ecosystems, is not accounted for in any models used to estimate the SCC [8].

Furthermore, the complexity continues as the predicted temperature rise of the earth changes. For example, the SCC is likely to be significantly higher if the increase in temperature is around 2°C opposed to 1°C, as at 2°C it is expected that the climate could start to become very unstable [9] and the cost of CO₂ could be extremely detrimental. Figure 2-2 shows estimates of the predicted temperature increases for several different RCP outcomes [10]. The grey areas on Figure 2-2 show the uncertainty in the predicted temperature increases. A global surface temperature change of 1.5°C is likely for all RCP scenarios except RCP2.6 [11]. As the models only predict a range for the expected temperature increase with specific emission outputs it is difficult to estimate the SCC accurately (i.e. if it was known, for certain, that there would be a temperature increase of 2°C then it would make valuing the

SCC simpler, as the damage could be more accurately predicted). The temperature rise uncertainty calculated in models (see Figure 2-2) again causes uncertainty in the SCC value.

If emissions stay at current levels the CO₂ levels are likely to reach over three times that of the preindustrial levels by 2100 [8]. If this was to happen then the temperature increase would be extremely high and the SCC would also need to be extremely high as the damages caused by a temperature increase of +4.5°C would be extreme. However, these are estimates of possible events with uncertainty.

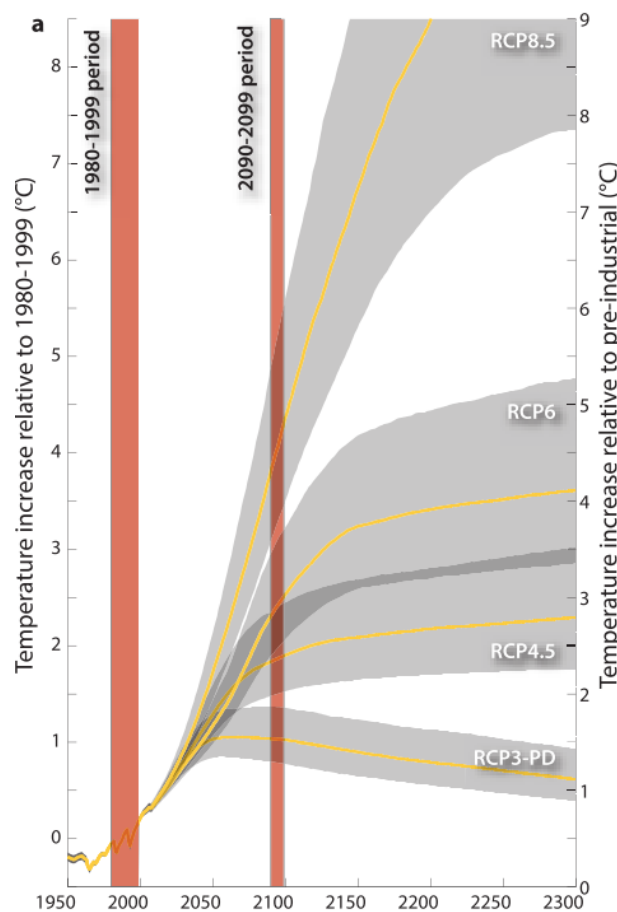


Figure 2-2 Temperature predictions for SRES scenarios and the RCP's [10]

The “tipping point” events which are triggered due to global warming and in turn can release large amounts of GHG's can be irreversible [9]. For example: the melting of ice sheets (such as the Greenland ice sheet), the reduction of the Amazon rainforest and the melting of the permafrost in the arctic. If these three events happen they will all release a large amount of GHG's (i.e. the Amazon would also not absorb the CO₂ it does now) which some scientists predict would cause damage that is irreversible [8]. These tipping point events

would clearly be disastrous for ecosystems but also from an economic standpoint. However, very few SCC predictions, using method 1, take into account these tipping point events. A recent study has taken into account tipping points and found the SCC increased by around 50% with conservative assumptions and by over 200% when using plausible rapid and high impacting tipping points [12].

The reality is that current models which predict the SCC, using method 1, are not detailed enough to take into account all of the complex issues and all of the damage caused from GHG emissions. Although, the scientific understanding of these issues is improving it is taking time and the SCC is likely to only increase once all of the damages are understood and accounted for. Furthermore, it is a very uncertain time in regards to GHG emissions and something needs to be done very soon to put a price on GHG emissions before a tipping point event occurs.

There is an alternative method for calculating the SCC which is method 2. This is a method which has been employed by many, including the UK, after the Paris Agreement [13]. The agreed maximum temperature increase which is believed to be safe is 1.5°C. In order for the planet to stay below this threshold each country has a CO₂ “quota” which it needs to meet. To meet these emissions targets the UK has set an SCC which it believes will ensure the emissions target is met, the method used for valuing the SCC is via a marginal abatement cost (MAC). With an increased SCC the carbon emissions are expected to decrease. This method reduces the need to calculate the cost of damage caused by increased CO₂ emissions and tipping points. Obviously this assumes that the 1.5°C threshold temperature increase is safe for the planet and the damage caused from this rise is minimal, if wrong the damages could again be disastrous. This method of calculating the SCC is likely to be more accurate to allow the UK to achieve its carbon emissions goal, and is calculated using economics opposed to attempting to value all of the variables required when using method 1.

The monetary carbon values used for the UK are significantly higher than the USA and the difference in cost between the two countries increases further for the future [13]. For example the USA and UK have a monetary carbon value used in ex post assessments of policies and projects of around \$40 and \$95 for 2014 and around \$75 and \$350 for 2050, respectively.

Clearly from the description of the methodologies used for calculating the SCC there are many negative impacts caused from increased GHG emissions such as flooding caused by rising sea levels, the melting of ice sheets (such as the Greenland ice sheet), the reduction of the Amazon rainforest and the melting of the permafrost in the arctic. If these negative environmental and economic impacts of increased CO₂ emissions are to be avoided or reversed a significant reduction in CO₂ emissions is required very soon.

2.1.3 Energy sources and energy linked problems

There are many sources of energy available for powering our society as we know it. Some energy sources are used for the production of more useful energy sources (i.e. combustion of fossil fuels to convert stored chemical potential energy into electrical energy at power plants). Many forms of energy can be stored allowing the energy to be released when required. (i.e. gravitational potential energy in water stored in hydroelectric dams, electrochemical energy stored in batteries and thermal energy stored in molten salt). Figure 2-3 shows a diagram of different energy storage and energy production technologies [14].

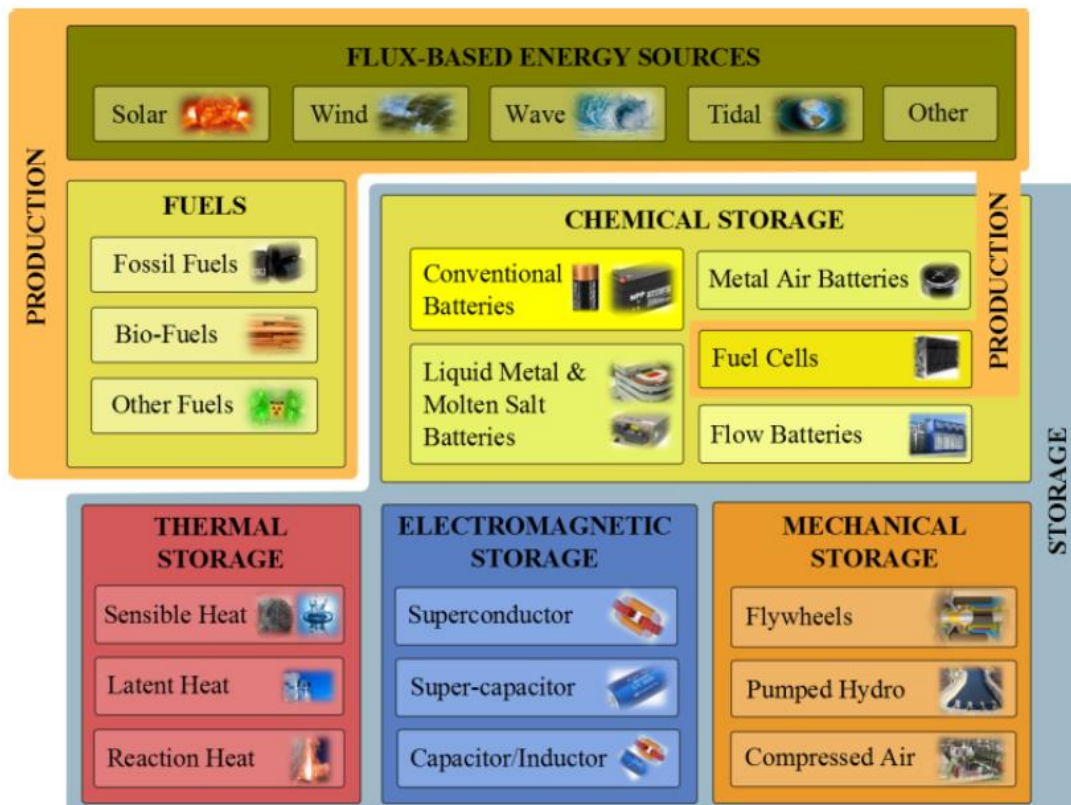


Figure 2-3 Diagram showing sources of energy for production and storage [14]

Currently approximately 26% of the UK's primary energy consumption is used specifically for DSH and DHW production [1]. The majority of this energy, 88%, comes directly from gas and oil with only 2% coming from renewable energy sources [1]. The large amount of energy used for DSH and DHW is not only for the UK, Figure 2-4 shows the final energy consumption of the EU-28 (European Union) for 2015; 25.4% of total energy consumption was used for households [15]. Figure 2-5 shows the energy consumption in EU-28 households, showing 79.2% of household energy consumption in Europe is used for DSH and DHW [16]. This equates to 20.1% of all EU-28 energy consumption is used for DSH and DHW.

When used for energy production gas and oil generate an average of 0.203kg/kWh and 0.245 kg/kWh of CO₂[1]. The amount of energy used annually for DHW and DSH in the UK is 35,426 thousand tonnes of oil equivalent [1] or 4.14×10^{11} kWh. This means on average 3.6×10^{11} kWh of energy is produced from gas and oil for DHW and DSH annually in the UK which results in an average production of 81 million tonnes of CO₂. Meaning, on average 2,892kg of CO₂ is emitted per household annually from gas and oil for DHW and DSH use, assuming the current amount of dwellings in the UK is 28,073,000 [17]. The UK emitted 514.4MtCO_{2e} in 2014, meaning the oil and gas used for DSH and DHW contributes to approximately 16% of all CO₂ emissions in the UK. It is important to note the CO₂ emissions from DSH and DHW are higher than the quoted 16% as this accounts for only the CO₂ emissions produced from gas and oil for DSH and DHW. Decarbonising DSH and DHW represents a huge challenge for the UK which is targeting a reduction of CO₂ emissions of 20% by 2020 and 80% by 2050 [2].

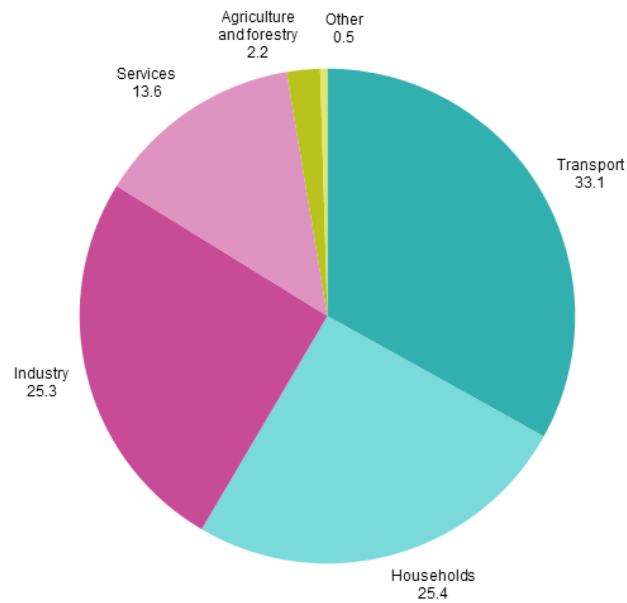


Figure 2-4 Final energy consumption (EU-28), 2015 [15].

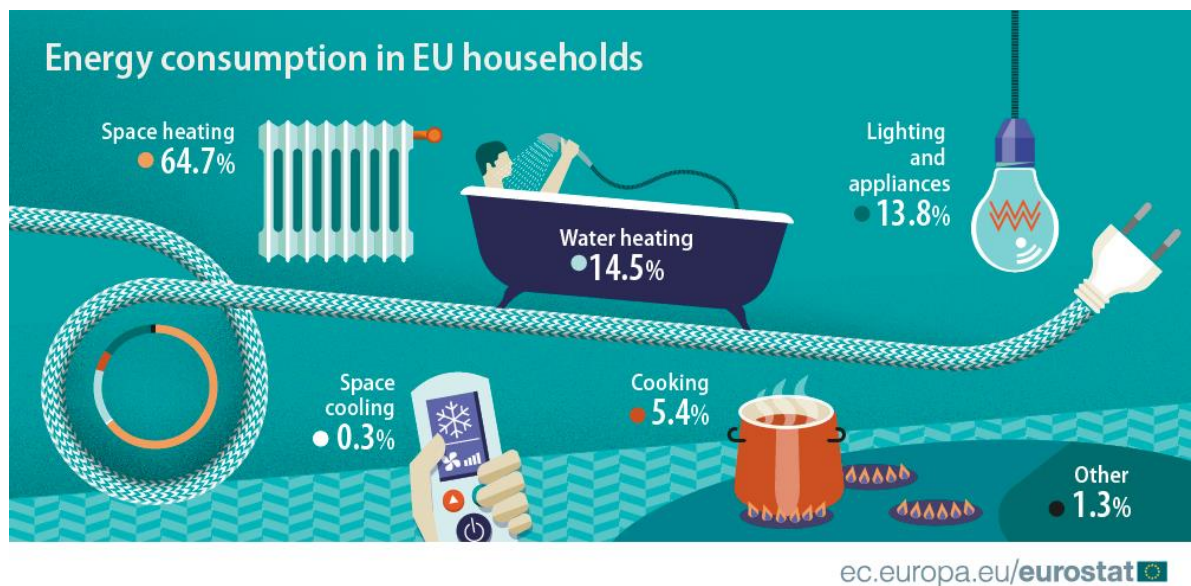


Figure 2-5 Energy consumption in EU households for 2016 [16]

If cleaner energy sources are used to produce the energy required for DHW and DSH it will significantly help the UK meet the CO₂ reduction targets and reduce pollutants emitted from traditional energy sources for DHW and DSH. The amount of energy utilised from renewable sources for DSH and DHW can be increased by effective Thermal Energy Storage (TES). In a domestic environment thermal energy is typically required when supply from renewable sources is low (i.e. thermal energy demand is high in the winter and low in the summer), TES can be used to bridge the gap between supply and demand [18–20].

2.1.4 Thermal energy storage

TES is a way of storing heat in a medium or material so that it can be used at a later time. Research suggests that the use of solar thermal energy storage has the potential to supply around 50% of the heat demand in Europe [21]. There are three main types of TES STES, LTES and TCES [14,22–25].

STES stores or releases heat by heating or cooling material. The amount of energy input is related to the mass, specific heat capacity of the storage material and the temperature difference of the storage medium between its initial and final states [14,22,26]. The storage mediums insulation dictates the success of STES. STES has a relatively low storage density (0.85 – 1.15 kJ/kg [14]) (Figure 2-6) and a high energy loss relative to latent and thermochemical energy storage. STES is a simple and cost effective method for storing heat [14] but it is not space efficient. The heat stored in STES materials can be expressed as $Q = mC_p\Delta T$ [22].

Energy is stored during the phase change of a material for LTES [14]. Heat is lost from the LTES material when the heat is being stored, resulting in unwanted energy losses [24]. LTES does not obtain the same energy density (100-340 kJ/kg for LTES [14]) as TCES (Figure 2-6) and the cost of LTES materials is relatively expensive [24]. The equation for the amount of heat stored in LTES materials is $Q = mL$ [22].

TCES stores energy via a reversible chemical reaction (i.e. $C + \text{heat} \leftrightarrow A + B$) [22]. For domestic use, when material A (typically an anhydrate salt or a sorption material) reacts with material B (typically water) the products are energy (heat) along with product C which is typically a hydrated salt or sorption material (e.g. magnesium sulphate heptahydrate). When material C is exposed to heat, energy is absorbed and material C dissociates into material A + B [24,27]. This principle, in theory, allows two materials (i.e. A + B) to be stored separately for an indefinite amount of time without degradation or energy loss and recombine to release stored energy [25]. Preliminary calculations show that sensible heat losses comprise to approximately 10% of total energy stored; this means the remaining 90% of energy can be stored loss-free [27,28].

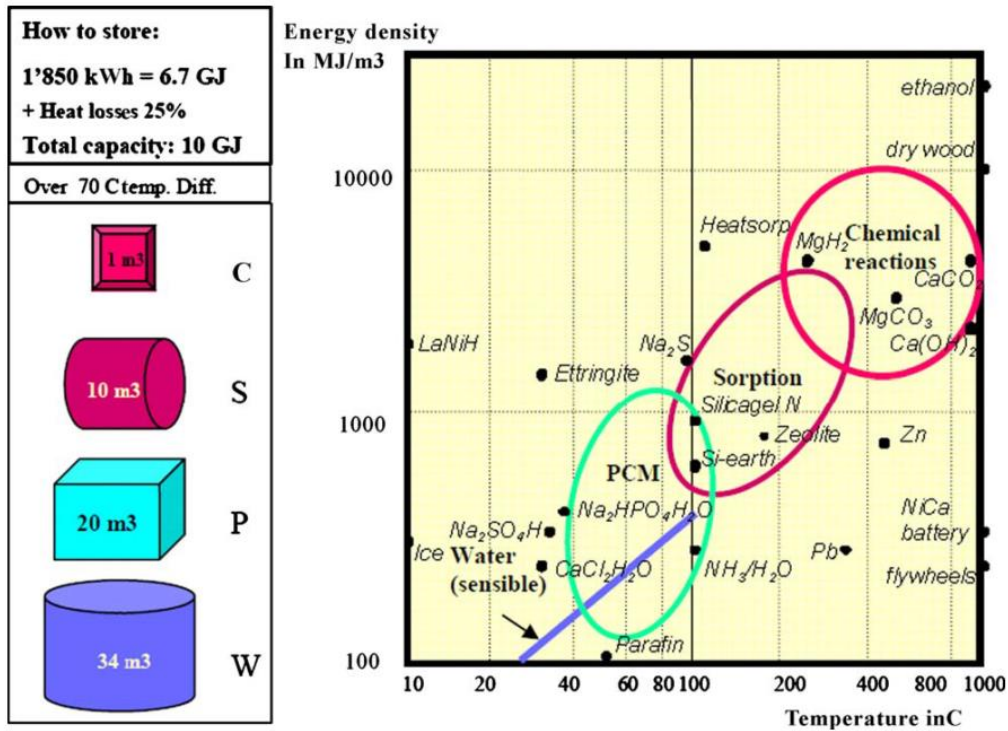


Figure 2-6 Energy density with temperature of different energy storage materials [29]

2.1.5 Sorption and chemical energy storage terminology

Adsorption occurs between two phases (i.e. solid and gas) with the occurrence of certain fields which are saturated with intermolecular forces, such as Van der Waals forces [30]. Typically adsorption is an exothermic process as the adsorbed material has lost a degree of freedom (i.e. $\Delta S < 0$). This then relates to the Gibbs free energy equation (see Equation 2-1).

$$\Delta G = \Delta H - T\Delta S \text{ Equation 2-1 [31]}$$

Where ΔG = change in Gibbs free energy, ΔH = change in enthalpy, T = temperature in Kelvin and ΔS = change in entropy. In order for a reaction to be spontaneous $\Delta G < 0$ hence, $\Delta H = (<0) + T(<0)$ must be negative, assuming T is temperature in kelvin and cannot be negative. As ΔH is negative this is an exothermic process.

Typically [29,32–34] adsorption is split into two types, physical (physisorption) and chemical (chemisorption).

Physisorption is a non-specific loose binding of the adsorbate on to the surface of the solid or liquid, Van der Waals type interactions. Multi layered adsorption is possible and physisorption is strongly dependent upon temperature. One physisorption molecule has two

degrees of freedom allowing for movement on the surface. The energy released in this reaction is generally less than chemisorption [30,35,36].

Chemisorption involves a more specific binding of the adsorbate to the solid or liquid. The bonding is through valence forces (i.e. covalent, ionic or electronic bonding of a gas or liquid onto the surface of the liquid or solid) [29,33,34]. The adsorbed molecules have zero degrees of freedom. It involves a chemical reaction and hence, only monolayer adsorption is possible. Chemisorption is often irreversible due to the large amount of energy required to break the chemical bonding [30,35,36].

2.1.5.1 Ambiguity in defining the processes taking place in sorption energy storage materials

The definition of adsorption and absorption is clear. Adsorption being the process of a substance binding to the surface of another [22,29,37,38]. Absorption is the process where a gas or liquid enters into the bulk of a liquid or solid binding with the material [22,29,32,37].

However, there appears to be some ambiguity or confusion in attempting to categorise the processes taking place in thermochemical energy storage materials. N'Tsoukpoe et al. [29] states the use of chemical storage, thermochemical storage, sorption storage, differs from one author to another creating a difficulty in finding a clear boundary between them. Yu et al. [32] states there is a difficulty distinguishing clear boundaries between terms (thermochemical, compact, sorption, chemical etc.). Ding et al. [37] states there is difficulty in making clear boundary distinctions between chemical storage, thermochemical storage and sorption storage. Figure 2-7 gives a classification of chemical and sorption storage however, the author (N'Tsoukpoe et al.) [29] does not give any definition of thermochemical without sorption.

There also does not appear to be any clear definitions of **chemical absorption** or **chemical adsorption**. The definition of physisorption and chemisorption is clear [33] [34]. Although, it is apparently difficult to establish exactly which process is taking place and, both may be occurring simultaneously within a material [32] [33]. This may be why it is difficult to define which process is occurring in a thermochemical energy storage system. This becomes even more difficult in the case of composite materials (i.e. salt hydrates within porous host matrixes). This may be the reason, for simplicity, why most authors simply refer

to the process as “sorption” energy storage [29] [37] [22] to include **chemical absorption**, **physical absorption**, **chemical adsorption** and **physical adsorption** processes.

In the case of heat of hydration from $MgSO_4$ there is also ambiguity which process is occurring. N’Tsoukpoe et al. [29] classes the process as chemisorption (**chemical adsorption**). Yu et al. [32] states chemical reactions corresponding to sorption mainly consists of two kinds of reactions: “co-ordination reaction of ammoniate with ammonia” and “hydration reaction of salt hydrate with water”. Yu et al. further states that both reactions are technically co-ordination reactions as molecules of ammonia or water vapour are attracted by metal ions to form co-ordinate bonds [32]. Moreover, it is still not clear if this should be classed as **adsorption** or **absorption** and many authors simple refer to it as a chemical reaction [32]. Aristov et al. [39] Investigates salt hydrates in host materials, more specifically $CaCl_2$ in silica gel. The paper refers to the water sorption of this material as solid absorption (chemical reaction) and liquid absorption which account for 10-15% and ~80% water sorption, respectively. It appears due to the complex nature of the sorption process, which may or may not include physical and chemical ad/absorption, it is best to simply refer to the process as a sorption reaction or whichever term is used it should be taken with reservations unless explicitly defined.

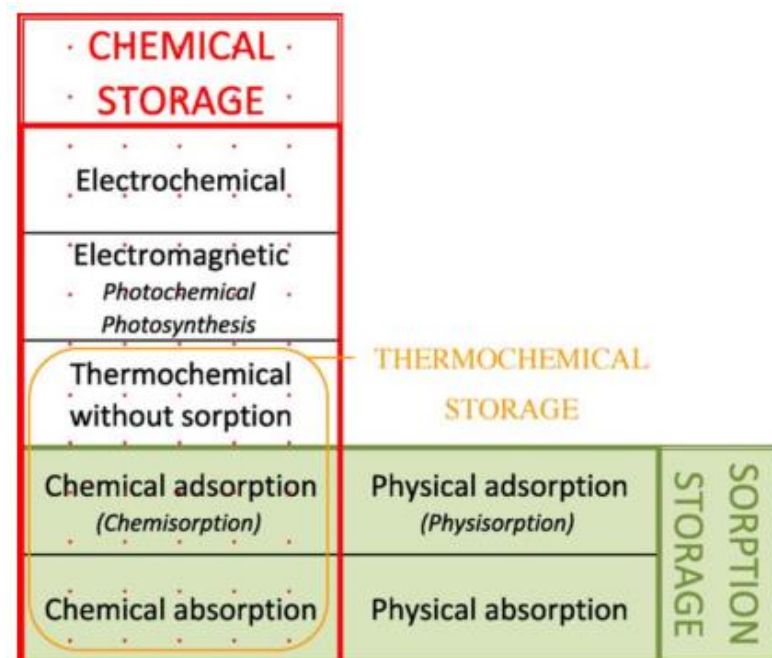


Figure 2-7 Chemical and sorption energy storage classification [29]

2.2 The reason TCES has potential for domestic interseasonal thermal energy storage

The reasons why TCES has so much potential for domestic interseasonal thermal energy storage include;

- Ability to be charged using a solar thermal collector in European summer times - Materials under investigation can store large amounts of heat after being charged at below 150°C.
- Ability to discharge (hydrate) in European winter conditions (typically with help of a borehole) - It is assumed 10°C and a p_{H_2O} of 1.3kPa is achievable in winter times.
- Thermal energy can be stored indefinitely with only approximately 10% sensible heat losses.
- Typically safe materials which is vital if the materials are to be used in a domestic setting.

Many of the materials under investigation for domestic thermal energy storage are either absorbents or salt hydrates. Many of which are used for everyday purposes such as water purification, bath salts and industrial absorbents. The most important reason why TCES materials are rapidly becoming a large research interest is due to their high energy densities (see Figure 2-6 and Figure 2-8) [25,36,40–42].

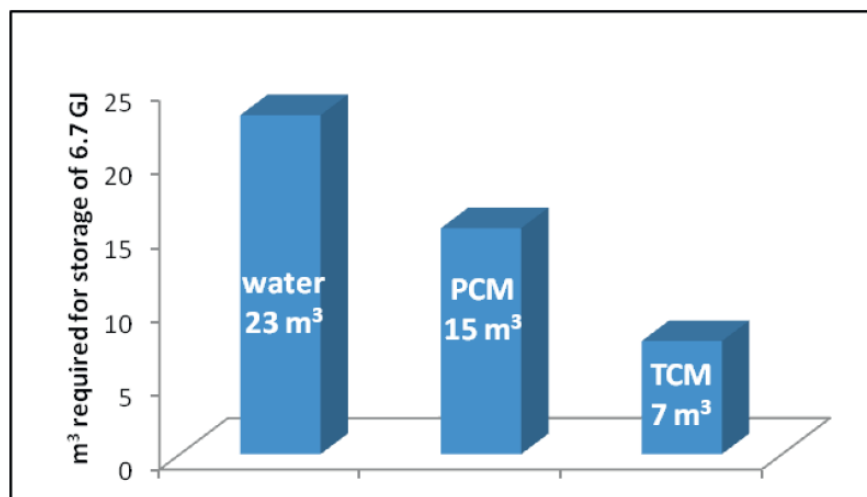


Figure 2-8 An indication of volume of storage material needed to store 6.7GJ/year of thermal energy for an average household [24]

The advantage in energy storage density means a TCES reactor system should be economically viable and have a small enough volume enabling it to be integrated within a domestic environment without using large amounts of valuable domestic real estate [41]. Table 2-1 highlights the advantages of TCES materials for domestic energy storage solutions.

Table 2-1 Comparison of different TES mechanisms based on various performance factors [22]

Performance Parameter	Type of Thermal Energy Storage		
	Sensible TES	Latent TES	Chemical TES (Sorption and Thermochemical)
Temperature range	Up to: 110 °C (water tanks) 50 °C (aquifers and ground storage) 400 °C (concrete)	20-40 °C (paraffins) 30-80 °C (salt hydrates)	20-200 °C
Storage density	Low (with high temperature interval): 0.2 GJ/m ³ (for typical water tanks)	Moderate (with low temperature interval): 0.3-0.5 GJ/m ³	Normally high: 0.5-3 GJ/m ³
Lifetime	Long	Often limited due to storage material cycling	Depends on reactant degradation and side reactions
Technology status	Available commercially	Available commercially for some temperatures and materials	Generally not available, but undergoing research and pilot project tests
Advantages	Low cost Reliable Simple application with available materials	Medium storage density Small volumes Short distance transport possibility	High storage density Low heat losses (storage at ambient temperatures) Long storage period Long distance transport possibility Highly compact energy storage
Disadvantages	Significant heat loss over time (depending on level of insulation) Large volume needed	Low heat conductivity Corrosivity of materials Significant heat losses (depending on level of insulation)	High capital costs Technically complex

A comprehensive review of thermochemical heat storage systems was conducted and the results suggest, as mentioned, that TCES is not at a stage ready for commercialisation [25,35,36]. There are still many issues which exist and need to be optimised including: the development of composite materials, reactor designs and economic feasibility investigations.

2.3 Possible domestic TCES material candidates

Recently there have been several papers looking at finding effective candidates for TCES, some studies include [35,36,43,44]. All studies have different criteria used to specify the most effective route to take however, several reoccurring key factors include [22,36];

- Cost
- Availability
- Cycling behaviour
- Hydration kinetics
- Dry state thermal conductivity >0.06 (W/mk)
- Pore Volume >1.7 (cm³/g)
- Toxicity and Safety
- Bulk Density >0.4 (g/cm³)
- Corrosiveness
- Porosity >65% (m³/m³)
- Energy storage density >200 (kJ/kg)
- Desorption/Charging temperature
- Specific surface area >15 for Macroporous,
>500 for mesoporous (m²/g)

A review paper by Abedin et al. [22] reviews TCES systems. The review presents data (see Table 2-2) which highlights MgSO₄ as a promising potential domestic TCES material. MgSO₄ has the largest energy density and the desorption (charging temperature) is within a suitable temperature range for domestic TES.

Table 2-2 Promising materials for thermochemical energy storage [22]

Thermochemical Material (C)	Solid Reactant (A)	Working Fluid (B)	Energy Storage Density of Thermochemical Material (GJ/m ³)	Charging Reaction Temperature (°C)
MgSO ₄ ·7H ₂ O	MgSO ₄	7H ₂ O	2.8	122
FeCO ₃	FeO	CO ₂	2.6	180
Ca(OH) ₂	CaO	H ₂ O	1.9	479
Fe(OH) ₂	FeO	H ₂ O	2.2	150
CaCO ₃	CaO	CO ₂	3.3	837
CaSO ₄ ·2H ₂ O	CaSO ₄	2H ₂ O	1.4	89

N'Tsoukpoe et al. [45] assessed 125 possible materials for domestic TCES. Figure 2-9 shows the 3 stage process used to cull the materials. The results showed three promising materials, one of these materials being MgSO₄. It must be noted this study investigated the material's potential on a small TGA and DSC (~10mg) scale. The materials will possible act very differently on a large scale. Table 2-3 gives a more numerical summary of the more promising salt hydrates assessed [45].

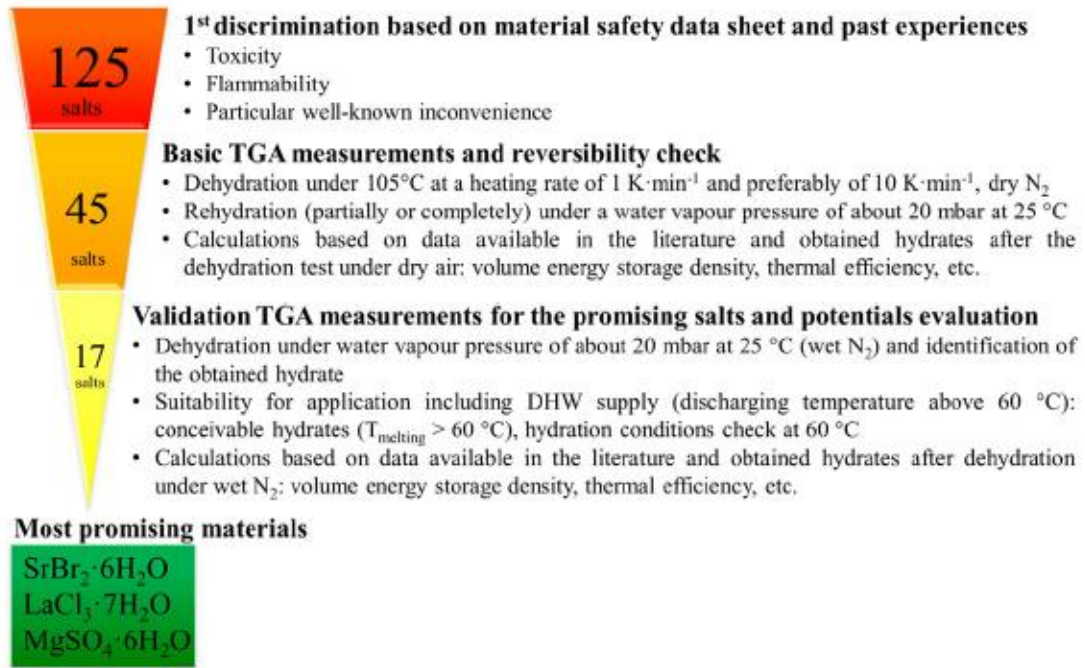


Figure 2-9 The screening process used for the salt hydrates assessed by N'Tsoukpoe et al. [45]

Table 2-3 Important thermodynamic characteristics of candidate salt hydrates after dehydration under a water partial vapour pressure ($p_{H_2O} = 21\text{mbar}$, 105°C) (references in table refer to references within the paper by N'Tsoukpoe et al. [45]).

Hydrated salt	Al ₂ (SO ₄) ₃ ·18H ₂ O	CaBr ₂ ·4H ₂ O	Ce(SO ₄) ₂ ·4H ₂ O	K ₂ CO ₃ ·1.5H ₂ O	LaCl ₃ ·7H ₂ O	La(NO ₃) ₃ ·4H ₂ O
Dehydrated salt	Al ₂ (SO ₄) ₃ ·8.5H ₂ O	CaBr ₂ ·3H ₂ O	Ce(SO ₄) ₂ ·2H ₂ O	K ₂ CO ₃ ·0.8H ₂ O	LaCl ₃ ·H ₂ O	La(NO ₃) ₃ ·1.5H ₂ O
T _{melting} (°C)	88	80–110 [28,55,56]	180	>80	91	86–95 [43,57]
ρ _s (t m ⁻³)	1.69	2.2	3.91	2.15	2.223	2.459 [43,57]
n	9.5	1	2	0.7	6	2.5
ΔH _r (kJ mol ⁻¹)	526.8	59.7	58 ^a	44.6	355.5	158.6
ΔH _{r,m} (kW h kg ⁻¹)	0.220	0.061	0.040	0.075	0.266	0.111
ΔH _{r,v} (kW h m ⁻³)	371	134	156	161	591	273
ΔH _{net} (kJ mol ⁻¹)	103.1	15.1		13.4	88.0	47.1
ΔH _{net,v} (kW h m ⁻³)	73	34		48	146	81
η (%)	19.6	25.3		30.0	24.7	29.7
ΔH _{r,v*} (kW h m ⁻³)	259	117		138	359	213
ΔH _{net,v*} (kW h m ⁻³)	51	30		41	89	63
Hydrated salt	LiCl·H ₂ O	MgCl ₂ ·6H ₂ O	MgSO ₄ ·6H ₂ O	Na ₂ S ₂ O ₃ ·2H ₂ O	SrBr ₂ ·6H ₂ O	SrCl ₂ ·2H ₂ O
Dehydrated salt	LiCl	MgCl ₂ ·4.7H ₂ O	MgSO ₄ ·2H ₂ O ^b	Na ₂ S ₂ O ₃	SrBr ₂ ·H ₂ O	SrCl ₂ ·H ₂ O
T _{melting} (°C)	99	117–118	88.5–93 ^b	–	88	100 [38]
ρ _s (t m ⁻³)	1.7	1.569	2.04 [58]	1.69 ^c	2.386	2.672
n	1	1.3	4	2	5	1
ΔH _r (kJ mol ⁻¹)	62.2	71.5	225.1	110.3	337.0	59.0
ΔH _{r,m} (kW h kg ⁻¹)	0.286	0.098	0.274	0.158	0.263	0.084
ΔH _{r,v} (kW h m ⁻³)	486	153	558	267	628	225
ΔH _{net} (kJ mol ⁻¹)	17.6	13.5	46.8	21.2	114.0	14.4
ΔH _{net,v} (kW h m ⁻³)	137	29	116	51	213	55
η (%)	28.3	18.9	20.8	19.2	33.8	24.4
ΔH _{r,v*} (kW h m ⁻³)	322	130	340	203	392	180
ΔH _{net,v*} (kW h m ⁻³)	91	25	71	39	133	44

Trausel et al [24] calculated theoretical energy densities of salt hydrates the results show MgSO₄ as a promising candidate material (see Table 2-4) as both its energy density (2.81 GJ/m³) and price per GJ (€73/GJ) are the 5th and 3rd best values presented, respectively.

Table 2-4 Energy densities and prices of selected salt hydrates for use as TCES materials [24]

Reaction	M (kg/mol)	ρ (kg/m ³)	Δh_r (kJ/mol hyd. salt)	Δh_m (kJ/kg hyd. salt)	Δh_v (GJ/m ³ hyd. salt)	Price (€/1000kg)	Price (€/GJ)
$\text{CaCl}_2 \cdot 6\text{H}_2\text{O} \leftrightarrow \text{CaCl}_2 \cdot 2\text{H}_2\text{O} + 4\text{H}_2\text{O}$	0.2190	1710	236.9	1082	1.85	116	107
$\text{CaCl}_2 \cdot 6\text{H}_2\text{O} \leftrightarrow \text{CaCl}_2 + 6\text{H}_2\text{O}$	0.2190	1710	361.2	1649	2.82	116	70
$\text{MgCl}_2 \cdot 6\text{H}_2\text{O} \leftrightarrow \text{MgCl}_2 + 6\text{H}_2\text{O}$	0.2033	1569	406.7	2001	3.14	154	77
$\text{MgCl}_2 \cdot 6\text{H}_2\text{O} \leftrightarrow \text{MgCl}_2 \cdot 1\text{H}_2\text{O} + 5\text{H}_2\text{O}$	0.2033	1569	360.9	1775	2.79	154	87
$\text{MgCl}_2 \cdot 6\text{H}_2\text{O} \leftrightarrow \text{MgCl}_2 \cdot 2\text{H}_2\text{O} + 4\text{H}_2\text{O}$	0.2033	1569	252.0	1239	1.94	154	125
$\text{Na}_2\text{S} \cdot 5\text{H}_2\text{O} \leftrightarrow \text{Na}_2\text{S} + 5\text{H}_2\text{O}$	0.1681	1580	312.2	1857	2.93	348	220
$\text{Na}_2\text{S} \cdot 5\text{H}_2\text{O}^b \leftrightarrow \text{Na}_2\text{S} \cdot 0.5\text{H}_2\text{O} + 4.5\text{H}_2\text{O}$	0.1681	1580	283.3	1685	2.66	348	242
$\text{Na}_2\text{S} \cdot 9\text{H}_2\text{O} \leftrightarrow \text{Na}_2\text{S} + 9\text{H}_2\text{O}$	0.2402	1430	532.7	2218	3.17	348	203
$\text{MgSO}_4 \cdot 7\text{H}_2\text{O} \leftrightarrow \text{MgSO}_4 + 7\text{H}_2\text{O}$	0.2465	1680	411.8	1671	2.81	77	73
$\text{Na}_2\text{SO}_4 \cdot 10\text{H}_2\text{O} \leftrightarrow \text{Na}_2\text{SO}_4 + 10\text{H}_2\text{O}$	0.3222	1464	563.4	1749	2.56	54	56
$\text{SrBr}_2 \cdot 6\text{H}_2\text{O}^c \leftrightarrow \text{SrBr}_2 \cdot 1\text{H}_2\text{O} + 5\text{H}_2\text{O}$	0.3555	2386	300.6	814.4	2.02	2400	2838

2.3.1 Summary of possible TCES material candidates

Based on volumetric energy densities MgCl_2 , Na_2S , CaCl_2 and MgSO_4 are the most promising candidate materials for domestic TCES [24,41]. However, the intention to study MgSO_4 for this research project and investigate further its potential as a domestic TCES material was reinforced after reviewing the literature by Abedin, N'Tsoukpoe and Trausel et al. which all identified MgSO_4 as a promising potential candidate material for domestic TCES [46,47]. The literature reviewed also provided an outline of the required characteristics that make a salt hydrate suitable for TCES.

2.4 The characteristics of MgSO_4 for TES

This section of work reviews literature which presents the characteristics of MgSO_4 for use as a TCES material.

2.4.1 The dehydration of MgSO_4

Studies [23,28,48,49] present experimental results of the dehydrating of MgSO_4 . Figure 2-10 shows TGA and DSC plots showing dehydration measurements for $\text{MgSO}_4 \cdot 7\text{H}_2\text{O}$, Figure 2-11 shows TGA dehydration results for the dehydration of $\text{MgSO}_4 \cdot 7\text{H}_2\text{O}$. The results show the mass loss from $\text{MgSO}_4 \cdot 7\text{H}_2\text{O}$ occurs in three distinct steps [28] [23] [48]. The first two steps which occur below 150°C can be seen to be endothermic (i.e. energy storing transitions). These two steps are a result of the loss of around 6.9 H_2O molecules [23,28,48]. The final loss of 0.1 H_2O molecules is exothermic and occurs at around 280°C . This dehydration process can be further confirmed with the use of in-situ X-

ray Diffraction (XRD) (Figure 2-12) [44]. This shows $\text{MgSO}_4 \cdot 7\text{H}_2\text{O}$ can be dehydrated at 150°C using a solar thermal collector achieving an 86% dehydration, equating to $\sim 350\text{kJ/mol}$ [23,28,48,49], confirming MgSO_4 as an ideal candidate material for domestic inter seasonal TCES.

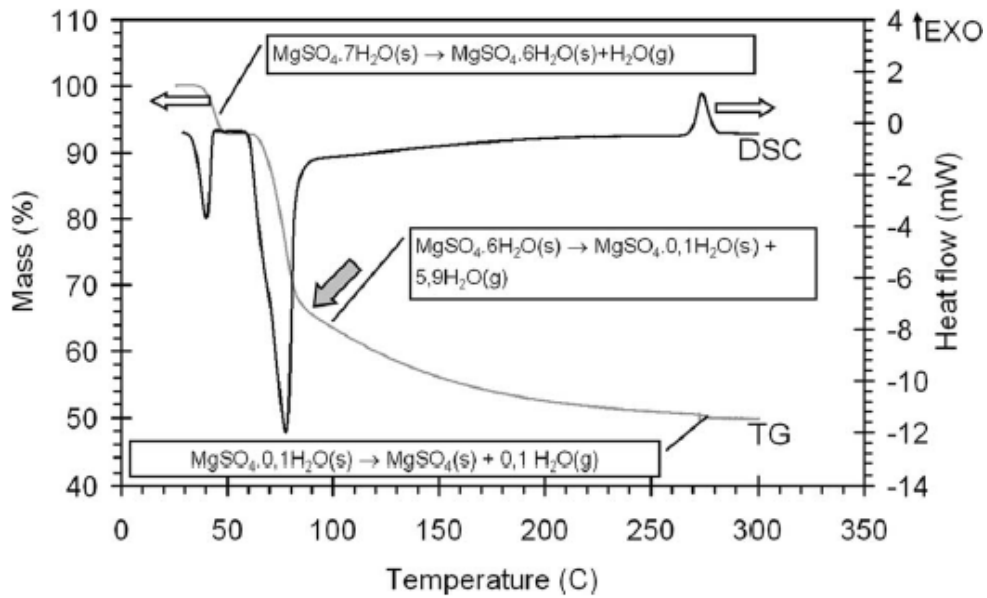


Figure 2-10 TGA mass loss data and DSC enthalpy measurements for the dehydration of $\text{MgSO}_4 \cdot 7\text{H}_2\text{O}$ [50]

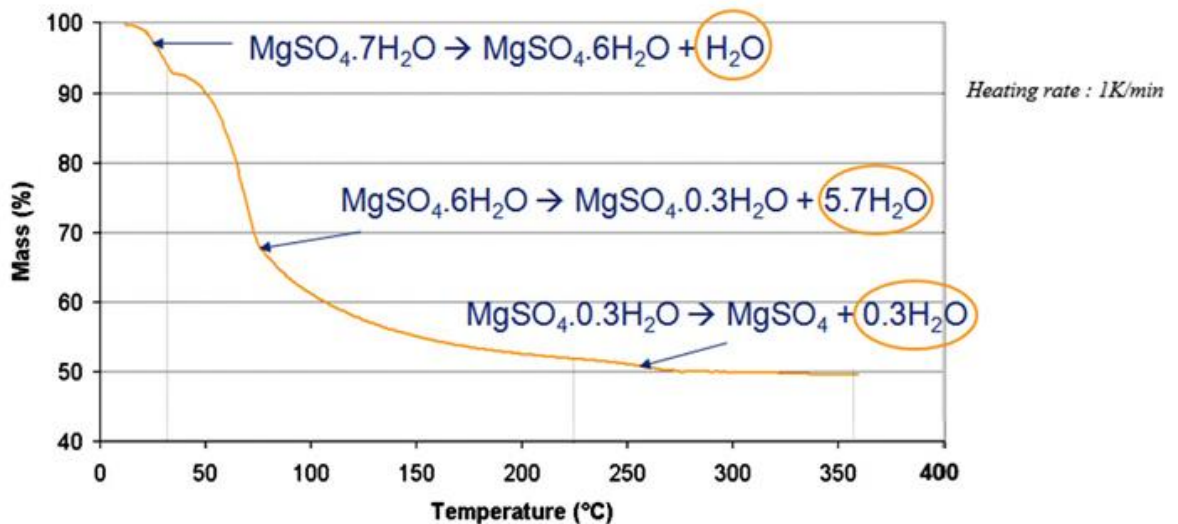


Figure 2-11 TGA mass loss measurements for the dehydration of $\text{MgSO}_4 \cdot 7\text{H}_2\text{O}$ [23]

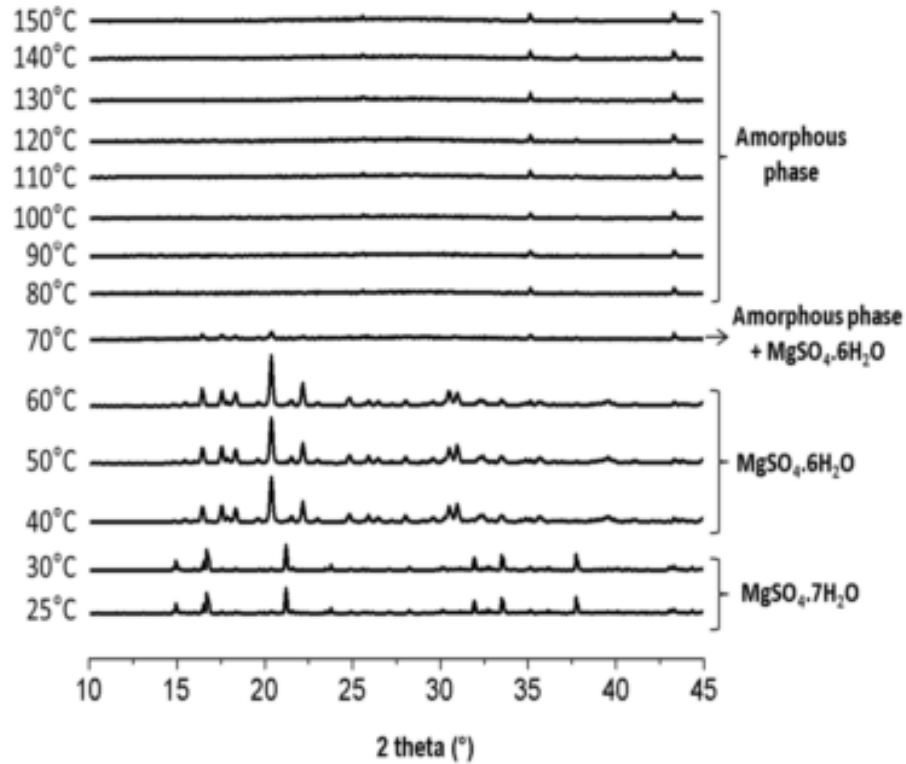


Figure 2-12 The changing XRD diffraction patterns of $MgSO_4 \cdot 7H_2O$ as it is dehydrated [51]

Hongois et al. [23] showed the distinct three step dehydration process of $MgSO_4 \cdot 7H_2O$ can be ‘smoothed’ out when $MgSO_4 \cdot 7H_2O$ is impregnated within a zeolite. Figure 2-13 shows TGA dehydration measurements of zeolites impregnated with varying wt% of $MgSO_4$. The authors state “ $MgSO_4$ does not behave like a salt hydrate when locked within the zeolite pores” [23]. The use of zeolites as host materials is discussed in more detail in section 2.5.1.

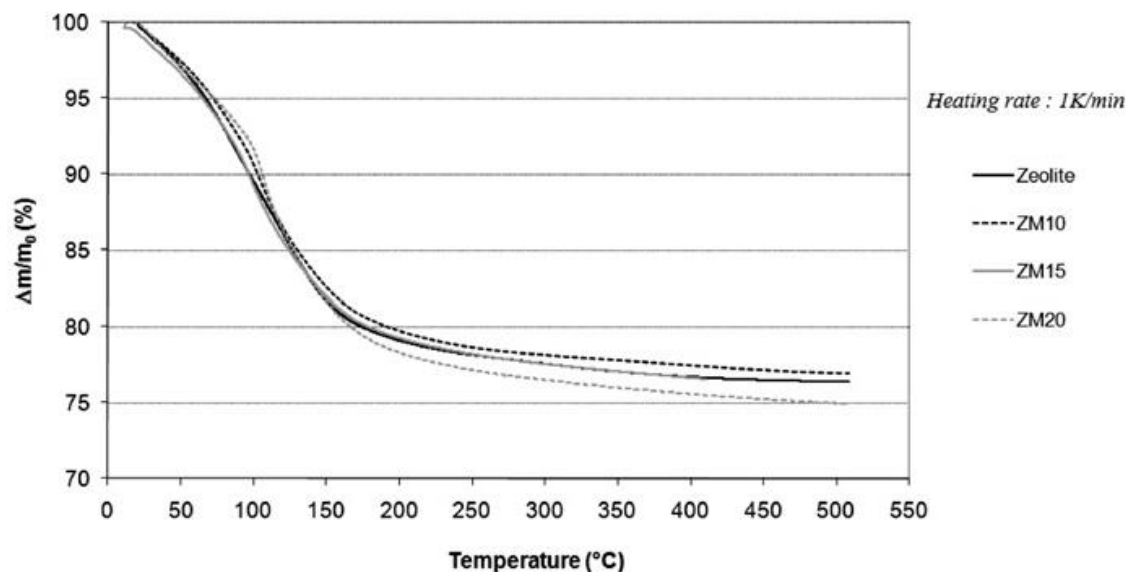


Figure 2-13 TGA measurements showing the mass loss of a zeolite and three zeolite + $MgSO_4$ composite materials [23]

2.4.1.1 Cracking and structural changes of $MgSO_4$ after dehydration

Van Essen et al. [28] used an SEM to take images of pure $MgSO_4 \cdot 7H_2O$ before any dehydration, after dehydration and finally after rehydration. A particle size of 38-106 μm was used. Results show after dehydration cracks appear and a smaller particle size is created, some particles ~ 1 -10 μm (Figure 2-14). Upon rehydration the size of particles was observed not to change size considerably. This behaviour is seen in other salt hydrates [52]. This could be due to the changes to the material porosity although; more research is needed [28]. Smaller particles and increasing porosity could prove to be beneficial to the hydration of $MgSO_4$.

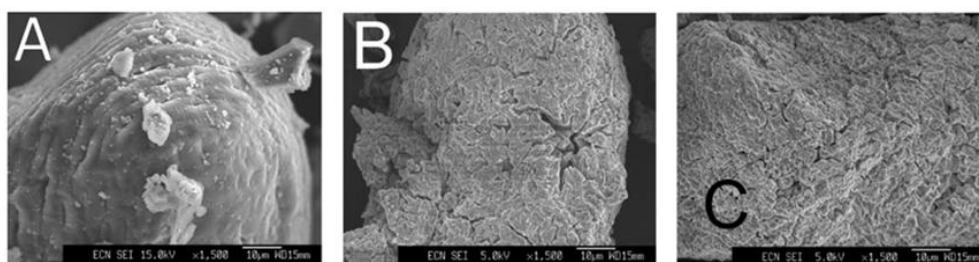


Figure 2-14 SEM images of $MgSO_4 \cdot 7H_2O$ before (a) after dehydration (b) and after rehydration (C) [50]

Zhang et al. [53] investigated the dehydration process of $MgSO_4 \cdot 7H_2O$ on a molecular dynamics scale. The dehydration described is similar to a through-hydration process suggested by Linnow et al. [46] and could verify the results of the study.

The MgSO_4 is said to become porous. The material becoming porous has been identified by other studies [28]. Zhang et al. [53] suggests for quicker dehydration kinetics a large surface area /volume ratio should be utilised, possibly explaining why zeolites enhance the kinetics of MgSO_4 [48,49].

2.4.1.2 Melting of MgSO_4 upon dehydration

Upon dehydration of $\text{MgSO}_4 \cdot 7\text{H}_2\text{O}$ a melting point of 50°C is observed [28] (seen in Figure 2-15, indicated by a grey circle). This melting point is problematic as it causes a reduction in the bed porosity of the material and the ability for vapour to travel through the material [23,28,48,49,52,54], which limits the hydration ability. Essen et al [28] investigated this problem by varying heating rates, sample and particle sizes. Results revealed low heating rates ($\leq 1^\circ\text{C}/\text{min}$), small particle size ($\leq 200\mu\text{m}$) and or small sample sizes ($\leq 5\text{ mg}$) all prevented melting from being observed. These constraints would be difficult to meet in practical applications. Figure 2-15 shows smaller particles result in a faster dehydration [50].

Whiting [48] and Hongois [23] used zeolite + MgSO_4 composite materials. In both cases no signs or mention of melting occurred while dehydrating the material to 150°C . If the use of host materials can diminish or eliminate all signs of melting this would reduce the constraints of particle size, heating rate and sample size, possibly simplifying the application of MgSO_4 as a TCES material in practical situations. More research is needed to assess the impact melting and hence, high heating rates have on the cycle stability and energy storing potential of MgSO_4 .

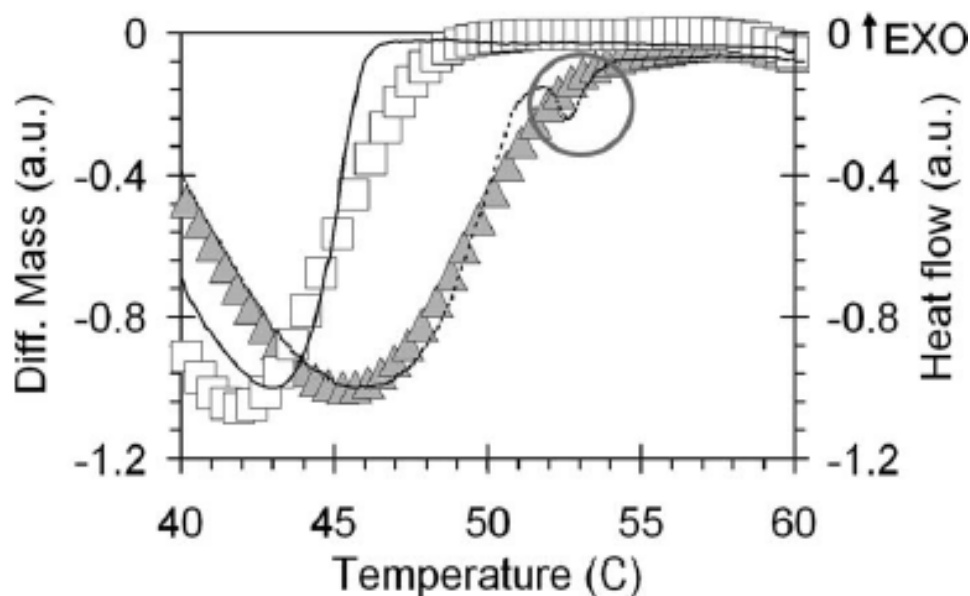


Figure 2-15 DSC dehydration measurements of $\text{MgSO}_4 \cdot 7\text{H}_2\text{O}$. Squares and triangles represent particles of size (20-38 μm) and (200-500 μm) respectively [50]

Increasing the water partial vapour pressure ($p\text{H}_2\text{O}$) while dehydrating $\text{MgSO}_4 \cdot 7\text{H}_2\text{O}$ increases the dehydration rate [55] [56]. Contradicting reasons are suggested for why this occurs, an increase in thermal conductivity of the humid air is one suggestion [56] or increased cracks cause increased vapour channels allowing for faster dehydration is another suggestion [55]. This phenomenon is called the Topley-Smith effect.

2.4.1.3 Heating rate effects on the dehydration of MgSO_4

Rammelberg et al. and Opel et al. [25,57] have investigated the effect heating rates have on the dehydration of salt hydrates. As the heating rate increases the temperatures at which the dehydration steps occur increases. This needs to be considered when testing the materials on a large scale as higher heating rates will result in a higher dehydration temperature required to achieve the same enthalpy compared to a lower heating rate. Again no studies have been undertaken into the affect this has on the energy storing potential or cycle stability of the material.

2.4.2 The hydration of MgSO_4

Most experiments on the hydration of MgSO_4 occurs at around 20-30°C, within a nitrogen-water atmosphere [23,28,48]. Hydration of MgSO_4 is a more linear process relative to the dehydration. Initial hydration occurs quickly and then decreases. Figure 2-16 shows DSC and TGA hydration measurements of 10mg samples of pure MgSO_4 with varying

particle sizes [28]. The particle size has very little effect on the hydration however, it is clear to see the rate of hydration change which occurs at around 300mins.

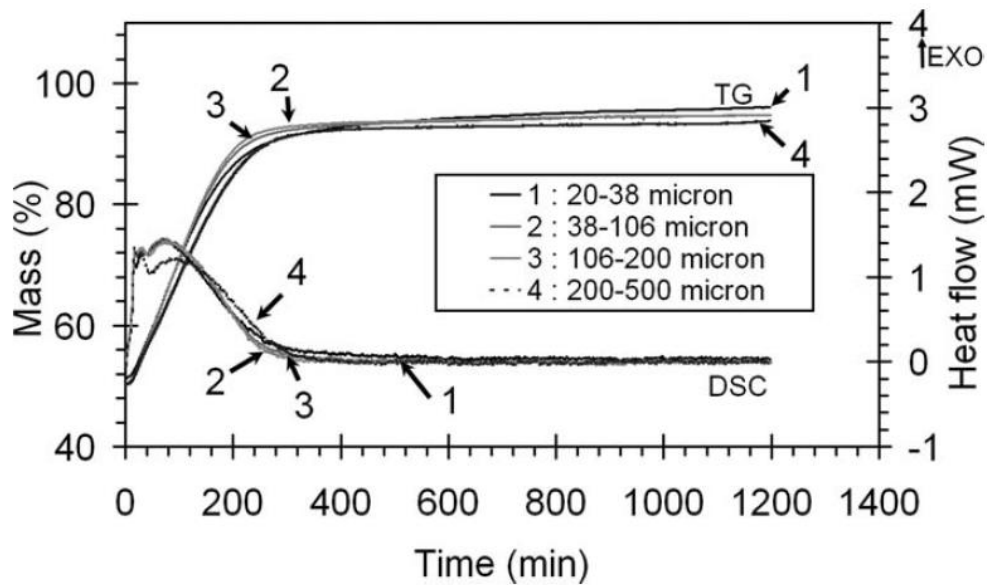


Figure 2-16 TGA & DSC hydration measurements of $MgSO_4$ with varying particle sizes [50]

$MgSO_4$, as a fine powder, is difficult to use within storage reactors as the material rapidly forms a skin of hydrated salt on the surface of the bulk powder when it reacts with humid air [23]. This is also known as agglomeration of the material [58]. This skin inhibits the fluid transfer and therefore reduces the reaction rate and limits the overall power output. This phenomenon is not explicitly noted by many authors although; Posern et al. [49] did mention salts could be ‘clogging’ pores of porous host materials and Van Essen et al. [28] did notice a small layer thickness results in quicker hydration times. When desorption occurs $MgSO_4$ becomes cracked and possibly more porous; this observation almost contradicts the results of the material forming a skin [23]. This is another difficulty in the application of pure $MgSO_4$ in large scale systems.

Linnow et al. [46] presents micrographs of the hydration process of $NaSO_4$, at 92% RH and $23^\circ C$, showing different stages of the hydration (Figure 2-17). Figure 2-17 shows the hydration of $NaSO_4$ is a through hydration process. The salt hydrate crystallizes first ($NaSO_4 \cdot 10H_2O$) before it forms into a solution (Na_2SO_4). Crystallisation acts as a barrier inhibiting hydration of concealed salt hydrates at lower hydration levels [23,46,49]. This is likely to be the same for the hydration of $MgSO_4$.

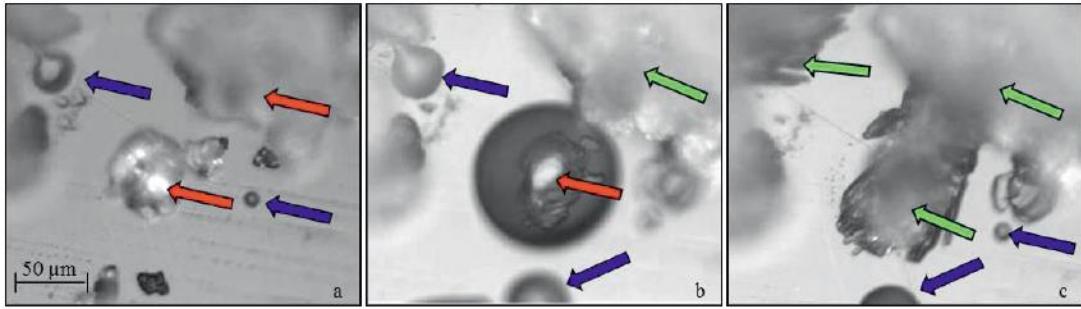


Figure 2-17 Micrographs of the hydration of NaSO_4 at 92% RH and 23°C after 2 hours (a), 3 hours (b) and 6 hours (c). Red arrows point to NaSO_4 green arrows to $\text{NaSO}_4 \cdot 10\text{H}_2\text{O}$ and blue arrows to $\text{Na}_2\text{SO}_2(\text{aq})$ [46]

2.4.2.1 Partial vapour pressure effects on the hydration of MgSO_4

Figure 2-18 shows Simultaneous Thermal Analysis (STA) measurements of the hydration of pure MgSO_4 at variable temperatures and water partial vapour pressure ($p_{\text{H}_2\text{O}}$) [28]. Clearly higher $p_{\text{H}_2\text{O}}$ hydrates the material much faster [23] [46]. Lower $p_{\text{H}_2\text{O}}$ or higher temperature reduces the hydration capacity to only 1 H_2O molecule. Similarly, Chipera and Vaniman et al. [59] and Ferchaud et al. [44] found MgSO_4 only converted to $\text{MgSO}_4 \cdot 6\text{H}_2\text{O}$ at 50°C when the $p_{\text{H}_2\text{O}}$ was 9.3kPa. Figure 2-19 [54] shows a graph of theoretical results plotted with experimental results, confirming the experimental results. The $p_{\text{H}_2\text{O}}$ needs to be considered when designing TCES systems using pure MgSO_4 .

The hydration process of MgSO_4 takes a large amount of time leading to poor power output [44]. Other studies [25,57] show that as the partial vapour pressure increases so too does the rate of hydration and therefore power output.

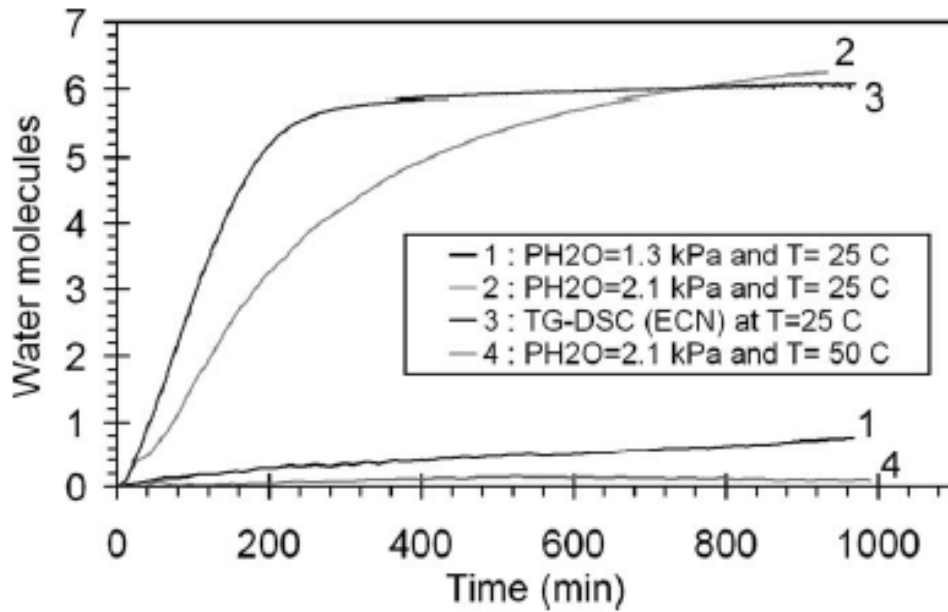


Figure 2-18 Simultaneous Thermal Analysis (STA) measurements showing the water uptake of $MgSO_4$ as it is hydrated under different conditions [50]

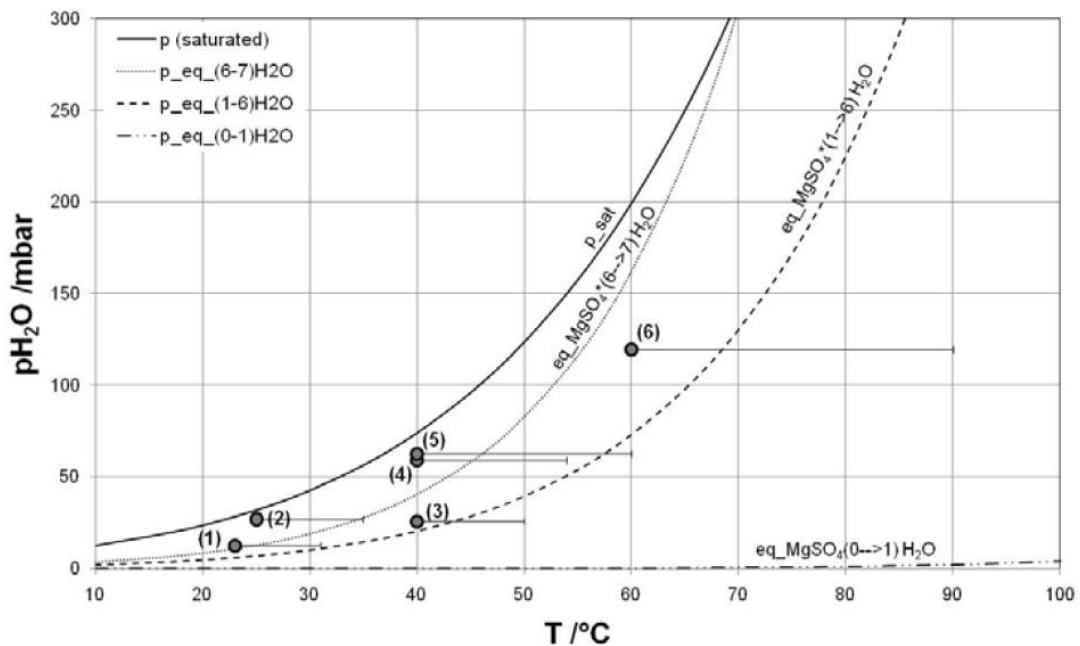


Figure 2-19 Equilibrium curves for the hydration of $MgSO_4$ [54]

Table 2-5 presents measurements from 6 hydration experiments of $MgSO_4 \cdot H_2O$ showing that the inlet temperature (θ) relative humidity (ϕ) and partial vapour pressure (p_{H_2O}) all play big parts in the observed temperature lift (ΔT_{max}) [54]. With increasing partial vapour pressure the maximum outlet temperature achieved is also increased.

Table 2-5 Variables used and delta T achieved in 6 hydration experiments of MgSO₄ monohydrate [54].

No.	$\vartheta_{in} / ^\circ\text{C}$	$\varphi / \%$	$p_{\text{H}_2\text{O}} / \text{mbar}$	$\Delta T_{\text{max}} / \text{K}$
1	23	45	12.5	8
2	25	85	26.9	10
3	40	35	25.8	10
4	40	80	59.0	15
5	40	85	62.7	20
6	60	60	119.6	30

Figure 2-20 shows hydration curves of MgSO₄ [46]. Red plots represent hydration humidity below the Deliquescence Relative Humidity (DRH) of MgSO₄.H₂O, blue plots represent hydration humidity above the DRH of MgSO₄.H₂O, green lines represent hydration humidity above the DRH of MgSO₄.6H₂O and the light blue plot represents hydration humidity above the DRH of MgSO₄.7H₂O. The results show the RH is required to be above the DRH of the required salt hydrate for that salt hydrate to form which is in agreement with Bertsch et al. [54]. Due to the high DRH of the magnesium sulphate heptahydrate the theoretical storage density of MgSO₄ changes from 2.3 to 2.1GJ/m³ [46]. To achieve a hydration up to the hexahydrate the RH% needs to be above ‘about’ 85% [46].

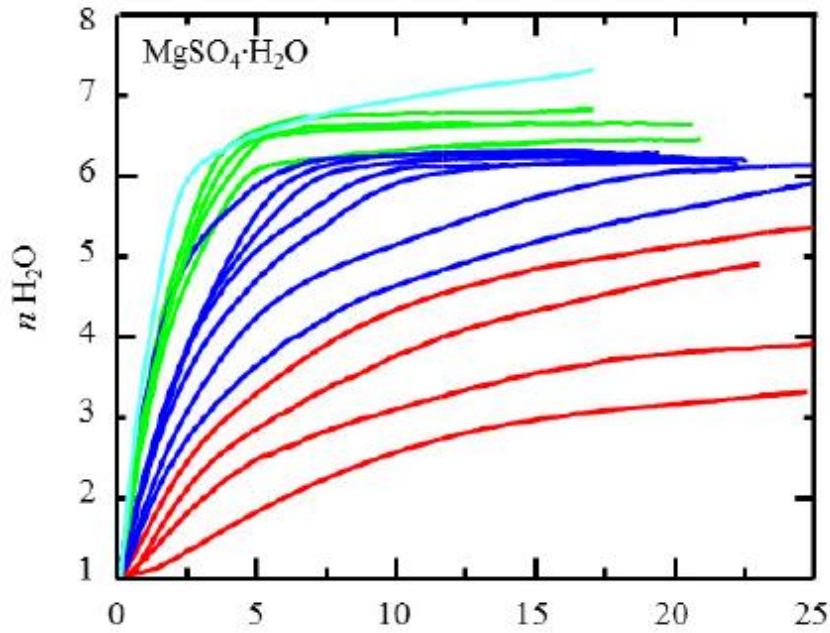


Figure 2-20 Water uptake hydration curves for MgSO_4 against time with different hydration humidity's (Red lines = below DRH of $\text{MgSO}_4 \cdot \text{H}_2\text{O}$, Blue lines = above DRH of $\text{MgSO}_4 \cdot \text{H}_2\text{O}$, green lines = above DRH of $\text{MgSO}_4 \cdot 6\text{H}_2\text{O}$, light blue lines = above DRH of $\text{MgSO}_4 \cdot 7\text{H}_2\text{O}$) [46].

2.4.2.2 Sample size and layer thickness effects on the hydration of MgSO_4

Figure 2-21 shows hydration results of various sample sizes of pure MgSO_4 [28]. All layer thicknesses hydrate fully however, smaller layer thicknesses hydrate faster. This faster hydration results in higher power output. This is seen with other salt hydrates including MgCl_2 [25]. Using small sample sizes and thin layer thickness will be difficult in practical applications of pure MgSO_4 .

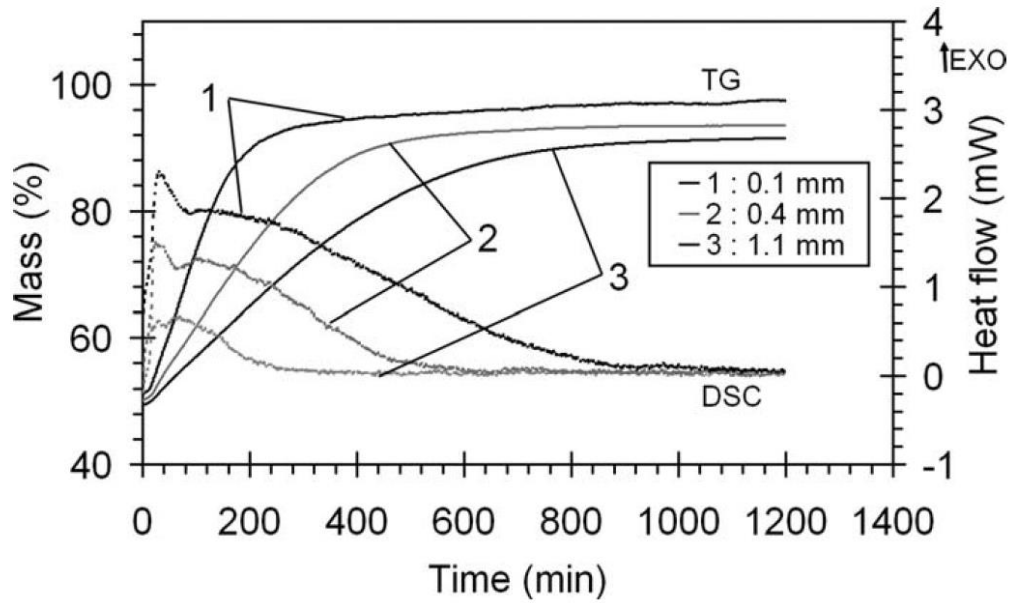


Figure 2-21 TGA & exothermic DSC hydration measurements for $MgSO_4$ showing the heat output with varying layer thickness [50]

2.4.2.3 Air flow rate effects on the hydration of $MgSO_4$

Hongois et al. [23] gives practical experimental results for a zeolite + $MgSO_4$ composite material, using a 200g sample, results are shown in Figure 2-22 by four different plots (A-D). Measurements suggest, using a fixed Relative Humidity (RH) of 50% and a temperature of $25^\circ C$, airflow rate highly dictates temperature rise and hence, power output [23].

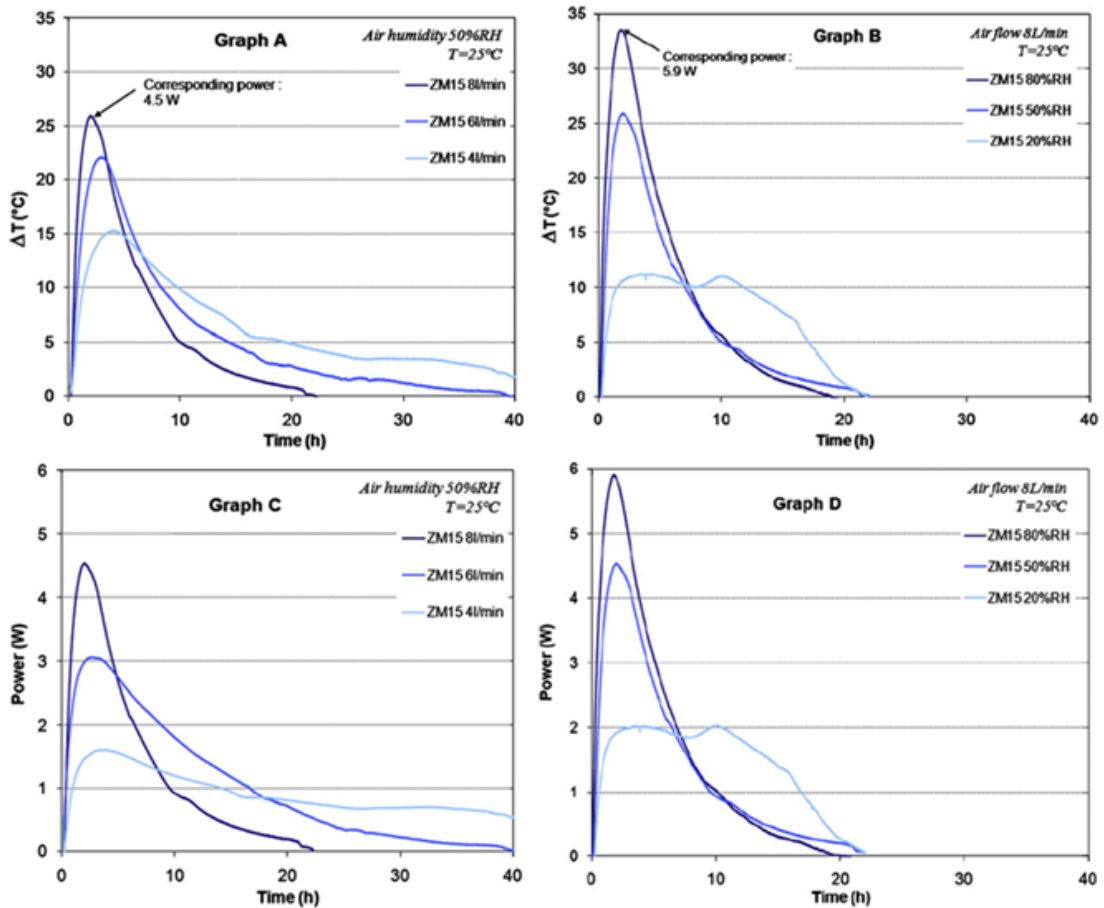


Figure 2-22 Experimental hydration measurements of zeolite/ $MgSO_4$ [23]

2.4.3 Summary of $MgSO_4$ characteristics section

There are many difficulties with the dehydration of pure $MgSO_4$ including damage caused from high heating rates, large sample sizes and large particle sizes. More research is needed into the effects these “damages” have on the energy storing potential of $MgSO_4$.

Hydration of pure $MgSO_4$ is also problematic including, high pH_2O required for complete hydration, larger samples sizes and layer thicknesses increase hydration time and the material agglomerates while hydrating further increasing the hydration time and potential

2.5 Promising host materials for TCES

Due to the problematic characteristics of pure $MgSO_4$ research has been conducted into using host materials to overcome and address this problem [23,48,49,60–63]. After impregnation the created composite material typically allows the $MgSO_4$ to be hydrated much more effectively as water vapour transportation is less hindered compared to a bulk mass of $MgSO_4$ alone [23,48]. This typically results in better power output. Also, dehydration

becomes more linear and does not occur in stages as MgSO₄ dehydration does. The Specific Surface Area (SSA) of a material plays an important role in the hydration kinetics. If the SSA is large typically the hydration kinetics will be fast [64].

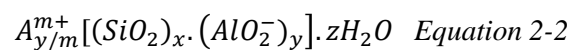
2.5.1 Zeolites

Zeolites are naturally occurring crystalline aluminosilicate materials with a three dimensional framework structure [65] [66]. Zeolites typically have very large surface areas and high porosity [67]. However, the naturally occurring zeolites tend to have many issues for use in practical applications such as impurities and varying composition [68]. For this reason zeolites are synthesized in laboratories to produce crystalline materials with a high purity, these are typically referred to as molecular sieves. The reason for this name is due to the structure of the zeolites. They have a cage like structure which can be used to “filter” out molecules from solutions [65].

Zeolites are used for many purposes [66] including water softening in washing powders (due to their ion exchange properties), adsorption heat storage, heavy metal removal [69] and petroleum cracking. The petroleum industry benefits significantly from the use of synthesized zeolites. Synthesized zeolites are orders of magnitude more active than the amorphous silica-alumina catalysts used before 1962 in the Fluid Catalytic Cracking (FCC) of heavy petroleum, the use of synthesized zeolites allows for a significantly higher yield of gasoline compared to the silica-alumina materials which were used before synthetic zeolites [68].

2.5.2 The structure of zeolites

The structure of zeolites gives them their characteristic high porosity and large surface area. The chemical composition of zeolites can be written as:



Equation 2-2 shows the generic zeolite equation [68], where A is a cation which has a charge of m, x+y is the amount of tetrahedral in each unit cell and this number is basically the Si/Al ratio and gives rise to the charge of the zeolite unit cell.

The main types of zeolites used in adsorption heat storage are types A, X and Y. Figure 2-23 shows the unit cell of type A and X/Y zeolites. Image 1 shows the sodalite cage (β-cage), image 2 shows the unit cell of zeolite A, image 3 the unit cell of zeolite X and Y,

image 4 the ion exchange sites on zeolite A (eight 1, three 2 and twelve 3 sites per unit cell) and image 5 the ion exchange sites on zeolite X and Y (16 – 1 sites, 32 – 1' sites, 32 - 2 sites, 32 – 2' sites, 48 – 3 sites and 32 – 3' sites per unit cell). The sodalite cages in the corners of the zeolite structures have a hexagonal face which is the opening to the interior of the zeolite structures [70]. The FAU zeolite has a Si/Al ratio of 1.5 [68].

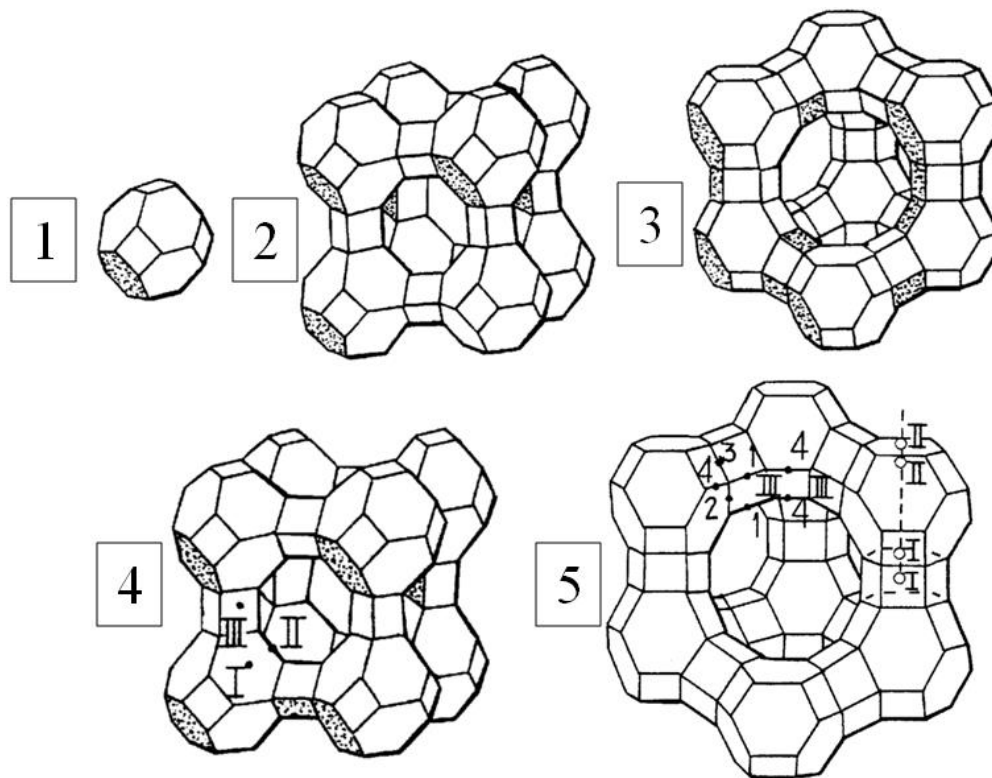


Figure 2-23 Zeolite Structures - Image 1 shows the sodalite cage (β -cage), image 2 shows the unit cell of zeolite A, image 3 the unit cell of zeolite X and Y, image 4 the ion exchange sites on zeolite A and image 5 the ion exchange sites on zeolite X and Y [71]

If 24 tetrahedra are linked together you get the sodalite cage for FAU (zeolite X and Y) shown below Figure 2-24. This sodalite cage is sometimes referred to as a β -cage [68]. The main void in the centre of the FAU structure is called the supercage or the α -cage. This α -cage has a diameter of 13.0×10^{-10} m [68,72]. It is difficult to picture the 3-dimensional layout of the FAU supercage as only 7 of the β -cages are visible in Figure 2-24 however, the supercage is surrounded by 10 β -cages. Figure 2-25 (right) shows a representation of the FAU supercage showing each of the 10 sodalite cages. The openings to the supercage are then connected to 4 more supercages through the windows on each supercage. The size of the openings to the centre of the super cage is 7.4×10^{-10} m [68,72]. The super cages are connected

to other supercages by a 12-membered-ring [72]. This means that the openings for molecules are only 7.4×10^{-10} m to pass through into the zeolite supercage.

Zeolite type A has a different structure than the FAU structure. It has 8 β -cages which are connected to each other by double four-membered rings. The zeolite-A has 6 “windows” which all connect to other supercages. The zeolite-A is essentially a cube shape. The diameter of the supercages are 11.4×10^{-10} m [73].

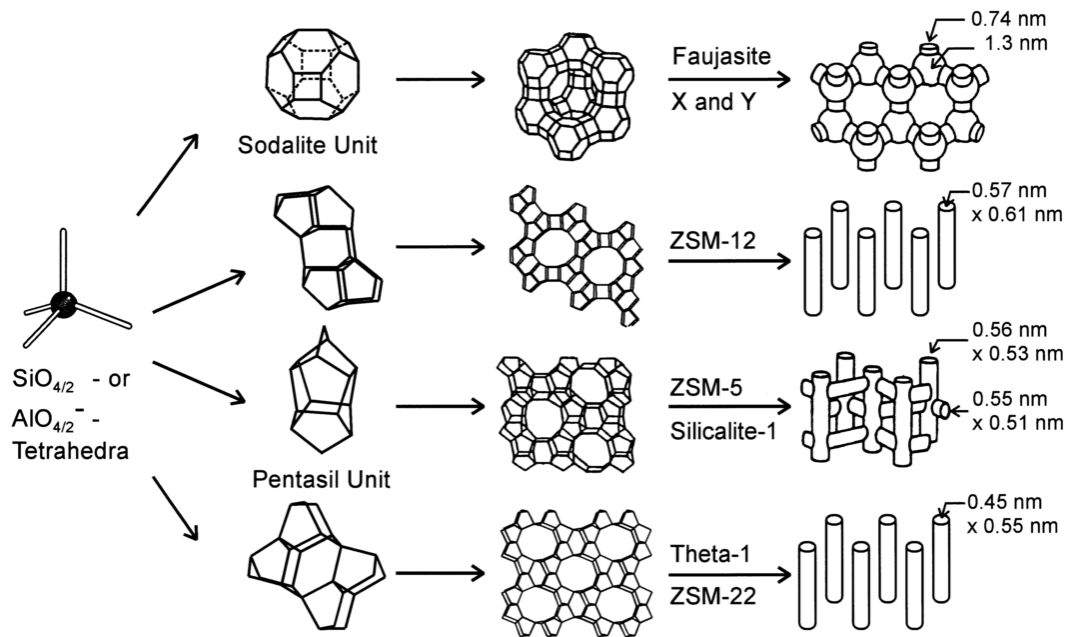


Figure 2-24 Diagram showing the building blocks of different zeolite structures [68]

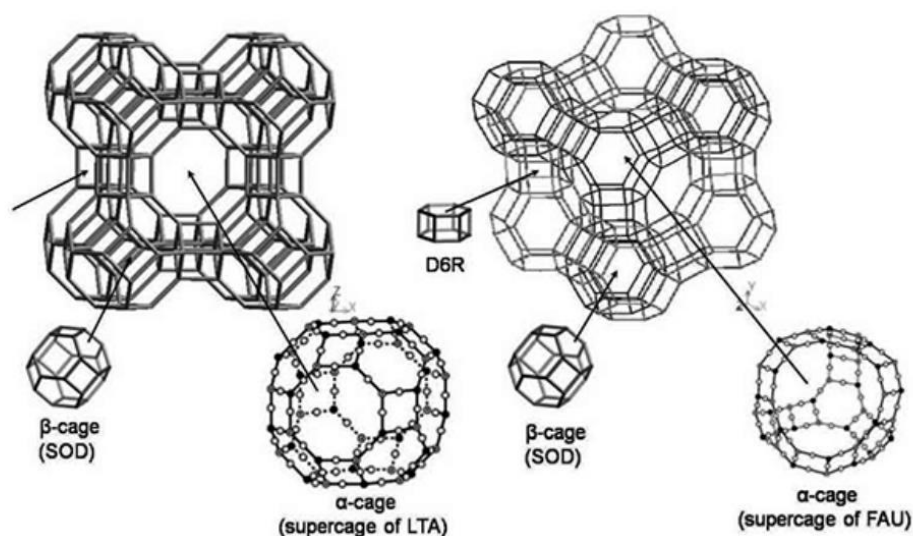


Figure 2-25 3-D representation of zeolite A (left) and Zeolite X and Y (right) showing their cage structure [73]

2.5.2.1 Zeolites for use as TCES materials

Zeolites can be used to store thermal energy by adsorption [20,40,43,62,63,74–78]. When zeolites adsorb water heat is released in the form of hydration enthalpy, the reason for the release of heat is explained in section 2.1.5. An ideal zeolite structure for heat storage will have a low Si/Al ratio (making the zeolite as negatively charged as possible allowing for more cations to be exchanged) high surface area (to allow a large amount of water adsorption), high density (to result in a higher energy density) and be cost effective. The energy density of zeolites for TCES is typically less than that of salt hydrates being used for TCES [20] however, TCES systems are more advanced using zeolites opposed to salt hydrates [25,74]. Zeolites typically do not suffer from many issues which salt hydrates, particularly $\text{MgSO}_4 \cdot 7\text{H}_2\text{O}$ and $\text{MgCl}_2 \cdot 6\text{H}_2\text{O}$, suffer from [79]. Zeolites have shown promising results when used in large scale systems [74,76,80].

2.5.2.2 Zeolite impregnation for TCES

Due to their large surface area and pore volume zeolites have been used as host materials for salt hydrates to enhance their properties and try to increase the energy density of absorbent materials. Many studies have created composite materials, adding salt hydrates into porous host absorbent materials [48,81,82]. The methodology for adding the salt hydrates into the porous hosts is typically via a wetness impregnation method [48,81,82].

Many studies have assessed impregnating different wt% of salt hydrates within the porous structure zeolites [23,48]. Most studies find the heat of sorption as well as the dehydration enthalpy increases with increasing wt% of impregnated $MgSO_4$ [23,48,60]. This is believed to be due to the increased vapour transportation and a higher reaction surface area within the pores.

Pore volume plays a vital role in dictating the speed of the hydration [77]. If the pores of the zeolite become blocked or diminished, due to high levels of impregnated material, the heat of hydration can become reduced [23,36,48]. This is also seen with zeolite beads prepared with higher wt% of binder [77,83].

Figure 2-26 shows hydration results from Whiting's et al. study [48], of various Zeolite + $MgSO_4$ composite materials. Due to different host material characteristics (i.e. Brunauer Emmett Teller (BET) surface area and pore volume) each material has different hydration properties. Materials Na-Y and H-Y containing 15 wt% of $MgSO_4$ provided highest heats of sorption (1090 J/g & 876 J/g, respectively). Results show there is strong correlation between BET surface area and pore volume measurements of each zeolite and the produced heat [48].

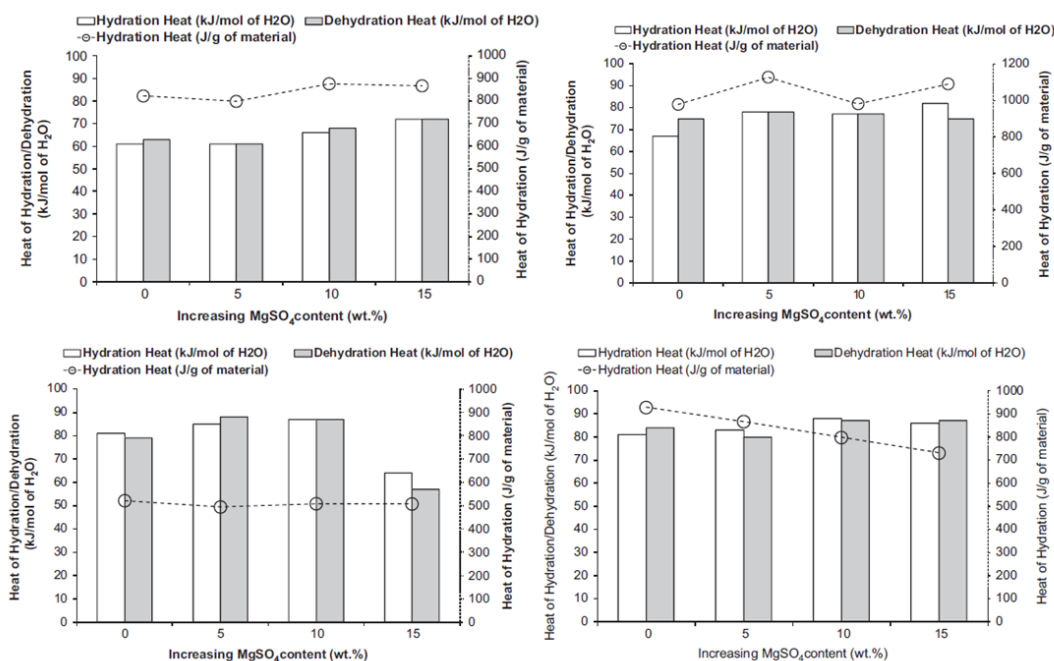


Figure 2-26 DSC-TGA measurements of various tested zeolite impregnated composites (H-Y, Na-Y, MOR and Na-X from top left to bottom right) [48].

Figure 2-27 shows water uptake increases with smaller pore size within porous glass impregnated with $MgSO_4$, due to capillary condensation and partial dissolution of the salt which would not occur within larger pores [46] these findings agrees with Linnow et al. Allouhi et al. and Baowan et al. [46,84,85]. This contradicts Whiting et al [48] who show larger pore volume leads to improved sorption. However, Linnow et al [46] discusses pore diameter not pore volume and does not consider the BET surface area of the glass. As the size of the pores surpass mesopores (2-50nm) and become macropores (>50nm), there is likely to be minimal adsorption [64].

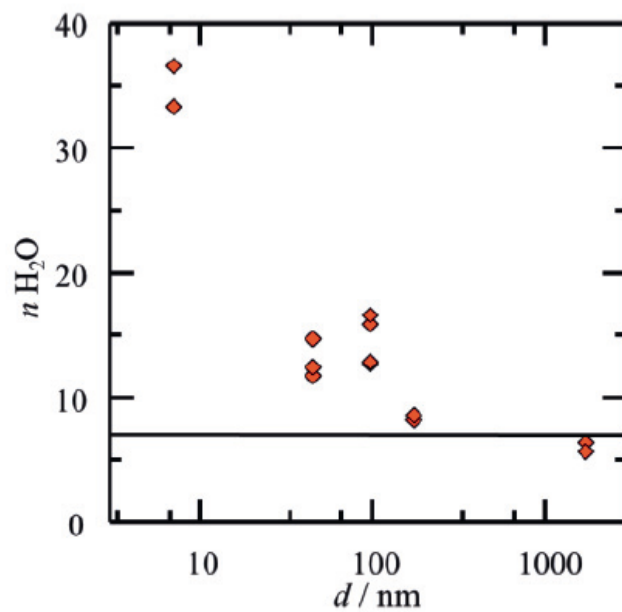


Figure 2-27 Pore size against amount of water uptake in porous glass impregnated with $MgSO_4$ [46]

It has been shown the temperature lift from zeolites can be low [40,62], the cost of the zeolites can be very high [40,86] and the density of zeolites can be low resulting in a large volume requirement [40]. Figure 2-28 shows the heat released from various impregnated absorbent samples. The impregnated samples achieve a much higher temperature rise.

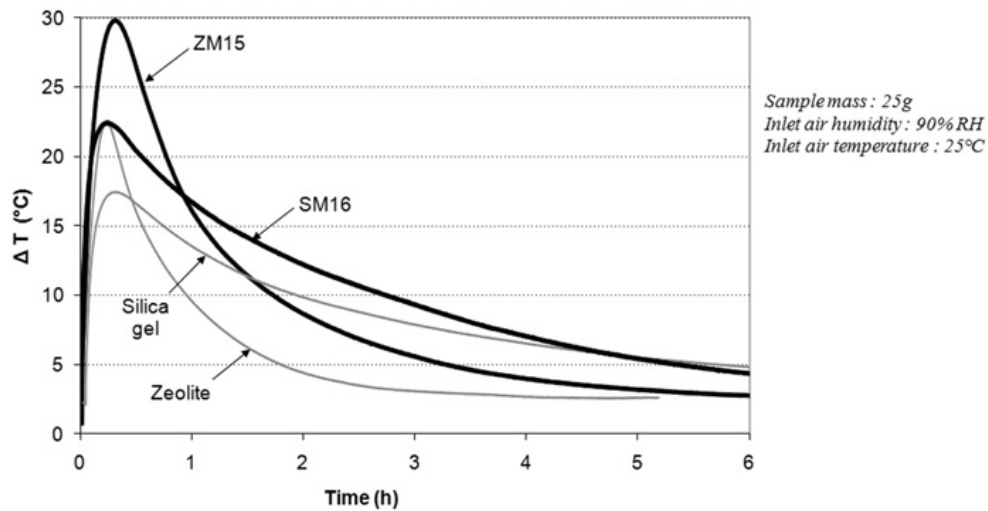


Figure 2-28 Temperature lift measurements of the hydration of various composite materials- SM16 = silica gel/MgSO₄, ZM15 – zeolite/MgSO₄[23]

2.5.2.3 Zeolite ion exchange for TCES

Another method used to try to improve the energy density of zeolites is through ion exchange. Zeolites can be put through an ion exchange process to replace the current ions with ions of higher selectivity to the adsorbed material. The hydration energy of zeolites depends on the amount of cations which are accessible to the adsorbed material which, for TES, is commonly water [87].

Water absorbed by zeolites is bonded in two main ways, weakly bound water on the surface and within the voids of the zeolite and secondly through strong interactions with the ions within the zeolite material [88]. The amount of ions within a zeolite type material and thus, the amount of ions which can be exchanged depends on the Si/Al ratio of the material [88], due to the cations balancing the net negative charge of the alumina silicate structure [87]. A lower Si/Al ratio also results in a more hydrophilic zeolite [89].

Molecular sieves adsorption properties, crystal cage and hydration can be altered by ion exchange [90]. Research has shown that ion exchange changes the water uptake of zeolites [91]. Zeolites characteristics can be enhanced using cation exchange[60,61,92]. Janchen et al. [61] used powdered zeolites while Stach et al [92] used 1g of an undisclosed form of zeolites and replaced Na⁺ ions for Mg²⁺ ions. As a result the zeolites show an increased water sorption amount (see Figure 2-29) [60,61,92]. Other studies have also reported an increase in hydration heat from zeolites after a Mg ion exchange [93,94].

The reasoning for the increased hydration enthalpy of zeolites with different ions is likely to be due to the hydration enthalpy of the ion which is within the zeolite. For example Na^+ and Mg^{2+} ions have a hydration enthalpy of -418 and $-1923 \text{ kJ/mol}^{-1}$ [95]. Mg^{2+} modified zeolites are likely to have more bonded H_2O around the Mg^{2+} ion sites and therefore, a higher hydration energy [88,94]. Contrastingly the Na^+ ion sites have a lower hydration energy [94].

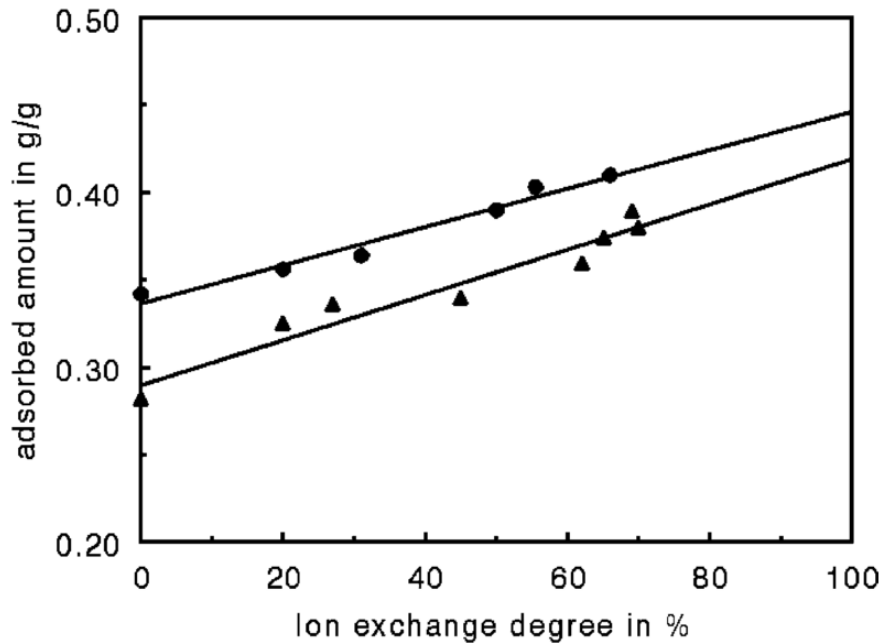


Figure 2-29 Amount of water absorbed vs. Mg ion exchange degree for Zeolite NaA and NaA

Cation exchange can be used to “fine tune” the pore size of the zeolites [61] which is dictated by the size of the ion. For example zeolite A with Na ions can be put through an ion exchange to replace the Na^+ ions for Mg^{2+} ions of a higher selectivity. If zeolite A has a pore opening of $4 \times 10^{-10} \text{ m}$, and the sodium ions are replaced with potassium ions the pore opening of this zeolite decreases from $4 \times 10^{-10} \text{ m}$ to $3 \times 10^{-10} \text{ m}$. However, if the sodium ions are replaced with Ca^{2+} ions within this same zeolite the pore opening will increase to approximately $5 \times 10^{-10} \text{ m}$.

2.5.2.3.1 Cation ion exchange capacity of zeolites

The amount of cations which can be exchanged and modified to change the characteristics of the zeolite (i.e. increased water adsorption) varies with each zeolite. Also, the definition of ion exchange capacity changes and different definitions mean different ion exchange capacities under different conditions [69].

Naturally occurring zeolites can have many impurities and this impacts the amount of cations which can theoretically be exchanged within the zeolite [69]. With pure zeolite substances, ones without the impurities, the amount of exchangeable cations is equal to the negative charge of the zeolite structure [69].

The actual experimental ion exchange capacity depends upon the experimental conditions used [69]. For example in some zeolites the cations are difficult to remove due to low mobility or strong bonding forces. For this reason zeolites can be pre-treated to be in the Na^+ form as Na^+ ions are easily removed and replaced [69]. The factor which is extremely important for the ion exchange capacity is the temperature of the solution the zeolite is submerged in when undergoing ion exchange [69]. However, the solution to mass ratio, exposure time, solution concentration and agitation rate are also important.

There are many different methods to measure the real ion exchange capacity including:

1. Repeated ion exchange process's with repeated replenishment of solution
2. One bath ion exchange using a high solution to mass ratio

This is relevant for the use of zeolites as thermal energy stores as it is desirable to create a zeolite which has been completely ion exchanged to increase the TES potential of the zeolite material.

2.5.2.4 Density of zeolites

For TES a zeolite which has the highest density to provide the highest energy density is desirable. The density depends on the zeolite structure, it also depends on the size and shape the zeolite is formed into. For example if the zeolite is formed into pellets etc. the bulk density will change with the size of the pellet as the packing density changes and therefore so will the bulk energy density [96]. The packing density is related to the void fraction of the packed bed. The void fraction will increase with increasing particle size and decreasing chamber diameter [96]. The size of the particle used has an influence on the pressure drop and permeability of the packed bed reactor. The smaller the particles used the smaller the void fraction, larger pressure drop and lower permeability. If the particle size is small enough a fluidised bed system could potentially be used, this is explained in more detail in section 2.8.

2.5.3 Attapulgite and vermiculite for use as TCES materials

Other materials which have been investigated as host materials for salt hydrates to create composite materials are attapulgite and vermiculite. Attapulgite is a clay mineral with typically a high surface area and a high porosity [97]. Vermiculite is also a porous material which expands when heated.

Similarly to zeolites as the impregnated wt% of the salt hydrate increases within each material the heat of hydration increases [41,49,62] (see Figure 2-30). Also a relatively large wt% amount of the salt hydrate can be impregnated within attapulgite due to its large porosity. Typically with zeolites the wt% impregnated is around 15wt% [23,36,48], whereas attapulgite is able to be impregnated with around 35wt% before any detrimental (i.e. pore blocking) impacts occur [49].

Casey et al. [36] assessed the potential of several host materials (zeolite, silica gel, activated carbon and vermiculite) and impregnated them with salt hydrates for TCES. The results suggested that vermiculite impregnated with MgSO_4 has the highest energy density. However, due to the slow kinetics of this material the vermiculite impregnated with CaCl_2 was suggested to be the most promising combination. Casey et al. [64] shows the results of these materials on a larger (1.5L) scale.

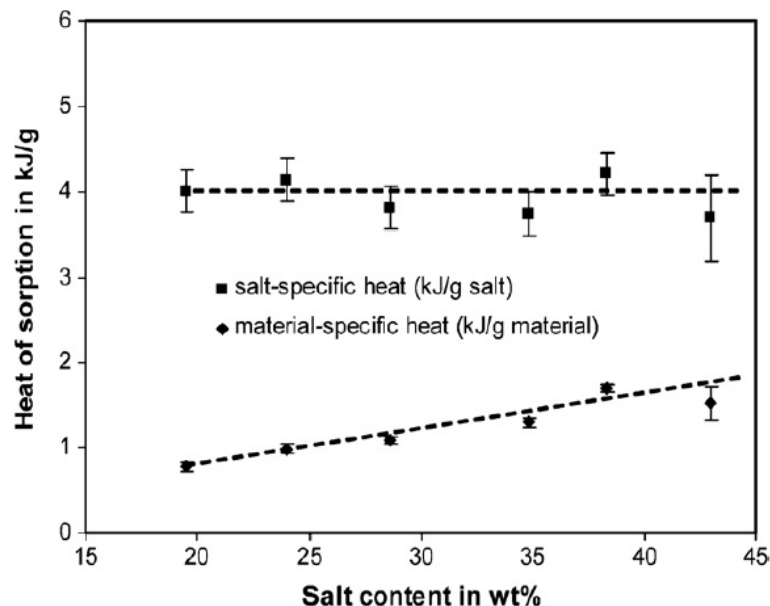


Figure 2-30 Measurements showing how salt content affects the heat of sorption of the impregnated material [49]

2.5.4 Carbon fibres and activated carbons for use as TCES materials

Carbon fibre and activated carbons typically have large porosity measurements [34]. Activated carbons are very absorbent and typically have a large surface area (500-1500m²/g) [34]. Carbon materials typically have a large thermal conductivity. These reasons are why carbon fibre and activated carbon are considered for use as host materials for salt hydrates to be used as TCES materials [36,98,99].

The disadvantage of carbon fibre is its poor thermal conductivity in the fibres radial direction[34], which can be further diminished if the absorbed material (i.e. MgSO₄) swells during absorption. More graphitized carbon fibre has a higher thermal conductivity however, higher graphitization results in a higher cost [100]

These materials have been shown to increase the thermal conductivity of salt hydrates significantly [98,99]. Aidoun et al. [98] investigated the effect of impregnating carbon fibres with NH₃-CoCl₂, the carbon fibre increased the power densities to a level comparable to chloride salts intercalated into graphite, which is a much more complex method of creating composite materials.

Although the thermal conductivity may be increased it has been shown that there are host materials which provide much better characteristics (energy density, lower cost) relative to activated carbons [36].

2.5.5 Silica gel for use as a TCES material

Silica gel is a commonly known mesoporous absorbent [42]. Due to its pore volume it has been investigated for use as a host material for salt hydrates [23,36,42,92]. Research shows that silica gel, relative to zeolite, can allow for lower desorption (charging) temperatures (~90°C) [42,92]. Table 2-6 shows data for a composite zeolite (NaLiX) and composite silica gel (KG5-88 + CaCl₂). The results show the silica gel performs better than the zeolite even though the silica gel was dehydrated (charged) with a lower temperature.

Table 2-6 Comparison of the specific heat storage density of absorbent materials compared to the heat capacity of water at different temperatures [92]

Storage material	Δh_{sp} [kJ/kg]			$\Delta h_{sp}/\Delta h_{spH_2O}$ [%]		
	313 K	333 K	353 K	313 K	333 K	353 K
Water	125	210	294	100	100	100
H ₂ O/NaLiX ¹	972	893	807	778	425	274
H ₂ O/KG5-88 + CaCl ₂ ²	1064	470	409	851	224	139

¹T_{des} = 483 K; ²T_{des} = 413 K.

Alone silica gel does not absorb large amounts of water [36,42]. Although, as with many of the host materials discussed above, the silica gel absorbs more water with increasing impregnation wt% of salt hydrates. As the wt% of salt hydrate impregnated increases, the pore volume is shown to decrease, as expected, but with a relatively large amount of impregnated material (40wt%) the composite materials do not show signs of degradation or pore blocking. Wu et al. [42] suggests 30wt% to be an optimal amount as above this value degradation is seen over several cycles suggesting a leakage of the salt from the pores, this study was also on a large (40kg) scale.

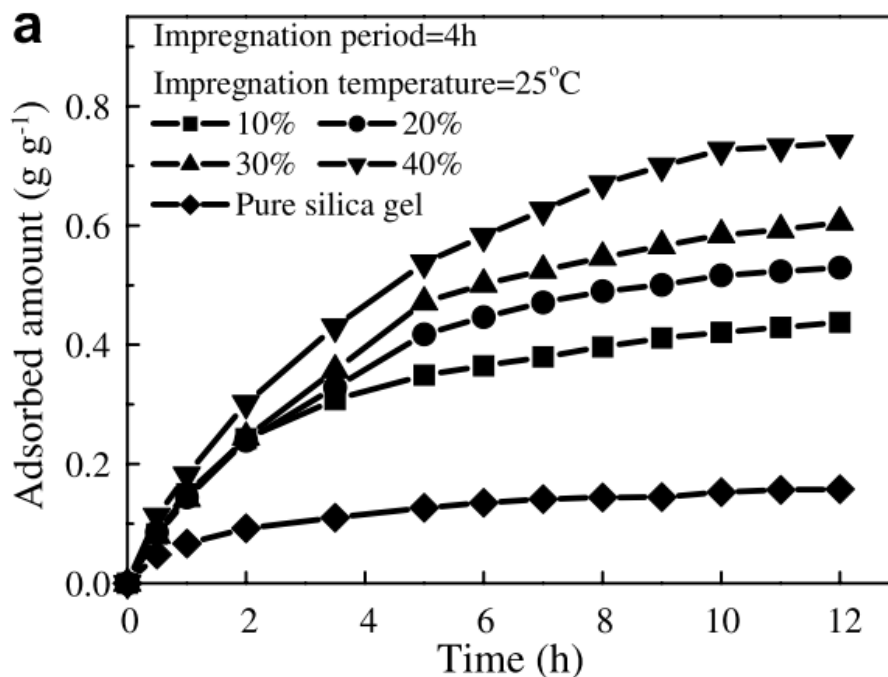


Figure 2-31 Effects of CaCl₂ concentration on the dynamic sorption characteristics of water on composite sorbents showing the absorbed amounts [42]

Although silica gel can be used as a host for composite materials its absorption capacities are not as promising as some other host materials [36]. Figure 2-32 shows vermiculite impregnated with CaCl_2 absorbed more water than silica gel impregnated with CaCl_2 . The majority of water is absorbed at a RH% which is below ~55% for the vermiculite composite. This is beneficial for domestic applications. Pure silica gel has much better sorption characteristics than pure vermiculite however, once impregnated with a salt hydrate this changes dramatically.

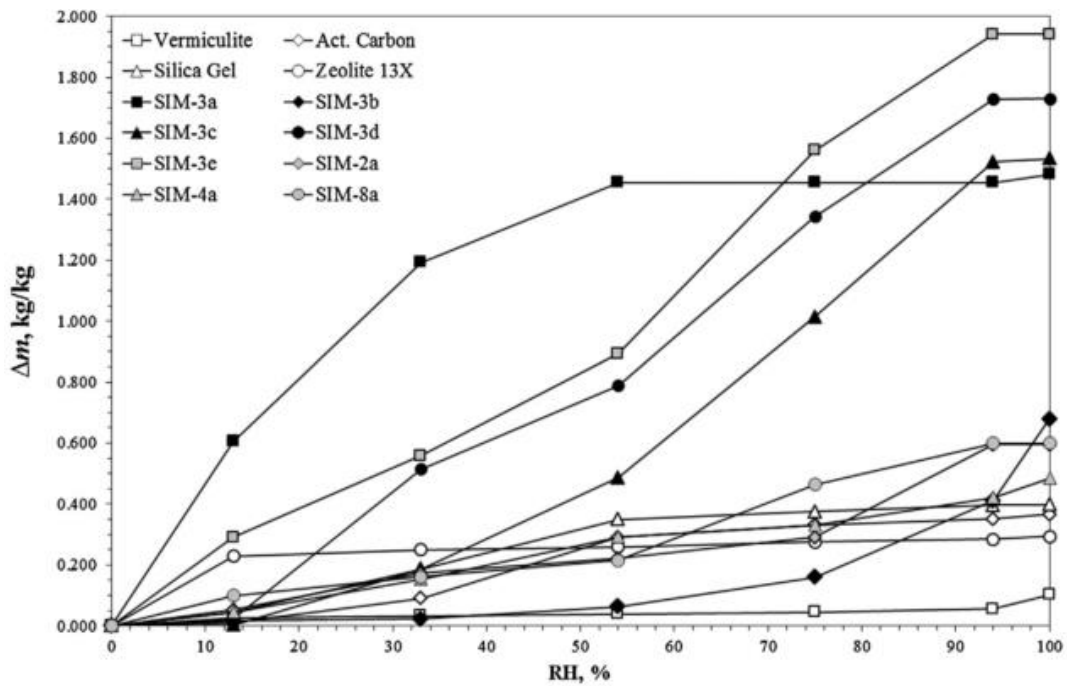


Figure 2-32 Moisture vapour sorption isotherms for the selective materials studied SIM-2a = silica gel + CaCl_2 , SIM-3a = Vermiculite + CaCl_2 . [36]

2.5.6 Summary of promising host materials for TCES

Table 2-7 shows the advantages and disadvantages of each of the potential host materials for TCES.

Table 2-7 Advantages and disadvantages of absorbent host materials

<u>Material</u>	<u>Advantages</u>	<u>Disadvantages</u>
Zeolite	<ul style="list-style-type: none"> • Most developed TCES systems • High surface area and pore volume 	<ul style="list-style-type: none"> • Energy density of systems • Cost of material • Lack of large scale sample preparation feasibility
Attapulgitite & Vermiculite	<ul style="list-style-type: none"> • Very porous material and good hosts • Cheap • Widely available 	<ul style="list-style-type: none"> • Lack of large scale research • Lack of research on sample preparation (i.e. particle / bead size to improve slow kinetics of MgSO₄ impregnated within vermiculite [36], [64])
Silica Gel	<ul style="list-style-type: none"> • Allows for typically lower desorption temperatures relative to zeolites. • Accommodates high impregnation amounts 	<ul style="list-style-type: none"> • Poor sorption characteristics when impregnated, relative to other materials [42] • Lack of research into varying beads size of silica gel.
Carbon Fibre & Activated Carbon	<ul style="list-style-type: none"> • Typically high thermal conductivity 	<ul style="list-style-type: none"> • Other hosts shown to be more promising • Typically very high cost • Minimal work on impregnation of salt hydrates

2.6 Sample preparation methodologies for creating TCES materials

As discussed host materials can be used to enhance the properties of salt hydrates. The shape and structure can also impact the TCES potential of a material. Below some common preparation methods for TCES materials are discussed.

2.6.1 Monoliths and bricks for TCES

Using TCES Materials (TCESM) formed into monoliths or bricks is novel with limited research. Pino et al. [75] investigated the use of zeolite 4A for heat storage. The purpose was to investigate the heat transfer characteristics of beads against monoliths. Results show monoliths typically have a global heat transfer coefficient which is 3-8 times greater than the zeolite beads [75]. This is a relatively novel study there is limited work for comparison however, the reason for the increased heat transfer is likely to be due to the enhanced thermal contact with the material and the heat exchanger or material used, this theory is supported by N'Tsoukpoe et al. [58]. More work is needed into the possibility of using TCESM shaped into monoliths and the preparation techniques itself (i.e. the amount of binder required).

2.6.2 Beads for TCES

Beads are a more common formation for TCESM. The formation of zeolite beads is typically carried out with the use of a binder material [77,83]. The less binder used in the creation of the beads the increased amount of water adsorbed by the beads [77,83]. The zeolite is likely to be much more absorbent than the binder material used. Table 2-8 shows the results of a TGA desorption of several beads created with and without a binder material. The results show that in all circumstances the binder free zeolite has a larger water adsorption capacity than the sample zeolite which uses a binder.

Table 2-8 Comparison of the desorption capacities in g/g of binderless and ordinary zeolite types A and X [77]

Zeolite	Isotherms at 298 K and RH = 33%	TG, desorption up to 723 K	TG, desorption up to 473 K
4ABF	0.250	0.266	0.200
4AK	0.220	0.231	0.180
13XBF	0.320	0.316	0.218
13XK	0.275	0.260	0.187

Janchen et al. [77] states that the use of binder free beads also results in faster hydration kinetics. Likely due to the increased pore volume which is not hindered by the binder material, this agrees with [23,36,48]. In contradiction, Janchen et al. [43] states the temperature rise achieved from zeolite beads prepared with and without binder is not vastly different. Suggesting although there is less zeolite the rate at which the beads hydrate is unchanged and possibly improved. This suggests the vapour transportation is not hindered by the binder. More work is required to understand this further.

Fakin et al. [83] states the size of the bead used does not impact the amount of water absorbed by the material. However, the size of the bead does impact the rate in which the material hydrates, the larger the bead the slower the hydration. This is due to the resistance against the moisture transfer into the centre of the beads. Larger diameter beads have more resistance to the moisture from the porous media. This is important as smaller beads typically result in a larger pressure drop when used in a packed bed reactor design.

N'Tsoukpoe et al. [58] discusses the correlation between bead size and permeability. This is an important consideration especially when working with powders which have a very small particle size. Mass transfer in adsorbent beds is usually considered through permeability analysis. Equation 2-3 is used to calculate the permeability of a bed.

$$K = \frac{n^3}{1-n^2} \cdot \frac{d^2}{180} \text{ Equation 2-3 [58]}$$

Where K = permeability of the bed, n = its porosity and d (m) diameter of the grains. The recommended values for an adsorbent bed are:

- Permeability = 10^{-12}m^2
- Effective thermal conductivity: $1 \text{ Wm}^{-1}\text{k}^{-1}$
- Heat transfer coefficient at interface between heat exchanger tube and adsorbents bed: $200 \text{ Wm}^{-2}\text{K}^{-1}$

A reasonable amount of research has been conducted into the use of beads for TCES. More research is required into larger scale testing as small testing can be misleading [58].

2.6.2.1 Pelletization for TCES

Many absorbents are made in a fine powder form and not easily sourced in a pellet or bead. A method for creating beads from powders is with the use of a pelletizing disc. Pelletization is an agglomeration technique that uses a spinning disc held at an angle where fine particles are added gradually. Moisture is added to the spinning particles and this causes the particles to agglomerate and form beads/pellets [101]. Figure 2-33 shows an example of a pelletizing disc. As the disc spins this carries the fine particles up, the angle of the disc, the size of the particles and the friction between the disc and the particles all dictate where the particles fall back down under gravitational forces. As the particles fall they roll in moisture and agglomerate with other particles forming larger particles. The size of the particles should be less than 150 μm in size and more than 60% of the particles should be less than 45 μm in size [101] which will lead to pellets with the maximum surface tension and capillary forces locking them together.

$$n_{cr} = \frac{42.3}{\sqrt{D}} \sqrt{\sin x} \text{ Equation 2-4 [102]}$$

Where n_{cr} = critical Revolutions Per Minute (RPM), D = disc diameter and x = disc inclination angle. Equation 2-4 is used to calculate the optimum angle and rpm ratio [102]. Gu et al. [102] shows that due to the friction created by the pan these value are not always correct and some trial and error is required depending upon the material used. Furthermore, optimizing the rpm and disc inclination can change the crushing pressure of the pellets produced. The larger the particle diameter the lower the crushing pressure required [102]. Gu et al. used a 40cm disc and found the optimum rpm and disc inclination to be 45 and 43°, respectively [102]. The amount of water added to the powder solution will dictate the size of the pellets created.

Pandey et al. [101], attempted to optimize agglomeration pelletisers for a steel company hence, this is a full scale assessment. The study made several conclusions.

- The time the material spends in the pelletiser increases the size of the pellets formed.
- Lower RPM causes larger pellets to be formed.
- Smaller particle size leads to pellets with a higher mechanical interlocking force which creates pellets with a higher crushing force.
- If the amount of moisture added to the material is above the critical amount the growth rate increases but the pellets are liable to become deformed.

- Over a specific RPM the amount of “undersized” pellets formed increases. This is accounted to the impact of pellets on pellets causing them to break.
- A higher feed rate requires a higher RPM which in turn leads to a reduction of pellets in the required size range.

From both of these studies it is apparent different materials and conditions require some trial and error to optimise the pellets created. However, there are several reoccurring themes from both studies;

- Increasing the moisture content will increase the pellet size.
- A smaller particle size will result in pellets with a higher crushing force.



Figure 2-33 An example pelletizing disc (letters A, B, C and D represent locations of where nozzles are located on this specific pelletizing disc). [101]

2.6.3 Honeycombs for TCES

It is possible to form absorbent powders into honeycomb structures for TES [43,103–106]. Studies [103–105] investigate Wakkanai Siliceous Shale (WSS) based honeycombs impregnated with CaCl_2 and LiCl , whereas Jänchen et al. [43] looks at zeolite based honeycombs with and without a binder. The pore volume and surface area of the WSS honeycombs are dramatically reduced with increasing wt% of the impregnated materials.

The reason for the creation of the honeycomb is an attempt to increase the hydration rates which should in turn increase the power output [103–106]. MgSO_4 suffers from slow hydration characteristics, possibly a honeycomb structure could improve this.

Figure 2-34 shows the hydration characteristics of different honeycomb structures. It is obvious as the wt% of CaCl_2 increases so does the energy output.

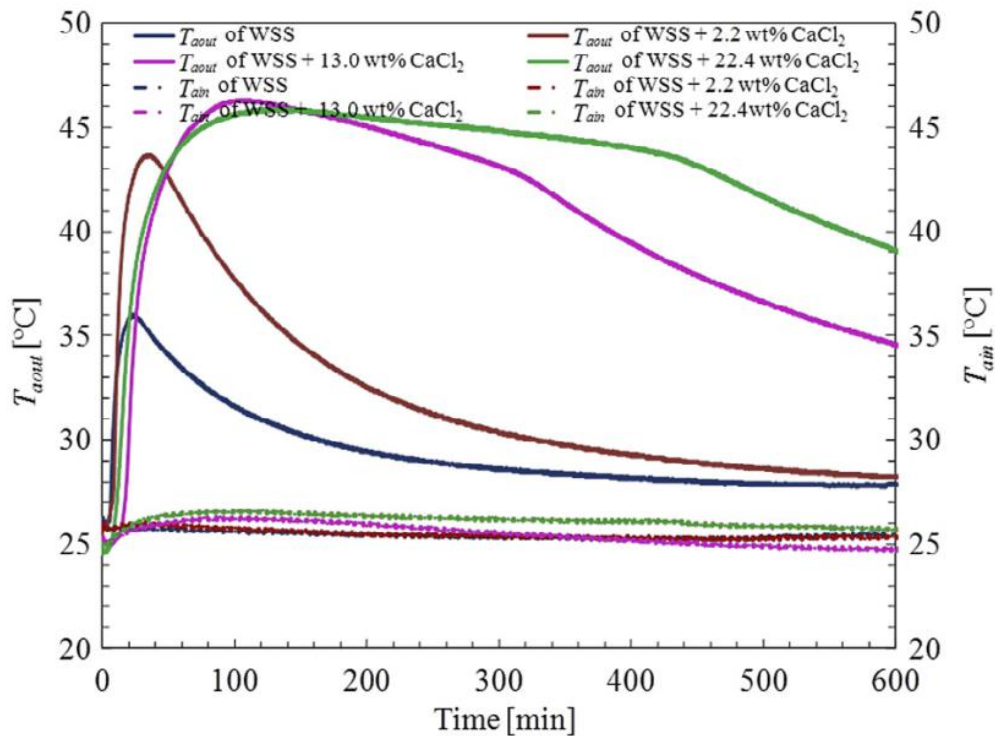


Figure 2-34 Inlet and outlet change in temperature with time for different honeycomb filters [103]

Jänchen et al. [43] concludes by stating the use of a honeycomb formation is more promising than beads, there does not appear to be any studies supporting this statement. Zondag et al. [106] states honeycombs cause increased adsorption.

The use of honeycombs is shown to be advantageous. Limited studies have been conducted and more are required comparing different formations. Investigations into the feasibility of creating honeycombs compared with other formations is required as the preparation methods for honeycombs is likely to be more costly [106].

2.7 Possible ways to create composite materials

The way in which composite materials are prepared should be considered for many reasons, including cost, simplicity and advantageous TCES characteristics. Below are commonly used ways to create composite materials [34].

2.7.1 Simple mixture for creating TCES composite materials

A simple mixture is the simplest method for creating composite materials. The ratio of each, the host material and absorbent (i.e. MgSO_4) are calculated and the selected mass of both materials are mixed together. This method is generally used when each material is in a granular form [34]. This method has been used by Posern [49] to investigate the TCES potential of MgSO_4 and MgCl_2 at varying wt% mixing levels.

2.7.2 Impregnation for creating TCES composite materials

Impregnation is typically used for activated carbons, carbon fibre, graphite fibre or expanded graphite [34]. This process typically dehydrates the host material to ensure all water content is lost. The host material is then exposed to an aqueous solution of the TCES material (i.e. MgSO_4). The composite material is then dehydrated to ensure removal of all water content from the salt solution. This leaves dehydrated TCES material fragments impregnated onto the host material. Impregnation is much simpler than Intercalation [98]. This method has been used in many studies for TCES [48,81,82].

Wu et al. [42] specifically investigates the impact the impregnation characteristics have on the sorption properties of the material. The variables which are changed are the impregnation temperature (25-80°C) and the impregnation time (1-8h). The results show significant changes in the water sorption amount, up to 18%. Most studies do not appear to consider these variables. This highlights the need for further studies to confirm these results.

2.7.3 Mixture or impregnation and consolidation for creating TCES composite materials

This method uses a mixture of TCES materials or impregnated composite TCES materials and compresses them. The compression can happen before the impregnation although; the compressed materials after impregnation would need to be dehydrated once more. More research is needed on this method.

2.7.4 Summary of the different preparation methodologies discussed

Table 2-9 summarises each of the sample preparation methodologies discussed.

Table 2-9 Advantages and disadvantages of the different composite preparation methods

<u>Preparation Technique</u>	<u>Advantages</u>	<u>Disadvantages</u>
Simple Mixture	<ul style="list-style-type: none"> • Simple method • Cost Effective 	<ul style="list-style-type: none"> • Not widely investigated
Impregnation	<ul style="list-style-type: none"> • Most common method for creating TCES composites. • Research shows its potential [23,48,98,100] 	<ul style="list-style-type: none"> • Separation can occur after de/hydration cycles [98] • Time consuming relative to simple mixture hence, more costly • Scaling difficulty • Limited research into feasibility
Mixture or impregnation and consolidation	<ul style="list-style-type: none"> • Enhanced thermal conductivity of material • Possibly enhanced energy density. 	<ul style="list-style-type: none"> • Difficult process hence, likely to be costly [98] • Not utilised vastly in TCES

2.8 Reactor designs and theory for TCES

This section describes reactor design theory, common reactor designs and also the literature on reactor designs specifically for TCES.

2.8.1 Reactor design theory for TCES

Depending on the particle size used in a TCES system there are two possible systems which are commonly used as reactors, not for TCES, which could be adapted for TCES use. The reactors are a packed bed or a fluidized bed reactor.

2.8.1.1 Packed bed reactor for TCES

If the particle size is relatively large (i.e. 3mm beads) it is likely the reactor would be a packed bed. A packed bed is a reactor which has a cylindrical column packed with material. Typically a liquid is passed into the reactor at the top and a gas enters at the bottom of the reactor and passes back out of the top [107]. However, in a TCES system it would be likely that the packed material would be an absorbent (i.e. zeolite or salt hydrate) and then the gas, likely humid air, will pass through the system hydrating the material and realising the heat of adsorption.

With a packed bed the important characteristics are the pressure drop through the reactor which depends upon the flow rate required and also achieving a uniform fluid flow to avoid areas of stagnation. The pressure drop of the fluid through the reactor is calculated using a friction factor correlation attributed to Ergun [107].

2.8.1.2 Fluidised bed reactor for TCES

If the particle size is small, for example a powder absorbent or salt hydrate, there is a possibility of using a fluidised bed reactor design. A fluidised bed is similar to a packed bed reactor however; the velocity of the fluid flowing through the packed bed is large enough to overcome the gravitational forces on the particles causing them to lift. This causes the particles to act like a fluid and if desired the particles can be transported like a fluid when in this state. This method allows for very good contact between the fluid and the solids. As the velocity of the fluid through the bed of particles is increased two things happen:

1. The pressure drop within the system increases up to the fluidisation point. After the point of fluidisation the pressure drop decreases slightly and becomes constant with increasing velocity.
2. The height of the bed stays constant up until the fluidisation velocity, at which point the bed height starts to increase with increasing velocity. Each of these two phenomenons is depicted in Figure 2-35.

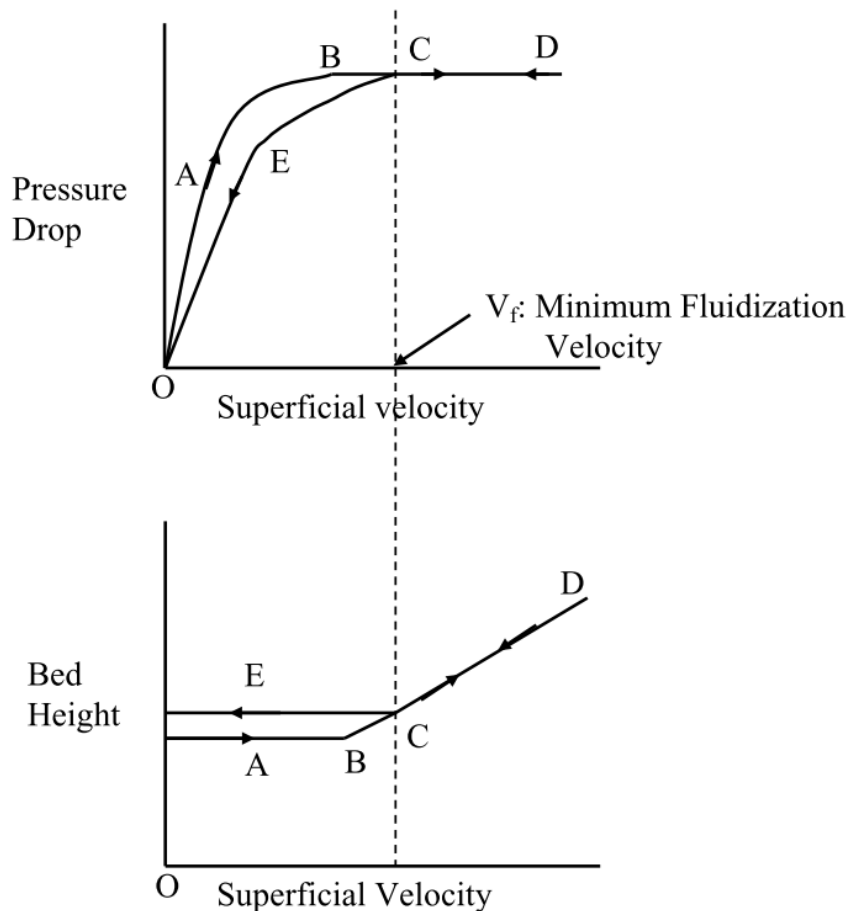


Figure 2-35 The trends in pressure drop and bed height with superficial velocity for a fluidised bed reactor (A = part of the curve where the Ergun equation can be used to describe the increasing pressure drop with increasing velocity, B = bed starts to expand while pressure drop remains constant. The force on the particles balances the net weight of the particles and separation of the particles begins, C = bed expands further but pressure drop remains constant, D = bed decreases with velocity but pressure drop remains constant, E = after the velocity is decreased below the superficial velocity the bed height remains constant but the pressure drop decreases with velocity. The bed height is higher than the original bed height after fluidization due to the particles becoming less packed, if left alone, over time the particles will return to the packed bed height.) [107]

If a circumstance takes place where the superficial velocity is very high and small particles are carried out of the reactor then they can be recovered either by filters or cyclone separators and returned to the reactor. This may be desirable to take advantage of high superficial velocities.

The type of fluidisation the particles within the bed are experiencing can be categorised as either particulate or bubbling fluidisation.

- Particulate fluidisation occurs in liquids as the velocity of the liquid exceeds the minimum fluidisation velocity. The bed height increases uniformly with velocity.
- Bubbling fluidisation takes place in gas systems. Large gas bubbles flow through the packed bed and with increasing velocity they grow in size until they are the same size as the reactor cross section. When the bubbles are the same size as the reactor cross section this state is known as slugging, see Figure 2-36.

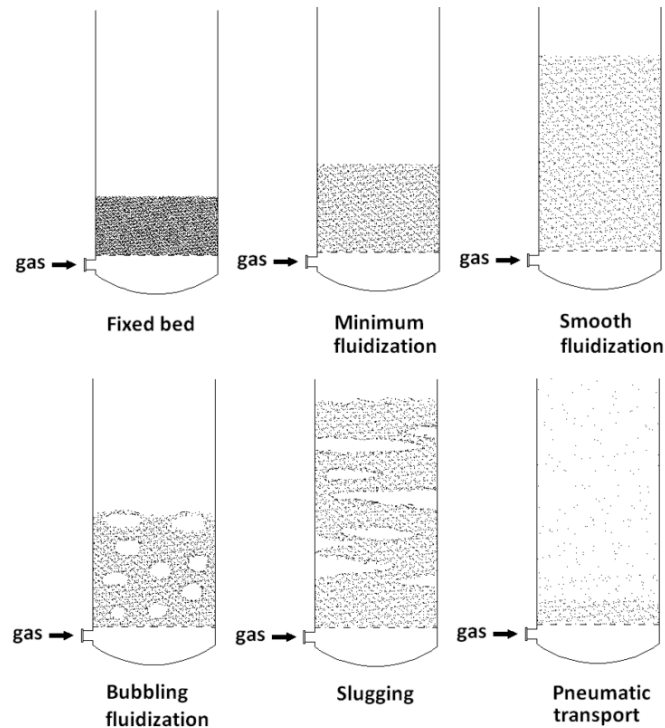


Figure 2-36 The different types of fluidisation [108]

The size and density of the particle impacts the fluidisation. Figure 2-37 shows a diagram with the classification of different powders and the way they act under fluidisation. Group A particles experience a large bed expansion before and after fluidisation as the velocity of the gas increases. Group B particles bubble as soon as the minimum fluidisation velocity is achieved. Group C particles have difficulty fluidising and group D particles spout readily [109].

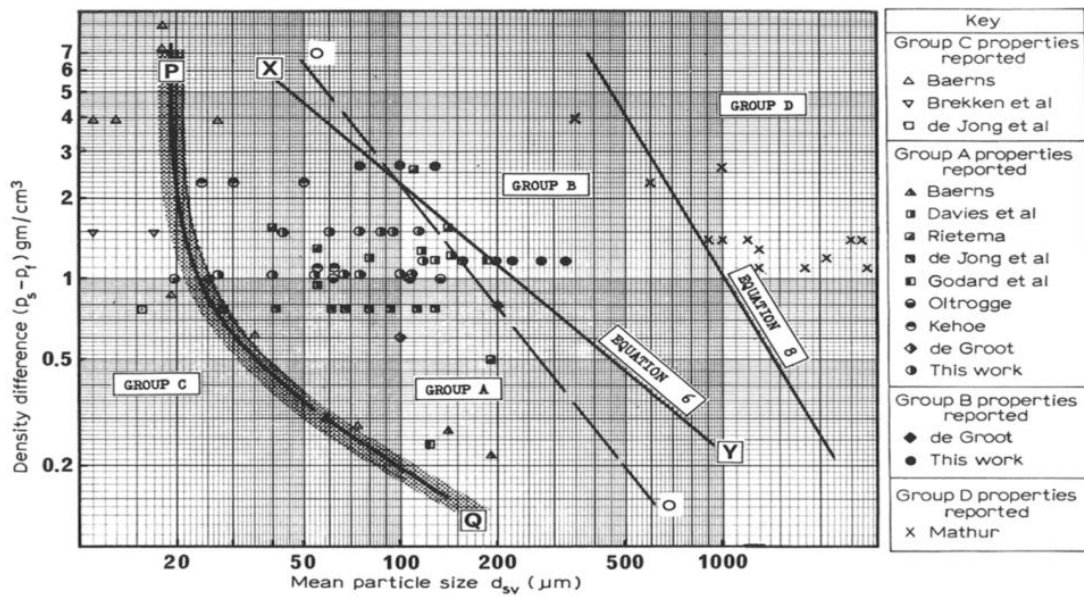


Figure 2-37 Powder classification diagram for fluidization by air [109]

2.8.2 Reactor designs for TCES

This section identifies and discusses possible reactor designs from previous studies. This ultimately helped identify and understand the advantages and disadvantages of each design. This section was used to deduce which design shows most promise and provide ideas for investigation and implementation for $MgSO_4$ into a large scale reactor.

TCES Reactor designs can be categorised into four main types: Open with integrated reactor, Open with separator reactor, closed with integrated reactor and closed with separate reactor.

Open reactors store material in one “bulk” store. Material is hydrated by external ambient conditions. Figure 2-38 shows a diagram of an open reactor design which has been implemented into a domestic environment. Abedin et al. [110] shows results from this open reactor. The **advantages** [110] include simple engineering as the reactor operates at atmospheric pressure. Simple design allows for minimal parts increasing effective energy density. Limited heat exchanger use, working fluid (typically air) operates as the heat transfer fluid exhausting hot air to the ambient. The working fluid is supplied from ambient. The **disadvantages** are they have less control on the hydration (discharge) process as hydration conditions are dictated by the ambient.

Closed Reactors store fluids and materials separate from the heat transfer fluid [110]. The TCES material is hydrated via internal substances (i.e. water vapour). **Advantages** [64] are the hydration conditions are more controlled as working fluid or vapour is created within the system. Enhanced control can allow for improved vapour transportation resulting in higher ΔT outputs. A **Disadvantage** [110] is that extra energy is required to create the working fluid or water vapour. The effective energy density is decreased as there is a working fluid store.

Integrated reactors store the TCESM in the same location to where the reaction takes place [86]. Figure 2-39 (left) shows an example of an integrated reactor design. **Advantages**, [86,111] are no material transportation is required and there are less engineering difficulties due to the simple design. **Disadvantages**, [86,111] are the hydration is less controlled and they typically have to discharge the complete material store.

Separate reactors store the TCESM within a different location to where the reaction takes place. Figure 2-39 (right) shows a schematic of a closed separate reactor design. **Advantages** [86,111] are they can optimize vapour and heat transfer from controlling the amount of material de/hydrated. There are minimal energy losses and there is no need to hydrate the whole energy store wasting sensible heat. All but the reaction chamber can be made from cost effective materials [111]. **Disadvantages** [86,111] are that energy is wasted transporting material the materials and there is more engineering difficulty.

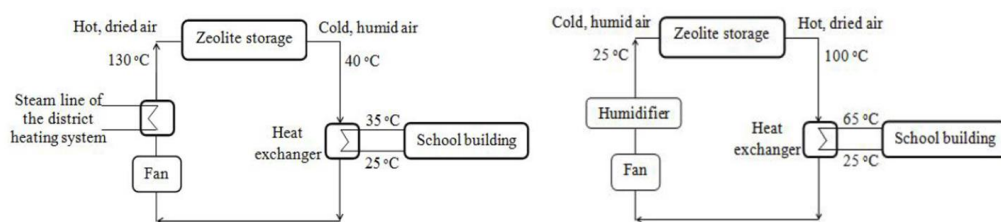


Figure 2-38 Charging and discharging diagrams of a zeolite system, respectively [110]

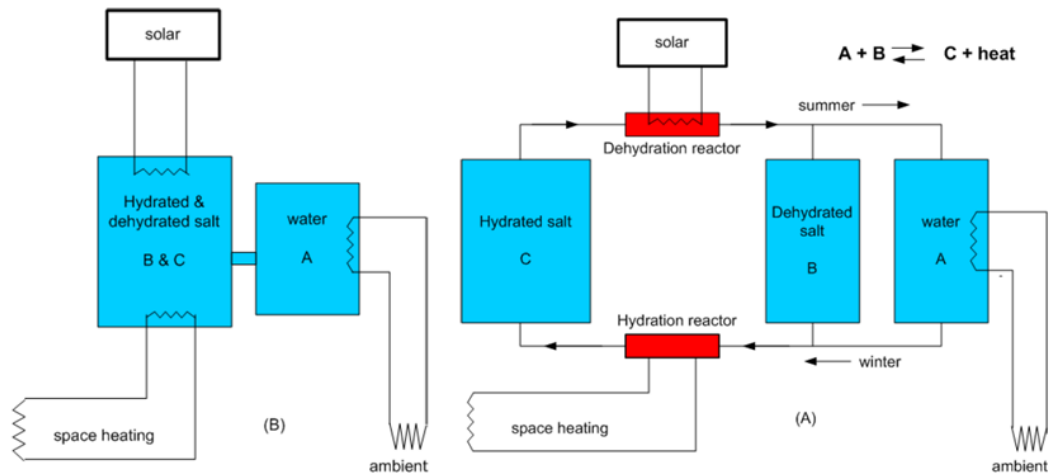


Figure 2-39 Integrated reactor design(left), Closed separate reactor design (right) [86]

Mette et al. [111] and Zondag et al. [86] investigated separate reactor designs, both stating the advantageous properties of separate reactors. Both studies investigated the characteristics of each reactor via numerical studies.

After a preliminary inventory research Zondag et al. [86] highlighted three possible designs shown in Figure 2-40 [86]. Results show the screw reactor has the most promise (see Figure 2-41) [86]. De Jong et al. [112] presents several novel designs (see Figure 2-42). They provide possible future designs which could be implemented.

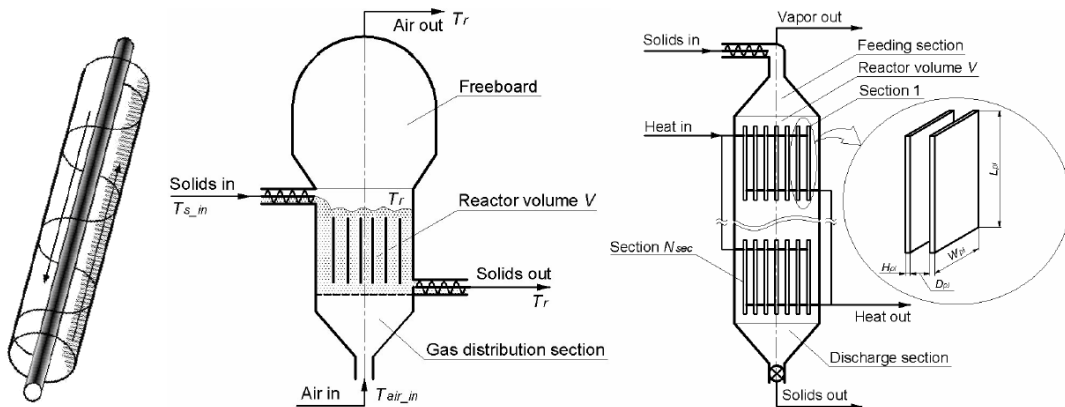


Figure 2-40 Three possible reactor designs for the use of powdered TCESM (screw reactor, fluidized bed reactor, gravity assisted bulkflow reactor) [86].

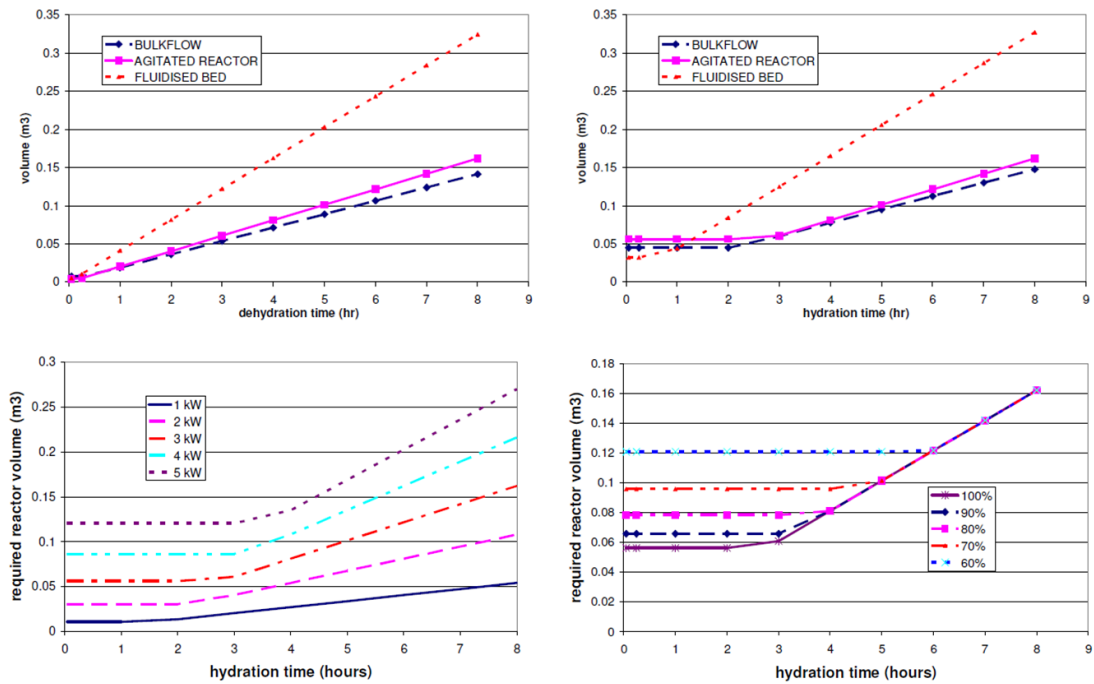


Figure 2-41 Reactor size against four constraints: dehydration time, hydration time, power output (of a screw reactor) and heat transfer (of a screw reactor) [86].

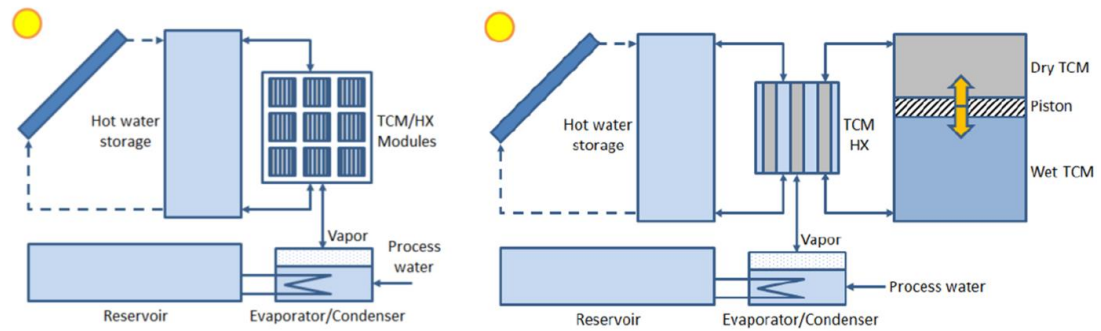


Figure 2-42 Modular thermochemical reactor design (left) Central reactor with vessel design (right) [112]

2.8.3 Summary of discussed potential reactor designs for TCES

Separate reactor designs appear to be the best choice, specifically a screw reactor. Studies highlight the possible engineering difficulty in transporting the material especially if it is a powder.

Reactor designs will be a vital component of the success of a TCES system. However, there does not appear to be vast amounts of research conducted comparing various configurations and their characteristics. This is believed to be because the current state of the

research appears to be focused more on material development, a logical choice due to the infancy of the subject.

2.9 Larger scale experimental results of TCES systems

TCES is in its infancy however, there are some large (~100kg+) notable investigations [27,74,80,110,113,114]. Some of the important findings are discussed below.

De Boer et al. [74], Abedin et al. [110], Finck et al. [80] all investigate the potential of a TCES system using zeolites. The systems from Abedin et al. [110] and Finck et al. [80] provide around 0.2 and 0.07kWh/kg, respectively. De Boer et al. [74] use a 150kg system and it is stated to provide 0.03kWh/kg. The oldest system (1996) is the one which achieves the highest kWh/kg, it is understood there are many other constraints to be considered (i.e. energy density, cost etc.). This 1996 system from Abedin et al. [110] is a functional zeolite open sorption system which provides a school with heating and air conditioning. The other two studies are lab prototypes.

Michel et al. [113] investigates a large scale (400kg) lab prototype and uses a salt hydrate (SrBr_2). It uses a novel modular tray system in attempt to enhance the permeability and hydration kinetics of the material. This is different from most open systems [74] which simply use a bulk store of material. The design can be seen in Figure 2-43. The system is shown to have an impressive power output 0.75-2W/kg which is significantly more than the required 0.3-0.8W/kg to achieve 3-4kW.

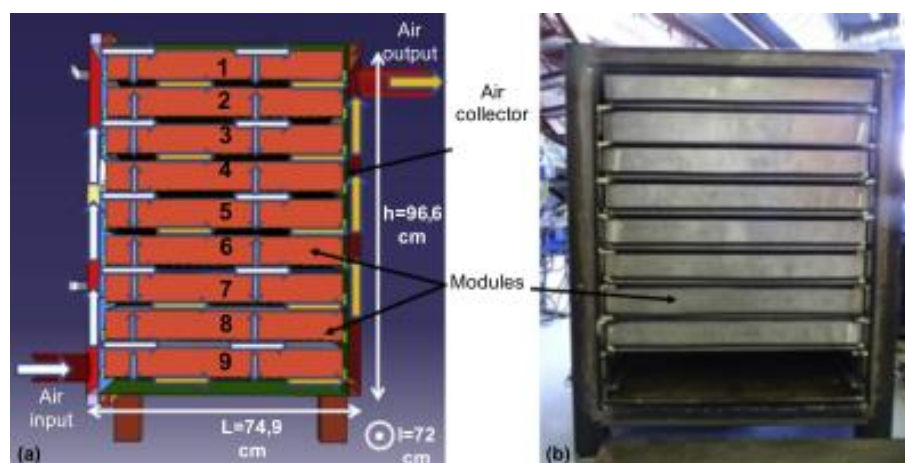


Figure 2-43 Novel salt hydrate tray reactor system [113]

Figure 2-44 is a large scale open sorption system, using a revolving drum filled with 70L of zeolite in granular form (1.6-2.5mm). The drum mixes the material while it is hydrating in attempt to increase the hydration kinetics. This is similar to the screw reactor proposed by Zondag et al. [86] where the mixing process was shown to improve the hydration kinetics [86]. The results are impressive with the system producing 1500W of power with 50kg of material which is significantly higher than other studies [74,80,110]. This system was dehydrated at 180°C, significantly higher than the maximum target dehydration value for use in a domestic environment of 150°C. Also, obviously with this system energy is required to “mix” the material.

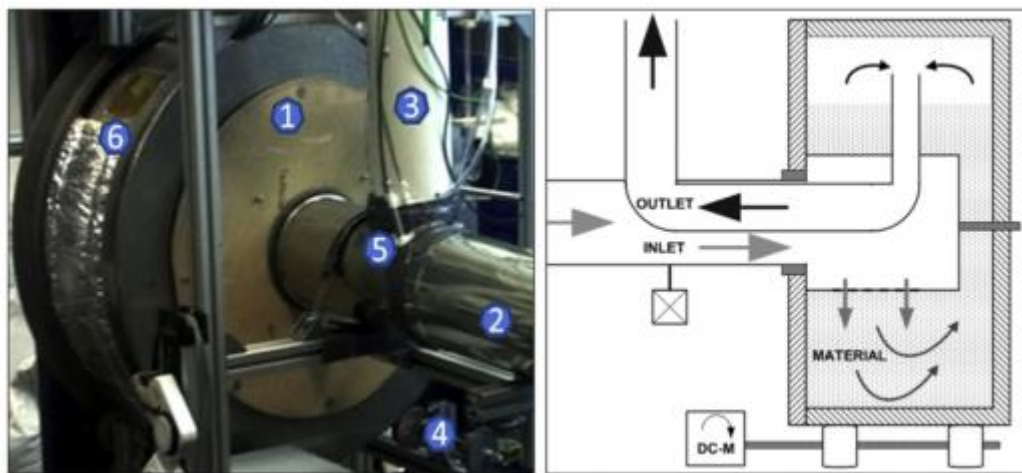


Figure 2-44 Open sorption drum reactor [114]

2.9.1 Summary of the large scale experimental results of TCES systems

Minimal large scale systems have been tested although they show potential. The majority of the large scale experiments use a material which has had minimal sample preparation. The material of choice for the larger scale systems is clearly zeolites, possibly due to their robust de/hydration characteristics.

Clearly further work is needed in large scale systems. Composite materials on a large scale should be promising. Reactor designs tested are all fairly simple and no closed or vacuum systems have been assessed on a large scale, possibly due to cost constraints. The use of MgSO_4 has not been used on a large scale, possibly due to its poor characteristics when used in a pure form. As research into TCES progresses the size and scale of the prototypes and systems will increase.

2.10 Conclusions of this literature review

It is clear to see, with all the studies discussed, that TCES is becoming an area with high interest. Research is being conducted into all different aspects of the process and is proving that there is potential. Also apparent are the gaps in research which need to be filled in order to make advances to TCES implementation into domestic environments.

The use of MgSO_4 as a TCES material has been shown to have potential but seems likely that it will be used within a host material due to its problematic hydration results.

From this literature review areas that are in need of further work, some of which were studied in this research project, are;

- Possibility of lower desorption temperatures and how this affects heat of sorption. It is shown [49] that a lower desorption temperature (110°C opposed to 130°C) has little effect on heat of sorption results.
- Establishing the true potential of MgSO_4 by investigating varying heating rates and cycle stability of the material.
- Development of composite materials, in attempt to reduce the problematic practical constraints of MgSO_4 [23,46,48,49]. Considering the host material and sample preparation.
- Experimental results for various reactor designs using MgSO_4 with an enhancing host material [28,86,110,112].
- Investigations into the affect sample formations (i.e. beads) have on the porosity and energy storage potential.
- Novel, lab scale, sample preparation techniques.

3 Chapter 3 - Methodology

3.1 Introduction to the methodology

This chapter describes the experimental methods used throughout this research for evaluation of the properties of the TCES materials tested. Each method was used to evaluate the TCESM at different mass which is important as the performance of TCES materials can change when tested at different scales as seen in chapter 2 (literature review).

This chapter is separated into 3 distinct sections. Each section explains the methodologies used for the practical experimentation and techniques used for characterising the TCES materials at different mass scales. These sections describe the methodology used for evaluating the performance of TCES materials at two distinct sizes ~10mg and 200g. This section also contains the preparation methodology used for the creation of the different samples tested.

Section 1 - Understanding the potential of TCES materials from lab experimentation on a small scale (~10mg)

The 10mg scale includes the methodology used for testing the TCES materials with different thermal analysis (DSC, TGA + RGA) and imaging (SEM + EDX) equipment to provide an understanding of the characteristics including composition, dehydration enthalpy, dehydration mass loss and dehydration decomposition analysis. This scale provided a baseline for the TCES materials potential which was compared to the larger scale size.

Section 2 - Understanding the potential of thermochemical materials from lab experimentation on a medium scale (200g)

The 200g scale includes the methodology used for testing the materials on a larger practical scale to understand characteristics such as power output, dehydration and hydration enthalpy and bulk density.

Section 3 - Sample preparation used for creating the composite TCES materials.

The sample preparation section examines the different methods used to create the composite TCESM and the ion exchange methodology used.

Five specific parts have been considered throughout this chapter for each methodology used.

1. Introduction and purpose of methodology –briefly introduces the methodology being used and the purpose for its use.
2. Instrumentation used – describes any equipment used for the methodology and explain any relevant background information on the methodology.
3. Experimental procedure – explains the methodology of the experiments with enough detail to allow the experiments to be reproduced.
4. Data collection – the data obtained from the experiments and how the data was used.
5. Justification – give reasons for the methodology used and explain the reasoning behind any explicit values used to justify the validity of the data collected.

3.2 Methodology used for the ~10mg scale tests of the TCES materials

To understand the potential of the TCES materials they were initially tested on a small scale. By testing a small sample size of the materials (<10mg) it was possible to understand the potential of the materials without the need for large amounts of material or consideration into the performance loss of the materials which can take place as the TCES materials are tested on a larger scale size (200g). To test the potential of the TCES materials at this scale several experimental methods were utilised, all of which are explained below in sections 3.2.1 - 3.2.5.

3.2.1 Small hydration chamber – Hydration of DSC, TGA + RGA and SEM+EDX samples

3.2.1.1 Introduction and purpose of the small hydration chamber methodology

If samples needed to be hydrated prior to the TGA+RGA, DSC or SEM+EDX testing they were hydrated using a custom built hydration chamber. The chamber allows for simultaneous hydration of both DSC and TGA samples. The hydration RH% and air flow rate can be controlled. The temperature of the humid air stream which hydrates the samples is controlled by a programmed microcontroller system.

3.2.1.2 Instrumentation used for the small hydration chamber methodology

Figure 3-1 shows a schematic of the small hydration chamber. First an air source was split and passed through two flow meters. The air source pressure was regulated to ensure the same flow rate was maintained.

Flow meter 1 controlled the flow of a dry air stream (the air was not completely dry however; it is referred to as dry for understanding). Flow meter 2 controlled the flow of the humid air stream. The output of flow meter 2 passed into a water container where it passed through a body of water to create a high humidity air stream. This air stream was then mixed with the air stream of flow meter 1. This mixed air stream then passed into the hydration chamber to hydrate the TCES samples. If a lower RH% air stream was desired the flow of flow meter 1 could be increased and the flow of flow meter 2 reduced.

The water container had a semi-submerged aluminium heat sink. The “cold” side of a TEC Peltier plate (40mm x 40mm) was attached to the centre of the heat sink and cooled the heat sink which in turn cooled the water. The outside of the Peltier plate was sealed with high strength sealant to prevent any leaks from the water container. The “hot” side of the Peltier plate was attached to an aluminium block which then connected to an air cooled heat sink. This heat sink had a fan and was used to cool the hot side of the Peltier plate. The Peltier plate was connected to a 12v regulated power supply which was connected to a relay. The relay was connected to an Arduino microcontroller. Connected to the Arduino microcontroller was a temperature sensor located at the entrance of the hydration chamber. This temperature sensor was monitored by the Arduino and if the humid air stream was above a set point temperature the Arduino activated a relay which turned on the Peltier plate which in turn cooled the water. The temperature sensor connected to the Arduino was a TMP36 analogue temperature sensor, in the same location was a thermocouple which was connected to a Datataker DT85 data logger which logged the temperature. At the entrance of the hydration chamber was a HIH-4000 series Honeywell humidity sensor which was also connected to the Datataker and logged the humidity of the humid air stream. The hydration chamber was constructed from 316 stainless steel and was insulated with Armaflex foam insulation. Between the lid and base of the hydration chamber was a sheet of silicone to reduce air leaks.

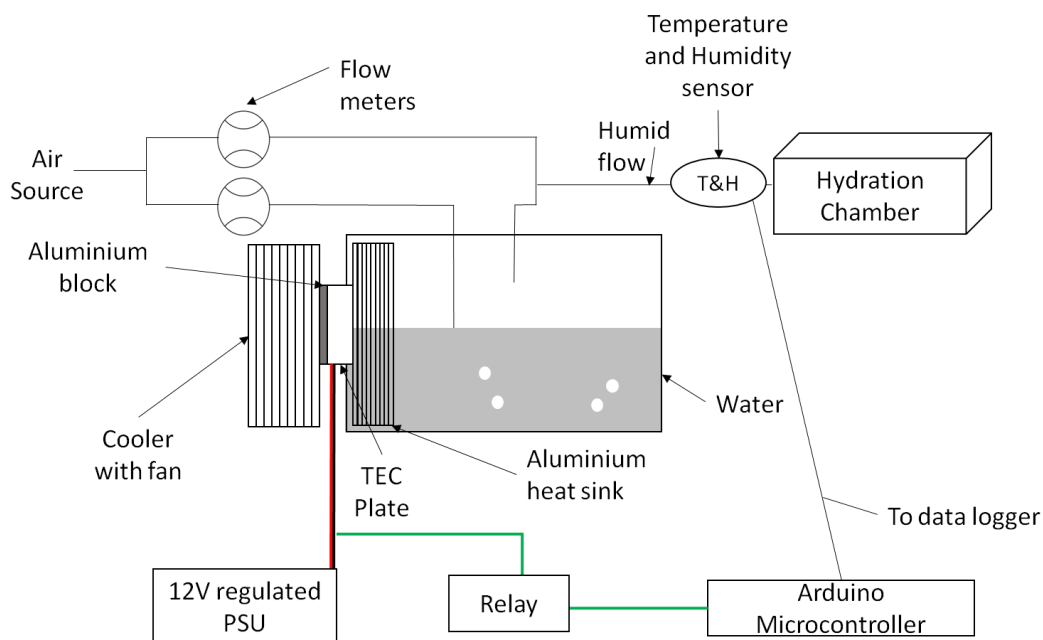


Figure 3-1 A schematic diagram of the small hydration chamber system

3.2.1.3 Experimental procedure used for the small hydration chamber methodology

The samples were hydrated at a partial vapour pressure of $\sim 1.3\text{kPa}$ at 20°C for a minimum of 18 hours unless otherwise stated. Once the samples were hydrated they were moved to the piece of equipment required for testing i.e. DSC or TGA.

3.2.1.4 Data collection for the small hydration chamber methodology

The data was collected from the sensors and stored on the Datalogger. The data was unloaded and formatted within a spreadsheet. Average values of RH% and partial vapour pressure were calculated and tabulated to ensure the hydration was carried out as required.

3.2.1.5 Justification of the small hydration chamber methodology

This partial vapour pressure ($1.3\text{kPa p}_{\text{H}_2\text{O}}$) was chosen as it is a vapour pressure which can easily be achieved in the UK winter. The hydration chamber was built and used for the hydration of small TCES material samples prior to testing. As the thermal analysis equipment (TGA or DSC) did not allow for hydration of the TCES samples an external device was required for the hydration prior to dehydration testing (i.e. the small hydration chamber). 18 hours of hydration time was assumed to be an ample amount of time for the hydration to reach the chosen hydration chamber conditions for the small ($<10\text{mg}$) samples.

This setup contained different pieces of equipment which all have their own uncertainty in the measurement values. For example, the humidity sensor used had an accuracy of +/- 3.50% and the thermocouple used was a class 1 T-type thermocouple with an accuracy of +/- 0.5°C.

Water saturation pressure (P_{sat}) is dependent upon temperature only. Hence, to calculate the uncertainty in P_{sat} at a set point of 20°C, temperatures of 19.5°C and 20.5°C (+/- 0.5°C uncertainty in the thermocouple) can be used. The two P_{sat} values calculated are 2.296kPa (for 292.85K) and 2.443kPa (for 293.85K) hence, the uncertainty in the calculated P_{sat} value is $(2.443-2.296)/2 = 0.0735\text{kPa}$. This means the measured P_{sat} for 20°C (293.15K) = 2.339kPa (+/- 0.0735kPa), as a percentage error this is 3.14%.

To calculate the combined uncertainty in a measurement (x) where the measured values are multiplied or divided together, the combined uncertainty (dx) in the measured value is give by Equation 3-1.

$$\frac{dx}{x} = \sqrt{\left(\frac{da}{a}\right)^2 + \left(\frac{db}{b}\right)^2 + \left(\frac{dc}{c}\right)^2 + \dots + \left(\frac{dn}{n}\right)^2} \quad \text{Equation 3-1}$$

The water partial vapour pressure is calculated as P_{sat} multiplied by the relative humidity. Using Equation 3-1 the uncertainty in the water partial vapour pressure can be calculated as shown in Equation 3-2. Where dx = the uncertainty in the water partial vapour pressure, x = the calculated water partial vapour pressure, $\frac{da}{a}$ = the uncertainty in the P_{sat} (3.14%), $\frac{db}{b}$ = the uncertainty in the RH% (3.50%).

$$\frac{dx}{x} = \sqrt{\left(\frac{da}{a}\right)^2 + \left(\frac{db}{b}\right)^2} \quad \text{Equation 3-2}$$

This equates to a percentage uncertainty in the water partial vapour pressure of 4.70%.

The hydration temperature and humidity will have an impact on the hydration of the TCES materials. However, as the hydration of the TCES materials tested throughout this thesis do not all hydrate in the same way (i.e. if a salt hydrate is being used the hydration profile is likely to be stepped opposed to linear) the impact the uncertainty in temperature and humidity due to the accuracy of the devices is difficult to calculate directly, especially as many of the samples tested were composite samples containing a mixture of different materials all with different hydration properties. This is the reason several samples of each

materials were tested several times in the devices (i.e. TGA and DSC). From this the experimental deviation in measurement could be established. The device used for testing the dehydration enthalpy of the TCES materials is very accurate and precise (i.e. DSC = temperature accuracy of $\pm 0.025^{\circ}\text{C}$ and enthalpy precision of 0.04% [115]). Throughout this thesis error bars have been added to graphs which show experimental data, where appropriate.

3.2.2 DSC dehydration enthalpy analysis methodology

3.2.2.1 Introduction and purpose of the DSC dehydration methodology

To analyse the dehydration enthalpy of each of the TCESM and understand the amount of energy required for dehydration (charging) and therefore interpret the expected amount of enthalpy released on hydration (discharging) a DSC was used.

3.2.2.2 Instrumentation used for the DSC dehydration methodology

A DSC is a device which is able to measure the heat flow of a sample, typically of around 10mg, when it is exposed to thermal changes in a controlled atmosphere and environment. The thermal changes are programmed into the device via software. Thermal changes include temperature ramps, isotherms and equilibrations [116].

A DSC measures the heat flow of a sample within a pan and the heat flow of a known empty reference pan when put through a thermal program. A known empty pan, identical to the sample pan, is used as a reference pan. The difference in heat flow between the sample and the reference is due to transitions within the sample, such as melts, crystallisations or dehydrations.

The DSC used throughout this work was a TA instruments Discovery DSC. The device has a temperature accuracy of $\pm 0.025^{\circ}\text{C}$, an enthalpy precision of 0.04% and is capable of a temperature range of $-180 - 725^{\circ}\text{C}$ [115]. The software used to analyse the data from the DSC and programme the device is TRIOS, a programme developed by TA Instruments. The Discovery DSC uses a chromel and constantan diffusion bond for the sample and reference stage to create a perfect thermocouple which is less sensitive to sample pan placement [115]. The sample pans used in this work were aluminium T-Zero pans with lids. The DSC used for this research has an auto sampler which allowed for loading and setting a test sequence for up to 50 samples. Once a sample was finished a robotic arm unloaded the complete sample and

loaded the next sample to be tested without the need for human intervention. To create an inert atmosphere for the samples nitrogen was used as a purge gas which was generated by a Genius 3051 Nitrogen & Air generator [117].

3.2.2.3 Experimental procedure used for the DSC dehydration methodology

Throughout this work a DSC heating rate of 5°C/min was used unless otherwise stated. The sample size used was approximately 5-10mg. In all tests the lid of the sample pans were punched with 5 holes to allow the escape of volatiles from the samples.

Once hydrated the samples were placed in the auto sampler of the DSC. As the hydration enthalpy of the samples could not be analysed directly a temperature program was used which measured the dehydration enthalpy and allowed for prediction of the hydration enthalpy. The temperature program dehydrated a hydrated sample twice. The enthalpy from the first dehydration minus the enthalpy from the second dehydration was used as a prediction for the hydration enthalpy value. The enthalpy from the first dehydration is a sum of the enthalpy for the dehydration process of the TCESM and also the enthalpy required for heating the sample (sensible heat). The second dehydration cycle is only a result of the sensible heat, as the material is already in a dehydrated state. An example of the temperature program profile used is shown in Figure 3-2. The enthalpy required for both the first and second dehydration was calculated using a sigmoidal integration between the 5 minutes isothermal period at 20°C and the 60 minutes isothermal period at 150°C to ensure the integration took place between two stable heat flow points.

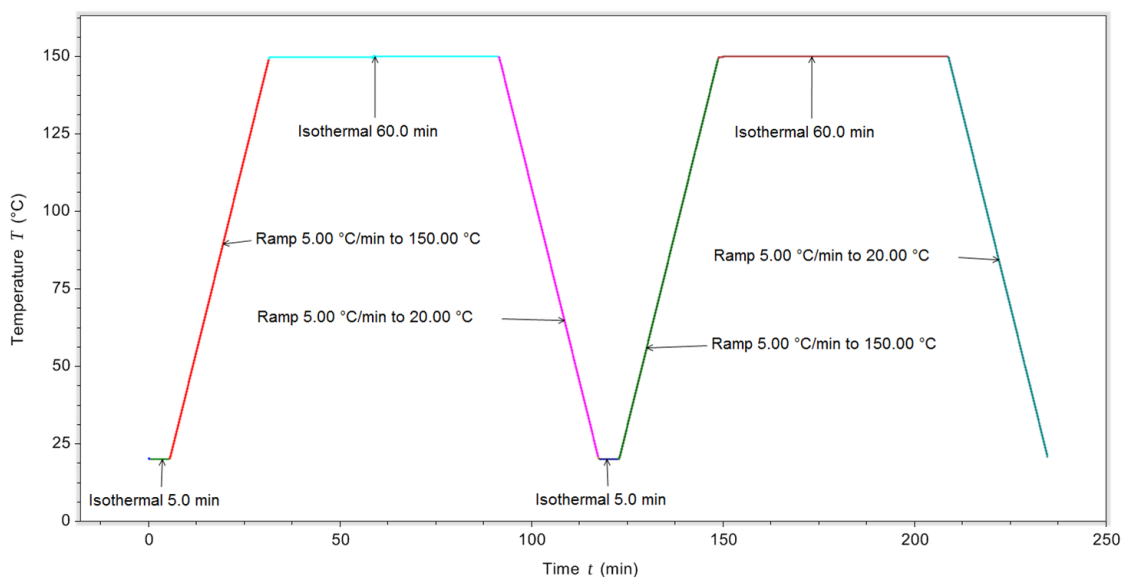


Figure 3-2 Example DSC temperature profile program

Each sample tested in the DSC was tested in powder form. If the sample was a pellet it was ground into a fine powder using a mortar and pestle. For example, the 13x ion exchange pellets produced were required to be crushed into a powder for the DSC testing. To do this 2g of the sample was weighed and ground into a powder, only <50mg was required for the tests.

3.2.2.4 Data collection used for the DSC dehydration methodology

The data recorded from each DSC test was the total dehydration enthalpy (ΔH_T), enthalpy due to dehydration (ΔH_D) and enthalpy due to sensible heat (ΔH_S). The enthalpy due to dehydration was calculated as:

$$\Delta H_D = \Delta H_T - \Delta H_S \text{ Equation 3-3}$$

This data was imported into a spreadsheet which calculated an average for each enthalpy value recorded for each experimental cycle. An overall average for each enthalpy recorded from the material tested was also calculated. For example, if 3 samples were tested for 3 cycles the data collected for each DSC test was 3 enthalpy values (ΔH_T , ΔH_D and ΔH_S) per cycle, an average for each cycle (i.e. 3 averages for each enthalpy value as there were 3 cycles) and an overall average for each enthalpy value for the material being tested. This means for a sample tested there would be 27 enthalpy values, an average for each ΔH_T , ΔH_D and ΔH_S for each cycle and a total average for ΔH_T , ΔH_D and ΔH_S from all 3 cycles.

3.2.2.5 Justification of the DSC dehydration methodology

The DSC was used to find the dehydration enthalpy of the TCESM on a small scale (~10mg). It has been used in many studies for this purpose [23,44,48]. The DSC data can be used to identify potential candidate materials which are likely to have good characteristics on a larger scale.

The need for calculation of ΔH_T and ΔH_S of the material opposed to only ΔH_T was for two reasons. First the hydration enthalpy cannot be directly measured in the current DSC setup and ΔH_D gives an indication of the hydration enthalpy. Secondly, ΔH_S is an important characteristic of the sample and must not be ignored. ΔH_S of the sample is essentially wasted energy when considering the use of TCES materials in an interseasonal system. It is intended the dehydration (charging) of the TCESM will take place when heat is not in demand within a domestic environment the sensible heat (ΔH_S) of the material will be dissipated into the surroundings and wasted.

A heating rate of 5°C/min was used as it provides high sensitivity (higher heating rates provide higher sensitivity) and also a good resolution (lower heating rates provide better resolution) [118].

The sample size used was large enough to provide a good sensitivity while also being small enough to provide good resolution and reduce the chance of thermal gradients in the sample [118].

Initially when a DSC is starting a test there can be anomalies in the recorded heat flow known as “start-up hooks”. To overcome these anomalies the isothermal periods are required if the enthalpy from the start of the test needs to be analysed, which it was for the tests in this research. The isothermal periods stabilise the heat flow which is useful for analysis. The integration to find the dehydration enthalpy was conducted between the isothermal points as this gives two linear heat flow points to integrate between.

The 60 minute isothermal period was used to stabilise the heat flow at 150°C and allow for the completion of dehydration at 150°C. Due to dehydration kinetics it takes time for the samples to dehydrate at each temperature point. If the isothermal period was not sufficiently long enough to allow the dehydration to happen it would result in the sample not being completely dehydrated and give less accurate results. A 60 minute isothermal period was used as it is sufficiently long enough for the samples to complete dehydration at 150°C with the used heating rate.

The samples were dehydrated from 20 - 150°C because vacuum solar thermal collectors can efficiently operate at 150°C [119]. It is important to evaluate the materials potential within this temperature range.

If the sample needed to be ground into a powder an ample amount (>2g) of the sample was ground in an attempt to provide an even distribution of the sample and reduce the chance of testing a sample which was not indicative of the whole sample created.

Several samples of each material were used in the DSC testing, this was done to identify any anomalous data and stop it being recorded and used as well as to identify experimental error.

3.2.2.6 Limitations of the DSC dehydration methodology

When the DSC samples were hydrated and placed within the DSC auto sampler ready for testing there was a chance that the samples could start to dehydrate or further hydrate in the ambient. Further hydration will not happen as the hygrothermal properties of the laboratory are regulated by large air conditioning units. The laboratory is regulated to around 20°C with a RH% <50%. Dehydration in the auto sampler did not happen as the samples are hydrated at 20°C at ambient pressure.

3.2.3 TGA (+ RGA) mass loss methodology

3.2.3.1 Introduction and purpose of the TGA (+ RGA) mass loss methodology

To analyse the dehydration mass loss with temperature of the TCESM a TGA was used. This information allowed for an understanding of the amount of water dehydrated from the TCESM tested. The data obtained from the TGA can be overlaid with the DSC data to confirm that endothermic DSC peaks are results of dehydrations as TGA mass loss peaks will be seen at the same temperatures. In this work the RGA was used predominantly for comparing water loss peaks from the TGA sample with TGA mass loss peaks.

3.2.3.2 Instrumentation used for the TGA (+ RGA) mass loss methodology

The TGA used in this work was a TA Instruments Discovery TGA. Attached to the outlet of the furnace of the TGA was an RGA. An RGA allows for analysis of gases released from the TGA sample with temperature. This allows for an understanding of the materials being

dehydrated or decomposed from the TGA samples. The RGA used in this work was a MKS Cirrus 2 RGA [120].

A TGA is a device which measures the changing mass of a sample with changing temperature and time. The Discovery TGA uses a proprietary thermobalance see Figure 3-3. The Discovery TGA is capable of a temperature range of ambient to 1200°C with a temperature precision of $\pm 1^\circ\text{C}$ [121]. The TGA can have temperature profiles programmed to it, similar to the DSC (see section 3.2.2), using the TRIOS software.



Figure 3-3 TA instruments discovery TGA balance [122]

An RGA allows the user to measure the gases released from the TGA samples. The way an RGA measures the gases present is as follows [123];

1. Gas molecules are passed into the RGA (via the capillary tube at the output of the TGA furnace) where they become ionised.

Within the RGA are filaments. These filaments are heated to high temperatures, when heated hot enough electrons within the filament gain enough energy to escape the metal work function [123] of the filament wire into the surrounding vacuum.

These electrons which have now escaped are accelerated using a potential difference. The energy the electrons gain is the potential difference value in eV. These electrons can now collide with gas molecules and ionise them.

2. Electrostatic lens

This part of the RGA is used for “directing” the created gas ions towards the quadruple mass filter, the lenses are a doughnut shape. When a potential difference is applied to a lens of this shape an electric field is produced which directs and accelerates the gas ions through the lens in a beam towards the quadruple mass filter.

3. Quadruple mass filter

The quadruple mass filter consists of 4 rods that are electrically biased. Due to the placement of the rods this creates a path through the electric field for specific M/e ions (mass to charge ratio) and all other ions which do not have the correct M/e ratio collide with and are neutralised by the 4 rods.

4. Ion detection

Now that only ions with a specific M/e ratio have passed through the mass filter they can be detected to give an indication of the amount of ions present. This process of detection can be done with a faraday cup. A faraday cup is simply a piece of metal which has a negative potential. When the ions pass over the faraday cup they are attracted to this negative potential and collide with the metal. This collision neutralises the ions and also induces a current within the faraday cup which is detected. This current is known and recorded as the ion current from the RGA. The higher the ion current the larger the number of ions present and therefore the higher amount of those gas molecules present in the gas released from the TGA sample.

3.2.3.3 Experimental procedure used for the TGA (+ RGA) mass loss methodology

In this research the RGA allowed measurement of the gases which were released from the TGA sample. Before the RGA could be used several things needed to happen;

1. The RGA needed to be pumped down to create a low pressure environment

2. A filament needed to be switched on – the MKS RGA used in this work had two filaments. Both filaments served the same purpose, there are two because the filaments burn out with time and the replacement can be time consuming.
3. Capillary heater needed to be switched on – This capillary heater reduces the chance of gases from condensing in the capillary tube and blocking it.
4. System bake needed to be switched on – this process “baked” the RGA in attempt to remove any condensed gas and reduce the background content of gases. This process is started before each RGA test.

The MKS software, Process Eye, was used along with add-on software from TA instruments. This add-on software allowed for several sample tests to be set up within the RGA software and be triggered automatically via the TGA software trigger. For example once sample 1 had completed a trigger was sent the RGA to stop recording data, next the TGA would unload sample 1 and load sample 2. Once sample 2 was loaded by the auto sampler and ready for testing the TGA software sent a trigger to the RGA software that sample 2 testing was about to begin and the RGA software started to record data.

The sample pans used in the TGA were open platinum pans of 100 μ L. The sample mass used was 2-4mg. The Discovery TGA also had an auto sampler which allowed for loading of multiple samples and the TGA would load and unload samples automatically.

In order to keep testing consistent to the DSC and to ensure comparison of data was possible the heating rate used in this work was 5°C/min. The purge gas used for the TGA was nitrogen which was produced by a Genius 3051 nitrogen and air generator [117].

The temperature program methodology was very similar to the DSC method. However, the TGA ramps the sample up to 150°C at 5°C/min, holds the sample isothermally for 120 minutes and then cools back to 35°C at 5°C/min. An example of the temperature profile used is seen in Figure 3-4.

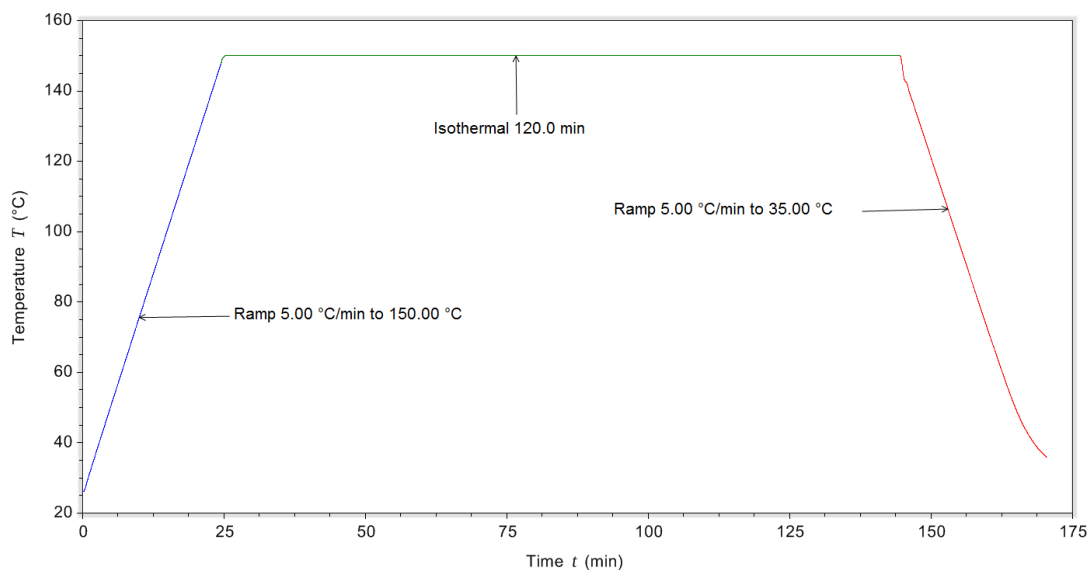


Figure 3-4 TGA Temperature Profile

The samples were prepared in the same way as the DSC samples (see section 3.2.2.5) and used in a powder form. The TGA samples were made from the same batch of powder that the DSC samples were made from. When preparing a sample to be tested in the TGA at least two samples of the same batch of material were used and tested. Each sample from a material batch was cycled several times. For each sample tested there was a corresponding RGA dehydration file which collected data of the expelled gas from the TGA samples from 0-300amu.

3.2.3.4 Data collection for the TGA (+ RGA) mass loss methodology

The data produced and used from the TGA experiments was the mass loss after 150°C dehydration. This data was stored in a spreadsheet where the data from each cycle is averaged and then finally an average for all cycles is found for each material. The differential of mass loss with time or temperature was produced and used to compare the peak mass loss with the peak in 18amu (H₂O) RGA ion current and the peak dehydration heat flow (DSC).

3.2.3.5 Justification of the TGA (+ RGA) mass loss methodology

The use of a TGA for analysis of dehydration mass loss specifically for TCESM has been utilised in many previous studies [45,124–126].

The sample mass used in the TGA was smaller than the DSC due to the amount of volatiles the capillary tube could handle. It was advised that it is not wise to allow more than 2mg of volatile material to pass through the capillary tube each test.

Two dehydration cycles were required for analysis of different endothermic heat flows of the DSC samples however, for the TGA samples only one dehydration cycle was needed to analyse the mass loss.

When testing samples in the DSC an initial equilibrate and isothermal period (5 minutes) was used to stabilise the heat flow in the DSC. The TGA did not need this initial isothermal stage as the “start-up hooks” were not a problem when analysing the TGA data. The isothermal period at 150°C was required and was used for the same purpose as in the DSC, to allow any excess water to be dehydrated at the set point temperature.

The dehydration temperature used in the TGA tests (up to 150°C) was to allow for comparison of the TGA and RGA data to the DSC and also due to 150°C being a temperature which is towards the upper most value to achieve efficient supply heat from a vacuum flat plate collector [119].

A full scan (0-300amu) for each RGA test was conducted as the scans did not take much time (~5 seconds) relative to the time taken for each sample test.

The comparison of the TGA differential peaks to the DSC and RGA data was to confirm each peak was due to a dehydration peak. An example of this data overlaid is shown in Figure 3-5 which shows how all of the peaks are at similar temperatures verifying the peaks are due to a dehydration transition.

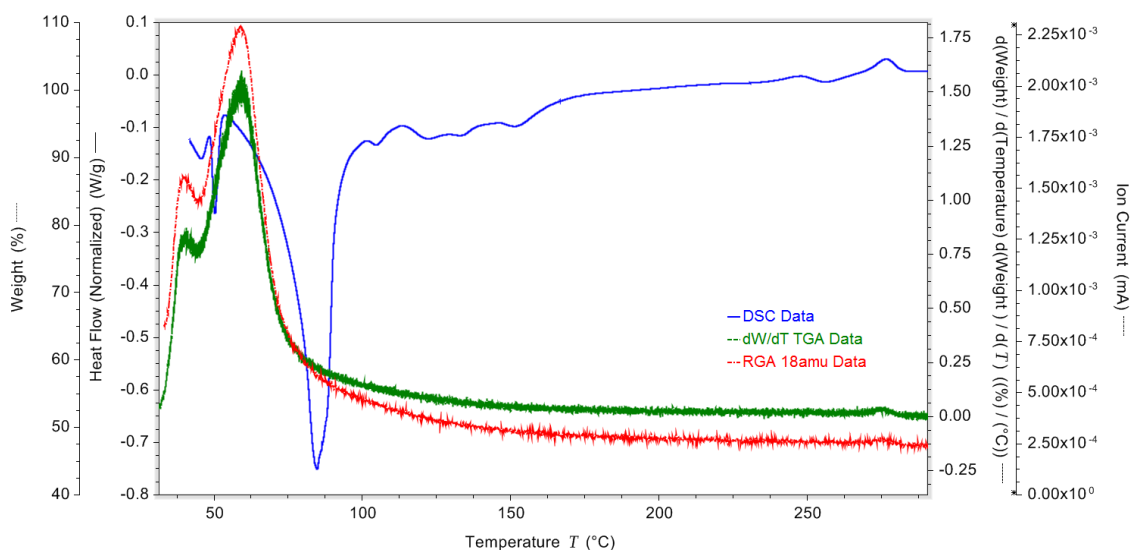


Figure 3-5 An example overlay of DSC, RGA and TGA data, showing the dehydration of $MgSO_4 \cdot 7H_2O$

3.2.3.6 Limitations of the TGA (+ RGA) mass loss methodology

The TGA did not have cooling to allow it to be cooled sub ambient and the tests needed to be started at around 30°C. This means that the data points for the first ~10 degrees of temperature (20-30°C) were lost. This is not a major problem as the materials still lost the same amount of mass but there was no data for temperatures below the start point of the tests.

3.2.4 SEM + EDX analysis methodology

3.2.4.1 Introduction and purpose of the SEM + EDX analysis techniques used

Throughout this work SEM and EDX analysis was conducted for analysing the composition and structure of the TCESM. EDX is a method which allows for elementary analysis without much sample preparation. It allows the analysis of the TCESM to ensure the composition of the samples and ion exchange took place satisfactory along with allowing the imaging of the samples structure.

3.2.4.2 Instrumentation used for the SEM + EDX analysis methodology

The device used throughout this research for SEM and EDX analysis was a Hitachi TM3030 table top SEM with attached EDX. This device is capable of magnifications up to 30,000x and requires minimal sample preparation.

3.2.4.2.1 The workings of Scanning Electron Microscopes (SEM)

SEM works by beaming electrons onto a sample and using a detector to detect the x-rays and electrons produced or scattered from the electron bombardment [127].

Electron microscopes work as described below [127];

1. Electrons are produced by an electron gun.
2. The electrons travel towards the sample through a vacuum. While travelling towards the sample the electrons are focused into a beam using electromagnetic lenses.
3. The electron beams hit the sample which causes electrons or x-rays to be ejected from the sample. The ejection is detected by different sensors and used to create an image of the sample. The different types of ejection are as follows;
 - a. X-rays – are produced when an electron collides with an atom within the sample and causes an electron to be ejected from the atom from a lower level shell causing a hole. An electron from a higher level shell drops down to the

lower energy level to fill this electron hole and releases energy in the form of an x-ray when it fills the hole. This type of emission is used for EDX analysis and is explained in more detail in section 3.2.4.2.2.

- b. Backscattered electrons - Electrons produced from the electron beam after colliding with the sample and being reflected off the atoms and not absorbed. The backscattered electrons can come from deeper within the sample giving more depth of the sample. A separate detector is used to detect these electrons.
- c. Secondary electrons – This takes place when the electrons from the electron beam hit the atoms in the sample and are absorbed. When the electrons are absorbed secondary electrons are ejected from the atoms in the sample. The detector for these electrons typically has a faraday cage with a large positive potential difference to attract the electrons towards the detector where the image is formed. These electrons are good for providing surface features.

3.2.4.2.2 *Workings of the EDX*

EDX allows for elemental composition analysis. EDX bombards the sample typically with electrons or X-rays. This process may excite the electrons of an atom within the sample. This excitation can result in the ejection of an electron from the inner shell of the atom. To fill the hole created by the ejected electron, an electron from a higher energy level shell fills the hole. This movement of electron from a higher to lower energy level results in the emission of energy from the atom. The difference in the energy between the lower and higher shells is the value of the emitted energy. This energy may be released in the form of an x-ray [127,128].

The energy released can be measured by an energy dispersive spectrometer. As the energy levels of the electron shells are quantised (i.e. they are restricted to specific energy level values and not continuous) and discrete to specific elements the composition of the sample can be found.

3.2.4.3 *Experimental procedure used for the SEM + EDX analysis*

The sample preparation for the SEM and EDX analysis was relatively simple for the TM3030. The samples needed to be adhered to a carbon stub (a thin layer of adhesive carbon). The stub is either 10 or 25mm in diameter. The carbon stub was first stuck to a metal disc, the sample was then placed on the carbon stub. Then using low pressure air the sample was blown to adhere the sample to the stub. The samples used throughout this research were

either powder or pellets. The pressure of the air was increased slowly to apply more pressure to the sample and ensure the sample was firmly stuck to the stub but also to remove any excess powder or loose particles from the sample. The sample was then placed on a sample stage and the height of the stage was adjusted to ensure the sample was the correct height within the SEM to produce an in focus image. The SEM was then pumped down to a low pressure to create an evacuated environment. Once pumped down the sample could start to be analysed.

When analysing the samples a 15kV potential difference was used for the SEM. For analysing the composition of a sample the TM3030 EDX software was used. The analysis used within the software was a dot scan. This scan allows the user to place a circle of different sizes on an image of the sample. The software then scans the composition within the defined circle area. Figure 3-6 shows an example of the circle used in a dot analysis, the atomic composition of the sample and an example EDX atomic spectrum from the dot analysis.

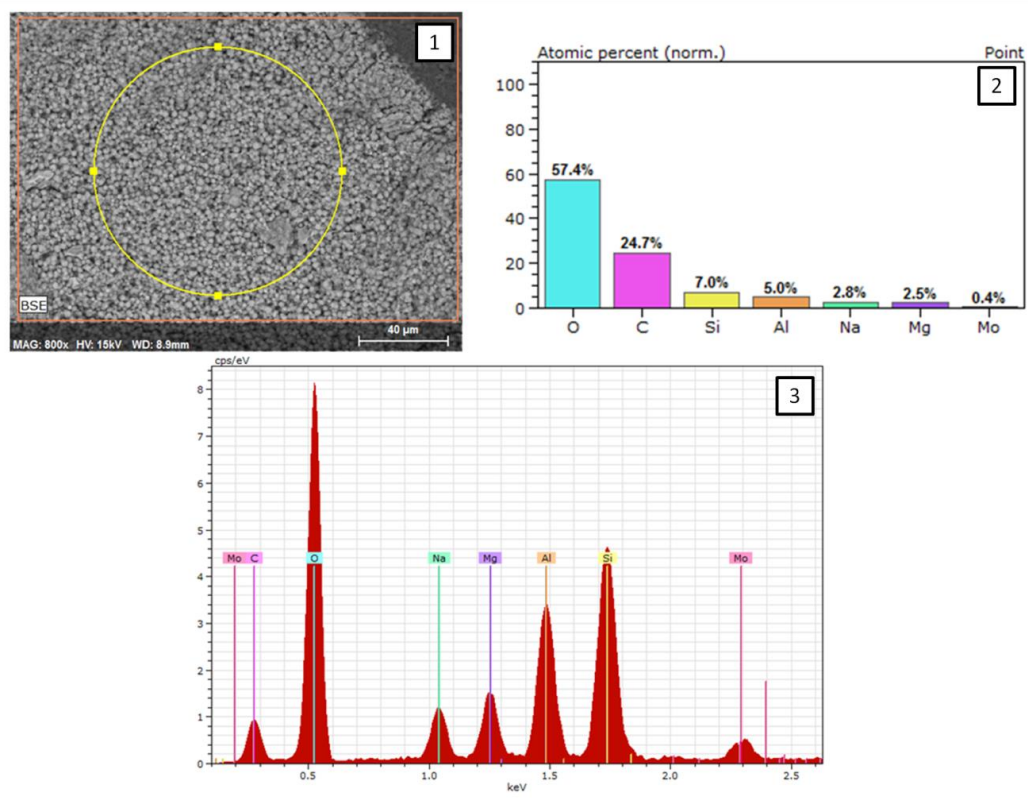


Figure 3-6 Image 1: Example EDX dot analysis, Image 2: Composition from dot analysis, Image 3: Example of an EDX atomic spectrum from the dot analysis.

To find the composition of a sample the dot analysis was run on the sample in at least 3 different locations of the sample to get an average value for each element. Table 3-1 shows an example of the data collected for the 13x pellets.

Table 3-1 Example EDX data showing elemental analysis of 13x pellets

EDX Mass percentage (%)				
Element	Test 1	Test 2	Test 3	Average
Oxygen	51.5706	46.4484	48.33497	48.78 (+/- 2.591)
Silicon	17.60165	18.58128	18.7324	18.31 (+/- 0.614)
Carbon	7.153292	13.79168	10.49403	10.48 (+/- 3.319)
Sodium	10.67362	8.31564	9.317145	9.44 (+/- 1.183)
Aluminium	11.80319	11.80206	12.08296	11.9 (+/- 0.162)
Magnesium	1.19765	1.060928	1.038486	1.1 (+/- 0.086)

For assessing the composition changes within the 13x ion exchanged samples the elements in question (Mg and Na) were normalised to get a % of Na to Mg content. Table 3-2 shows an example of the data collected for an ion elemental analysis.

Table 3-2 Normalised Mg and Na EDX example for 13x pellets

Normalised Mg and Na element percentage (%)				
	Test 1	Test 2	Test 3	Average
Mg	10.08864	11.31467	10.028223	10.48 (+/- 0.726)
Na	89.91136	88.68533	89.971777	89.52 (+/- 0.726)

3.2.4.4 Data collection used for the SEM + EDX analysis

For each sample tested multiple locations of the sample/s were imaged and scanned using the EDX. For each scan the data produced was;

1. SEM images of sample with the location of the EDX scan
2. EDX elemental mass percent analysis
3. EDX elemental spectrum analysis

Once this data was collected it was imported into a spreadsheet for analysis, examples of the results are shown in Table 3-1 and Table 3-2 above.

3.2.4.5 Justification of the SEM + EDX analysis

SEM and EDX analysis has been used in previous research by many authors for analysis of surface structure and composition of TCESM [23,36,67]. This method allows for the testing of samples without much preparation meaning the samples are not contaminated which could result in anomalous results.

3.2.4.6 Limitations of the SEM + EDX analysis

The air used to adhere the samples to the carbon stub may cause a hydration to some of the samples. However, this method reduced the damage to the samples which could be caused from applying pressure to them to stick them firmly to the carbon stub. Also, it was advised the samples used would need to be blown by air to remove any excess particles because if there were any loose particles when the sample was pumped down the loose particles could damage the SEM.

3.2.5 Nitrogen vapour sorption testing methodology

3.2.5.1 Introduction and purpose of the nitrogen vapour sorption testing methodology

To understand the porosity of the TCESM a nitrogen vapour sorption technique was used. This method allows for analysis of pore size, pore surface area, pore volume and surface area of a sample. This was important for this research as the performance of a TCESM has been shown to be impacted by its porosity characteristics. It was shown in the literature review (chapter 2) that samples with higher surface area and a larger pore volume perform better. One reason for the increased performance from higher pore volume is increased vapour transportation which results in faster hydration and higher power output.

3.2.5.2 Instrumentation used for the nitrogen vapour sorption testing methodology

For the nitrogen sorption analysis a Micromeritics Tristar 2 3030 was used. This device uses physical adsorption and capillary condensation principles to acquire porosity data on the sample being tested.

3.2.5.2.1 Nitrogen sorption theory

The procedure first evacuates a sample and then exposes it to low cryogenic temperatures. Then the sample is exposed to a testing gas (in this case nitrogen) at different pressures. For each pressure the amount of gas adsorbed by the sample is measured. With increasing pressure the amount of gas adsorbed increases.

As the adsorption stage progresses first the micropores in the surface area of the sample are filled, then the free surface becomes completely covered by the nitrogen gas and finally the larger pores are filled due to capillary condensation of the nitrogen gas. Once the adsorption process has finished the desorption process takes place which reduces the pressure the sample is exposed to which desorbs the nitrogen from the sample. The amount of gas adsorbed by the sample at each desorption pressure is also recorded. These two data sets are used to describe the adsorption and desorption isotherms.

The nitrogen molecules are bound to the surface of the sample by surface forces and are only weakly bound, which is why they are easily adsorbed and desorbed.

There are 6 types of adsorption isotherms [129], Figure 3-7 shows an example of each of the 6 adsorption isotherm types.

1. Narrow pores filled at low pressures. Common in microporous materials (<2nm) - zeolites, activated carbon, charcoals and MOF's. Very high surface area.
2. Non-porous solid or one with very large pores (50nm), seen from high pressure saturation. Typical of mesoporous materials (2-50nm).
3. No plateau is seen. Solid with large pores
4. Similar to type 2 but with hysteresis
5. Capillary condensation takes place at intermediate pressures. Associated with mesoporous materials (2-50nm). Experiences hysteresis.
6. Non porous absorbent which has a uniform surface. Adsorption occurs layer by layer which is why you get the steps on the graph. Bulk condensation occurs eventually.

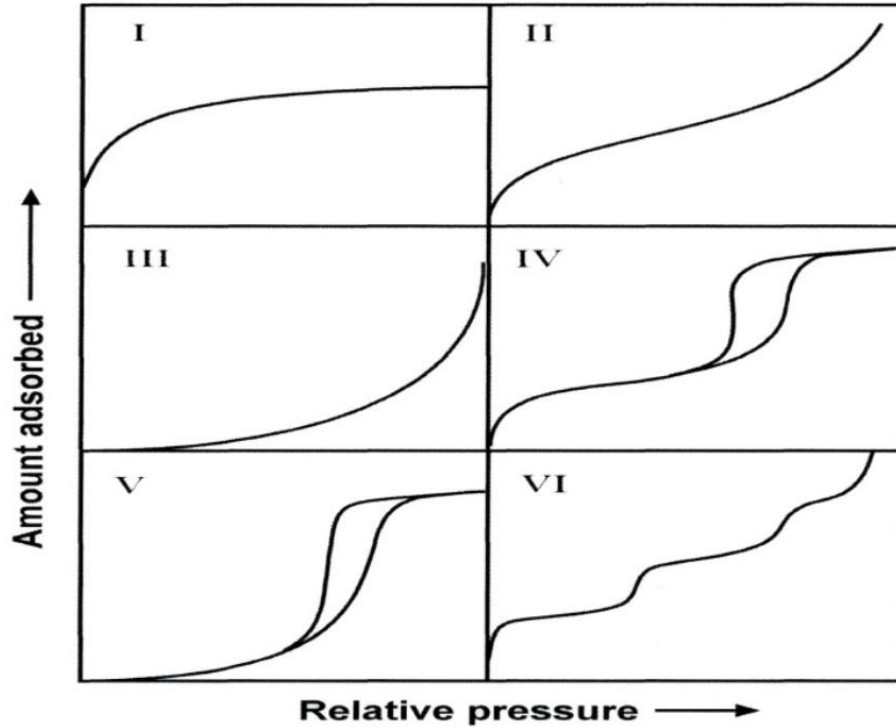


Figure 3-7 Types of adsorption isotherms [129]

For calculating the surface area of the samples the BET model is used. For calculation of the pore volume the BJH model is used.

Specific surface area from monolayer adsorption can be calculated from nitrogen adsorption with Equation 3-4

$$SSA = \frac{q_m \sigma N_a}{m} \text{ Equation 3-4}$$

Where q_m = the monolayer capacity of the sample (moles), σ = surface area occupied by one molecule at analysis temperature (0.16nm^2 per molecule of nitrogen), N_a = Avagadro's number and m = mass of sample.

3.2.5.2.2 Experimental procedure for the nitrogen vapour sorption testing

For the nitrogen sorption testing a small amount of sample was tested, typically around 1g. The sample was loaded into a glass sample container with a spherical bottom; the mass of sample added was recorded.

The samples were then exposed to a nitrogen purge gas at a temperature of 170°C, to degas and remove any excess water from the samples, for a period of 4 hours. A Micromeritics Flowprep 060 was used for the degassing process. The sample was then weighed to check the degassing did not cause a change in mass due to dehydration. A glass filler rod and seals were attached to the glass sample container and the sample was sealed with a rubber bung to stop the sample coming into contact with the humid air.

When ready to be tested the rubber bung was removed from the sample container and the sample was then attached to the Tristar sorption apparatus. The device control software then lifted the Dewar tank filled with liquid nitrogen to cool the sample to 77K. The testing then began by evacuating the sample tube and measuring the amount of nitrogen adsorbed by the sample with increasing pressure.

3.2.5.3 Data collection for the nitrogen vapour sorption testing

The data collected from the Tristar software included data for each relative pressure (P/P_0) point tested. This included Isotherm linear plot vs absorbed quantity, BET surface area and BJH adsorption and desorption pore distribution. This gave data for;

- Surface area (cm^2/g)
- Cumulative surface area of pores (cm^2/g)
- Cumulative pore volume (cm^3/g)
- Average pore width (nm)

Once collected this data was imported into a spreadsheet where the values were tabulated and compared to all samples tested.

3.2.5.4 Justification of the nitrogen vapour sorption testing

This method for measuring the porosity characteristics of the TCESM has been used in many previous studies [42,48,103,105]. It provided valuable data which could be used to assess the impact the impregnation of salt hydrates has on the porosity and therefore energy and power output of the materials.

3.3 200g Scale testing of the TCES materials

3.3.1 Custom built 200g dehydration hydration chamber.

3.3.1.1 Introduction and purpose of the 200g dehydration hydration chamber

To test the TCES materials on a practical scale, a 200g scale dehydration and hydration chamber was built in the lab.

3.3.1.2 Instrumentation used for the 200g dehydration hydration chamber tests

The reactor chamber of the system is cylindrical and 75mm in diameter and 155mm in height. When testing TCES material pellets it is able to contain 200g of material. All of the tests conducted within the chamber were with 200g of TCES material. A schematic of the system is shown in Figure 3-8.

The humidity generation cylinder shown in Figure 3-8 is the same setup as shown in Figure 3-1 however; the output goes into the 200g chamber not the small hydration chamber. The T_A temperature shown in Figure 3-8 goes to the Arduino microcontroller to regulate the humid air stream temperature. Between the 316 stainless steel plates and the 75mm cylinder there is a sheet of silicone, to create an air tight seal between the TCESM and the ambient. Wrapped around the 75mm cylinder is wool insulation of 20mm and a thermal conductivity of 0.04W/mK. Thermocouple temperature sensors are placed at the inlet and outlet of the 75mm cylinder and also next to each of the humidity sensors. There are additional temperature sensors next to the humidity sensors to calculate the partial vapour pressure of the air at the point of RH% measurement. The humidity sensors used are HIH-4000 series Honeywell humidity sensors. All of the sensors, other than the temperature sensor which feeds into the arduino, are connected to a DT85 Datalogger data logger.

At the inlet of the 75mm cylinder there is a fine mesh base which is raised off the bottom of the cylinder and this is where the TCESM sit. This mesh is used to achieve an even air flow distribution through the TCESM.

3.3.1.3 Experimental procedure used for the 200g dehydration hydration chamber tests

The 200g system dehydrated the samples using a temperature controlled hot air gun. All of the materials were dehydrated with an inlet temperature of approximately 145°C which resulted in an outlet temperature of approximately 125°C (+/- 5°C). When the material was

being dehydrated the ball valves closest to the hot air gun and the output of the TCESM chamber were opened and the ball valve closest to the humidity generator was sealed. This was to direct the hot air flow into the TCESM chamber but also protect the humidity sensors and equipment around the humidity generator, as this equipment did not have a temperature rating up to 150°C. The humidity sensors were not placed in the same location as the thermocouples within the 75mm cylinder as they were not rated up to 150°C. The top humidity sensor was removed when the TCESM were being dehydrated. The materials were all dehydrated for 3.5 hours. Once dehydration was complete all ball valves were sealed to provide air tight containment for the TCESM and allow the TCESM to cool down.

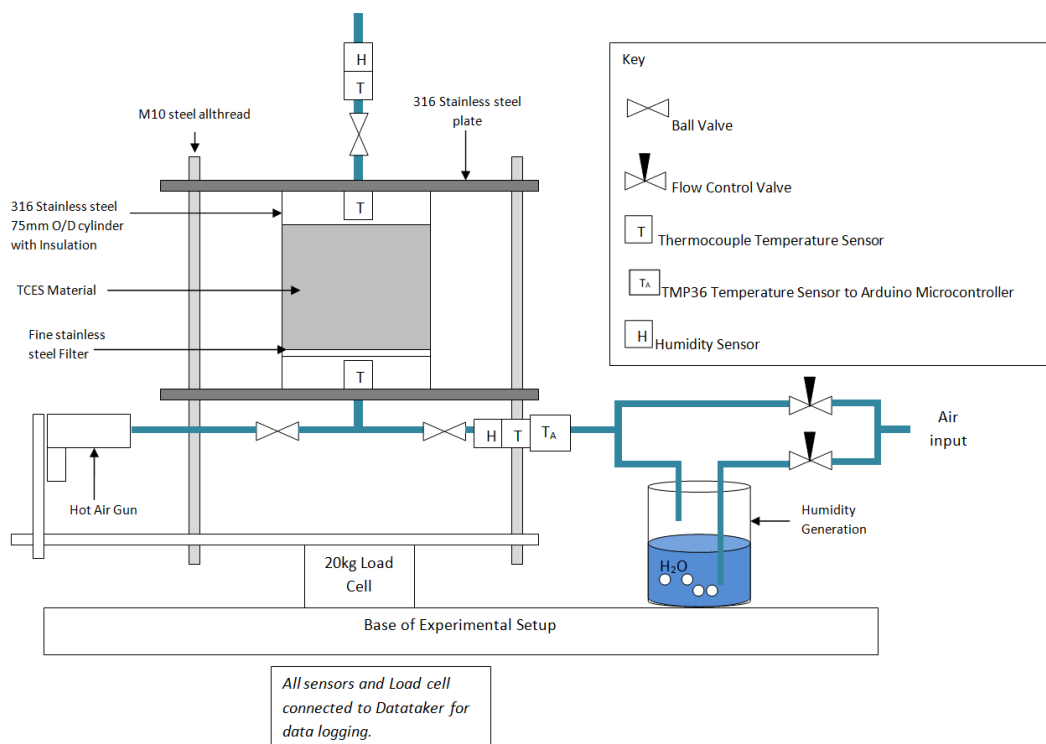


Figure 3-8 200g dehydration hydration setup

The hydration of the TCESM took place after the TCESM had cooled down to ambient temperature after a dehydration process. First all of the sensors which were disconnected for the dehydration were reconnected, including the output temperature and humidity sensors. Next the valve which connects the humid air line input to the chamber was opened and the air output valve at the top of the chamber was opened. Unless otherwise stated the TCESM were hydrated with a flow rate of 10L/min at ~1.3kPa partial vapour pressure at 20°C. Each of the samples was hydrated for 24 hours.

After a TCES material was created in a batch of 200g and ready for testing the material was;

1. Placed within a Carbolite convection oven and dehydrated to 150°C. The heating rate used was 1°C/min and was held isothermally at 150°C for 3 hours.
2. Cooled from 150°C overnight within the oven.
3. Taken out of the oven and 200g of material was weighed using a 0.01mg precision micro balance.
4. Transferred to the 200g dehydration and hydration chamber.

3.3.1.4 Data collection for the 200g dehydration hydration chamber

To calculate the power output of the 200g TCES material tests Equation 3-5 was used.

$$\text{Overall energy output (J)} = E_{out} = \sum_{t_i}^{t_0} 10P \text{ Equation 3-5}$$

The reason for the 10 in Equation 3-5 is due to the data logger taking readings every 10 seconds not every second.

$$\text{Where } P = \text{power } \left(\frac{J}{s}\right) = Q_{heat} + Q_{loss} \text{ Equation 3-6}$$

$$Q_{heat} = \text{heat produced from TCESM hydration per second} = \dot{m} C_p \Delta T \text{ Equation 3-7}$$

Q_{loss} is the heat loss from the pipe per second.

Table 3-3 Numerical values used for heat output calculations

Symbol	Description	Value	Units
\dot{m}	Mass flow rate of air	2.0067×10^{-4}	kg/s
ρ	Density of air at 20°C	1.205	kg/m ³
C_p	Specific heat of air at 20°C	1.005	kJ/kg
t_0	Start time of hydration	0	s
t_i	End time of hydration	-	s

3.3.1.5 Justification of the 200g dehydration hydration chamber methodology

This 200g testing system gave an understanding of how an open TCES system would work under the test conditions on a small scale. The workings would be very similar to a large scale open TCES system.

The majority of the hydration for all samples happened within the first 10 hours, meaning most of the power and energy output was within the first 10 hours. For continuity each sample was hydrated for the same length of time (24 hours). This was also important because even though the majority of the energy output was in the first 10 hours the TCESM become more loaded with water over the 24 hour hydration. Meaning the dehydration process will require more energy if the samples are more hydrated. All of the samples were dehydrated for 3.5 hours which was found to ensure all samples were dehydrated to the same state.

The initial oven dehydration, before the testing within the 200g chamber, was done to ensure the samples were all weighed in the same dehydrated state. 150°C was used as this temperature allows for dehydration of 6.9 of the 7 water molecules from magnesium sulphate heptahydrate [28].

The 150°C oven dehydration was also used before weighing the samples for the bulk density calculations (see section 3.3.2). The bulk density and 200g hydration data was used to calculate the energy density of the samples. If the initial oven dehydration was not conducted to the same temperature, for both the 200g testing and the bulk density tests the results would not be accurate. This is because the samples being measured could be to a different initial hydration level leading to different amounts of material being tested because the density of the material changes with different hydration levels.

3.3.2 Bulk density measurements

3.3.2.1 Introduction and purpose of the Bulk density measurements methodology

An important characteristic for TCES materials is the bulk density. This is important as the bulk density of TCES materials can be significantly different to the density of the same material. This is because TCES materials are typically used in a pellet form which creates voids in the packing of the material reducing the bulk density. TCES material A may have a higher energy output in (J/g) than TCES material B but depending upon the way in which the materials are used in a reactor the energy density (J/m³) of TCES material B may be higher

than TCES material A. The space the material takes up is vitally important for domestic environments due to the lack of free space.

3.3.2.2 Experimental procedure for the Bulk density measurements

Each TCES material was first dehydrated to 150°C within a Carbolite convection oven. The materials were heated at a rate of 1°C/min and held isothermally for 3h, before cooling naturally within the oven. Once cooled 200g of the samples were weighed. The 200g of sample was then placed in a 30mm internal diameter x 1m long acrylic pipe. This pipe was used as it has smooth uniform sides. Once filled the height of the sample within the tube was recorded. The sample was then removed from the tube and then refilled and the height was again recorded. This was repeated for at least 5 times for each sample and an average for the height was recorded. Then using the equation for density $\rho = \frac{m}{v}$ the bulk density for each sample was calculated.

3.3.2.3 Justification of the Bulk density measurements methodology

Although the samples were unlikely to change in size significantly if they were in a hydrated or dehydrated state the reason for the 150°C dehydration before testing was to be consistent with the 200g dehydration hydration tests (see section 3.3.1). In the dehydration hydration tests the samples were first dehydrated in the same way they were for the bulk density tests. The mass of sample used in the 200g tests and the bulk density tests was the same. The bulk density tests and the 200g dehydration hydration tests were then used to calculate the energy density of the TCESM.

If the oven dehydration did not take place the mass of material within the bulk density tests may be significantly different from the mass of material within the 200g dehydration hydration testing resulting in wrong energy density values. This is due to the ambient hydration of the TCESM which can be significant >20% mass change. This would mean when calculating the bulk density of a hydrated sample only 80% of the mass of the sample could be the material and the other 20% could be water taken up from the ambient hydration. This would result in a higher bulk density value because less material is actually being tested, which would result in a higher energy density value (J/m³).

Each of the material's bulk density was measured at least five times and averaged. This ensured that experimental error could be established from the tests and included within the values.

3.4 Sample preparation methodology

3.4.1 Introduction to the sample preparation methodology

Throughout this research several different sample preparation methods were utilised to create composite materials for TCES. The sample preparation methods consist of creating composite materials by impregnating a commercially produced pellet with a solution, creating composite materials using a custom methodology and creating composite materials using a pellet press. The preparation used for TCESM can impact their performance and characteristics (see chapter 2).

3.4.2 Incipient wetness impregnation method

3.4.2.1 Experimental procedure for the incipient wetness impregnation

An incipient wetness impregnation was used for the 13x pellets + MgSO₄ pellets and also for the activated carbon and activated alumina materials. First 13x pellets were dried, with a heating rate of 1°C/min, to 150°C within a Carbolite convection oven and held isothermally at 150°C for 3h. The pellets were then allowed to cool. The pellets were then weighed using a 0.01mg precision balance. Once the weight of the pellets was established a saturated MgSO₄ solution was added to the pellets. The saturated MgSO₄ solution was created by adding MgSO₄.7H₂O to Deionised (DI) water at 20°C while being mixed with a magnetic stirrer. The salt was added slowly to allow it to dissolve; the amount dissolved was 71g in 100ml of DI water. The solution was slowly added to the dried 13x pellets which absorbed the solution. The maximum amount of solution which was absorbed by the 13x pellets was 5.9ml per 10g. This volume of solution was used for all of the impregnation of the different wt% 13x pellets.

Different concentrations of MgSO₄.7H₂O + H₂O (DI water) solutions were mixed. Each of the solutions was made to be 40g in weight. The mass of MgSO₄.7H₂O added to the solutions was calculated from knowing that the 12.9wt% 13x sample absorbed a maximum of 5.9ml of solution. From this three different solutions, to create different wt% below 12.9wt%, were calculated to find the amount of MgSO₄.7H₂O required to be added to each solution. For each impregnation 10g of dried 13x pellets were used. Table 3-4 shows the amount of MgSO₄ which was added to each solution. The mass of MgSO₄ used was calculated knowing that MgSO₄.7H₂O has an amu of 246.52 g/mol, MgSO₄ = 120.4 g/mol hence, 120.4/246.52 = 0.488x of MgSO₄.7H₂O is MgSO₄. The 5.9ml of solution mass was a measured value and

weighed using a 0.01mg precision balance. From this measurement and the % amount of $MgSO_4$ in each solution the wt% of each impregnated 13x pellet was calculated.

Table 3-4 The amounts of $MgSO_4$ added in each impregnated 13x pellet.

Mass of $MgSO_4 \cdot 7H_2O$ (g)	$MgSO_4$ mass (g)	Mass of H_2O added (g)	$MgSO_4$ % in solution	5.9ml of solution mass (g)	Calculated wt% of $MgSO_4$ within 13x pellets
12.880	6.285	27.120	15.71%	6.439	9.2
10.277	5.015	29.723	12.54%	6.324	7.3
6.440	3.143	33.560	7.86%	5.882	4.4

The different concentration solutions were added to the pellets and mixed and then left for 90 minutes to maximise the absorption.

Once absorbed the samples were then placed back in the oven where they were heated, at a ramp rate of $1^\circ C/min$, to $150^\circ C$ and held isothermally for 3h at $150^\circ C$ until being cooled slowly within the oven.

3.4.2.2 Justification of the incipient wetness impregnation methodology

40g of solution was made as this is a large enough volume to allow for a satisfactory mixing of the solution to dissolve all of the $MgSO_4$ added.

The 13x pellets were impregnated in this way to create different wt% samples, and not by varying the amount of saturated $MgSO_4$ solution absorbed by the 13x pellets, to create a sample of even consistency. 5.9ml was the maximum amount absorbed by the pellets, this amount was used for each impregnation. If less was used the even consistency of the pellets may have changed and some pellets may have had a higher wt% than others in the same sample batch which could lead to errors when analysing the samples.

3.4.3 Modified wetness impregnation method

3.4.3.1 Experimental procedure for the modified wetness impregnation

Zeolite-Y powder was dried in a Carbolite convection oven, using a ramp rate of $1^\circ C/min$, to $150^\circ C$. The powder was then held isothermally for 3 hours until being cooled. Once cooled the desired mass powder was weighed using a 0.01mg precision balance. The desired mass of

MgSO₄.7H₂O needed depending upon the wt% required was calculated, accounting for the loss of 7 H₂O molecules, and weighed. Once weighed DI water was added to the MgSO₄.7H₂O and the MgSO₄.7H₂O was dissolved into a solution. This MgSO₄ solution was then mixed with the zeolite-Y powder. As the MgSO₄ was dissolved it was able to impregnate the pores of the zeolite-Y. Once mixed the solution was dried in the oven with the same drying procedure used for the zeolite-Y.

The excess water from the solution was removed when dried in the oven. The material when dried in the oven formed into a flaky substance. For testing the material was ground back into a fine powder.

3.4.3.2 Justification of the modified wetness impregnation methodology

Throughout this research absorbent powders, namely zeolite-Y, have been impregnated with MgSO₄ and their properties have been tested. The way in which the absorbent was impregnated with the MgSO₄ was different to the incipient wetness impregnation described in section 3.4.2. As the zeolite material was in a powder form it was not possible to assess the amount of solution the material could absorb in the same way it was for the 13x pellets. For this reason the methodology for impregnation was different.

When the MgSO₄ solution was made from MgSO₄.7H₂O, Mg²⁺ ions were formed in the solution. These ions could ion exchange with the ions in the zeolite. However, if this did take place the ions which were displaced by the Mg²⁺ ions would still be present in the finished powder.

3.4.4 Ion exchange methodology for the 13x pellets

3.4.4.1 Experimental procedure for the Ion exchange of the 13x pellets

13x pellets were put through an ion exchange process to replace the Na⁺ ions with Mg²⁺ ions. The ion exchange tests were conducted with 10g of 13x pellets (3.2mm). A saturated solution of MgSO₄ was created using 100ml of DI water and 71g of MgSO₄.7H₂O at 20°C. The MgSO₄.7H₂O was mixed with the DI water using a magnetic stirrer until completely dissolved. The 10g of 13x pellets were then added to the solution. Initially a lot of the pellets floated in the solution, to encourage the pellets to sink they were mixed with a magnetic stirrer on the slowest stir speed for around 5 minutes, after stirring all of the pellets had sunk in the solution. The solution and pellets were not stirred again.

The solution with the sunk pellets was then left for the desired time period for the ion exchange to occur. Once the time period was over the pellets were filtered out of the MgSO_4 solution using filter paper. For every 10g of 13x pellets 100ml of DI water was used to wash the pellets. Once washed any excess water was dried and the pellets were then placed in a Carbolite convection oven. The pellets were heated, with a ramp rate of $1^\circ\text{C}/\text{min}$, to 150°C . They were held isothermally at 150°C for 3 hours until being slowly cooled.

3.4.4.2 Justification of the ion exchange methodology for the 13x pellets

10g of pellets were left in a saturated MgSO_4 solution and mixed overnight, 24 hours later all of the pellets had broken down into the solution and no pellets remained. For this reason, all future ion exchange tests were completed with minimal stirring of the pellets to reduce the chance of damage to the 13x pellets.

The washing of the pellets was performed to remove any excess salt solution which was on the pellets to avoid salt recrystallisation within the pores or on the surface of the 13x pellets which could cause pore blocking and ultimately reduce their performance.

3.4.5 Pellet creation from powders using the pellet press

3.4.5.1 Experimental procedure for pellet creation from powders using the pellet press

For explanation purposes the method for creating the ZMK material, which consists of 45wt% Zeolite-Y, 35wt% of MgSO_4 and 20wt% of binder has been explained. First the absorbent material (zeolite-Y) was dried using a Carbolite convection oven, using a ramp rate of $1^\circ\text{C}/\text{min}$, to 150°C . The sample was held isothermally at 150°C for 3 hours until being cooled slowly within the oven. The required amount of zeolite-Y absorbent was then weighed out. The amount of each component could vary depending on the composition of the sample being made. The binder material used was an attapulgitic clay material (Tygris KU20). This material was also dried in the same way as the zeolite-Y. After both the clay and the zeolite-Y had been weighed the materials were mixed. The clay material needed to be ground into a fine powder before mixing; to do this a blender was used. The zeolite-Y was then mixed with ground clay in the blender. Next, the amount of MgSO_4 required was calculated and the correct amount of $\text{MgSO}_4 \cdot 7\text{H}_2\text{O}$ was weighed, accounting for the loss of $7\text{H}_2\text{O}$ molecules, using a 0.01mg precision balance. The $\text{MgSO}_4 \cdot 7\text{H}_2\text{O}$ was then blended and mixed with the zeolite-Y and clay. Once mixed DI water was added to this mixture to form a slurry and allow the MgSO_4 to impregnate the zeolite-Y.

After the solution was mixed it was placed in a Carbolite convection oven and heated, with a heating rate of 1°C/min, to 150°C. The material was held isothermally for 3 hours before being cooled within the oven. Once cooled the material was removed from the oven. The material formed into a hard “slab” like structure. The material was broken down and ground, using the blender, back into a fine powder. DI water was then added; the amount of DI water added depended on the material and was done to allow the powder to be worked into a soft clay consistency. The water was added gradually to ensure none of the material became saturated which could have resulted in the MgSO₄ dissolving and being washed out of the zeolite-Y pores.

To form the pellets a custom pellet press was built. The press had a worm drive which forced the material through the end of the press which had many 4mm diameter holes in. The soft clay consistency material was added to the pellet press to be formed into pellets. When initially formed the pellets were still wet and were not handled for this reason. The formed pellets dropped from the pellet press on to a tray and were then placed within the oven. They were dried within a Carbolite convection oven, using a heating rate of 1°C/min, to 150°C. The pellets were then held isothermally for 3 hours until being cooled. The drying process removed any excess water from the pellets and dried them ready for use. The dried pellets were hard and brittle.

3.4.5.2 Justification of the pellet creation from powders using the pellet press methodology

Throughout this research it was found that some materials were difficult to source in pellet form but can be sourced in powder form more readily. One example of this was the zeolite-Y (ammonium) powder. This material was sourced in a powder but was difficult to source in a pellet or bead form. For this reason a methodology which enabled the creation impregnated pellets from powder absorbents was developed.

A blender was used to grind the materials into powders, it was seen as a better choice than a mortar and pestle as it was quicker and created a fine and even consistency powder.

The process of adding DI water to the mixture dissolved the MgSO₄·7H₂O and allowed the MgSO₄ to enter the pores of the zeolite mix. When the MgSO₄·7H₂O was dissolved Mg²⁺ ions were formed in the solution. These ions could ion exchange with the ions in the zeolite.

However, if this did take place the ions which were displaced by the Mg^{2+} ions would still be present in the finished pellets.

The first dehydration of the mixture, after all materials were mixed and DI was added to the mixture to create a slurry, was done to allow the MgSO_4 to enter the pores of the zeolite when in a solution impregnate and recrystallise within the zeolite pores once the mixture was dried removing any excess water.

3.5 Summary of methodology chapter

This chapter explained all of the methods used to conduct the research detailed within this thesis and generate the data presented in the latter chapters. The methodology has been described in sufficient detail to allow all work to be reproduced. All of the methods used have been justified where appropriate.

This methodology was required to carry out the research testing, data collection and analysis to reach the research aims described in section I and chapter 1 of this thesis.

This methodology was broken down into three distinct sections.

1. The methodology used for characterising the TCESM on a small (~10mg) scale. This section outlined the experimental apparatus used for thermal characterisation and imaging including DSC, SEM and TGA. This scale size allowed for understanding of the potential of the TCESM.
2. The methodology used for characterising the TCESM on a (~200g) scale. This methodology was used for understanding the performance losses experienced by the samples from a small (10mg) scale. This section of the methodology included the methods and equipment used to test the materials on a 200g scale including bulk density and hydration energy output.
3. The methodology used for creating all of the different TCES material samples used throughout this research was outlined in this section.

4 Chapter 4 – Characterization of MgSO₄, zeolite-Y and composite materials

Chapter 4 investigates the small scale characteristics of MgSO₄, zeolite-Y and composite materials of zeolite-Y impregnated with MgSO₄. It is important to understand the small scale (~10mg) characteristics of these materials because when the materials are used at a larger scale (i.e. 200g+) the characteristics may change due to scaling losses. When testing at a small scale the energy output of the materials will be close to the theoretical potential of the materials. By understanding the materials potential and properties on a small scale it allows a prediction of the materials characteristics on a larger scale to be made.

For testing the material on a small scale thermal analysis devices were used. The devices used were a DSC, TGA+RGA and SEM+EDX. The characterization throughout this chapter will consider the following;

- Dehydration enthalpy which allows for predicted hydration energy output of the materials
- Cycle stability of the materials to understand if there are any degradation impacts of repeated cycling
- Heating rate impacts to assess if higher or lower dehydration heating rates impact the energy output characteristics of the materials
- Slow kinetics to understand how the heating rate impacts the rate of dehydration and therefore the way in which the energy is stored and also the amount of energy which is stored.

4.1 Initial DSC, TGA and RGA characterization of MgSO₄.7H₂O

Figure 4-1 shows overlaid measurements from the DSC, TGA and RGA showing the dehydration of MgSO₄.7H₂O to 300°C. It is seen that all of the DSC, TGA & RGA measurements agree on the dehydration temperatures and hence, temperatures required to charge and store energy within MgSO₄. From the TGA measurements it is difficult to distinguish the three step loss of water however, the DSC and RGA measurements show the three step process clearly. The loss 1H₂O molecule takes place at a peak temperature of 45°C, the loss of 5.9 H₂O molecules takes place at a peak temperature of 86°C. The last 0.1 H₂O

molecules are lost at around 277°C and can be seen on the DSC measurements to be exothermic and not endothermic like the previous 6.9 H₂O molecules.

Figure 4-1 shows the change in mass from 110-150°C is only (2.6%) and is unlikely to have a great effect on the energy density if the MgSO₄.xH₂O is only dehydrated to 110°C opposed to 150°C (see section 4.2.2 for more details).

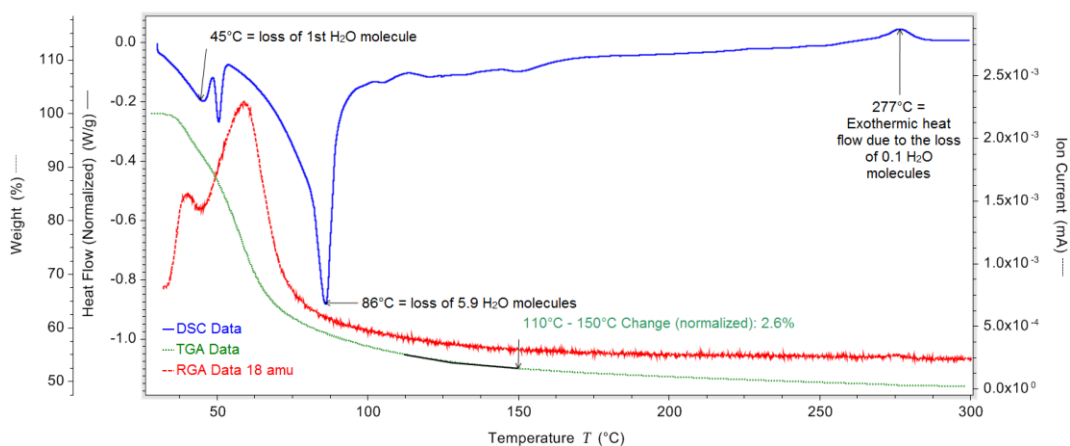


Figure 4-1 MgSO₄.7H₂O dehydration to 300°C overlay showing measurements from TGA, RGA and DSC showing the dehydration process

4.2 MgSO₄.7H₂O heating rate effects and cycle stability investigations

To assess the effect the dehydration heating rate has on MgSO₄.xH₂O several samples were dehydrated at various heating rates within both a TGA (with attached RGA) and a DSC. The chosen heating rates used were 1, 2, 5 and 10°C/min.

4.2.1 Sudden dehydration peaks from MgSO₄.xH₂O with high heating rates

Figure 4-2 shows the DSC dehydration data of MgSO₄.7H₂O for each heating rate. Figure 4-3 shows the dehydration RGA data showing 18amu (H₂O) volatiles leaving the MgSO₄.7H₂O. The first endothermic peak on each DSC plot is a result of the loss of 1 H₂O molecule. The second large endothermic peak, taking into account the TGA data, is due to a calculated loss of around 5.9 H₂O molecules. From Figure 4-3 it is seen the peak temperature for H₂O leaving the MgSO₄.7H₂O increases with increasing heating rate, the plots also appear to become more volatile with higher heating rates. This phenomenon is due to the dehydration kinetics of the MgSO₄.xH₂O and is explained in more detail in section 4.6.

It is clear from Figure 4-2 as the dehydration heating rate increases the heat flow has many more sharp endothermic peaks. From the RGA data (Figure 4-3) it is seen that the peaks are a result of water suddenly leaving the material.

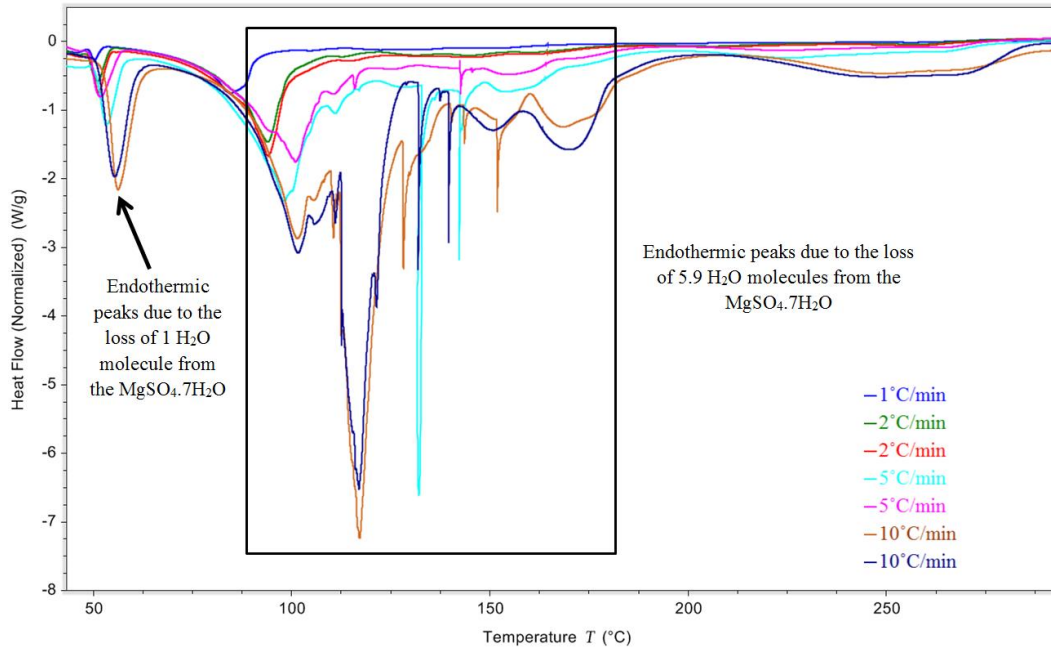


Figure 4-2 DSC measurements for several heating rates, showing volatile behaviour with increasing heating rates.

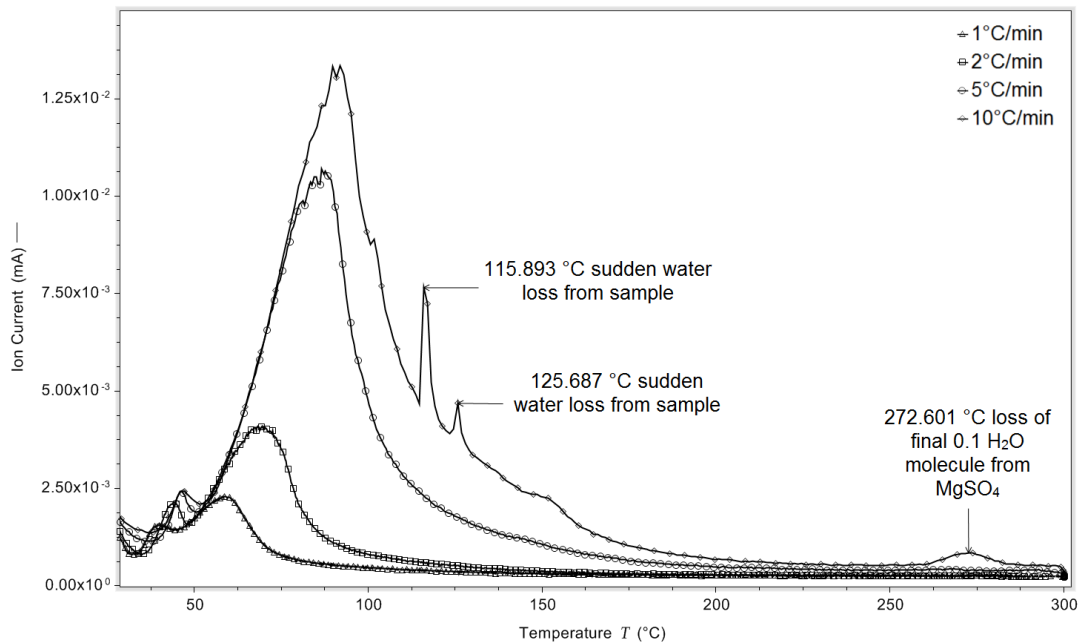


Figure 4-3 Ion current as a function of temperature for MgSO₄.7H₂O at 4 different heating rates

4.2.2 Using lower temperatures for the dehydration of $MgSO_4$

Along with varying heating rates the $MgSO_4 \cdot xH_2O$ samples were dehydrated to different maximum dehydration temperatures (110 and 150°C) in both a TGA and DSC. At these temperatures the samples were held isothermally for sufficient time to allow for further volatile water to escape. Figure 4-4 shows TGA measured data for several samples. Table 4-1 shows the enthalpy of each sample calculated from the DSC tests. There is a small change in dehydration enthalpy and the mass loss measured between the 110°C and 150°C sample sets. The DSC results show around 102 J/g difference in the enthalpy between the two dehydration temperatures, which is only a ~7% loss. These results indicate the possibility of using a lower dehydration temperature while maintaining most of the energy storage potential. A lower dehydration temperature would allow a higher efficiency to be achieved using a flat plat solar thermal collector which would result in more solar gains and more usable energy output from the collector.

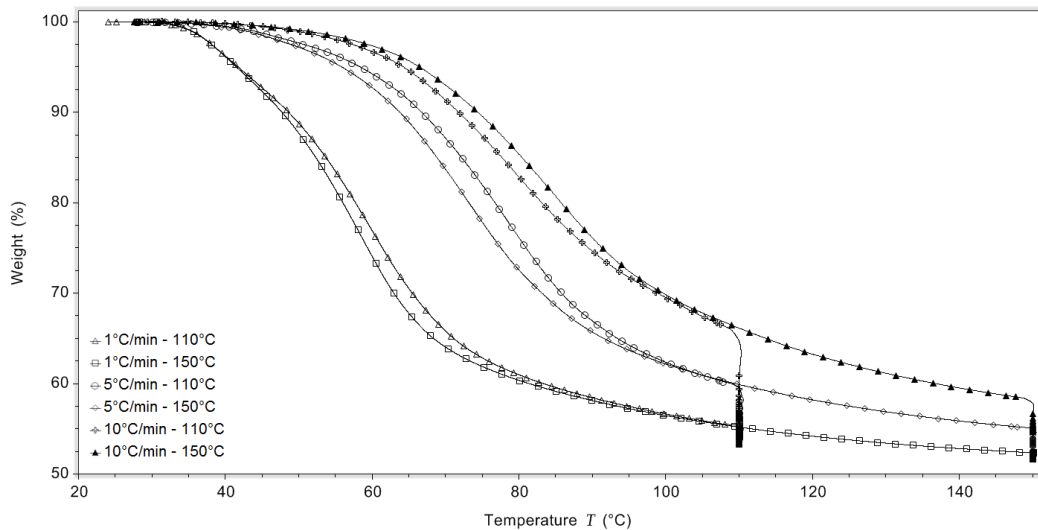


Figure 4-4 TGA dehydration measurements for $MgSO_4 \cdot xH_2O$ dehydrated with several heating rates and isothermal periods, showing little difference in mass loss between dehydration temperatures of 110°C and 150°C.

Table 4-1 Average dehydration enthalpy compared to the maximum dehydration temperature for $MgSO_4 \cdot xH_2O$.

Sample No.	Heating Rate ($^{\circ}C/min$)	Dehydration Temperature ($^{\circ}C$)	Enthalpy (Normalised) (J/g)	Average Enthalpy (J/g)
1	1	110	1230.6	
2	5	110	1330.1	1284
3	10	110	1291.5	
4	1	150	1429.4	
5	5	150	1382.1	1386
6	10	150	1347.3	

4.2.3 Structural changes of $MgSO_4$ following de/hydration cycles

As the dehydration heating rate increases the material becomes more damaged and fractured as show in Figure 4-5 (images 1-6) confirming the results obtained from recent studies [28]. These fractures and cracks should facilitate the hydration and dehydration process. Images 7 and 8 on Figure 4-5 show the $MgSO_4$ after a $1^{\circ}C/min$ dehydration followed by a rehydration. The images show the $MgSO_4 \cdot xH_2O$ has become fractured into small pieces which are stuck together to form a larger fragment of the $MgSO_4 \cdot xH_2O$. The hydration of the $MgSO_4$ appears to form small channels throughout the larger grains of the $MgSO_4 \cdot xH_2O$.

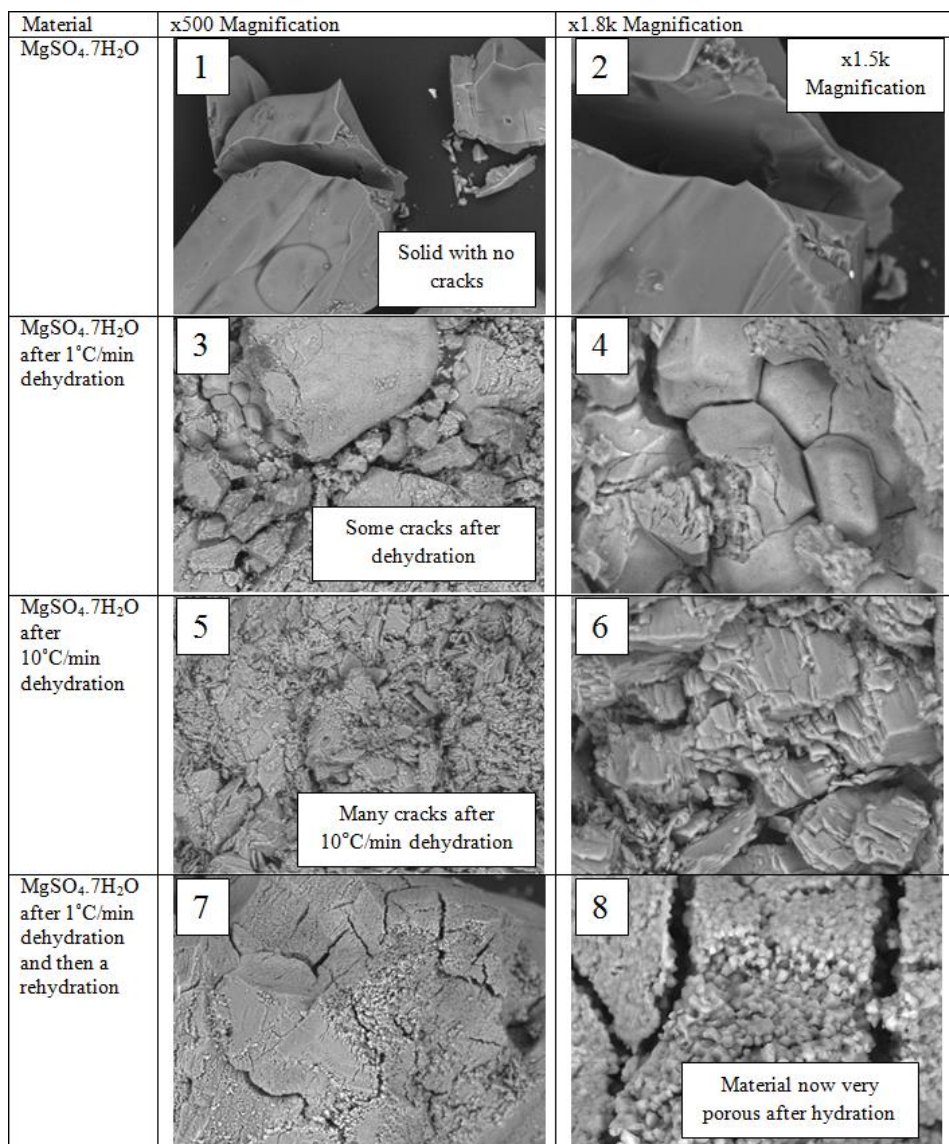


Figure 4-5 SEM Images of MgSO₄ after dehydration with different heating rates and images of MgSO₄ after rehydration

4.2.4 High hydration levels of MgSO₄ using 1.3kPa pH₂O

Figure 4-6, Figure 4-7 and Figure 4-8 shows the TGA dehydration data of MgSO₄.xH₂O after heating rates of 1, 5 and 10°C/min, respectively. The first plot (highest starting mass) on each figure shows the initial dehydration of MgSO₄.7H₂O. The following plots show the dehydration of MgSO₄.xH₂O after a rehydration. It is clear that after each cycle the MgSO₄.xH₂O hydrates to the same level of ~MgSO₄.5.5H₂O. This is a much higher level than has been suggested by other studies, which show the material only hydrates to MgSO₄.H₂O using the same hydration conditions. The hydration level of the MgSO₄.xH₂O shown in Figure 4-7 increases with successive cycles until cycle 6. At this point the material

rehydrates to the same level with each cycle. This observation suggests the increased de/hydration cycles may improve the hydration characteristics of the $\text{MgSO}_4 \cdot x\text{H}_2\text{O}$. It must be noted that these test are on a small (4-10mg) scale and may not scale to large systems and material quantities. From Figure 4-6, Figure 4-7, Figure 4-8 and Table 4-2 it appears using the hydration conditions, which are readily achievable during the UK winter, a dehydration enthalpy of $\sim 1200\text{J/g}$ is achievable.

4.2.5 Heating rate effect on the cycle stability and dehydration enthalpy of MgSO_4

To assess the impact varying dehydration heating rates have on the cycle stability and energy storage potential of MgSO_4 cycle stability testing was conducted. Each sample was hydrated with the same conditions ($p_{\text{H}_2\text{O}} = \sim 1.3\text{kPa}$) for the same time and then dehydrated within both a TGA and a DSC. This de/hydration was repeated several times. For this experiment 1, 5, and $10^\circ\text{C}/\text{min}$ heating rates were used.

Table 4-2 shows the DSC dehydration enthalpy results of $\text{MgSO}_4 \cdot x\text{H}_2\text{O}$ after being dehydrated with three dehydration heating rates (1, 5 and $10^\circ\text{C}/\text{min}$). From the TGA data (Figure 4-6, Figure 4-7 and Figure 4-8) and Table 4-2 it is apparent that $\text{MgSO}_4 \cdot x\text{H}_2\text{O}$ is very stable with no observable cycle degradation. This stability does not appear to be influenced by the dehydration heating rate used as each $\text{MgSO}_4 \cdot x\text{H}_2\text{O}$ sample has very similar dehydration enthalpy. This confirms that for a small (4-10mg) scale sample size the $\text{MgSO}_4 \cdot x\text{H}_2\text{O}$ de/hydration levels are unchanged when using a heating rate of 1, 5 or $10^\circ\text{C}/\text{min}$.

Table 4-2 Enthalpy data showing dehydration enthalpy (after a 150°C dehydration) and cycle stability of MgSO_4

Heating Rate ($^\circ\text{C}/\text{min}$)	1	5	10
Enthalpy (normalized) (J/g) Cycle No.1	1429.4	1382.1	1347.3
Enthalpy (normalized) (J/g) Cycle No.2	1268.1	1284.4	1340.3
Enthalpy (normalized) (J/g) Cycle No.3	1315.8	1244.9	1094.2
Enthalpy (normalized) (J/g) Cycle No.4	1303.7	1052.5	1275.8
Enthalpy (normalized) (J/g) Cycle No.5	1279.6	1216.4	1218.0
Enthalpy (normalized) (J/g) Cycle No.7	1296.3	1217.9	1208.2
Average (J/g) – not including erroneous values	1292.7	1240.9	1260.6

Figure 4-9, Figure 4-10 and Figure 4-11 show the DSC dehydration plots for $\text{MgSO}_4 \cdot x\text{H}_2\text{O}$ samples with heating rates of 1, 5 and $10^\circ\text{C}/\text{min}$, respectively. The plots appear to show the materials dehydration characteristics changing with each cycle. The first cycles possess two dominant endothermic losses at around 45°C and $60\text{-}100^\circ\text{C}$ (for a heating rate of $1^\circ\text{C}/\text{min}$). The temperature range shifts higher with increasing heating rates. However, after the first cycle the first peak is lost, this is expected as the first peak is the loss of the 7th H_2O molecule which is not present in the successive cycles as the $\text{MgSO}_4 \cdot x\text{H}_2\text{O}$ does not rehydrate to $\text{MgSO}_4 \cdot 7\text{H}_2\text{O}$. The 2nd and 3rd cycles have a peculiar “w” shaped endothermic peak in the temperature range of $50\text{-}70^\circ\text{C}$ (i.e. much lower than the first dehydration cycle endothermic peak). After the 3rd cycle all successive cycles become very similar, there is only a large endothermic peak in the range of $50\text{-}70^\circ\text{C}$, which is again a much lower temperature range than the first dehydration endothermic peak. These dehydration characteristics are observed with all three tested heating rates. The shift in peak dehydration enthalpy, to lower temperatures, is a positive result as it gives rise to the potential of using a lower dehydration temperature while still achieving the same storage potential.

It is clear (Table 4-2) that after the first dehydration cycle the dehydration enthalpy achieved for all three dehydration heating rates tested on the $\text{MgSO}_4 \cdot x\text{H}_2\text{O}$ is very similar and the data does not suggest any cycle degradation.

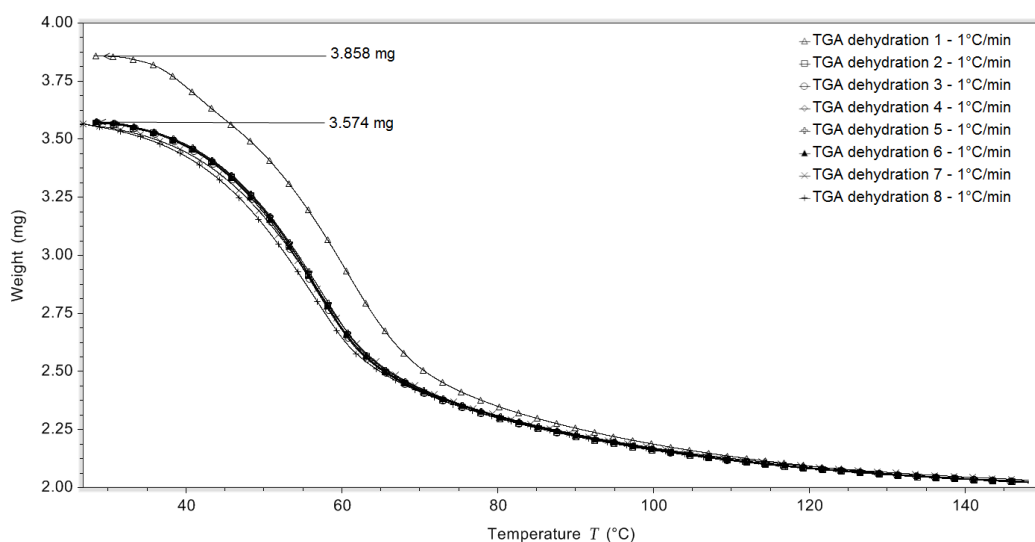


Figure 4-6 TGA measurements showing cycle stability of MgSO_4 using a $1^\circ\text{C}/\text{min}$ heating rate

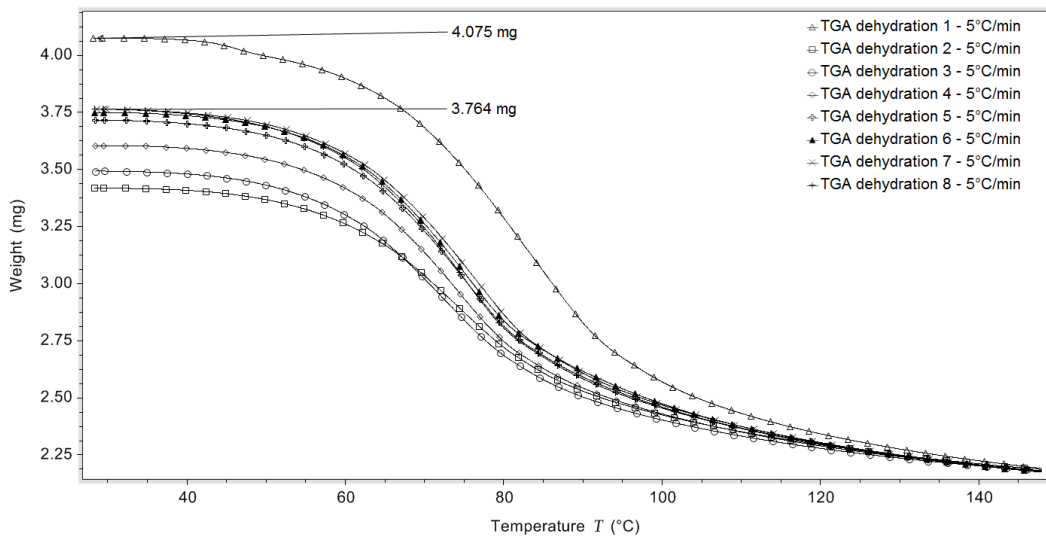


Figure 4-7 TGA measurements showing cycle stability of MgSO₄ using a 5°C/min heating rate

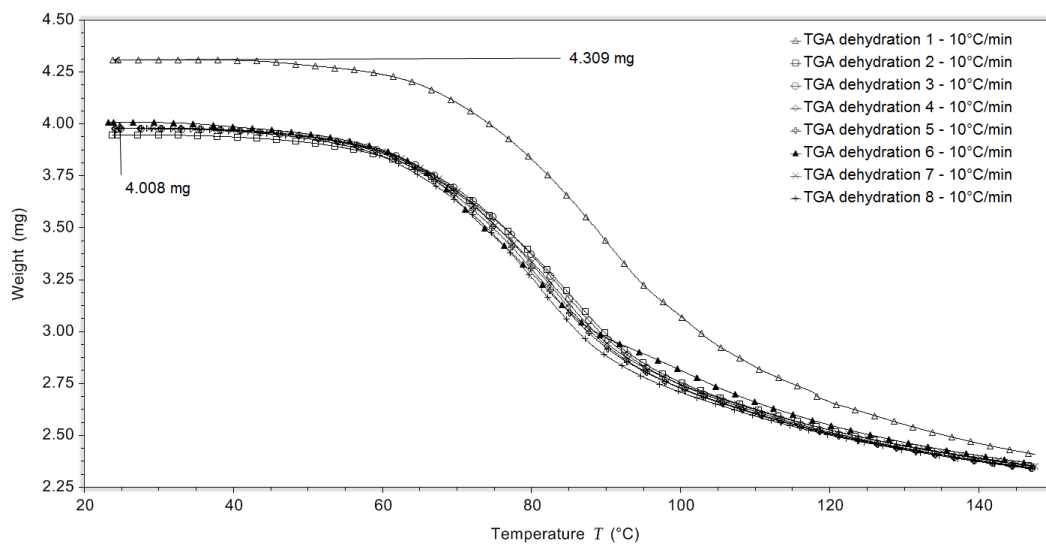


Figure 4-8 TGA measurements showing cycle stability of MgSO₄ using a 10°C/min heating rate

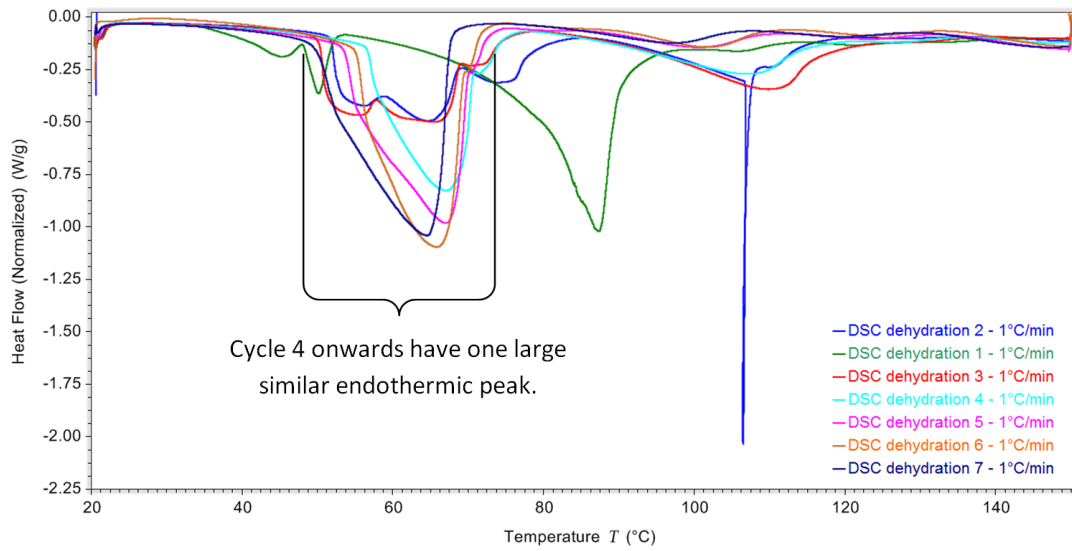


Figure 4-9 DSC measurements showing cycle stability of $MgSO_4$ using a $1^\circ C/min$ heating rate

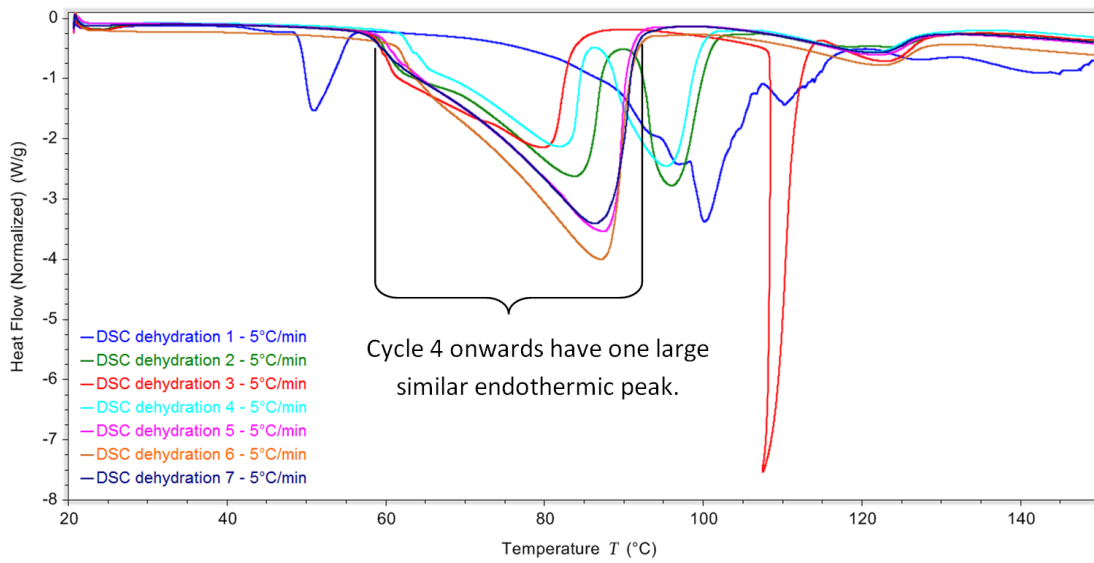


Figure 4-10 DSC measurements showing cycle stability of $MgSO_4$ using a $5^\circ C/min$ heating rate

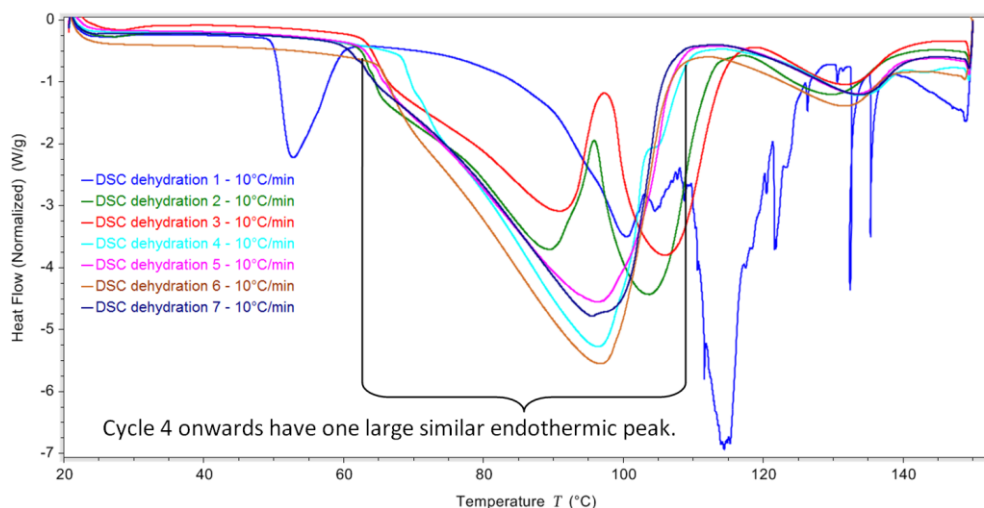


Figure 4-11 DSC measurements showing cycle stability of $MgSO_4$ using a $10^\circ C/min$ heating rate

4.2.6 Slow kinetics of $MgSO_4$

The only apparent discrepancy between the TGA dehydration of the $MgSO_4 \cdot xH_2O$ in Figure 4-6, Figure 4-7 and Figure 4-8 was the temperature range for peak mass loss. As the heating rate increases the peak dehydration temperature shifts to a higher range. This was also observed from the RGA data (Figure 4-3). The shift in dehydration temperature is due to the dehydration kinetics of the $MgSO_4 \cdot xH_2O$.

The dehydration kinetics of the $MgSO_4$ increases with successive cycles due to increased vapour channels. The reasons for this were believed to be;

- The peak dehydration temperature of the $MgSO_4 \cdot xH_2O$ decreases with successive dehydration cycles, shown in Figure 4-9, Figure 4-10 and Figure 4-11.
- The SEM data (Figure 4-5) shows increased amount of “cracks” with increasing heating rate.
- The vapour sorption results (Figure 4-20, Figure 4-21 and Figure 4-22) show higher pore volume for $MgSO_4$ after extra dehydration cycles.

The results of a more detailed investigation of the changing dehydration kinetics of the $MgSO_4 \cdot xH_2O$ are presented in section 4.6.

4.3 Zeolite cycle stability investigations

Zeolite-Y ($SiO_2:Al_2O_3$, mole ratio 5.1:1) was chosen for composite material creation due to previous studies indicating of the potential of zeolites for adsorption heat storage [67,130]

but more specifically as this material has a large BET surface area ($925\text{m}^2/\text{g}$). Before the composite materials (zeolite impregnated with MgSO_4) were created the zeolite was subjected to a cycle stability analysis, similar to the analysis performed for the MgSO_4 samples.

4.3.1 Thermal storage potential of zeolite-Y

Figure 4-12 shows the DSC data for several dehydration cycles of zeolite-Y up to 150°C . The zeolite was hydrated using the same conditions used for the MgSO_4 samples and dehydrated using a heating rate of $5^\circ\text{C}/\text{min}$. Figure 4-12 shows the endothermic heat flow for the zeolite starts at around $-0.2\text{W}/\text{g}$ at 20°C and gradually increases to $-0.55\text{W}/\text{g}$ at 120°C . After 120°C the endothermic heat flow decreases until around 150°C .

After each dehydration the zeolite was put through another dehydration to 150°C without any exposure to the environment, this ensured no hydration could occur. This was done to measure the zeolites heat flow which was due to the specific heat capacity of the material. It was seen that the heat flow which was due to the specific heat of the zeolite had an average value of $165\text{J}/\text{g}$.

After conducting a dehydration enthalpy analysis on the zeolite-Y samples the average achieved enthalpy was $615\text{J}/\text{g}$. This means that the zeolite-Y had a performance of 79% (performance = dehydration enthalpy/ total enthalpy * 100). As the material is to be dehydrated (charged) in the summer months and discharged in the winter all of the sensible heat will be lost. For the zeolite-Y the amount of energy stored in chemical bonds was 79% of the original total enthalpy required for dehydration. This result along with the low temperature range, in which the materials dehydration enthalpy peaks at 120°C , highlights the materials potential for use as a domestic TCES material itself.

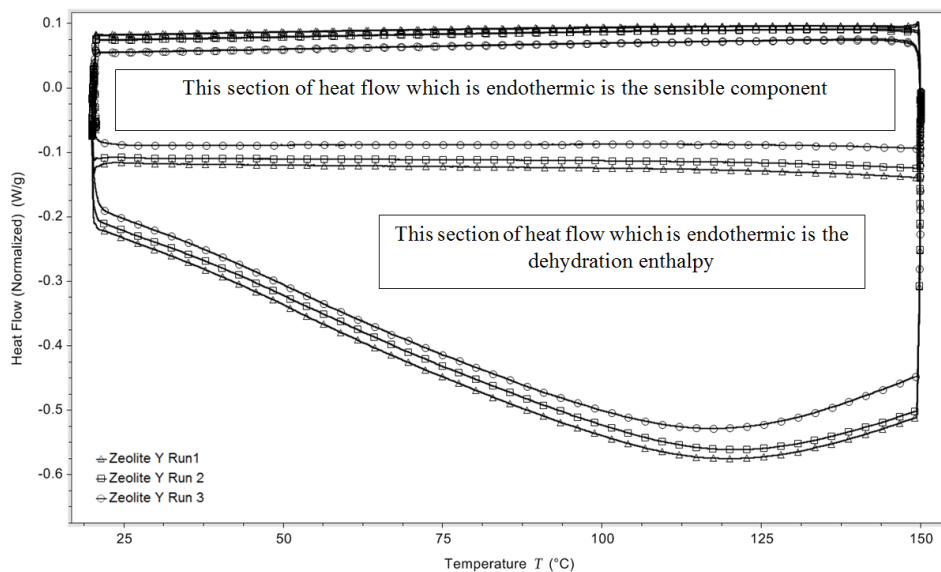


Figure 4-12 DSC measurements used for evaluating the dehydration enthalpy of hydrated zeolite-Y

4.4 Composite TCES materials analysis

The composite materials created consisted of varying weight ratios of MgSO_4 and zeolite-Y. The selected wt% ratios of MgSO_4 and zeolite-Y were 15,20,25,30 and 35wt%.

4.4.1 Composite TCES materials enthalpy analysis

Figure 4-13 shows the DSC dehydration data for all composite materials. For these tests a heating rate of $1^\circ\text{C}/\text{min}$ was used. The materials appear to exhibit characteristics from both the MgSO_4 and the zeolite-Y. The two sharp endothermic peaks from the MgSO_4 and the slowly decreasing endothermic heat flow from the zeolite-Y. As the wt% of magnesium sulphate increases within the composite materials so does the negative heat flow of the two distinct endothermic peaks seen at around $60\text{-}100^\circ\text{C}$. This is a characteristic of the magnesium sulphate and was also seen in Figure 4-9, Figure 4-10 and Figure 4-11.

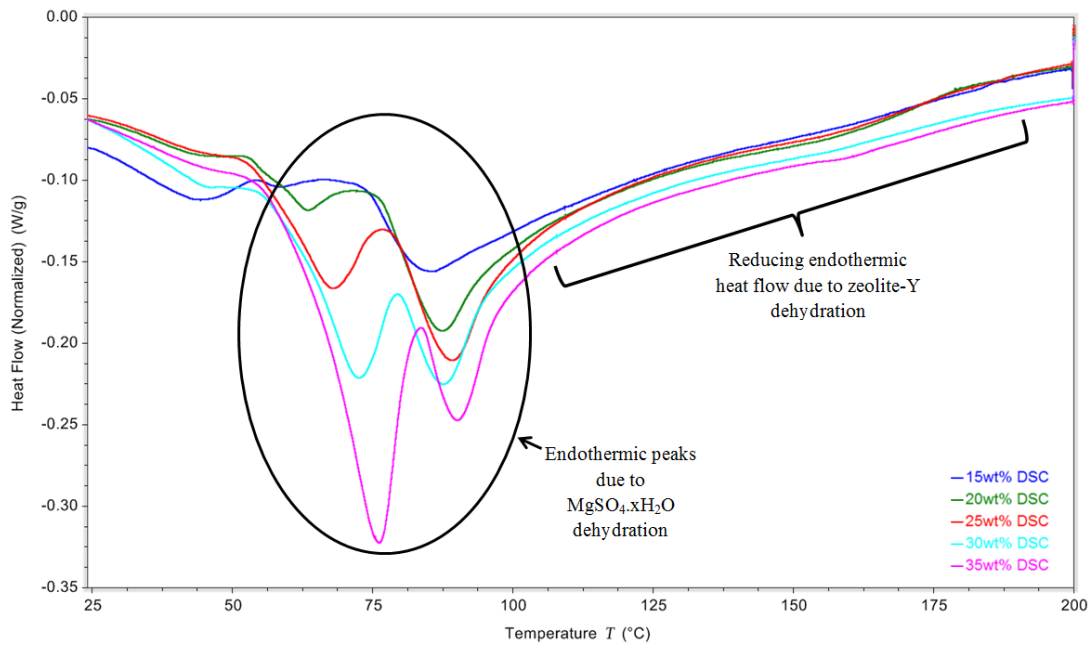


Figure 4-13 DSC dehydration measurements for the hydrated composite materials

Figure 4-14 shows the averaged DSC dehydration enthalpy results for the composite materials and zeolite-Y. It was apparent with increasing wt% the dehydration enthalpy increases. Also with increasing wt% of $MgSO_4$ the sensible component does not increase, resulting in less wasted energy. No degradation was observed with increasing wt% as expected [23,99].

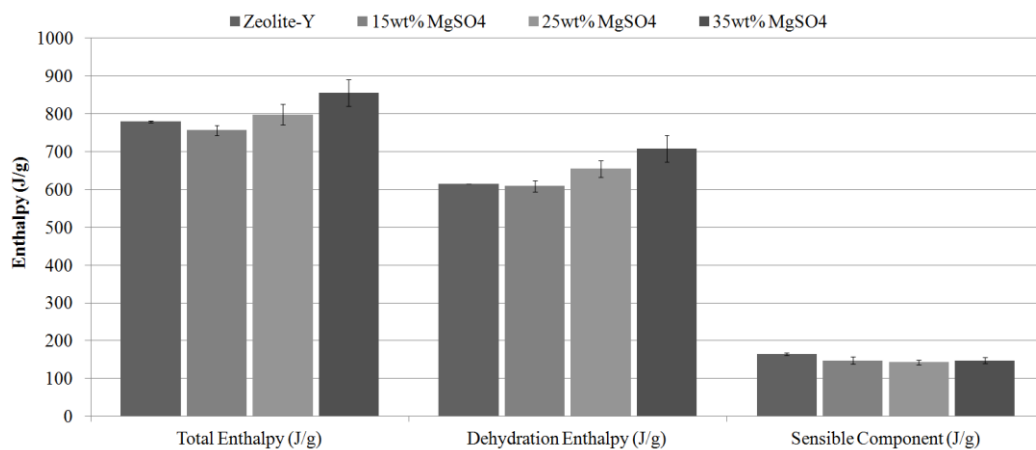


Figure 4-14 Achieved dehydration enthalpy for each composite material.

Figure 4-15 presents the DSC averaged dehydration enthalpy and the performance of each composite material and the zeolite-Y. As the wt% of $MgSO_4$ in the composite samples increased so too did the performance %. This was due the increased dehydration enthalpy of

the composite samples with increasing wt% and was also due to the sensible component staying very similar or even possibly decreasing with increasing wt%. This means the percentage of wasted energy for the higher wt% samples is reduced. For comparison the sensible component for the 35wt% and 15wt% material was approximately 17% and 20%, respectively. The sensible component of the sample was likely to decrease with increasing wt% as the sensible component of MgSO_4 was lower than the zeolite-Y's sensible component.

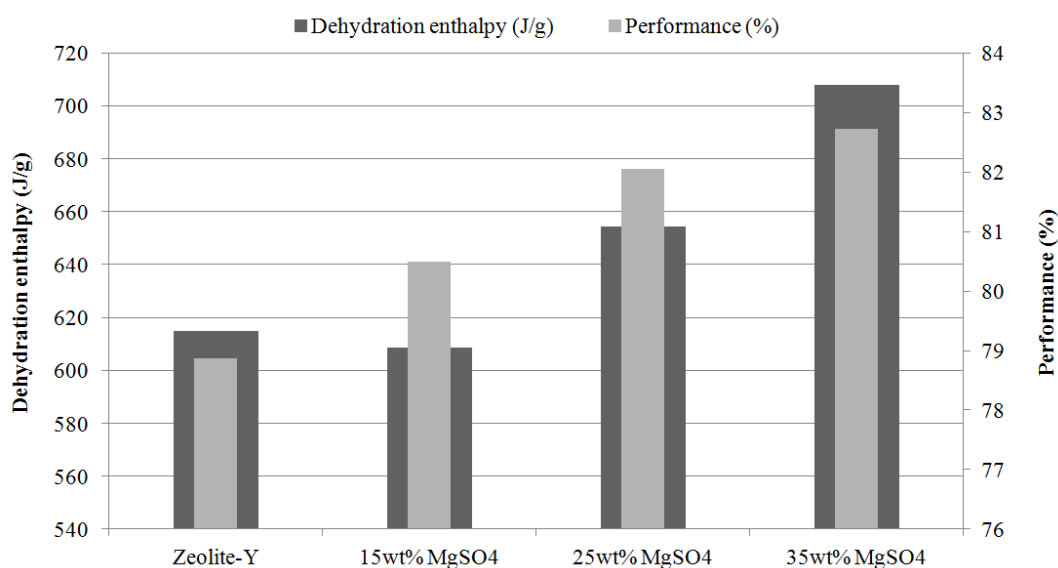


Figure 4-15 Dehydration enthalpy and performance of composite materials and zeolite-Y

The TGA data (Figure 4-16) shows the decreasing mass loss with increasing wt% of the magnesium sulphate in the composite materials. The tests were conducted using a heating rate of $1^\circ\text{C}/\text{min}$. The results were expected as the magnesium sulphate lost significantly more mass relative to the zeolite. No degradation was evident due to the high wt% of the material which was expected to be observed due to a pore blocking effect [23,99] from the high levels of magnesium sulphate. This was a positive result for the composite materials and was also in agreement with DSC results (Figure 4-14).

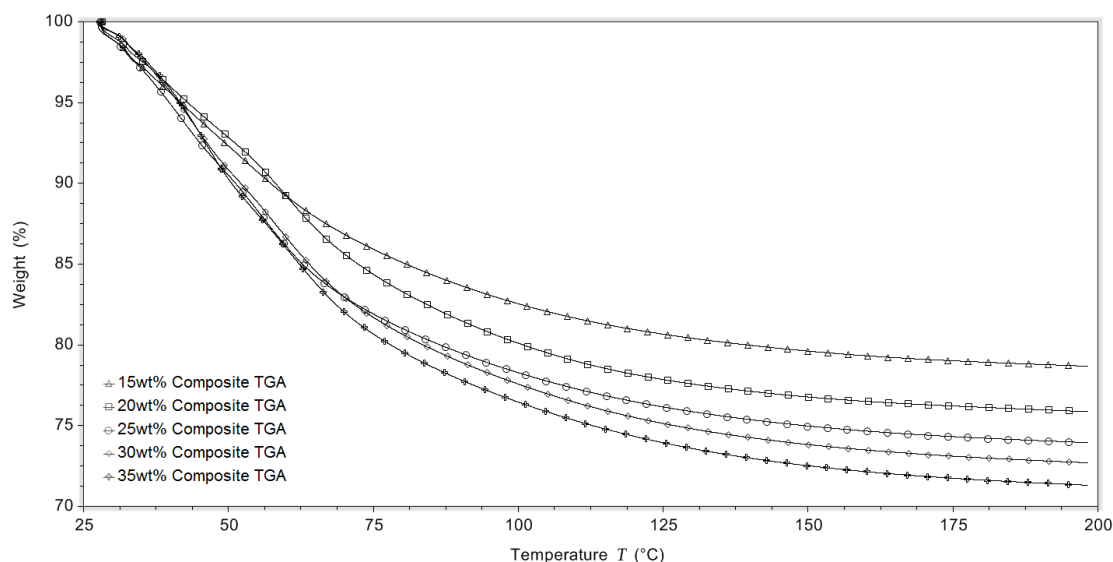


Figure 4-16 TGA dehydration measurements for the composite materials

4.4.2 Composite TCES materials dehydration heating rate effects

To assess the impact high heating rates have on the composite samples a heating rate test, similar to the MgSO_4 tests was carried out. Using DSC, TGA+RGA samples 15, 25 and 35wt% were dehydrated using heating rates 1, 5 and $10^\circ\text{C}/\text{min}$. As the MgSO_4 shown increasing volatile behaviour with increasing dehydration heating rates it was expected as the wt% of each composite sample increased there would be an increasing volatile behaviour.

Figure 4-17 shows the DSC dehydration data using a $10^\circ\text{C}/\text{min}$ heating rate for each composite sample tested. It was expected as the wt% of the sample increased the DSC plot would become more volatile similar to that seen in Figure 4-2. The results show as the wt% increased the plots do not become any more volatile. Figure 4-17 shows the highest, expected to be the most volatile, $10^\circ\text{C}/\text{min}$ heating rate. This was a positive result and suggests the composite material was unaffected by high heating rates, behaving in a similar way to the pure zeolite.

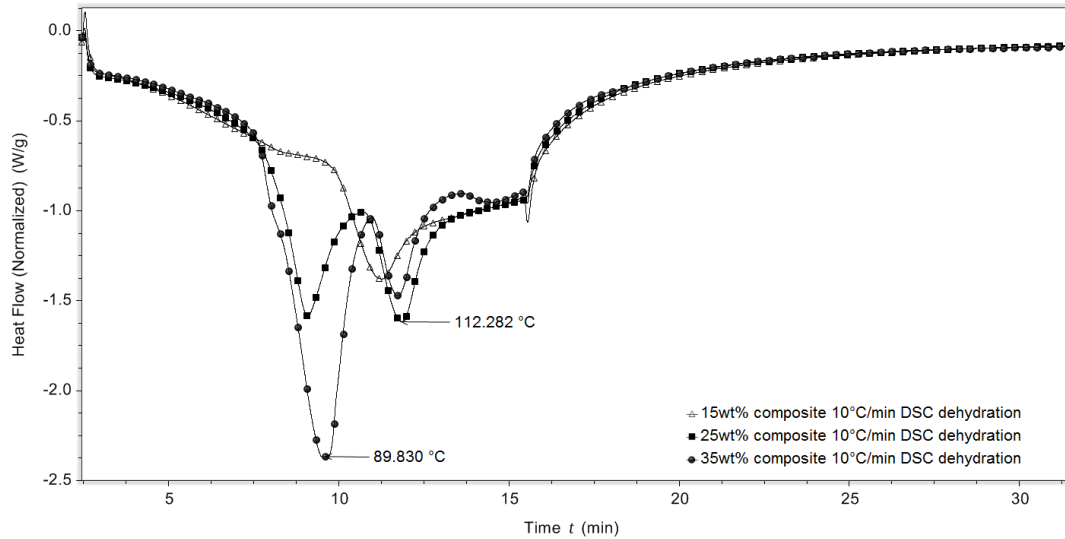


Figure 4-17 DSC dehydration measurements for the 35wt% composite sample

Figure 4-18 shows the differential (dW/dT) of the TGA data for the 35wt% composite material and how the increasing heating rate affected the peak mass loss. Displaying the differential of mass loss with time the peak mass loss temperature becomes much clearer to see graphically. As the heating rate was increased the peak mass loss temperature also increased, this was the expected result [57]. This analysis method was also conducted for both the 15 and 25wt% composite materials. The data from this analysis was plotted and can be seen in Figure 4-19.

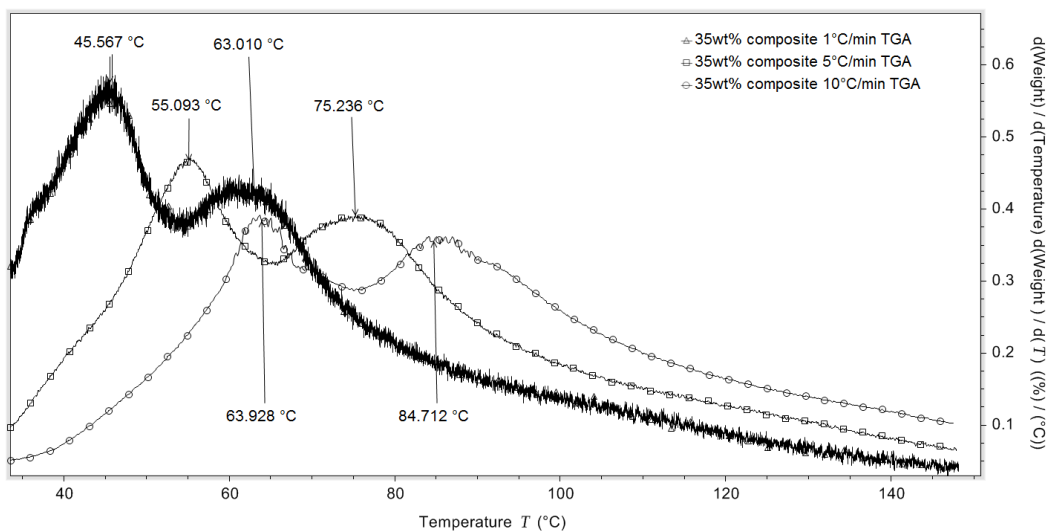


Figure 4-18 Differential TGA dehydration data for 35wt% composite sample

Figure 4-19 shows the results of the peak mass loss temperatures with each heating rate. It was expected with increasing heating rate the peak mass loss temperature would also

increase. However, depending upon the materials this change in peak mass loss temperature will change in magnitude. For example (Figure 4-2) shows MgSO_4 was greatly affected by increasing heating rates. For this reason with increasing wt% within the composite materials the peak mass loss temperature was expected to rise. However, from Figure 4-19 this was not seen. The use of the zeolite within the material appears to have reduced the volatility of the material caused by high heating rates, this was a positive result. This means a higher wt% material, with a higher dehydration enthalpy, can be used and extract its energy while using the same peak dehydration temperature as a lower wt% material. For example the peak mass loss temperature for the 15wt% and 35wt% material when using a $10^\circ\text{C}/\text{min}$ heating rate was very similar at 85.2°C and 85.7°C , respectively.

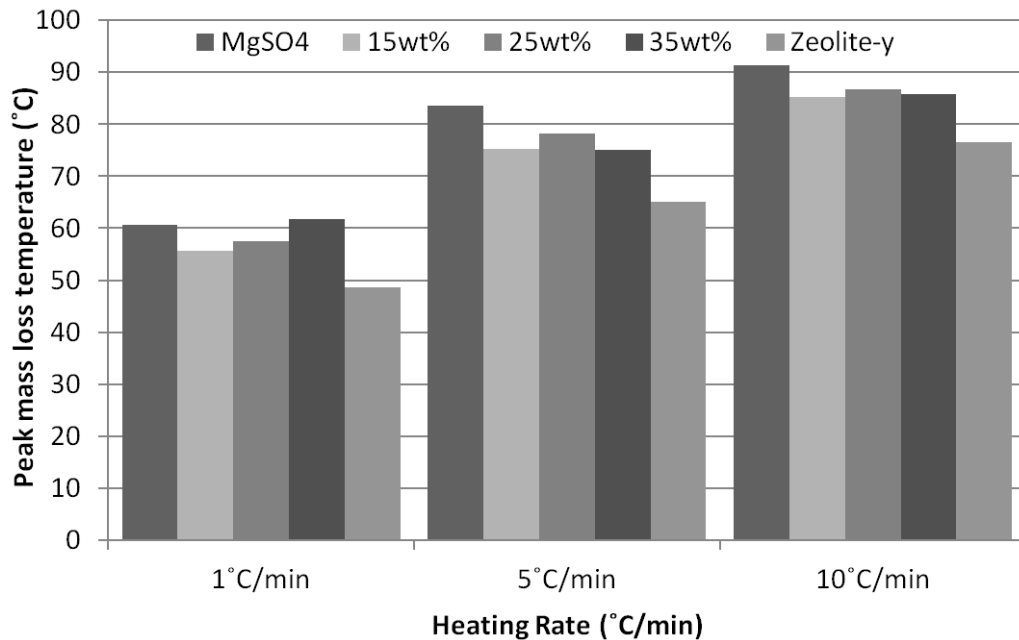


Figure 4-19 Comparison of slow kinetics of each composite sample.

From the experiments performed heating rates appeared to have a minimal impact on the dehydration characteristics of the composite materials. One possible suggestion as to why this occurred was due to the superior surface area of the zeolite which increased the dehydration kinetics of the material nullifying the expected heating rate effects.

4.5 Nitrogen vapour sorption measurements

Figure 4-20, Figure 4-21 and Figure 4-22 show the results of the nitrogen vapour sorption tests of MgSO_4 , zeolite-Y and composite materials. The results show as the wt% of MgSO_4 increased within the composite materials the pore volume (Figure 4-20) and BET surface area

(Figure 4-21) decreased whereas the average pore diameter (Figure 4-21) increased. Sample MgSO_4 DI and zeolite Y DI were both of the samples which were dissolved/mixed within DI water before being dehydrated within the oven.

Figure 4-20 shows the MgSO_4 had the highest pore volume. It was expected with increasing wt% of MgSO_4 in the composite materials the pore volume would increase, this did not happen. The pore volume of the composite materials decreased with increasing wt%. The reason suggested for this was due to the preparation method of the samples. First the MgSO_4 was initially dehydrated in an oven in a powder form and then it was degassed at 170°C before being tested. This means the MgSO_4 was essentially dehydrated twice which caused more cracks in the material. The composite materials were created by dehydrating the solution containing the aqueous MgSO_4 solution within the oven. When dehydrated it was likely the MgSO_4 solution re-crystallised directly into MgSO_4 instead of crystallising in to $\text{MgSO}_4 \cdot 7\text{H}_2\text{O}$ first and then dehydrating to MgSO_4 . The composite material was then ground into a powder and degassed at 170°C before being tested. This method was essentially dehydrating the MgSO_4 crystals only once meaning it was likely there was less cracks caused to the material which explained the lower than expected pore volume of the composite materials.

To test this, zeolite-Y and MgSO_4 were mixed with DI water and then both dehydrated within the oven. Then both samples were degassed at 170°C before being tested. This was a similar preparation method used for the composite materials (i.e. the MgSO_4 re-crystallised when initially being dehydrated within the oven and then was only essentially dehydrated once in the degassing procedure hence, reducing the cracks to the material).

The results show the MgSO_4 which was essentially dehydrated once (labelled as MgSO_4 DI on Figure 4-20) had a pore volume significantly smaller than the MgSO_4 samples. This means that the additional dehydration step causing more cracks resulted in a larger pore volume. This supported the claim (see section 4.2.6) that the vapour transportation properties of the MgSO_4 will increase with increasing dehydration cycles.

Figure 4-22 shows the changing cumulative pore volume against pore diameter. The majority of the pore volume from the zeolite was from pores in the 2-4nm range. For the MgSO_4 sample the majority of the pore volume was from pores 16-32nm in size. The MgSO_4

DI sample had much less pore volume from the 16-32nm range meaning the extra dehydration cycle caused cracks which resulted in pores within the 16-32nm range.

With increasing wt% of $MgSO_4$ in the composite samples the BET surface area and pore volume declined. As there was no wt% value when the composite materials had a sudden drop in either the BET surface area or pore volume, which would of indicated pore blocking, this makes selecting a composite material for larger scale simple and the 35wt% sample would be chosen as there did not appear to be any negative properties of this composite material and it had the highest dehydration enthalpy and the highest performance %.

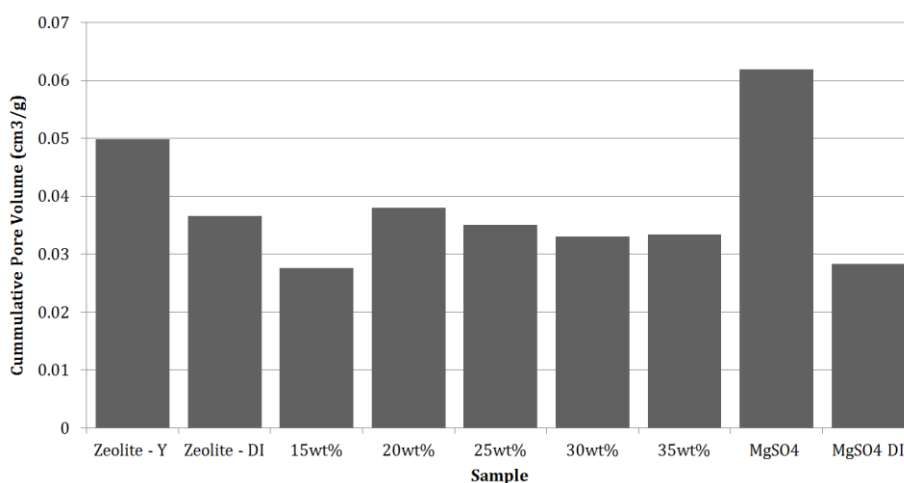


Figure 4-20 Cumulative pore volume of each composite sample, zeolite-Y and $MgSO_4$

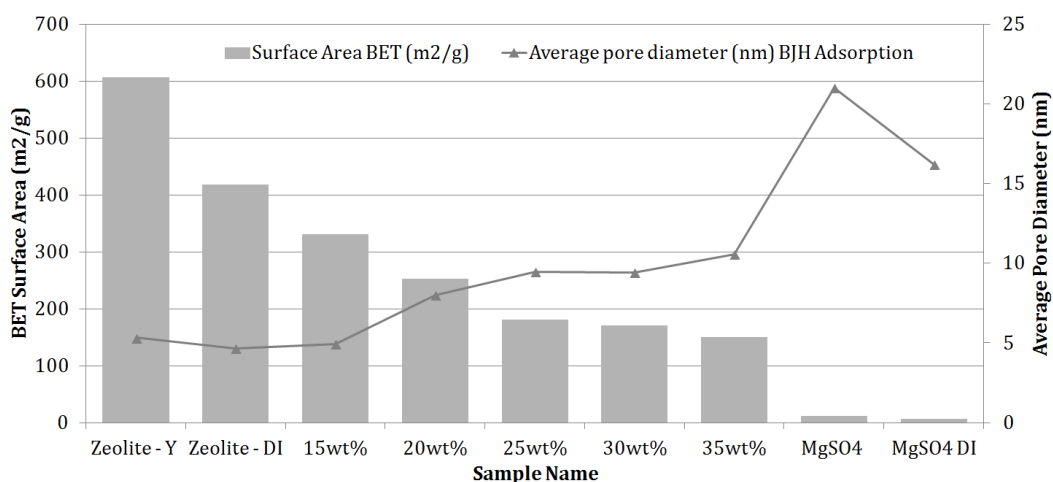


Figure 4-21 BET surface area and average pore diameter of each composite sample, zeolite-Y and $MgSO_4$

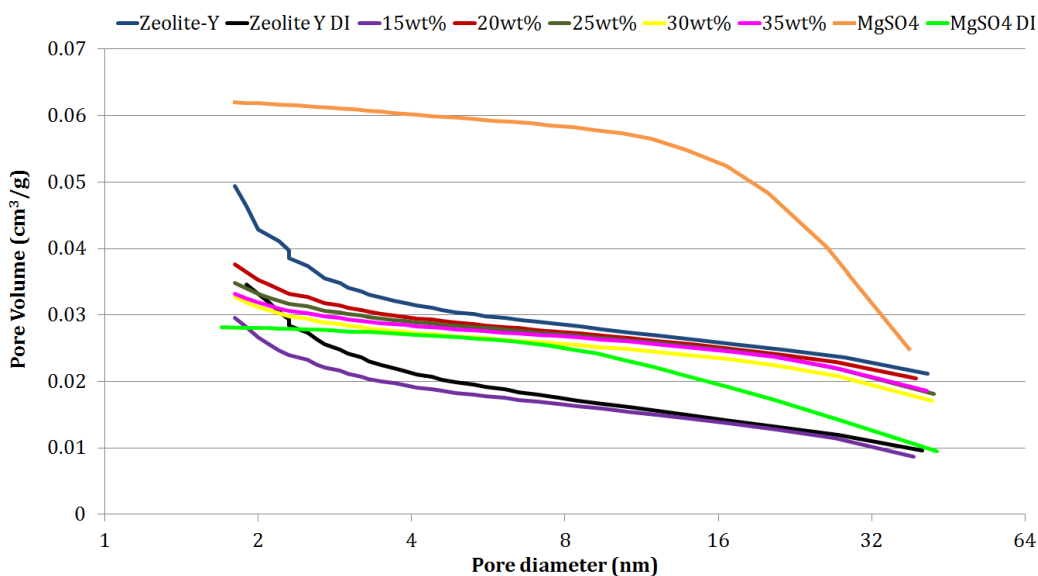


Figure 4-22 Cumulative pore volume against pore diameter of $MgSO_4$, zeolite-Y and the composite materials

4.6 Introduction to further slow kinetics tests

The dehydration of salt hydrates is a kinetic process and with increasing heating rate the point at which the dehydration takes place will be shifted to a higher temperature. This kinetic process is seen in section 4.1 where the peak dehydration temperature of the $MgSO_4$ shifted to a higher temperature.

To investigate this further additional tests have been conducted to look at the impact the dehydration kinetics of $MgSO_4 \cdot xH_2O$ had on the energy storage potential of the material. This is an important consideration and may change the way in which $MgSO_4$ is charged when utilised in a thermal energy storage system. To test the dehydration kinetics of $MgSO_4$ several investigations were conducted:

- $MgSO_4 \cdot 7H_2O$ -90°C.** $MgSO_4 \cdot 7H_2O$ was dehydrated within the DSC and TGA up to 90°C with varying heating rates (1, 5 and 10°C/min). The samples were rehydrated at 56%RH. These experiments were conducted to assess the enthalpy of the samples when they were not completely dehydrated (complete dehydration occurs at around 150°C) and also to assess the isothermal enthalpy and isothermal mass loss of the samples.

- **MgSO₄·7H₂O-150°C-75%RH.** MgSO₄·7H₂O was dehydrated within the DSC up to 150°C with varying heating rates (1, 5 and 10°C/min). This experiment was conducted for 5 cycles and for each cycle the samples were rehydrated at 75%RH. This experiment was to assess how the overall dehydration enthalpy and also the isothermal enthalpy changes with successive cycles and heating rates and if the dehydration kinetics became worse with higher hydration humidity.
- **MgSO₄·7H₂O-90°C- No isotherm.** These tests were conducted in the DSC and dehydrated MgSO₄·7H₂O to 90°C but with no isothermal period at 90°C. This allowed for an understanding of the impact not having an isothermal period had on the MgSO₄·xH₂O when using high heating rates.
- **MgSO₄·7H₂O-90°C- Grain size.** This section looked at how the grain size of the MgSO₄·7H₂O impacted the dehydration enthalpy of the material. MgSO₄·xH₂O was dehydrated within the DSC and TGA up to 90°C with a 5°C/min heating rate. The samples were rehydrated at 56%RH.

The isothermal enthalpy is the amount of heat which is required to hold the sample at an isothermal period. If the sample being tested is not going through any transitions the isothermal enthalpy will be zero. If MgSO₄·xH₂O is not held at the maximum dehydration temperature for an isothermal period and allowed to immediately start to cool a part of the isothermal enthalpy would be lost. This means that potential dehydration enthalpy would be lost due to an isothermal period that is too short. This loss of enthalpy due to a short isothermal period was investigated further here. The reduction in dehydration enthalpy, if an insufficiently long isothermal period is used, is due to the dehydration kinetics of the MgSO₄. By evaluating the isothermal enthalpy it was possible to get an understanding of the dehydration kinetics of the MgSO₄.

For the DSC analysis of the TCES materials it is important to consider the length of the isothermal period. If it is not sufficiently long enough it results in significantly different values depending on the heating rate used.

4.6.1 $MgSO_4$ -90°C slow kinetics analysis

For each of the samples the slow kinetics were investigated using an isotherm enthalpy analysis, which is a method developed by the author of this thesis. Figure 4-23 shows an integration of the 60 minute isothermal period at 90°C used to evaluate the isothermal enthalpy.

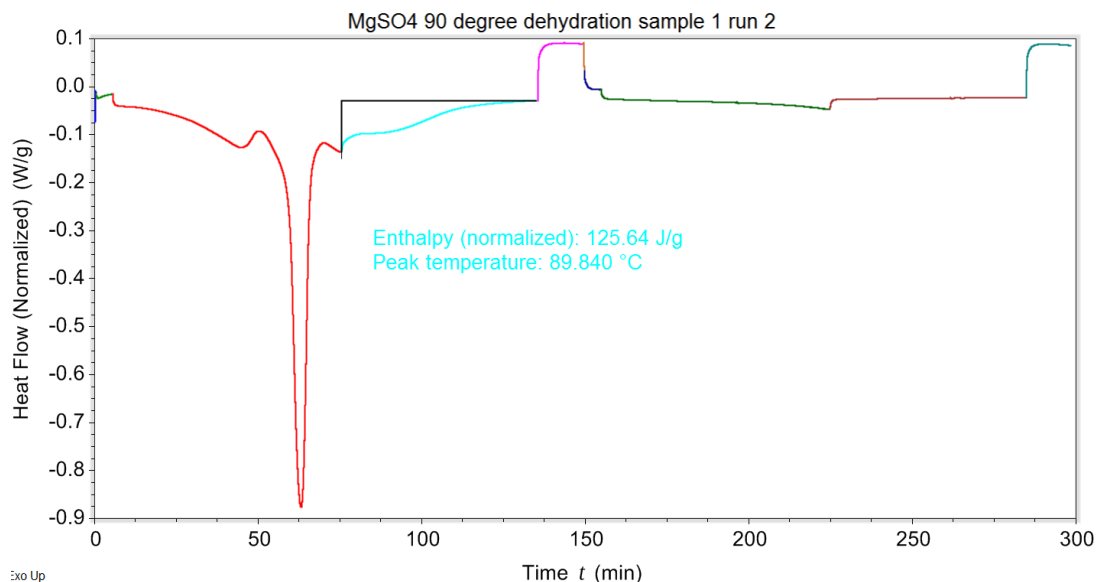


Figure 4-23 Illustration of an example isotherm enthalpy analysis conducted on a sample dehydrated to 90°C

Figure 4-24 shows the complete enthalpy, dehydration enthalpy and sensible enthalpy for $MgSO_4 \cdot xH_2O$ when dehydrated to 90°C using different heating rates. The second cycle for each sample resulted in a reduction of enthalpy as the $MgSO_4$ did not hydrate back to $MgSO_4 \cdot 7H_2O$. Each of the sensible components was very similar for each heating rate suggesting that the state of dehydration was the same for each sample (i.e. if the samples were more hydrated than another sample the sensible enthalpy would be measured higher as there would be enthalpy required to further dehydrate the sample).

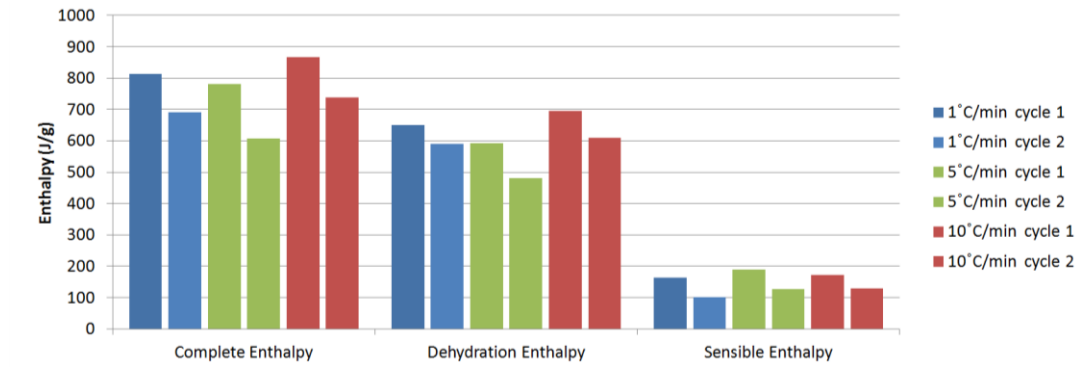


Figure 4-24 Enthalpy analysis for each of the heating rates tested

Figure 4-25 shows the dehydration isotherm enthalpy of $\text{MgSO}_4 \cdot x\text{H}_2\text{O}$ when dehydrated to 90°C . The isothermal enthalpy increased with increasing heating rate. The isotherm enthalpy for the second cycle decreased for the 5 and $10^\circ\text{C}/\text{min}$ samples but increased for the $1^\circ\text{C}/\text{min}$ samples. Also, it was seen that the % of total enthalpy which is accounted to the isothermal period increased with increasing heating rate. This means due to the slow dehydration kinetics of the $\text{MgSO}_4 \cdot x\text{H}_2\text{O}$ when using higher heating rates the $\text{MgSO}_4 \cdot x\text{H}_2\text{O}$ dehydrates more in the isothermal period than when using lower heating rates, which was expected as the dehydration is a kinetic process.

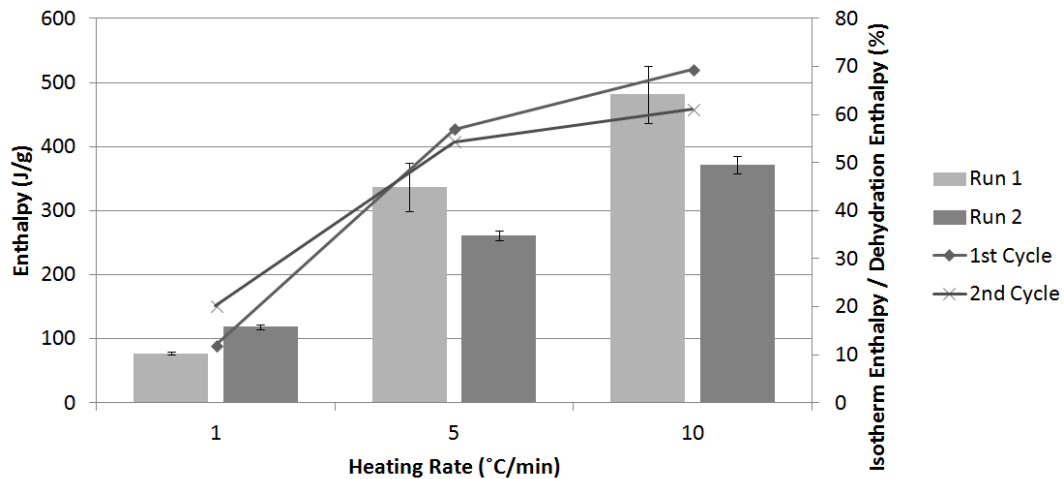


Figure 4-25 Isotherm enthalpy for each of the $\text{MgSO}_4 \cdot x\text{H}_2\text{O}$ samples when dehydrated to 90°C at different heating rates

Figure 4-26 shows the $\text{MgSO}_4 \cdot x\text{H}_2\text{O}$ total mass loss (%) when dehydrated to 90°C , using 3 different heating rates tested over 4 cycles. The $\text{MgSO}_4 \cdot x\text{H}_2\text{O}$ appeared to lose a similar mass % independent of the heating rate used. This was important as it confirmed that the total

enthalpy was the same (Figure 4-24) and the total mass loss was the same (Figure 4-26) for the $\text{MgSO}_4 \cdot x\text{H}_2\text{O}$ samples dehydrated to 90°C independent of the heating rate used.

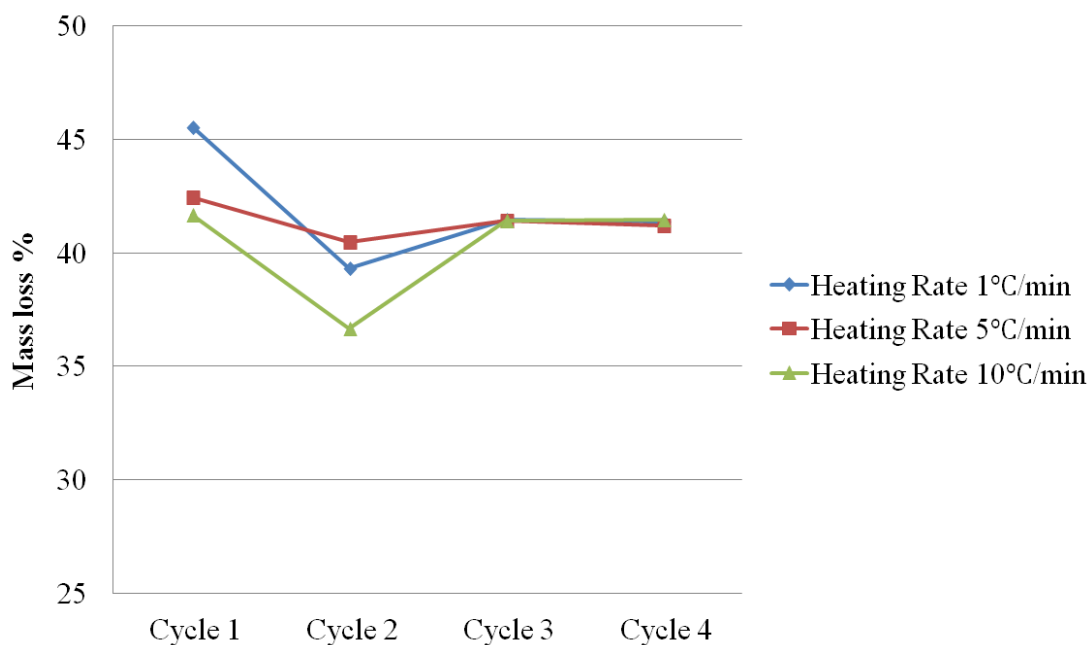


Figure 4-26 Mass loss of $\text{MgSO}_4 \cdot x\text{H}_2\text{O}$ against cycle number with different dehydration heating rates

Figure 4-27 shows the average enthalpy required per % mass loss for $\text{MgSO}_4 \cdot x\text{H}_2\text{O}$ when dehydrated to 90°C with different heating rates. The enthalpy per mass loss was very similar for each heating rates tested. With this information it was suggested that the isotherm enthalpy increase for increasing heating rates was a result of slow dehydration kinetics (see Figure 4-25) and not a result of higher heating rates requiring more enthalpy to dehydrate the material to the same level.

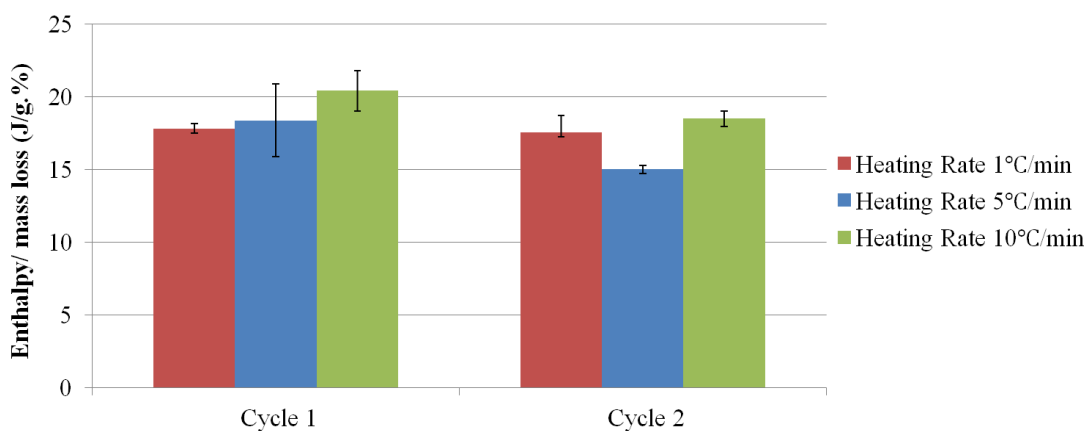


Figure 4-27 Enthalpy per mass loss for each $\text{MgSO}_4 \cdot x\text{H}_2\text{O}$ sample dehydrated with different heating rates

Figure 4-28 shows the isothermal mass loss for each of the $\text{MgSO}_4 \cdot x\text{H}_2\text{O}$ samples when dehydrated with different heating rates. The higher the heating rate used the higher the isothermal mass loss (the amount of mass lost while the $\text{MgSO}_4 \cdot x\text{H}_2\text{O}$ was being held at 90°C). After the first cycle the mass loss for each heating rate stayed the same and the dehydration kinetics did not improve with successive cycles.

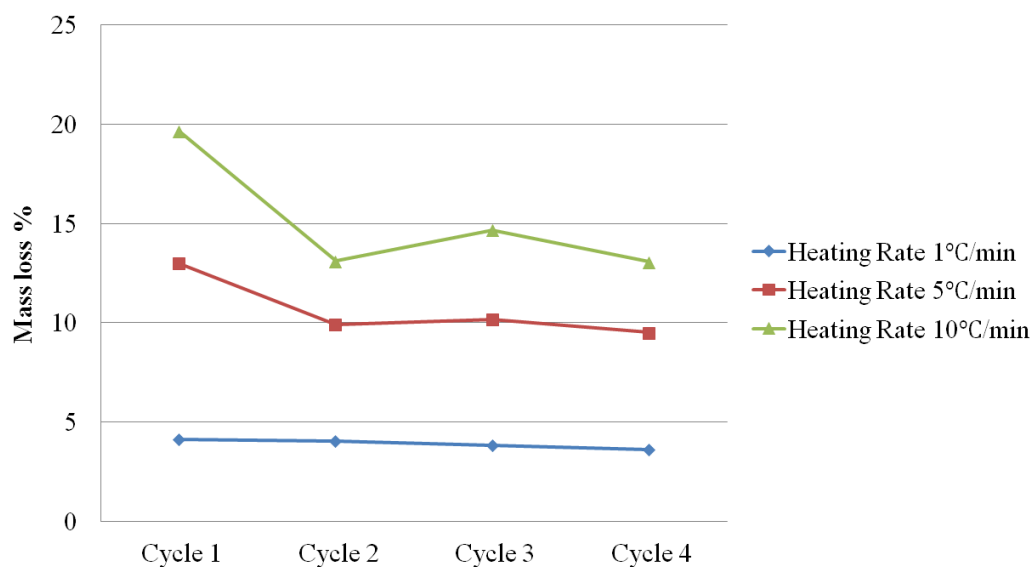


Figure 4-28 Isothermal mass loss % of the $\text{MgSO}_4 \cdot x\text{H}_2\text{O}$ samples dehydrated with different heating rates

4.6.1.1 Sub conclusion for MgSO_4 - 90°C slow kinetics section

From section 4.6.1 the conclusion was there appeared to be a correlation between the isothermal dehydration enthalpy and the heating rate used. A higher heating rate resulted in a higher isothermal dehydration enthalpy and also a higher isothermal mass loss. The overall dehydration enthalpy for the samples appeared to be similar (around 610J/g) irrespective of the heating rate used. The repeating cycles also did not appear to change the mass loss in the isothermal period of the samples, suggesting that the slow kinetics did not improve with successive cycles.

As the enthalpy per percentage mass loss was very similar for each cycle and each sample it was concluded that the increased enthalpy in the isothermal period for the higher heating rate samples (5 and 10°C/min) was a result of the $\text{MgSO}_4 \cdot x\text{H}_2\text{O}$'s slow dehydration kinetics. This means it is important to consider the length of the isothermal period if dehydrating a TCES material which is affected by heating rates, such as $\text{MgSO}_4 \cdot x\text{H}_2\text{O}$, as an insufficient isothermal period will result in a reduction of dehydration enthalpy and therefore a reduction

in the amount of energy that is stored even through the material is at the same temperature as a material dehydrated with a lower heating rate.

4.6.2 $MgSO_4$ -150°C-75%RH slow kinetics measurements

The average $MgSO_4 \cdot xH_2O$ enthalpy values seen in Figure 4-29 were an average of all the cycles neglecting the first cycle. This was because the $MgSO_4 \cdot xH_2O$ was initially $MgSO_4 \cdot 7H_2O$ and the $MgSO_4$ does not hydrate back to this state. Some variation in the enthalpy values could be seen, without TGA data the reason for this could be additional water leaving the 1°C/min sample opposed to the 10°C/min sample. However, the sensible component of each sample is the same suggesting after the dehydration each sample was dehydrated to the same level.

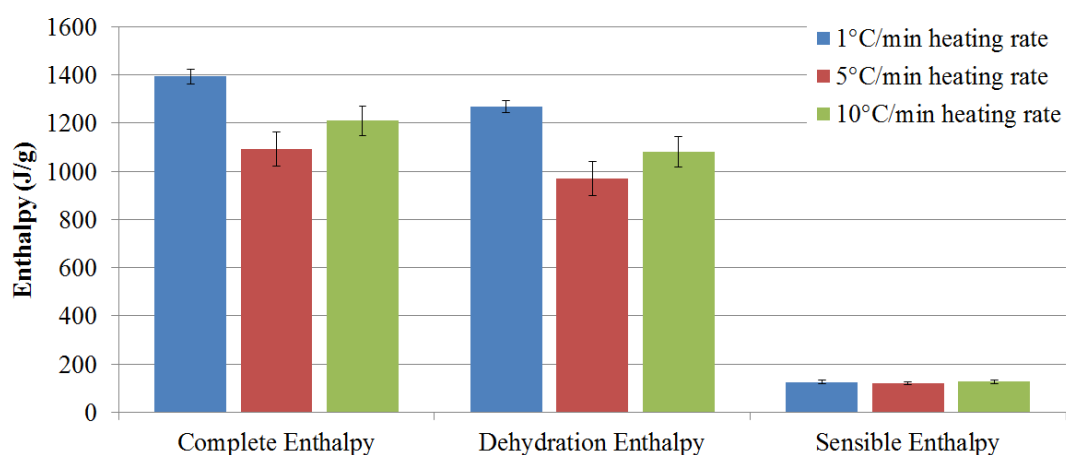


Figure 4-29 Total average enthalpy values for $MgSO_4 \cdot xH_2O$ dehydrated with different heating rates

Figure 4-30 shows the percentage the isothermal enthalpy was of the total enthalpy (i.e. isothermal enthalpy / total enthalpy * 100). There was a trend for the higher heating rates (5 and 10°C/min) the % decreased with increasing cycles.

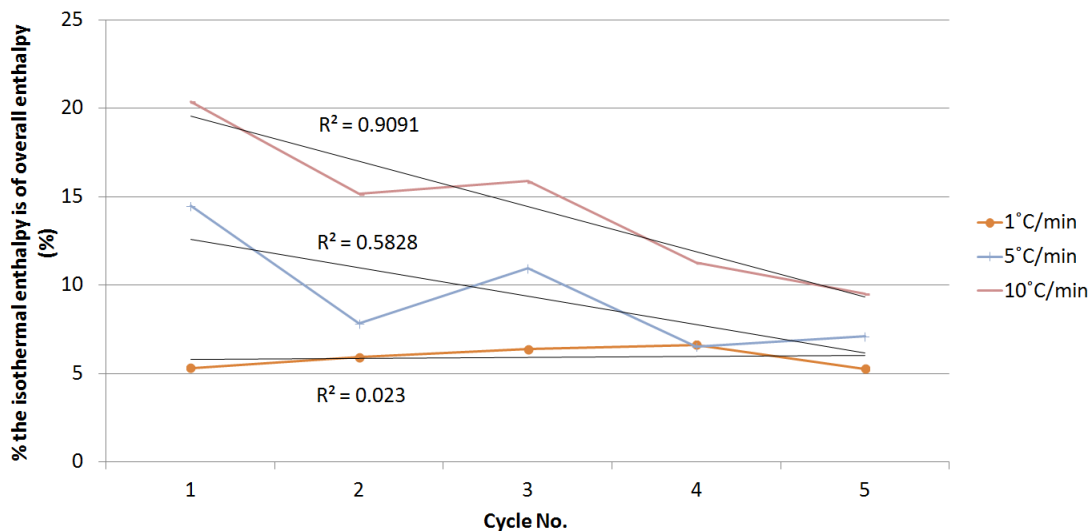


Figure 4-30 Percentage isothermal enthalpy is of total dehydration enthalpy for $MgSO_4$ samples dehydrated to $150^\circ C$ within the DSC

4.6.2.1 Sub conclusion of the $MgSO_4$ - $150^\circ C$ -75% RH slow kinetics section

Section 4.6.2 showed how increased heating rates resulted in increased dehydration enthalpy in the isothermal periods. However, the percentage did appear to decrease with successive cycles suggesting the dehydration kinetics improved this was also suggested from the $MgSO_4$ dehydration plots (see Figure 4-9, Figure 4-10 and Figure 4-11). This was likely due to the repeated dehydration to $150^\circ C$ which caused fractures in the $MgSO_4 \cdot xH_2O$ resulting in faster dehydration kinetics.

4.6.3 $MgSO_4$ dehydration enthalpy analysis without an isothermal period

It has been shown in the previous sections (4.6.1 & 4.6.2) with an increasing dehydration heating rate the percentage of dehydration enthalpy and mass loss in the isothermal period, of the overall dehydration enthalpy and mass loss increased. To further assess if the isothermal period does impact the dehydration enthalpy and therefore the energy storage potential of $MgSO_4$ a dehydration of $MgSO_4 \cdot xH_2O$ was performed with a small isothermal period of 5 minutes. The reason for the isothermal period was to allow analysis of the DSC data, which would be difficult to do accurately if there was no isothermal period.

Figure 4-31, Figure 4-32 and Figure 4-33 show the dehydration of $MgSO_4 \cdot 7H_2O$ within the DSC up to $90^\circ C$ after an initial dehydration up to $90^\circ C$, with i) a normal isothermal period (60 minutes) and ii) a 5 minute isothermal period, with heating rates of $1^\circ C/min$, $5^\circ C/min$ and $10^\circ C/min$, respectively.

For Figure 4-31 the endothermic heat flow for each of the samples was very similar with no apparent dehydrations. This was expected as the sample heated with a heating rate of $1^{\circ}\text{C}/\text{min}$ had enough time to dehydrate completely at 90°C before the material was then cooled back down. The plot was expected to look as it did and the endothermic heat flow was due to the samples sensible heat. The difference in the two sets of heat flow in Figure 4-31 was due to shifting baseline in the samples. Figure 4-32 and Figure 4-33 had a different heat flow plot compared to Figure 4-31.

Figure 4-32 has a dehydration peak at around 71°C , this peak when integrated only accounted for $2.5\text{J}/\text{g}$. Figure 4-33 has a much more distinct dehydration peak which peaked at around 69°C but starts at around 30°C . This peak, when integrated, was around $45\text{J}/\text{g}$.

The reason for these peaks seen in Figure 4-32 and Figure 4-33 was because of the slow dehydration kinetics of the MgSO_4 . When the material was dehydrated with a high heating rate the material does not have enough time to dehydrate completely before being cooled, this means on the second dehydration when the sample should only exhibit endothermic heat flow due to its specific heat capacity the material was still being dehydrated.

This is an important consideration for charging TCES materials and specifically MgSO_4 . If too high a heating rate is used with an insufficient isothermal period the material could be partially dehydrated (charged) which will result in reduced energy density from the material and also a reduced performance percentage.

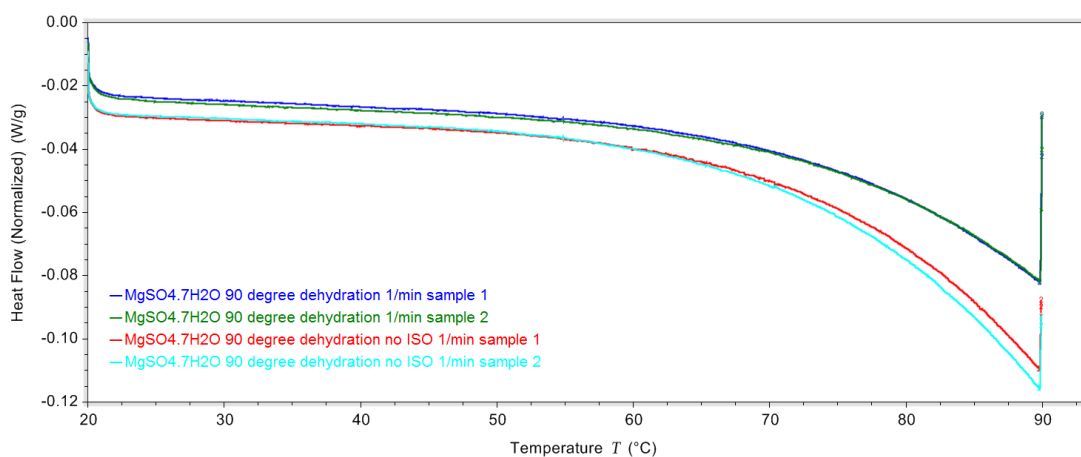


Figure 4-31 Dehydration of $\text{MgSO}_4 \cdot 7\text{H}_2\text{O}$ to 90°C with a heating rate of $1^{\circ}\text{C}/\text{min}$ and 5 minute isothermal period

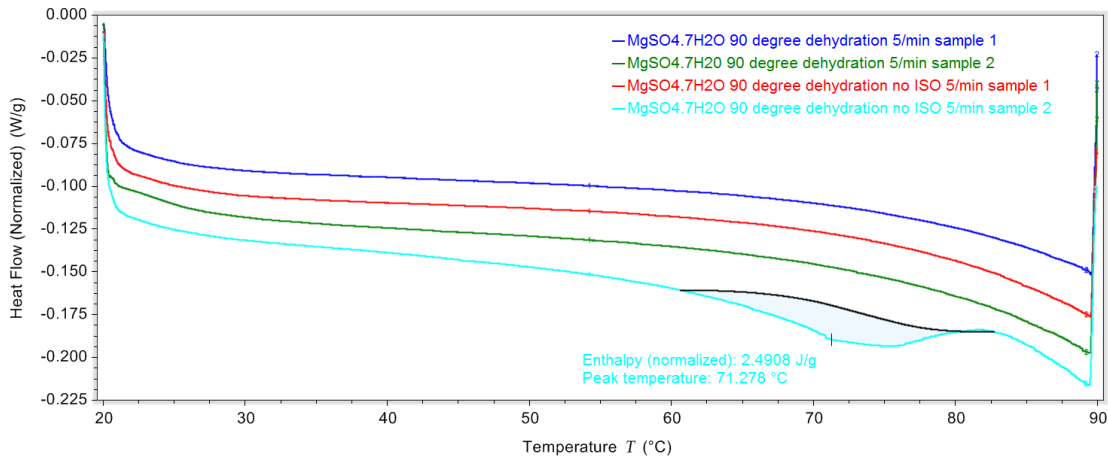


Figure 4-32 Dehydration of $MgSO_4 \cdot 7H_2O$ to $90^\circ C$ with a heating rate of $5^\circ C/min$ and 5 minute isothermal period

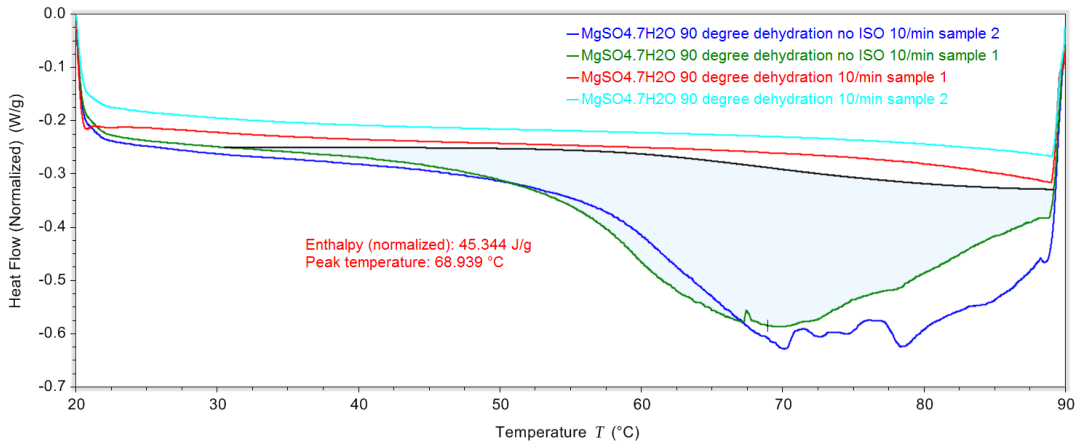


Figure 4-33 Dehydration of $MgSO_4 \cdot 7H_2O$ to $90^\circ C$ with a heating rate of $10^\circ C/min$ and 5 minute isothermal period

4.6.3.1 Sub conclusion from the $MgSO_4$ dehydration enthalpy analysis without an isothermal period

Section 4.6.3 showed clearly the length of the isothermal period is important to “extract” as much of the dehydration enthalpy from the $MgSO_4 \cdot xH_2O$. The lower the dehydration enthalpy the lower the amount of energy (heat) input into the material. However, if the $MgSO_4 \cdot xH_2O$ does not have enough time to dehydrate then the $MgSO_4 \cdot xH_2O$ is not completely charged essentially becoming a less energy dense material. Also, the efficiency of the material will essentially decrease as the sensible enthalpy stays the same, which is lost in a system, meaning a higher percentage of the energy input will be lost if the $MgSO_4 \cdot xH_2O$ is only partly dehydrated.

4.6.4 $MgSO_4$ particle size effect on slow kinetics

In order to assess if the grain size had an effect on the dehydration of $MgSO_4 \cdot xH_2O$ several tests were conducted. Three different grain sizes were used; see Table 4-3 for descriptions of the particles used. Figure 4-34 shows an image of each of the different grains used. For the medium DSC tests two of the grains were used, for the large DSC tests only 1 grain was used.

Table 4-3 Description of the different particles of $MgSO_4 \cdot 7H_2O$ used

Grain Size	Description of particles
Small	Very fine grains
Medium	2 x grains of diameter < 1.5mm
Large	1 grain with a diameter > 1.5mm. With a mass <10mg

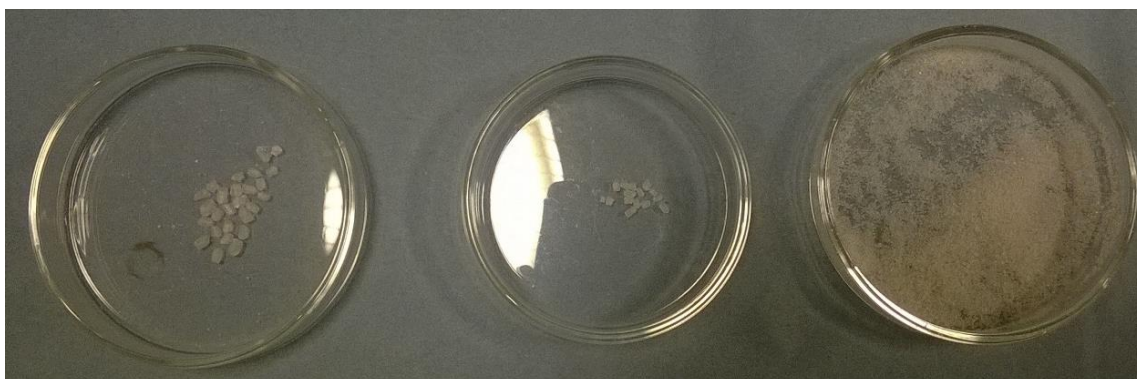


Figure 4-34 Samples used for particle size tests – Images show each of the samples used. Large, medium and small from left to right (see Table 4-3 for details of particles).

Figure 4-35 shows the DSC plots for each of the different samples used. It was difficult to make any conclusion regarding the differences between the large and medium particles results. However, clearly there was a difference with the smaller “powdered” samples compared to the larger particles. The peak dehydration occurred at a lower temperature for the powdered samples ($80^\circ C$ opposed to $88^\circ C$). Also the peak dehydration enthalpy was significantly reduced for the powdered samples. This resulted in the isothermal period

starting as a much lower heat flow value for the powdered samples than for the medium and larger samples.

As the difference between the medium and large samples was difficult to distinguish their DSC values were averaged together. Also the TGA tests were run with either small grains or “grains” which meet the medium criteria or are larger. This was one of the limitations of the grain size study, as the samples can be reasonably different and not uniformly prepared samples, this can result in more uncertainty in the measured data.

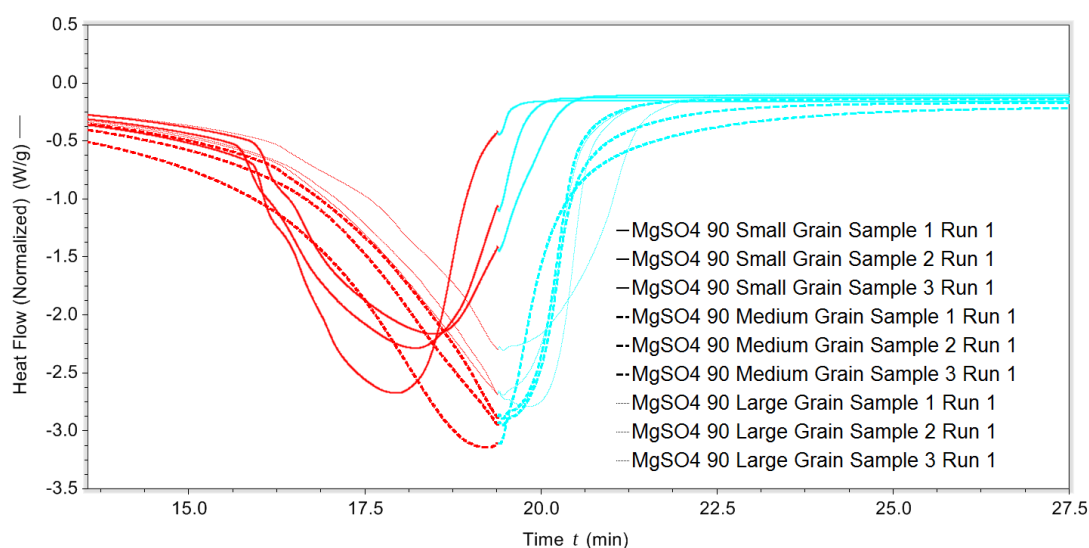


Figure 4-35 DSC plots for the three different grain sizes dehydrated to 90°C with a heating rate of 5°C/min.

Figure 4-36 shows the average enthalpy for small and medium/large grains. It was unknown why the medium/large grains have such a significantly higher enthalpy than the small grains however, it was clear that the grain size was having an impact on the dehydration kinetics.

Figure 4-37 shows the average TGA mass loss for both of the grain sizes. The variation in mass loss (water loss) overlaps and no conclusion could be made regarding if one grain size loses more or less mass. This means that because both small and large grain sizes lose the same amount of mass (water loss) they should have the same dehydration enthalpy as they are the same chemical.

Figure 4-38 shows the enthalpy per percentage mass loss (J/%). For the first cycle the energy per percentage mass loss was higher for the larger grain samples compared to the

small grain size. This means that for the first dehydration more energy was required to dehydrate the larger grains to the same dehydration level as the small grains. For the second cycle the energy per percentage mass loss for both the small and the larger grains overlaps. This means the energy was considered to be the same for these samples.

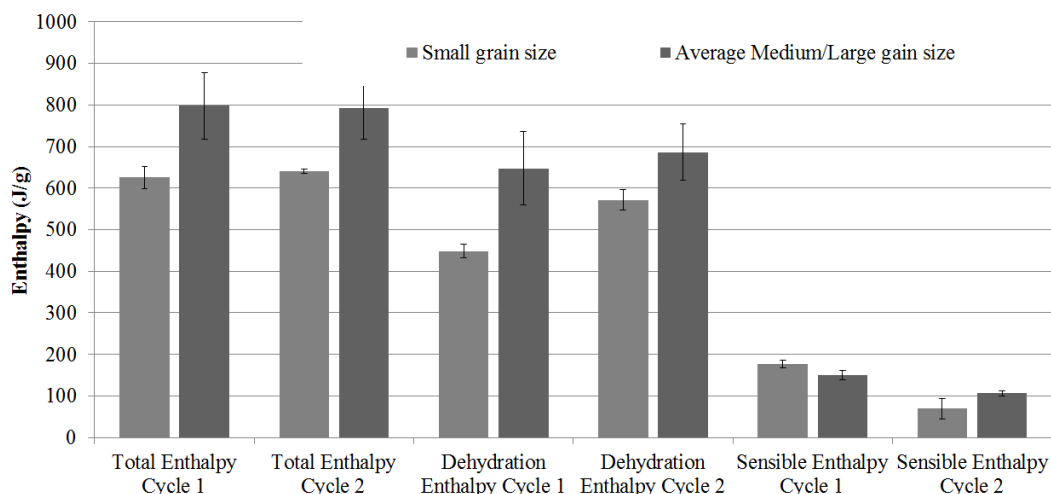


Figure 4-36 Average DSC enthalpy measurements for each grain size

The reason for the higher enthalpy for the larger grains for the first cycle was not known. One explanation may be extra enthalpy was required for the breaking of the larger grains to allow the water to escape the $MgSO_4$ which also explains the slow kinetics phenomenon seen. If this was true the extra enthalpy will not be released in the form of hydration heat when the material is rehydrated which makes the charge discharge efficiency decrease.

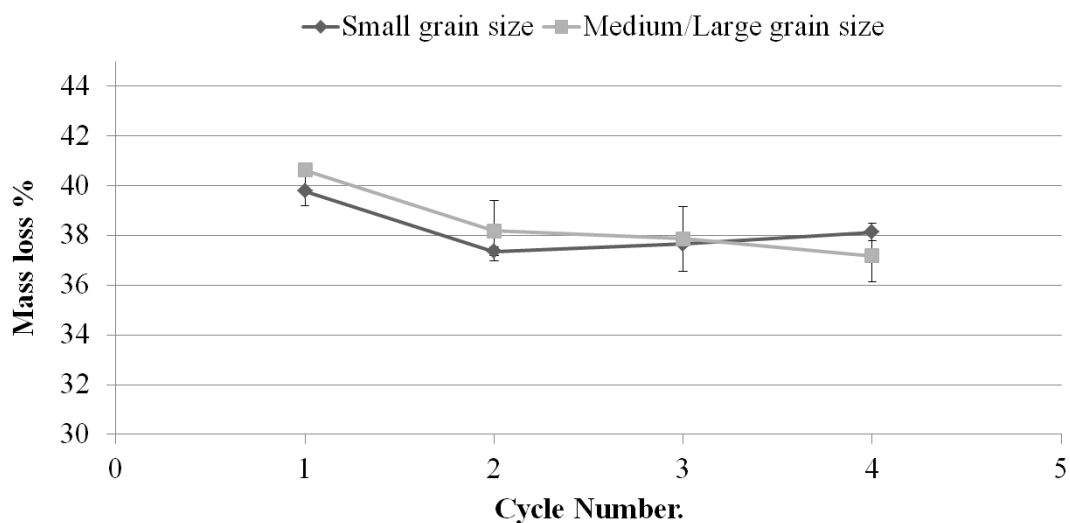


Figure 4-37 Average TGA mass loss data for the different grain sizes

From Figure 4-36 it was seen that the sensible component was similar for each sample. This means that after the dehydration each samples final dehydration state was the same. This further reinforced the finding that the extra enthalpy for the dehydration of the larger grain sizes was due to the breaking of the grains and not due to a less hydrated sample.

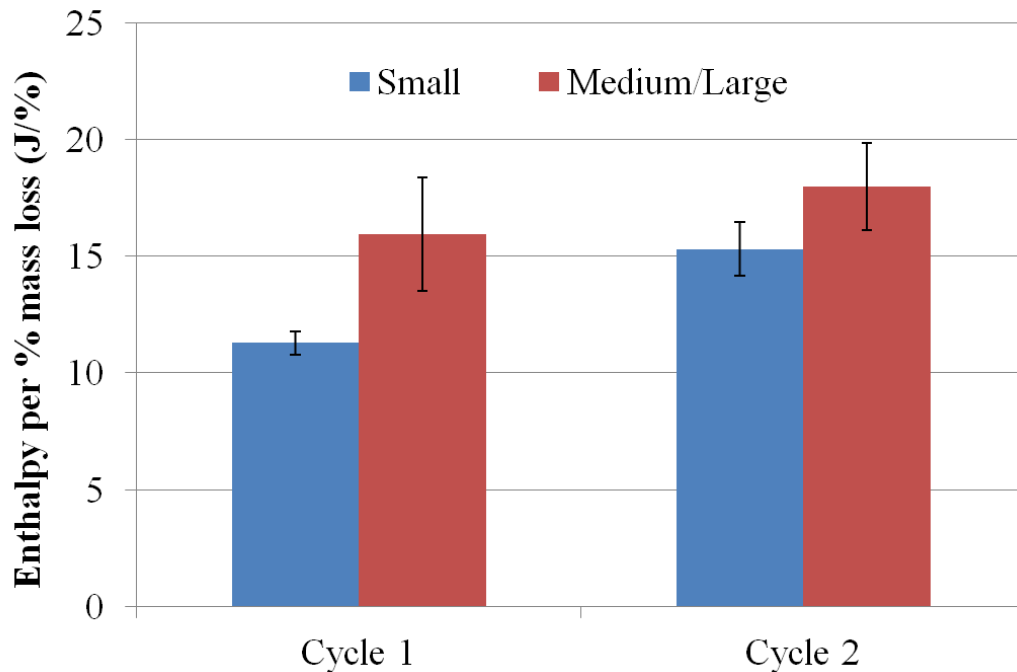


Figure 4-38 Enthalpy per % mass loss for each of the grain sizes (J/%)

Figure 4-39 shows an analysis of the isotherm enthalpy for both grain sizes. The small grain MgSO_4 had a much lower isothermal enthalpy than the other two (medium and larger) samples for the first cycle. This was a result of more mass loss from the medium and large samples in the isothermal period, which was due to their slow dehydration kinetics. This data highlights the importance of the isothermal period for the larger grains sizes.

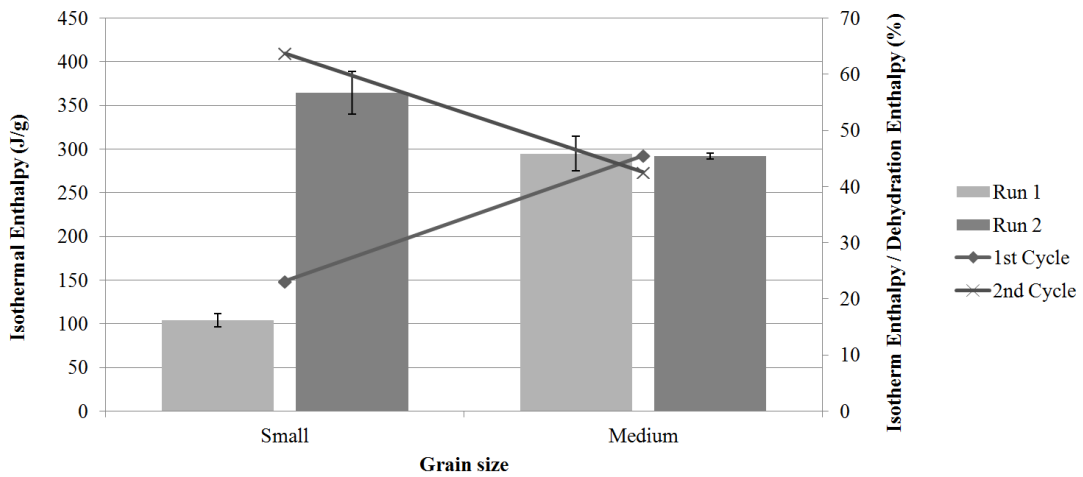


Figure 4-39 Isothermal enthalpy for each grain size

Figure 4-40 shows the isothermal mass loss of the small and larger grain sizes and also the percentage of mass loss in the isothermal period relative to the overall mass loss of the samples. It was seen that the isothermal mass loss was significantly higher for the larger grain sizes in the first dehydration cycle, which explains the high isothermal enthalpy for the larger grains in the first dehydration cycle (seen in Figure 4-39).

However, after the first cycle the isothermal enthalpy (Figure 4-39) and the isothermal mass loss (Figure 4-40) for both the small and the larger grains became very similar. This means that the slower kinetics which were seen in the larger grains are only an issue for the first dehydration cycle. Although, the isothermal period was still critical for all grain sizes as a significant percentage of mass loss and dehydration enthalpy take place in this period (around 25% of the mass loss and 45% of the dehydration enthalpy was in the isothermal period after the first dehydration cycle).

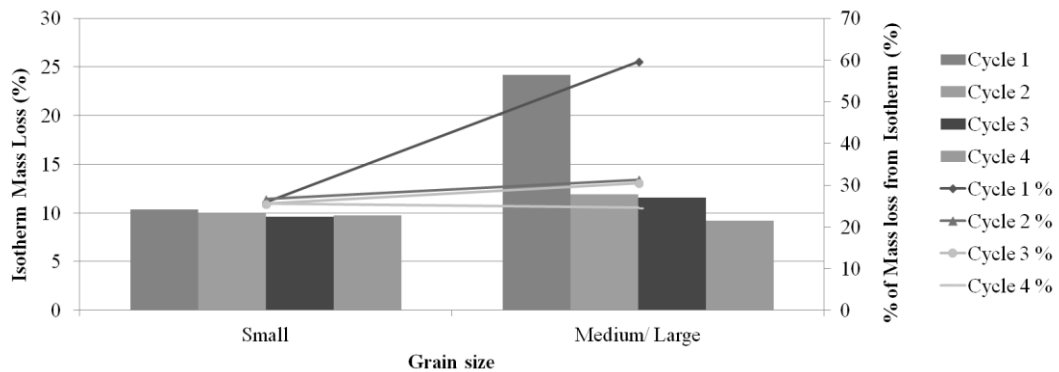


Figure 4-40 Isothermal mass loss and isothermal mass loss % for small and medium/large grain sizes

Figure 4-41 and Figure 4-42 show the TGA dehydration cycle plots for the small (Figure 4-41) and the larger grains (Figure 4-42). The TGA dehydration plots for the small grain sizes (Figure 4-41) were very similar for all samples and all cycles. The TGA dehydration plots for the larger grain sizes (Figure 4-42) were the same for all samples and cycles except for cycle 1. Cycle 1 had a significantly different dehydration mass loss profile and significantly more of the mass was lost at higher temperatures and in the 90°C isothermal period. This data allows for visualization of the data shown in Figure 4-40 which shows the first dehydration cycle of the larger grains was very different from the following dehydration cycles and also very different from all of the small grain dehydration cycles.

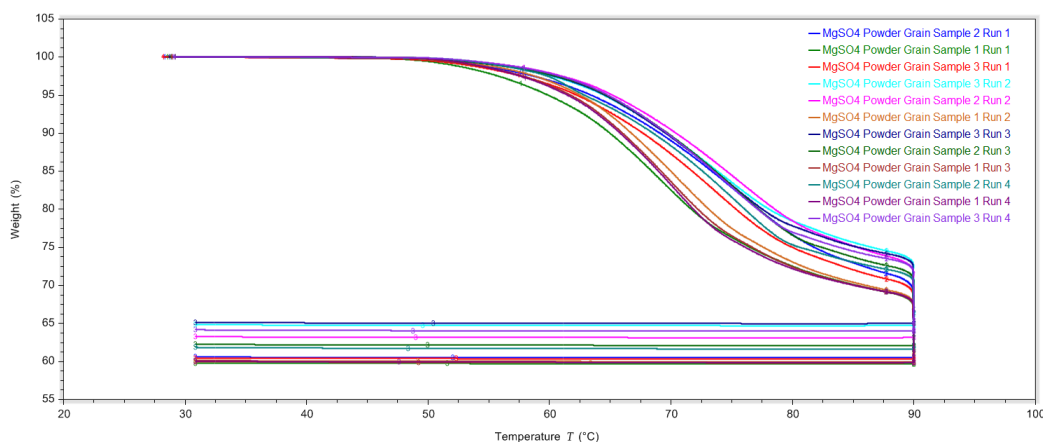


Figure 4-41 TGA plots for small grain sizes showing the similar dehydration cycles for all samples and runs

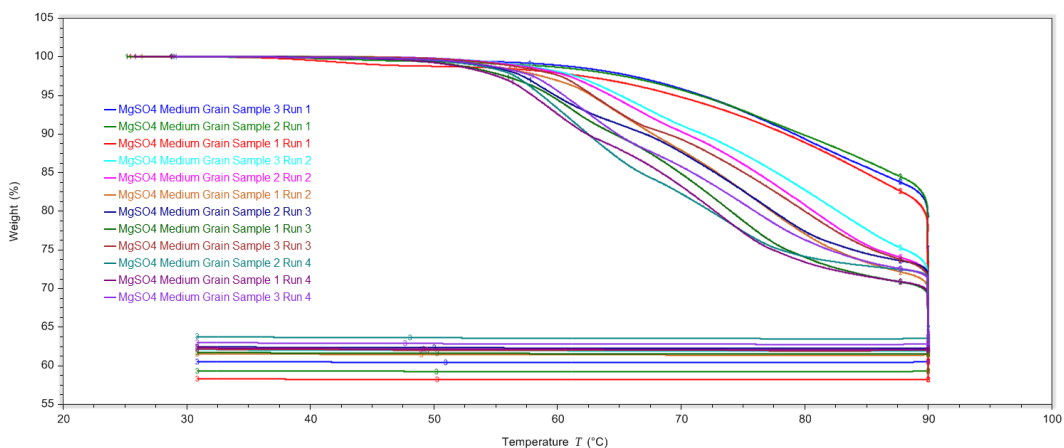


Figure 4-42 TGA plots for larger grain sizes showing the similar dehydration cycles for all samples except for the first dehydration cycle.

4.6.4.1 Sub conclusion from this section on MgSO₄ particle sizes effect on slow kinetics

The data from section 4.6.4 shows that larger grains of MgSO₄·7H₂O require more enthalpy for dehydration to the same level (same % mass loss) as smaller grain sizes when being dehydrated to 90°C. Also, the larger grain sizes have slower dehydration kinetics than the smaller grain size. This means that the isothermal period at 90°C is more critical for the larger grain sizes. These conclusions are only seen for the first cycle of the samples.

For the second cycle the characteristics are very similar for both grain sizes. The amount of enthalpy required per percentage mass loss was the same and the isothermal stage enthalpy and isothermal stage mass loss percentage was the same for both the small and larger samples.

If MgSO₄ is to be used in a large scale system consideration of the grain size used is needed as in a larger system the grain size characteristics may not be the same after only one cycle and may require several cycles to break the grains down to allow them to have the same dehydration characteristics as the smaller grains shown in this research. This means it is advisable to use small grain sizes in larger systems to avoid any delay in achieving the faster dehydration kinetics and higher dehydration to hydration efficiency seen for the smaller grain sizes.

4.7 Conclusions from chapter 4

The hydration conditions used for all samples in, sections 4.1 to 4.4 are achievable in winter conditions in the UK. These conditions have been shown to allow both zeolite and MgSO₄ to hydrate to a level which allows for relatively large total dehydration enthalpies (781J/g and 1265J/g for zeolite and MgSO₄, respectively). The main findings of this section of research are:

- TGA and DSC de/hydration cycles show the MgSO₄ dehydration enthalpy achieved for each cycle was very similar and there are no signs of degradation. This was also the case for 1, 5 and 10°C/min dehydration heating rates.
- As MgSO₄ is de/hydrated multiple times the materials apparent slow kinetics improve.
- With the use of the TGA and connected RGA the sharp volatile peaks shown on DSC dehydration plots of MgSO₄ are shown to likely be volatile water leaving the sample.
- The heating rates used have very limited effect on the composite materials peak dehydration temperature.

- This research has shown MgSO_4 has characteristics which appear to improve with successive de/hydration cycles and shows potential for use as a domestic inter-seasonal TCES material. The use of zeolite-Y to create a composite material further enhances the characteristics of MgSO_4 . To further confirm these findings hydration tests are required.
- Higher dehydration heating rates cause more cracks to occur in the MgSO_4 which should result in better dehydration kinetics. This is likely to be the same for the hydration kinetics although the DSC setup used will not allow for hydration testing.

4.7.1 Slow kinetics section conclusions

Section 4.6.1 shows a correlation between isothermal stage dehydration enthalpy and the heating rate used when dehydrating $\text{MgSO}_4 \cdot x\text{H}_2\text{O}$ to 90°C . A higher heating rate results in a higher isothermal stage dehydration enthalpy and also a higher isothermal stage mass loss. The overall dehydration enthalpy for the samples appears to be similar (around 610J/g) irrespective of the heating rate used. The repeating cycles also do not appear to change the mass loss in the isothermal period from the samples, suggesting that the slow kinetics do not improve with successive cycles. The enthalpy per percentage mass loss is very similar for each cycle meaning the increased enthalpy in the isothermal period for the higher heating rate samples (5 and $10^\circ\text{C}/\text{min}$) is a result of the samples dehydration.

Section 4.6.2 shows the increased heating rates result in an increased dehydration enthalpy in the isothermal periods when $\text{MgSO}_4 \cdot x\text{H}_2\text{O}$ is dehydrated to 150°C following 75% RH hydration. These were similar results of those found in section 4.6.1. The isothermal stage enthalpy does appear to decrease with successive cycles at the higher heating rates, suggesting the dehydration kinetics improve this was also suggested from the MgSO_4 dehydration plots (see Figure 4-9, Figure 4-10 and Figure 4-11).

Section 4.6.3 shows clearly the length of the isothermal period is important to “extract” as much of the dehydration enthalpy from the material at a set dehydration temperature (i.e. 90°C). Tests were conducted to show the impact and importance of the isothermal period when using higher heating rates. The $1^\circ\text{C}/\text{min}$ samples were not impacted by a short isothermal period (5 minutes) however, the $5^\circ\text{C}/\text{min}$ and $10^\circ\text{C}/\text{min}$ samples were impacted by a short isothermal period (5 minutes) and a 5 minutes isothermal period was too short to completely dehydrate the $\text{MgSO}_4 \cdot x\text{H}_2\text{O}$ due the slow dehydration kinetics of the MgSO_4 .

Section 4.6.4 shows the grain size of $\text{MgSO}_4 \cdot x\text{H}_2\text{O}$ used when dehydrating the material has an impact on the temperature at which mass is lost. A larger grain size loses more mass and requires more enthalpy at a higher temperature than a smaller grain size. The mass lost from all grain sizes was the same however; more enthalpy is required for the first dehydration of larger grains compared to smaller grains. After the first dehydration cycle the characteristics for the different grain sizes was the same.

The heating rate and isothermal period used when dehydrating $\text{MgSO}_4 \cdot x\text{H}_2\text{O}$ is important as higher heating rates dehydrate more (store more energy) in the isothermal period than lower heating rates. The grain size used when dehydrating $\text{MgSO}_4 \cdot x\text{H}_2\text{O}$ is important, at least for the first cycle, as the enthalpy required for the dehydration is higher for the same mass loss compared to a smaller grain size, resulting in a lower efficiency for larger grains. For interseasonal TES it is likely the TCES material will be charged with a very slow heating rate and the slow dehydration kinetics of $\text{MgSO}_4 \cdot x\text{H}_2\text{O}$ will not be a problem however, if $\text{MgSO}_4 \cdot x\text{H}_2\text{O}$ is to be used as a shorter term thermal energy store (i.e. several days) the material could be charged with a much higher heating rate and then the isothermal period used would need to be considered in order to store the most amount of thermal energy within the $\text{MgSO}_4 \cdot x\text{H}_2\text{O}$ for a given maximum temperature.

5 Chapter 5 – Understanding the larger scale (100g+) characteristics of MgSO₄ and investigating sample preparation methods for MgSO₄ for use as a TCES material.

5.1 Introduction to chapter 5

This chapter presents results from the initial testing of MgSO₄ and zeolite-Y at a more practical scale (i.e. 50g+). The results of these preliminary experiments identified some major issues associated with the use of MgSO₄ and zeolite-Y in a granular or powder form.

However, the small scale (DSC) testing did show that MgSO₄, zeolite-Y and composite materials made from MgSO₄ and zeolite-Y have the potential to be used as seasonal heat storage materials due to a high energy output. For these reasons research was undertaken to assess the potential of using different preparation approaches to form these powders into other forms (i.e. pellets or beads) to reduce the negative properties of MgSO₄ while extracting a high energy output from it.

5.2 Issues using MgSO₄ and zeolite as TCES materials

The measured total dehydration enthalpy values of MgSO₄, zeolite-Y and the composite materials from the DSC and TGA experiments were large enough (i.e. 781J/g and 1265J/g for zeolite-Y and MgSO₄, respectively) to allow work to commence on testing the materials at a larger scale. The results of these initial characterisation tests are presented below.

5.2.1 MgSO₄ agglomeration issues

The first tests were conducted with 75g of MgSO₄.7H₂O. The 75g MgSO₄.7H₂O was first dehydrated within an oven in a Pyrex beaker. From the previous small scale measurements it was shown that a high heating rate had no effect on the storage potential of the material other than the initial cracking. This cracking is believed to be beneficial to the vapour transportation within the material. For this reason the first test was conducted using pure MgSO₄ with a dehydration (regeneration) temperature of 150°C, heating rate of 10°C/min and an isotherm of 3h at 150°C. The material was cooled within the oven, which is a very slow process (<0.5°C/min). After the dehydration there was 45g of the MgSO₄.xH₂O remaining.

Only 49% of the initial mass of $\text{MgSO}_4 \cdot 7\text{H}_2\text{O}$ should remain after a dehydration to 150°C hence, the 45g of $\text{MgSO}_4 \cdot x\text{H}_2\text{O}$ which remained was higher than expected which means the $\text{MgSO}_4 \cdot 7\text{H}_2\text{O}$ did not dehydrate to MgSO_4 .

When removed from the oven the $\text{MgSO}_4 \cdot x\text{H}_2\text{O}$ was very solid and it took some force to remove it from the beaker (see Figure 5-1). Once removed it was in several large “clumps” which were not ideal for use within the reaction chamber. To solve this it was ground into a powder using a mortar and pestle. This is one of the issues when using pure $\text{MgSO}_4 \cdot x\text{H}_2\text{O}$ as a TCES material in an open reactor in a powder form. The material becomes solid and bonds to itself when dehydrated.



Figure 5-1 Image of $\text{MgSO}_4 \cdot 7\text{H}_2\text{O}$ in a beaker after a heating to 150°C , with a 3h isotherm, showing the solid structure which was formed

Once the $\text{MgSO}_4 \cdot x\text{H}_2\text{O}$ had been ground into a powder it was placed in the reaction chamber (see Figure 5-2). The chamber used was a stainless steel container (316) which had an inlet at the bottom on the left hand side and the outlet near the top of the container on the right hand side, the inlet and outlet are shown in Figure 5-2. This design was an attempt to ensure the air flows through all of the $\text{MgSO}_4 \cdot x\text{H}_2\text{O}$ to allow all of the material to hydrate. The $\text{MgSO}_4 \cdot x\text{H}_2\text{O}$ was hydrated with humid air with a partial vapour pressure of 1.3kPa at 20°C .

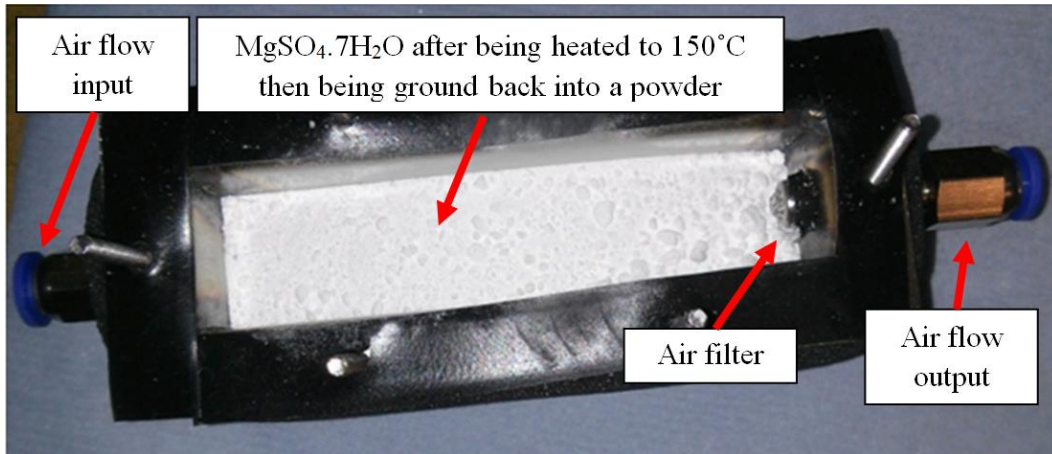


Figure 5-2 Ground $MgSO_4 \cdot xH_2O$ in the reaction chamber after being heated to $150^\circ C$

The $MgSO_4 \cdot xH_2O$ did not hydrate as expected. The hydration air “pushed” a hole through the material directly above the inlet allowing the air to travel directly to the outlet (see Figure 5-3). The top layer of $MgSO_4 \cdot xH_2O$ also seen in Figure 5-3 hardened and agglomerated meaning the $MgSO_4 \cdot xH_2O$ under the top hard layer was not coming into contact with humid air. This agglomeration when hydrated was another example of the problems of using pure $MgSO_4 \cdot xH_2O$ in a powder form.

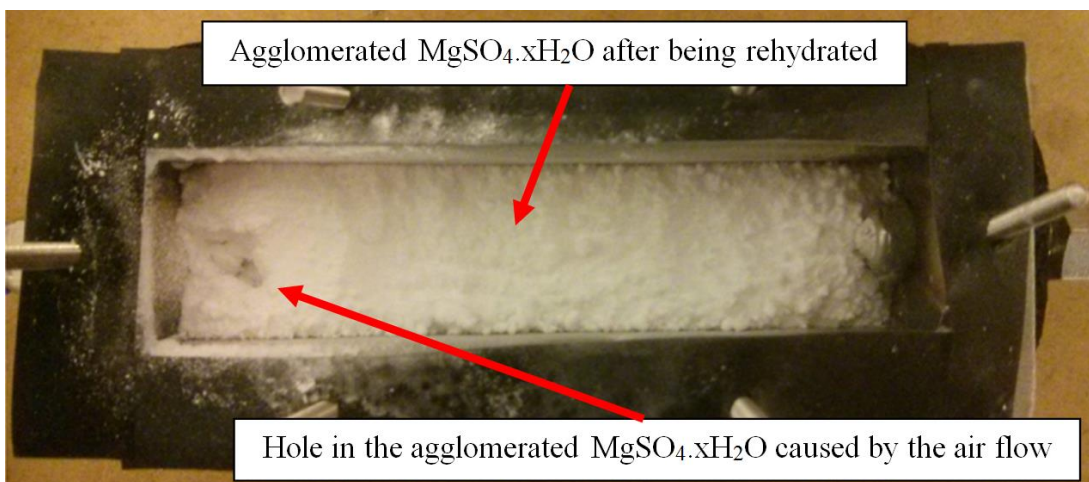


Figure 5-3 $MgSO_4 \cdot xH_2O$ after hydration in reactor showing agglomeration

5.2.2 $MgSO_4$ permeability issues

Not only does the $MgSO_4$ become solid when dehydrated from $MgSO_4 \cdot 7H_2O$ to $MgSO_4 \cdot xH_2O$ and also agglomerate when $MgSO_4 \cdot xH_2O$ is hydrated with humid air becoming solid and reducing the air flow, $MgSO_4 \cdot xH_2O$ as a powder has a very low permeability making it difficult to pass air through the material.

As the small hydration chamber described in section 5.2.1 had a flaw with the inlet and outlet positions a new hydration chamber was designed and built. This system (see Figure 5-4) consisted of an acrylic tube of 30mm in diameter. Within the tube was a plunger which could be adjusted in height to accommodate different volumes of material. At the bottom of the hydration chamber was an air inlet with the outlet attached to the plunger at the top of the chamber. The material was placed in the bottom of the chamber between the air inlet and outlet. This design ensured the air must pass through a small diameter column of material to get to the outlet.

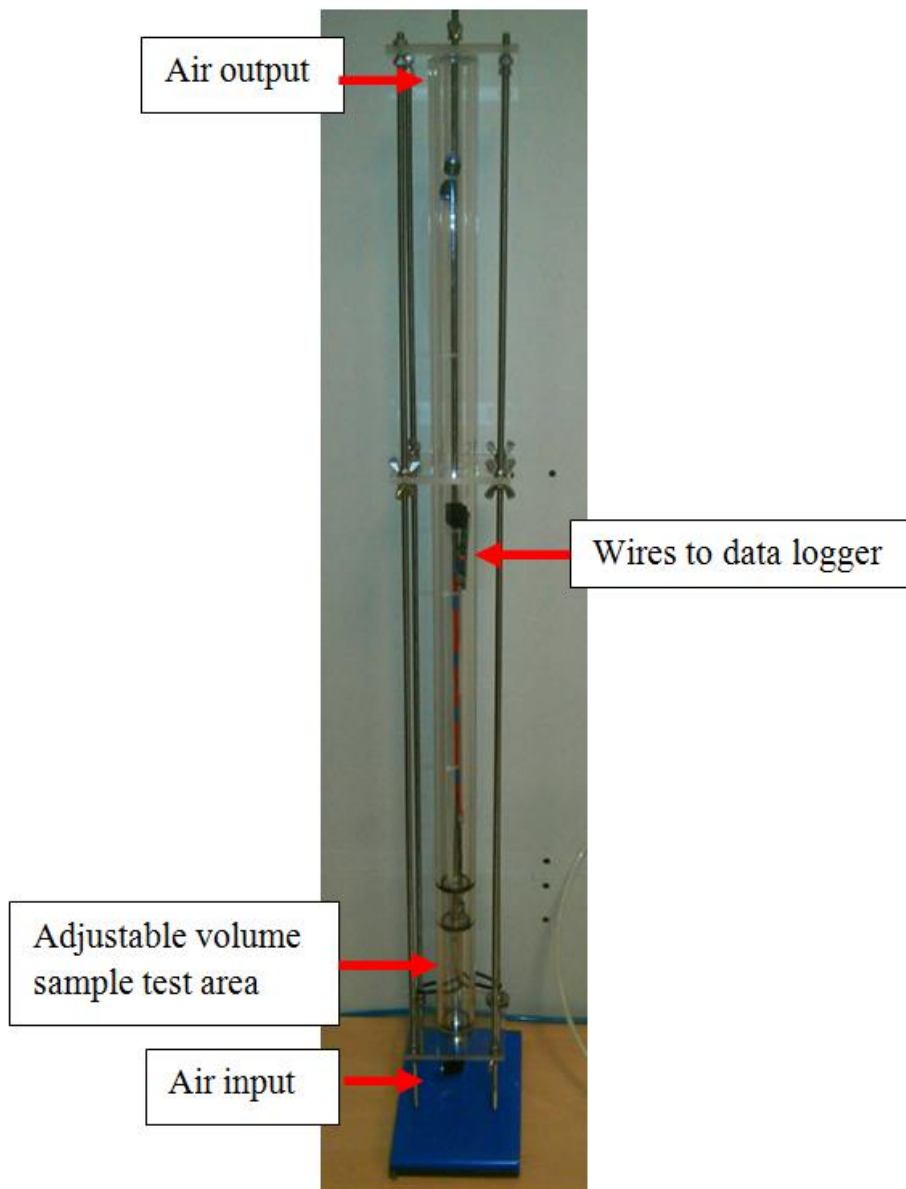


Figure 5-4 Image of empty plunger hydration chamber

200g of $\text{MgSO}_4 \cdot x\text{H}_2\text{O}$ was dehydrated to 150°C , at a heating rate of $1^\circ\text{C}/\text{min}$, and held isothermally for 3 hours. The material was then taken out of the oven, re-weighed (to ensure 100g was being used) and then crushed into a powder. The material was then placed back into the oven and dehydrated again using the same conditions. After the oven had cooled to 50°C the container with the $\text{MgSO}_4 \cdot x\text{H}_2\text{O}$ in was plugged with a rubber stopper to provide an air tight seal. The material was left to cool for $4 \frac{1}{2}$ hours in ambient conditions to ensure the material was at ambient temperature before any hydration occurred. Once cooled the material was placed within the plunger reactor for the hydration to begin. The $\text{MgSO}_4 \cdot x\text{H}_2\text{O}$ powder was hydrated with humid air (5L/min flow rate, 1.3kPa pH_2O).

To achieve the 5 L/min flow rate through the hydration chamber and the $\text{MgSO}_4 \cdot x\text{H}_2\text{O}$ powder a pressure of around 10psig was required. This was very high for such a small flow rate and results in a permeability of $1.8 \times 10^{-14} \text{ m}^2$ through the chamber when the MgSO_4 powder was inside, much lower than the suggested permeability for absorbent beds of 10^{-12} m^2 [58].

The $\text{MgSO}_4 \cdot x\text{H}_2\text{O}$ powder packed itself densely and stuck to itself within the chamber. This means when the 5 L/min flow rate was put through the material the bed of $\text{MgSO}_4 \cdot x\text{H}_2\text{O}$ powder became fluidised (see Figure 5-6). This is another problem when using MgSO_4 powder. It is not ideal for the bed to be fluidised with such small flow rates as fluidised beds require larger chamber volumes for the material to expand into.

Figure 5-5 shows the increase in temperature seen from the $\text{MgSO}_4 \cdot x\text{H}_2\text{O}$ powder hydration. It was seen that the $\text{MgSO}_4 \cdot x\text{H}_2\text{O}$ initially hydrated and reached its maximum power output at around 1h into the hydration. After reaching its maximum power output the materials power slowly decreased over time.

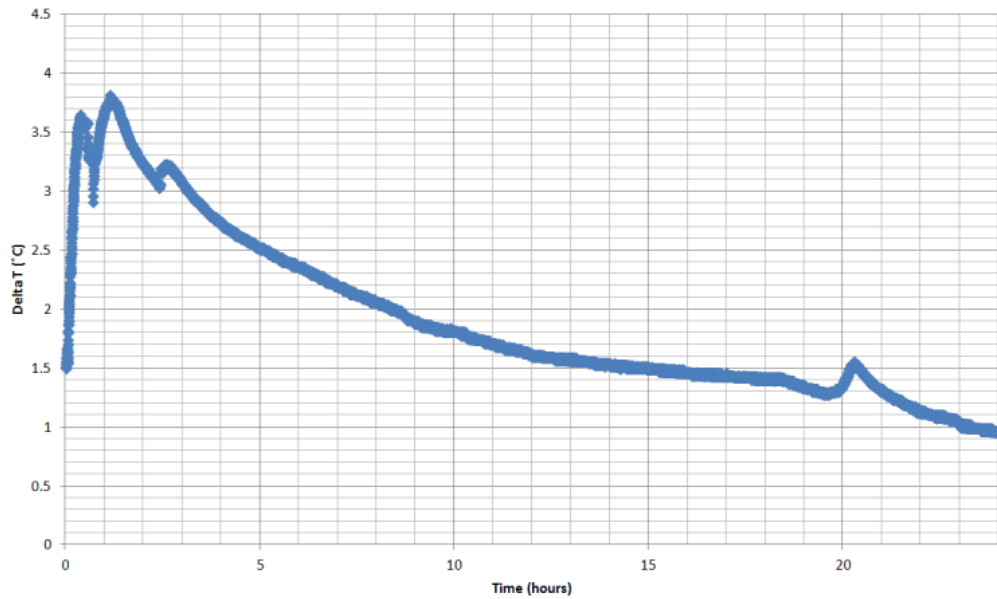


Figure 5-5 Delta T vs. time for the hydration of MgSO₄

Even though the material was essentially a fluidised bed when being hydrated the MgSO₄.xH₂O still agglomerated and became very hard. This agglomeration resulted in further permeability issues and the flow rate through the bed decreased with time over the hydration period. The peak at around 20h seen on Figure 5-5 was due to the pressure being turned up to 20psig which was needed to achieve a flow rate of 5 L/min at this stage in the hydration. This suggests that the material had not completely hydrated but the vapour transportation became so poor the MgSO₄.xH₂O hydrated slowly. Another explanation was the agglomeration of the MgSO₄ encapsulated the dehydrated MgSO₄ stopping the humid air from coming into contact with the dehydrated MgSO₄ reducing the material available for hydration.

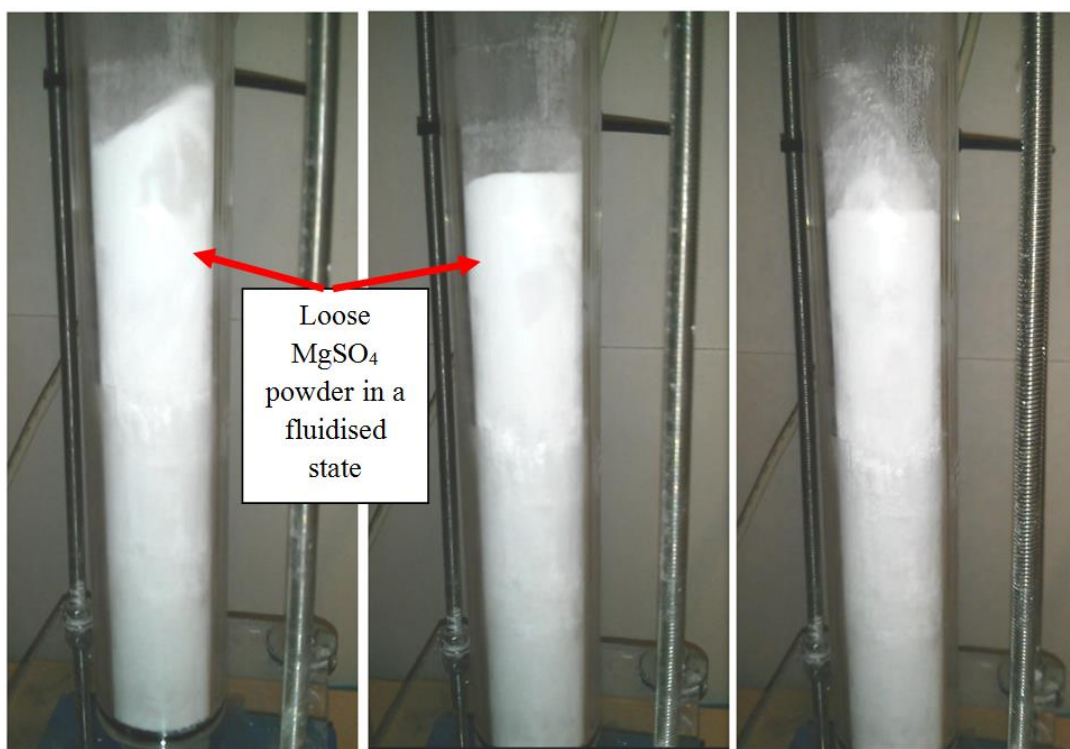


Figure 5-6 Stills from a video of MgSO₄ hydration showing the fluidisation effect caused.

After the MgSO₄.xH₂O hydration the powder was very hard and difficult to remove from the chamber.

5.2.3 Zeolite permeability issues

Zeolite-Y powder was used in the plunger reactor also. The zeolite was first dehydrated to 150°C the same as the MgSO₄. Once dehydrated it was transferred into the plunger reactor where the 100g of zeolite required 410mm of height in the chamber (i.e. a bulk density of 345kg/m³).

Although the zeolite did not agglomerate while being dehydrated or hydrated the material had very poor permeability which was lower than the permeability for the MgSO₄ powder. The zeolite was considered for use due to its large surface area however, the zeolite was sourced as a very fine powder and packed very tightly in the hydration chamber. This packing formed an almost impenetrable seal for the air. When the hydration began the zeolite powder was forced upward within the reactor and the air failed to leave the reactor, hence the permeability could not be assessed. This caused a pressure build up in the hydration chamber.

5.3 Initial investigations into sample preparation methodologies

It was established from the initial testing (section 5.2) of the MgSO_4 and the zeolite-Y that the MgSO_4 and zeolite-Y in a powder cannot or should not be used in reactors due to poor permeability of both materials and agglomeration and hardening of the MgSO_4 . For this reason investigations into potential sample preparation methods which could be used to reduce the negative properties of the zeolite and MgSO_4 , but take advantage of the high energy density of the MgSO_4 , were carried out.

After preliminary research many different ways to create shaped particles from powder materials presented themselves as potential preparation methods to be used for MgSO_4 and zeolite-Y powder. Several methods are described below and their suitability for further research has been commented on. Each of the methods preliminary results has also been presented below.

5.3.1 Investigation into the potential of using a pelletizing disc for TCES sample preparation

Using a pelletizing disc involves adding powder to a revolving disc held at an angle of around 43° . As the disc spins the powder is carried up the outside of the disc by frictional and centrifugal forces. Then depending on the angle and disc RPM the powder rolls back down the disc closer to the centre at the bottom. Once at the bottom the powder is again carried back up the outside of the disc and this process repeats. To get the powder to form into beads a fine mist of water is added. This mist of water allows multiple powder particles to stick together (agglomerate) due to the surface tension of the water. As the particles move up and down the disc they roll over each other and the beads collect more particles and grow in size.

For these preliminary experiments a rig was constructed utilising a 40cm diameter disc. This disc was attached to a motor which spun the disc from the centre. The motor was held in place with a clamp stand which allowed the angle of the disc to be altered.

Figure 5-7 shows two images of material in the pelletizing disc, the motion of the particles are seen in these images. The particles were sent up the disc on the outside and then due to gravitational forces fell back down the pan closer to the centre. This motion of the particles was the correct motion to allow the particles to roll over each other and agglomerate.



Figure 5-7 Image of material in pelletizing disc showing the anticlockwise agglomerating motion of particles into beads

Figure 5-8 shows the pellets created with the pelletizing disc. The size of pellets created using this method varied significantly and the only way to ensure all of the pellets created were of a uniform size was to sieve the samples after agglomeration. This means that there would material waste if the pellets were required to be a specific size.

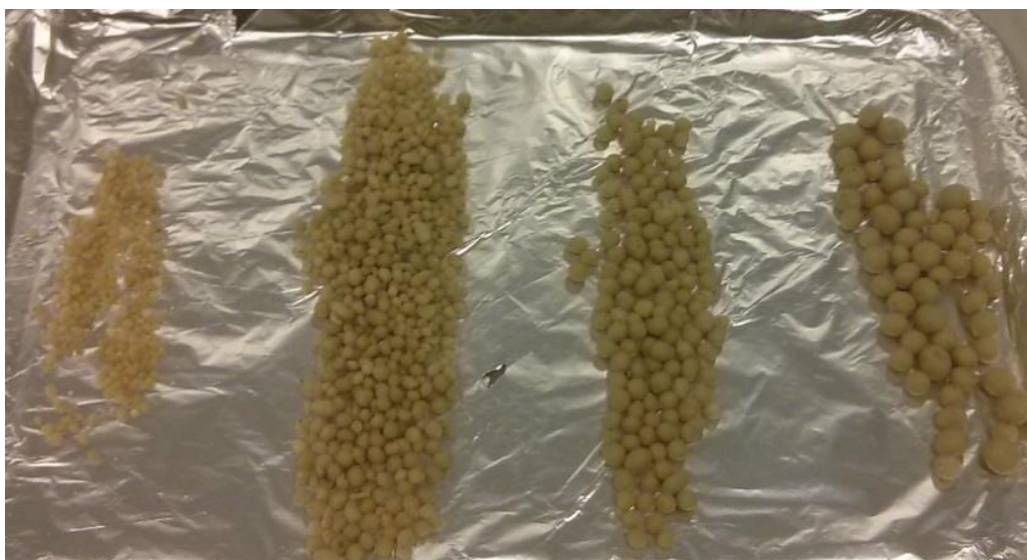


Figure 5-8 Image of pellets created with the pelletizing disc

Figure 5-9 shows beads created using the pelletizing disc after a 3 hour bake in the oven at 150°C. The beads, once baked, became very hollow and almost became shells. This was not ideal as it would result in a lot of wasted space in a reaction chamber and a low density material.



Figure 5-9 Image of beads created with pelletizing disc after an oven bake at 150°C

Due to the time constraints, variation in the size of the beads produced and the poor quality and low density beads produced after the baking process this method was not used for further testing.

5.3.2 Investigation into the potential of hand rolling beads for TCES sample preparation

As the agglomerated beads were shown to be very soft and fragile, which allows them to break down to a powder easily; it was necessary to consider a new way to create the beads. One possible solution was to create a “paste” and then use a rolling tray to roll the paste into beads. The beads created using this method, as they are formed using more force than the beads created using the pelletizing disc, may be denser and be a better method for creating the beads.

This process used a sausage gun to compress the paste and extrude it in the desired diameters as a “sausage” of paste. This sausage was then rolled using a rolling table. The rolling table and sausage gun used is shown below.



Figure 5-10 Image of sausage rolling table (left) and sausage gun (right)

To test if this technique was a possibility a small batch (~10g) of $\text{MgSO}_4 + \text{KU20}$ (50wt%) paste was created, hand rolled into beads and then baked. It was possible to create a “paste” from this composite material. The paste was hand rolled into beads and then dehydrated. The initial results were very promising. However, the paste was too dense to be used in a sausage gun and blocked the gun. Furthermore, trying to use the rolling table with a rolled sausage did not work as the material stuck to the rolling table. For this reason this preparation method was not taken any further.

5.3.3 Investigation into the potential of using a pellet press for TCES sample preparation

For the next preparation methodology tested a modified aluminium meat grinder was used to form pellets from a paste. Paste of the TCES composite material was passed through the meat grinder. At the end of the grinder the standard plate was replaced with one which had ~50 x 4mm holes. This method created consistent pellets which were fairly strong and did not break down, like the agglomeration pellets, once baked. This was the method which was chosen for creating composite pellets for the rest of this chapter.

To optimise the methodology for creating the pellets using the pellet press several experiments were carried out. The composite material which was chosen to be used was 50wt% MgSO₄ and 50wt% binder material (KU20). This composition was chosen as it had been shown from smaller scale tests that it created robust pellets and also this material contains the binder and MgSO₄ which would both be used in the final composite material choice.

The pellet preparation optimisation experiments which were carried out considered the heating rate used to dehydrate the pellets after they had been formed and also the methodology used to create the pellets (i.e. mixture or impregnation). The samples created were named as followed Mix 1, Mix 5, Impreg 1 and Impreg 5 which are pellets formed using a mixture method and dehydrated at 1°C/min or 5°C/min and pellets created using an impregnation method and dehydrated at 1°C/min or 5°C/min, respectively. The impregnation and mixture methodologies used are briefly described below.

Mixture methodology

- Dry Products (MgSO₄.7H₂O and KU20) ground into a powder and mixed.
- DI water added to the ground powder to form a paste.
- Paste formed into 4mm pellets using the modified pellet press.
- 4mm pellets were baked to 150°C using the appropriate (dependant on the sample required) heating rate.

Impregnation methodology

- KU20 ground into a powder and dried to 150°C within an oven.
- DI water added to $\text{MgSO}_4 \cdot 7\text{H}_2\text{O}$ to form an aqueous solution.
- MgSO_4 aqueous solution added to the dry KU20 powder and mixed.
- Mixed solution baked to 150°C using the appropriate (dependant on the sample required) heating rate.
- Oven dried material re-ground into a fine powder.
- DI water added to the fine powder to form a paste.
- Paste formed into 4mm pellets using the modified pellet press.
- 4mm pellets were baked to 150°C using the appropriate (dependant on the sample required) heating rate.

As can be seen from the two different preparation methodologies above the impregnation method had many more steps and was a more time consuming method. The amount of time required for each method would need to be taken into consideration when selecting which method is preferred. The time for each method was not considered in this research and only the TCES properties of the materials were considered.

Once created the different pellets samples were then tested in the DSC, SEM+EDX and characterised using nitrogen sorption analysis.

The reason these two different preparation variables (dehydration heating rate and impregnation or mixture) were chosen was because the changing initial dehydration heating rate should change the pore characteristics (i.e. pore size and volume) and the mixture (Mix) or impregnation (Impreg) variables may change where the majority of the MgSO_4 was located. It was postulated that more of the MgSO_4 would be located within the pores of the host material when using the impregnation method than when using the mix method.

However, if there was no energy density difference between the Mix and Impreg samples it will be beneficial to use the Mix method as this required less preparation steps.

5.3.3.1 SEM analysis of pellets created with different preparation methods

To visually analyse each of the pellets prepared with the different preparation methods an SEM analysis was conducted. If any changes had occurred due to the preparation method used (Impreg or Mix) or due to the initial dehydration temperature used (1 or 5°C/min) the SEM analysis would allow for visual confirmation.

5.3.3.1.1 SEM analysis of the mix 1°C/min pellets

All of the various locations imaged show a densely packed structure. There appeared to be limited vapour channels or high levels of porosity. On most, if not all of the images, there was the presence of dolomite. These results were expected as a higher heating rate should have caused a higher porosity.

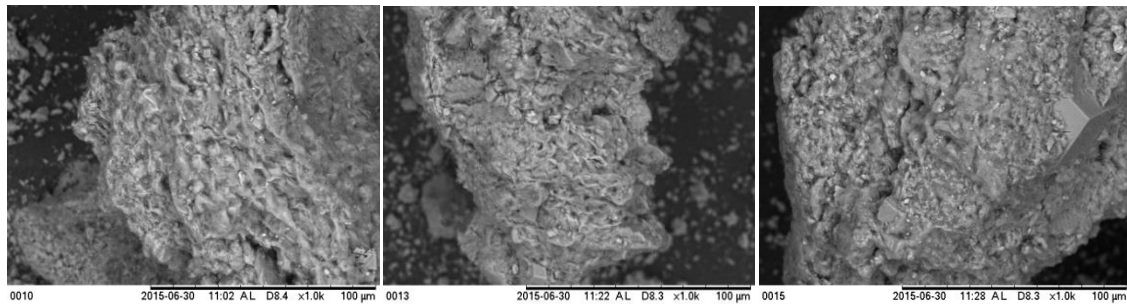


Figure 5-11 Three SEM images of the mix 1°C/min pellets

5.3.3.1.2 SEM analysis of the mix 5°C/min pellets

Locations appeared much less “fluffy” relative to the 1°C/min samples. Locations appeared to be much more cracked with small fractures. Locations appeared to have a rougher surface with possibly a high surface area.

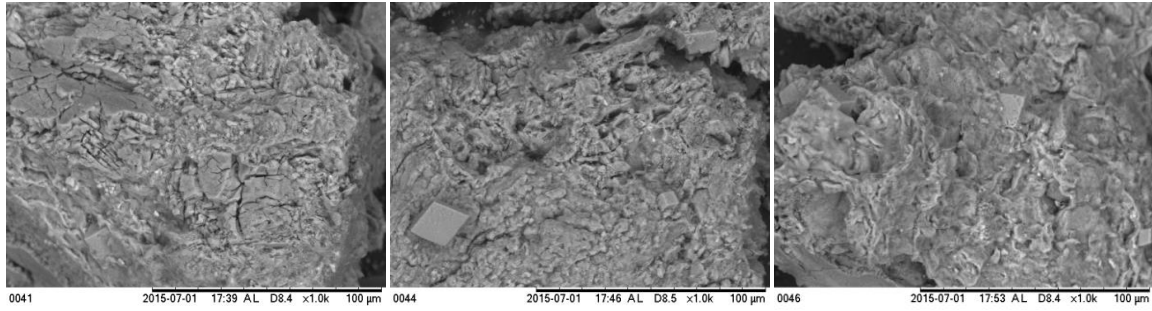


Figure 5-12 Three SEM images of the mix 5°C/min pellets

5.3.3.1.3 SEM analysis of the impregnation 1°C/min pellets

This sample appeared to have an abundant amount of dolomite. The surface structure appeared to change with location from very uneven to relatively smooth. However, in all of the locations there was a presence of large cracks/voids/tunnels this was something which was not present in the mixture samples.

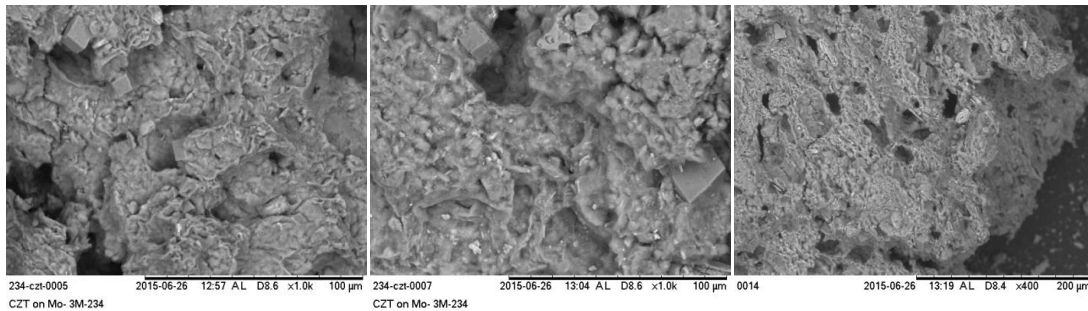


Figure 5-13 Three SEM images of the impreg 1°C/min pellets

5.3.3.1.4 SEM analysis of the impregnation 5°C/min pellets

This sample had the largest amount of voids/tunnels. The surface changed slightly with each location however, the rough very uneven surface was the most common. The “fluffy” surface appeared to be gone.

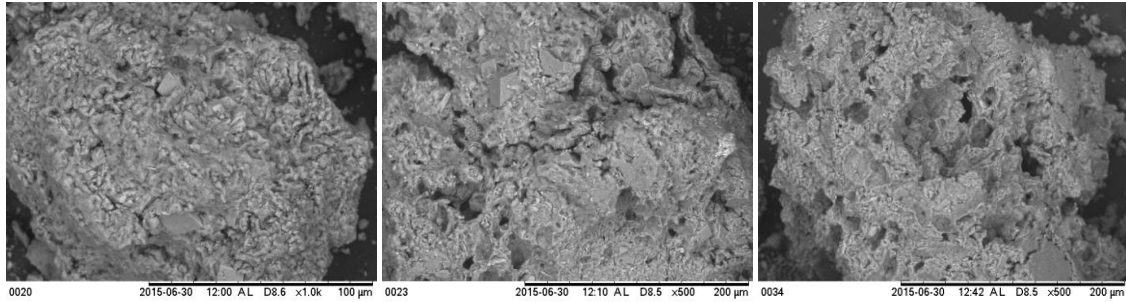


Figure 5-14 Three SEM images of the impreg 5°C/min pellets

5.3.3.1.5 *Conclusions from the SEM images of the pellets prepared with the pellet press methodology*

From assessing each of the images the higher heating rate removes of the “fluffy” sample surface seen in the 1°C/min samples which was changed to an almost “creased” looking surface with cracks. It was unclear if this will be beneficial or detrimental to the surface area.

The different sample preparation method used (mix of impregnation) did appear to cause a difference. Each of the impregnation samples showed signs of deep “tunnels” or voids in more than one location. This would be beneficial for creating vapour channels through to the centre of the sample. Furthermore, the 5°C/min impregnation sample appeared to have the most signs of voids and tunnels. From the SEM findings it was predicted that the 5°C/min impregnation samples would have the highest porosity.

5.3.3.2 *EDX composition analysis of the pellets prepared with the pellet press methodology*

Figure 5-15 shows the average composition for each of the samples tested. Only the elements which were most abundant and expected are shown in Figure 5-15. There did not appear to be any trend in the data which suggested that each of the pellets compositions tested was similar.

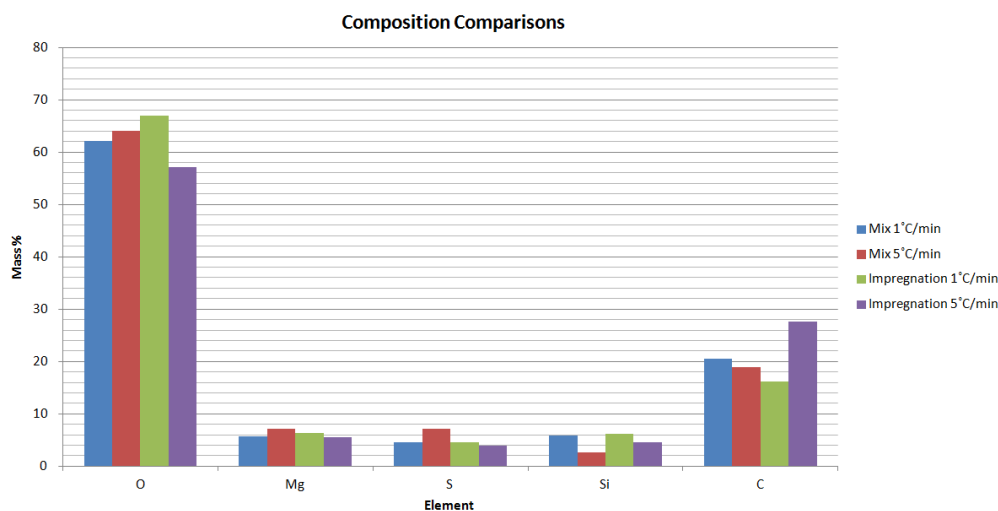


Figure 5-15 EDX elemental data for each of the different sample preparation methods

5.3.3.3 Nitrogen vapour sorption test results of the pellets prepared with the pellet press methodology

To characterise the surface area, pore volume and pore diameter of the different preparation methods a nitrogen sorption analysis was conducted. The data from these tests allowed for a quantitative comparison of the different materials physical characteristics and also the potential corroborate the SEM analysis.

Figure 5-16 shows the cumulative pore volume for each of the preparation methods. It appeared that the increased heating rate (i.e. 5°C/min) increased the pore volume, as expected. This was due to the increased rate of initial dehydration which forces larger pores in the material as the water was driven off. However, the change in the pore volume between the impregnation samples was much less relative to the change in the mix samples. The Mix 5°C/min sample had the highest overall pore volume.

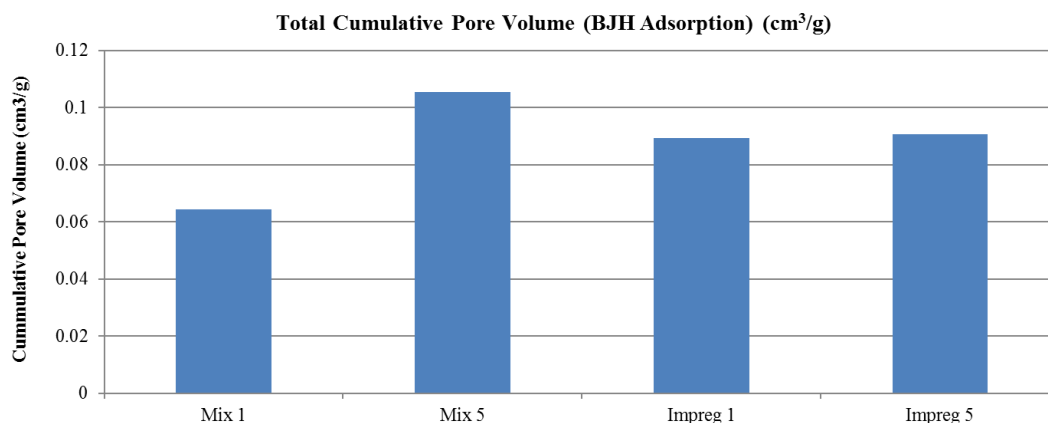


Figure 5-16 Total cumulative pore volume for each of the different preparation methods

Figure 5-17 shows the average pore size for each sample increased with increasing initial dehydration heating rate. Both the Mix and Impregnation 5°C/min samples had very similar average pore size. Regarding the BET surface area this was slightly inconclusive. It was expected as the heating rate was increased so too would the surface area however, the Impregnation 5°C/min sample had a lower surface area than the impregnation 1°C/min sample.

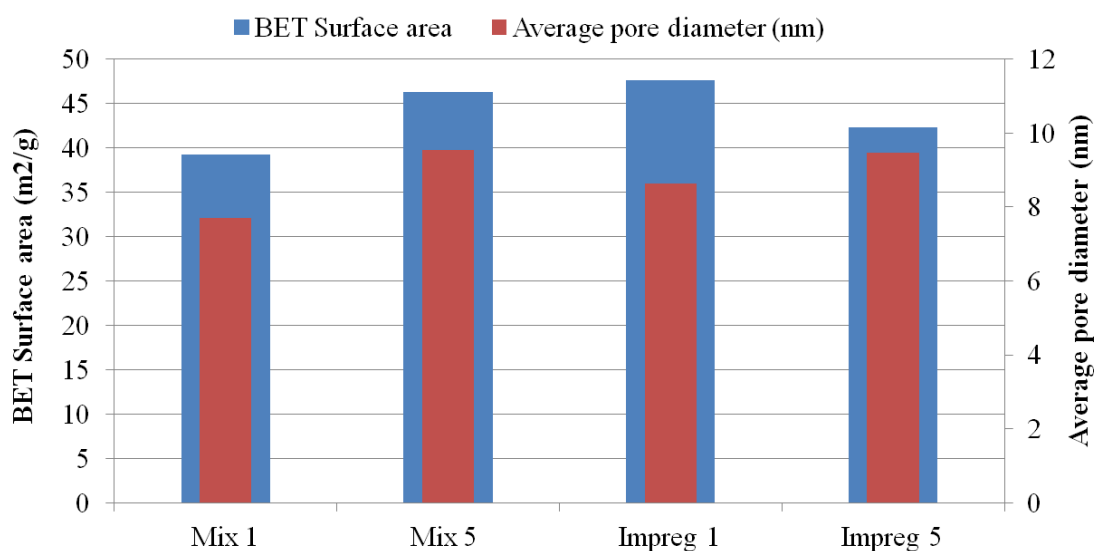


Figure 5-17 BET surface area and average pore diameter for each of the different preparation methods

Taking all of the vapour sorption data into consideration it appeared, assuming the energy density was unaffected; that the 5°C/min Mix preparation method had the most promising properties with the largest pore volume and also the largest average pore diameter. Although,

the BET surface area was slightly lower than the Impreg 1 sample the two former characteristics were assumed to outweigh the slight surface area reduction. This data suggested that the sample preparation method did have an impact of the characteristics of the material.

5.3.3.4 200g enthalpy results and 10mg DSC analysis results for the different pellets created

This section of work presents the 200g hydration enthalpy results and the DSC dehydration enthalpy results to compare how the samples reacted at different scales.

The four differently prepared composite pellets were put through DSC dehydration cycle tests. The samples were first hydrated and then dehydrated to 150°C within the DSC. The DSC tests were conducted to evaluate the dehydration enthalpy of the materials and verify if the preparation method had an impact on the energy storage characteristics.

In order to compare each of the preparation methods (Mix 1, Mix 5, Impreg 1 and Impreg 5) two samples of each preparation method were prepared for DSC testing. All 8 of the samples were then hydrated together and then dehydrated within the DSC. Once all were dehydrated this process was repeated and the 8 samples were put through another hydration followed by another DSC dehydration. The DSC dehydration results for each preparation method were then averaged.

The DSC analysis conducted on each of the samples was the standard DSC enthalpy analysis used throughout this research. The samples were first hydrated with an air stream with 1.3kPa of p_{H₂O} (56%RH at 20°C). The samples were then dehydrated from 20°C to 150°C with a heating rate of 5°C/min. The samples were then cooled back to 20°C. This dehydration followed by a cooling step was then repeated again. This allowed for measurement of the total enthalpy required to dehydrate the sample, the dehydration enthalpy (enthalpy required for the dehydration process) and the sensible enthalpy component (the enthalpy required to heat the sample in a hydrated state to, in this case 150°C, not taking into account the enthalpy required for the dehydration process).

Figure 5-18 shows the dehydration enthalpy of each of the different sample preparation methods. Also shown on Figure 5-18 is the performance ratio. The performance ratio is the ratio of energy which is output from the material compared to the energy input. The performance ratio in turn allows for deduction of the wasted energy. The samples with the

highest performance ratio were both of the samples which were initially dehydrated with a heating rate of 1°C/min. The difference between Mix 1 and Impreg 1 was 41 J/g. Interestingly the Mix 5 and Impreg 5 samples had an average difference of 6 J/g. The performance ratio of these samples followed the same trend as the dehydration enthalpy. Mix 1 had the higher performance ratio followed closely by Impreg 1 then Mix 5 and Impreg 5 were very similar and within 3% of each other. Hence, it appeared the sample preparation change which had the biggest impact on the dehydration enthalpy and performance of the samples was the initial dehydration temperature and not the preparation method (i.e. mix or impregnation).

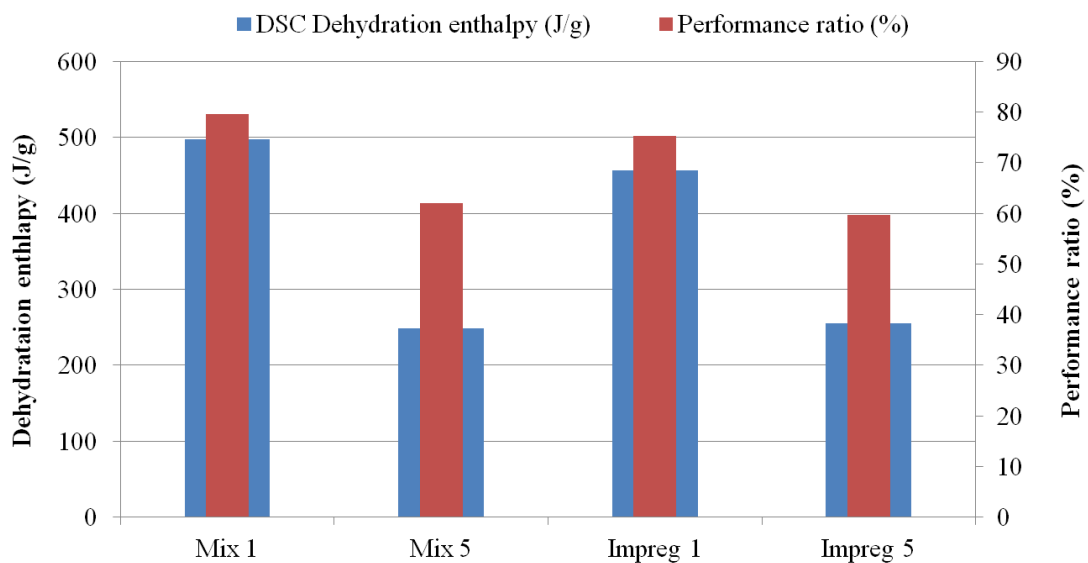


Figure 5-18 DSC dehydration enthalpy and performance ratio for each sample preparation method

Figure 5-19 shows the dehydration enthalpy of each prepared pellet overlaid with the average pore diameter of each prepared pellet. As the dehydration enthalpy increased the average pore diameter decreased. The pore diameter will have an impact on the rate of hydration and dehydration as it will change the vapour transportation throughout the material.

A paper authored by Linnow et al. [131] investigated the hydration of $MgSO_4$ in porous glass with different pore sizes. This paper reported that with increasing pore size a higher RH% is required to hydrate the $MgSO_4$ to the same level as a smaller pore size. The difference in pore sizes tested varied from 7nm to 1700nm which is a large range and the difference in the pore size of the samples tested in this research is between 7.7 and 9.5nm so the difference in the hydration level would likely be small. However, this work could explain

the reason for the higher dehydration enthalpy and higher hydration enthalpy outputs from the 1°C/min samples as they had the smallest average pore diameter.

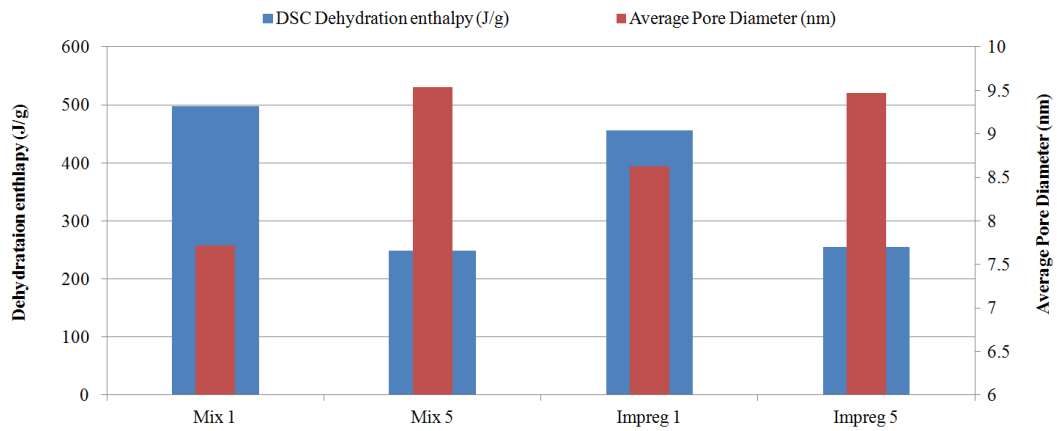


Figure 5-19 DSC dehydration enthalpy and average pore size for each sample preparation method

Figure 5-20 shows the dehydration enthalpy from the DSC tests overlaid with the hydration energy output from the 200g test results. The dehydration enthalpy and hydration enthalpy should in theory be the same value. This means that any difference in the DSC dehydration enthalpy and the 200g hydration enthalpy can be attributed to scaling losses (the percentage of energy lost between the DSC dehydration enthalpy and the 200g hydration enthalpy results) in the samples. The results from the 200g tests do show a similar trend to the DSC dehydration results as Mix 1 and Impreg 1 had the highest hydration energy output. However, the Impreg 1 had the highest 200g enthalpy output followed by Mix 1, Mix 5 and finally Impreg 5.

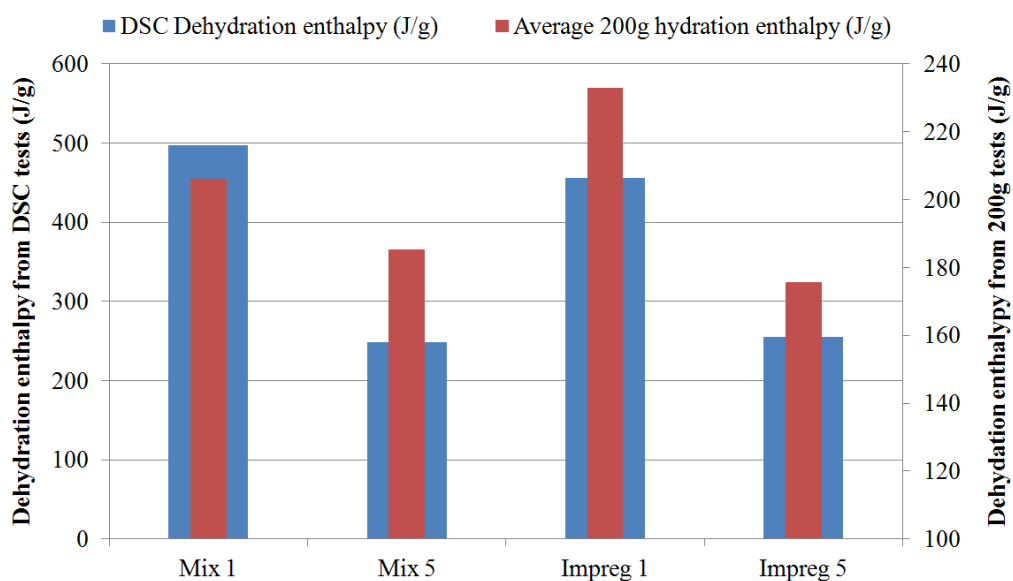


Figure 5-20 DSC dehydration enthalpy and 200g hydration enthalpy for each sample preparation method

The 200g hydration results were significantly lower than the DSC dehydration enthalpy results. Figure 5-21 shows the DSC dehydration enthalpy overlaid with the scaling losses of each sample. The scaling losses for the Mix 1 and Impreg 1 samples were much higher than the Mix 5 and Impreg 5 samples. The reason for this was believed to be because the 5°C/min samples had a larger average pore diameter (see Figure 5-19) which reduced the amount of vapour channels in the pellets which were blocked by either the binder or the MgSO₄. This was not seen in the DSC samples as the tests were conducted with a significantly smaller sample size (10mg) not the whole pellets which were used in the 200g testing. The blocking of pores and the reduction of vapour transportation in larger scale experiments is what drives the scaling losses. The material still has the same theoretical potential which is shown in smaller size experiment's, for example DSC tests however, the same energy output is not achieved under the same conditions due to the pore blocking and reduction in vapour transportation which stops some parts of the absorbent material from being hydrated and releasing hydration energy.

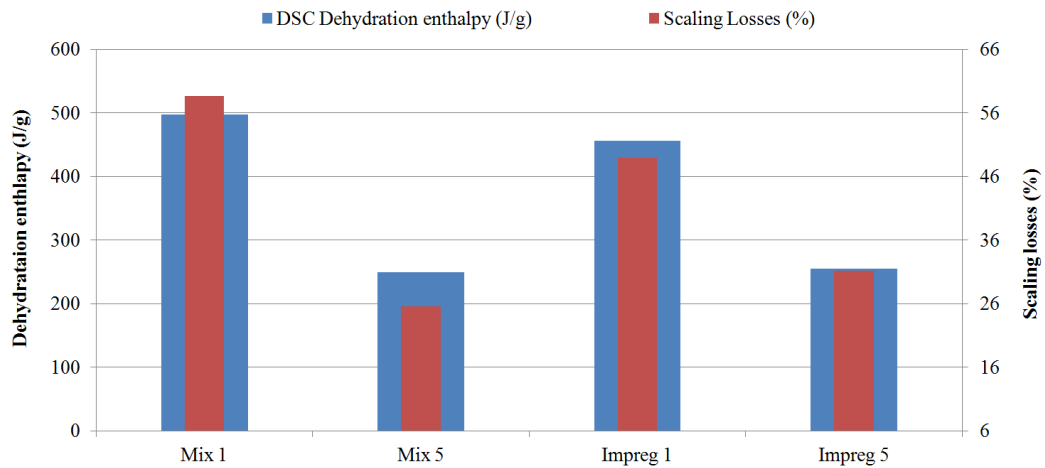


Figure 5-21 DSC dehydration enthalpy and scaling losses for each sample preparation method

Although the Mix 1 and Impreg 1 had the highest scaling losses they still output the highest hydration enthalpy. To calculate the energy density, a very important characteristic for domestic interseasonal heat storage as space is a constraint, the bulk density of each of the samples was measured. Figure 5-22 shows the 200g hydration enthalpy output overlaid with the energy density of the samples. The energy density was calculated using the 200g hydration enthalpy data not the DSC dehydration enthalpy as this gave an energy density value which the materials were expected to achieve when used at a large scale.

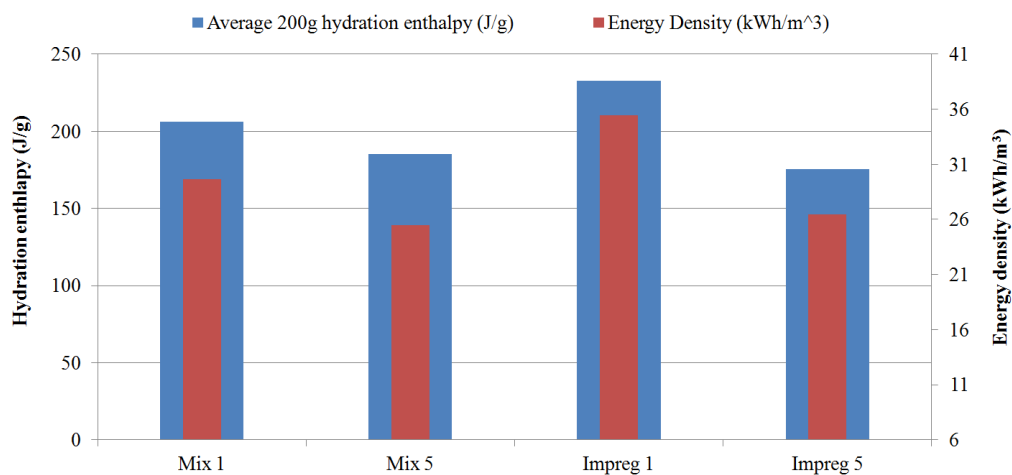


Figure 5-22 200g hydration enthalpy and energy density for each sample preparation method

Throughout this chapter the experiments were conducted with an average air water partial vapour pressure of 1.3kPa which equates to (56%RH at 20°C). If this value could be increased to 68%RH at 20°C then the hydration enthalpy (energy output) would increase and result in the energy density of the sample effectively increasing. If a higher water partial

vapour pressure was to be used it is likely a separate water tank would be required in the system to increase the humidity of the ambient air. This obviously would increase the size of a system and therefore reduce the effective energy density of the system. However, if the material used can now output more energy but requires a water tank the amount of energy which is able to be stored in the system may still be higher than that of a system which only hydrates the material to a lower, for example 1.3kPa of air water partial vapour pressure.

5.4 Conclusions of chapter 5

The Impreg 1 sample had the highest 200g hydration energy output and also the largest bulk density which resulted in the Impreg 1 having the highest energy density. The Mix 1 sample had the highest performance ratio. The best sample to use at a larger scale would depend on the cost of the volume in the household, where the system is being installed and the cost of energy for that household. If the space of the household is at a very high premium then it is likely that the Impreg 1 material would be chosen. However, if the system was to be placed in an area with plenty of space (i.e. under a back garden) then it is likely that the best material to choose would be the one that has the highest conversion of input energy to output energy (i.e. Mix 1). The decision would also depend on the cost of the preparation method which will ultimately change the cost of the material. These materials all had the same composition and hence the cost of the materials would be the same however, the Impreg samples had a preparation method which required more steps, which would likely mean the cost of using the Impreg samples would be higher.

There are many different variables which need to be considered and adapted to best fit the needs of each user when planning on installing an interseasonal TCES system such as cost of space in the domestic environment.

6 Chapter 6 - Investigation into potential host materials for impregnating with MgSO₄

6.1 Introduction to chapter 6

The research presented in this chapter considers potential host materials for MgSO₄. However, the purpose was to consider potential host materials which can be readily purchased in a pellet or bead form. This was important as it enables the possibility of impregnating MgSO₄ into the host matrix and the material to be used on a large scale without the time constraints of producing the materials using the novel pellet preparation method.

Composite materials have been studied for their property to increase the energy density of porous absorbent materials with the addition of salt hydrates [48,81,82]. The methodology used for adding the salt hydrates into the porous hosts is typically the wetness impregnation method [48,81,82].

Another method used to improve the energy density of absorbent materials is through an ion exchange process. Absorbent materials, particular zeolites can be put through an ion exchange process to replace the current ions with other ions having higher selectivity to the material. The hydration energy of zeolites depends on the amount of cations which are accessible to the adsorbed material which, for domestic TCES, is commonly water [87]. Molecular sieves adsorption properties, crystal cage and hydration can be altered by ion exchange [90]. Research has shown that ion exchange changes the water uptake of zeolites [91].

The materials considered in this chapter were 13x molecular sieve pellets (a zeolite material), activated alumina beads and activated carbon pellets. The 13x molecular sieve powder and zeolite-Y powder was also used to create composite pellets using the pellet preparation method for comparison purposes. Finally the 13x pellets were also put through an ion exchange process to assess how this changed their TCES properties.

The objective of this chapter was to understand the performance of 13x molecular sieves, activated alumina and activated carbon for domestic TCES after MgSO₄ impregnation. The research presented in this chapter also investigated MgSO₄ which was impregnated within different absorbent materials (13x molecular sieve and zeolite-Y), using the novel pellet

preparation method, for comparison. When impregnated with MgSO_4 the energy storage density of these materials should have increased.

The effect of Mg^{2+} ion exchange with Na^+ ions within the 13x crystal lattice was also investigated. The ion exchange enhancement was shown to provide an improvement to the energy output of the 13x molecular sieves. This chapter reports the methods used to create the composite materials and the effect that it has on the thermochemical properties of the materials.

The pellets formed using the novel pellet preparation method are referred to as 13xMK. This methodology was also used to create the zeolite-Y pellets from powder and this material is referred to as ZMK. The 13x pellets which were prepared using the ion exchange methodology are referred to as 13x Mg Ion zh, where z is the ion exchange time period length in hours. The activated alumina and activated carbon materials are referred to as AA+ MgSO_4 and AC+ MgSO_4 , respectively. The activated alumina and activated carbon samples were impregnated with the maximum amount of MgSO_4 which was possible after one wetness impregnation method using a saturated MgSO_4 solution and subsequently dried to 150°C to remove excess water.

6.2 13x pellet investigation results

The first part of this chapter focuses on the results from the 13x material. It compares the 13x pellets and powders against the zeolite-Y powder used previously in this thesis. Next the 13x pellets are impregnated with MgSO_4 using the wetness impregnation method. 13x powder and MgSO_4 were formed into pellets using the pellet preparation method and the results of both 13x pellets were compared. This section also discusses the 200g hydration and dehydration results of the 13x + MgSO_4 composite materials. Finally the 13x pellets were put through an ion exchange under different conditions.

6.2.1 Comparison of 13x powder, 13x pellets and zeolite-Y powder absorbents

Initial experimental tests assessed the dehydration heat flow and energy storage characteristics of the 13x powder, 13x pellets and zeolite-Y powder with the DSC plots presented in Figure 6-1. The endothermic heat flow was due to the enthalpy required for dehydration (water loss) and the sensible heat required for heating the samples up to 150°C . Sigmoidal integration of the DSC measurements was used to estimate the average total

enthalpies reported in Table 6-1. It was clear that zeolite-Y had the highest dehydration enthalpy (total enthalpy minus the sensible heat enthalpy).

Table 6-1 DSC determined averaged enthalpies of absorbent zeolite materials over the temperature range of 20 - 150 °C

	13x pellets	13x powder	Zeolite-Y powder
Dehydration enthalpy + sensible enthalpy (J/g)	626	725	781
Dehydration enthalpy only (J/g)	479	589	615

The lower endothermic heat flow and dehydration enthalpy measured for the 13x pellets compared to the 13x powder was due to the binding material used to bind and hold the powder in pellet form. The binding material reduced the total amount of 13x material per unit weight, available for water sorption.

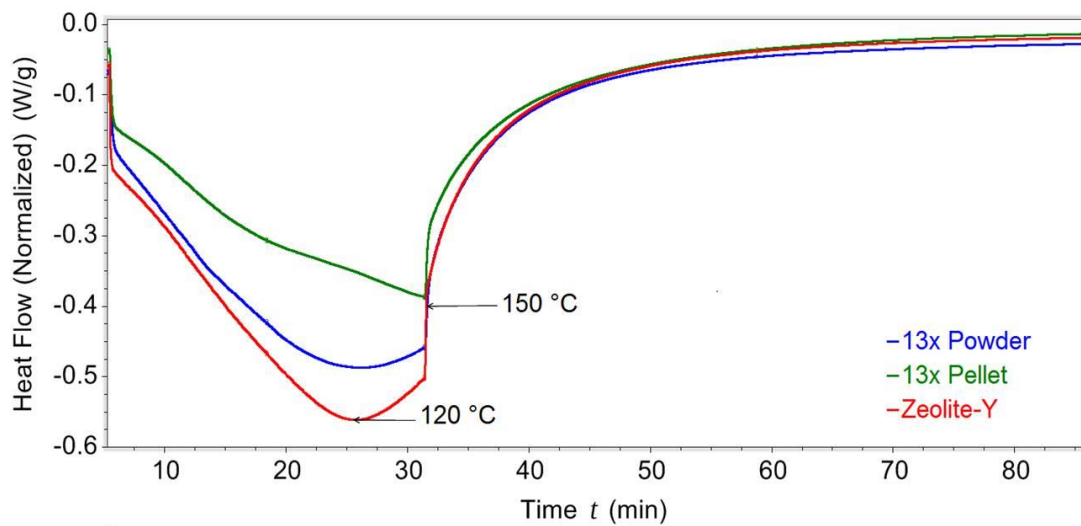


Figure 6-1 DSC dehydration plots of zeolite-Y, 13x powder and 13x pellets showing the dehydration enthalpy and sensible enthalpy.

6.2.2 Comparison of 13x materials with different absorbed quantities of MgSO₄ prepared using the wetness impregnation method

The wt% of MgSO₄ absorbed by 13x pellets was varied using the wetness impregnation method, leading to different dehydration enthalpies. The DSC calculated dehydration enthalpy (first cycle enthalpy minus second cycle enthalpy) measurements and TGA determined mass loss for 13x samples with varying wt% of MgSO₄ are shown in Figure 6-2. It was evident that increasing wt% of MgSO₄ leads to a decrease in dehydration enthalpy. This was corroborated by the TGA mass loss data which also decreased with increasing wt% of MgSO₄.

The predicted enthalpy for each sample is indicated by the green bars in Figure 6-2. The predicted values were calculated based on the DSC determined dehydration enthalpies for both pure MgSO₄·7H₂O and 13x pellets. MgSO₄·7H₂O had a dehydration enthalpy of 1118J/g when dehydrated with the same temperature program used for the 13x pellets (ramp rate 5°C/min and maximum temperature of 150°C). The dehydration enthalpy of the 13x pellets was determined to be 479J/g. Due to the significantly higher dehydration enthalpy of MgSO₄·7H₂O it was expected that the dehydration enthalpy of the impregnated pellets would increase with increasing wt% of MgSO₄, leading to a more energy dense material with higher dehydration enthalpy. The mass loss (water loss) of the samples with impregnated MgSO₄ did not increase with increasing MgSO₄ content. However, the MgSO₄ and the 13x materials do not hydrate (discharge) and dehydrate (charge) as anticipated when combined in a composite form, as explained in section 6.2.3 of this chapter. Similar research has also reported lower than expected heats of sorption from MgSO₄ impregnated zeolites. [48].

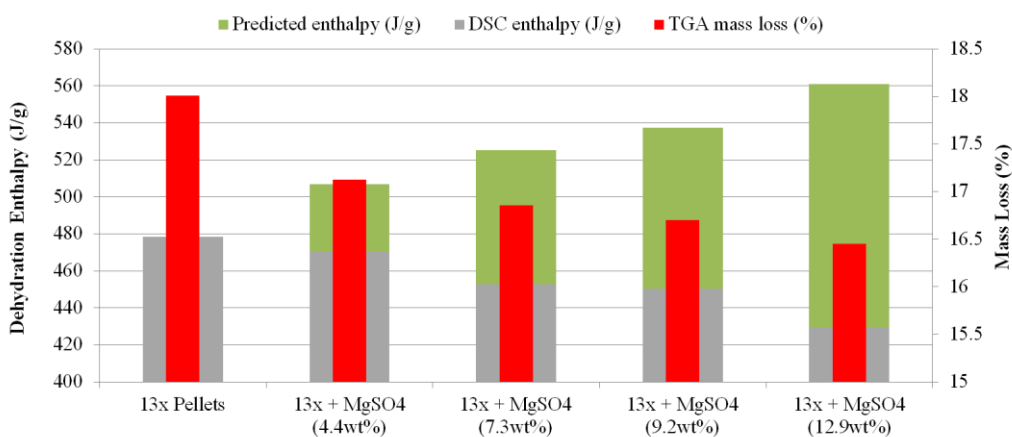


Figure 6-2 Graph showing average dehydration enthalpy, mass loss and predicted dehydration enthalpy for 13x samples with different wt% of MgSO₄ created using the wetness impregnation method.

6.2.3 Analysis of DSC plots for composite 13x + MgSO₄ materials to determine cause of lower than expected dehydration enthalpies

Figure 6-3 shows the DSC dehydration plots for each of the composite materials tested after the hydration process. Figure 6-3 shows that the DSC dehydration heat flow plot is significantly different for the ZMK composite material (a composite material consisting of zeolite-Y, MgSO₄ and a binder) when compared to the 13x materials tested and 13xMK (composite material consisting of 13x, MgSO₄ and a binder). Both ZMK and 13xMK were pellets produced in the laboratory, using the pellet preparation method, and were both crushed into a powder for the DSC and TGA tests.

From Figure 6-3 at 73°C the MgSO₄ sample exhibits a strong endothermic peak correlated to a loss of 6 water molecules, which was established from analysis of the DSC and TGA results of MgSO₄·7H₂O dehydration. The dehydration peak is also present (green plot) for the ZMK material. This was the only composite material tested in which the MgSO₄ dehydration was seen. This peak was the reason the ZMK material exhibits an average DSC dehydration enthalpy of (715J/g) and it indicates that the MgSO₄ is rehydrating and subsequently dehydrating within the zeolite material.

To determine if the loss of the MgSO₄ dehydration peak was due to the wetness impregnation method used to create the 13x + MgSO₄(Xwt%) pellets, a sample of 13xMK material was created with the same MgSO₄ content as the 13x+MgSO₄(12.9wt%) sample.

The DSC heat flow plot for this material is presented in Figure 6-3 and appears similar to all of the 13x samples which do not exhibit the MgSO_4 dehydration peak. The average dehydration enthalpy of the 13xMK sample was 487J/g, a similar value to the pure 13x pellet sample, which was 479J/g. This value was significantly higher than the 13x+ MgSO_4 (12.9wt%) sample (433J/g) due to the amount of binder within the pellets. The amount of binder in the 13xMK pellets can be controlled whereas the sourced 13x pellets had a set amount of binder from the manufacturer. The laboratory developed preparation method leads to higher dehydration enthalpy (J/g) than the standard wetness impregnation method. Other characteristics such as hydration enthalpy or hydration rate (power output) could be improved if different preparation methods are utilised.

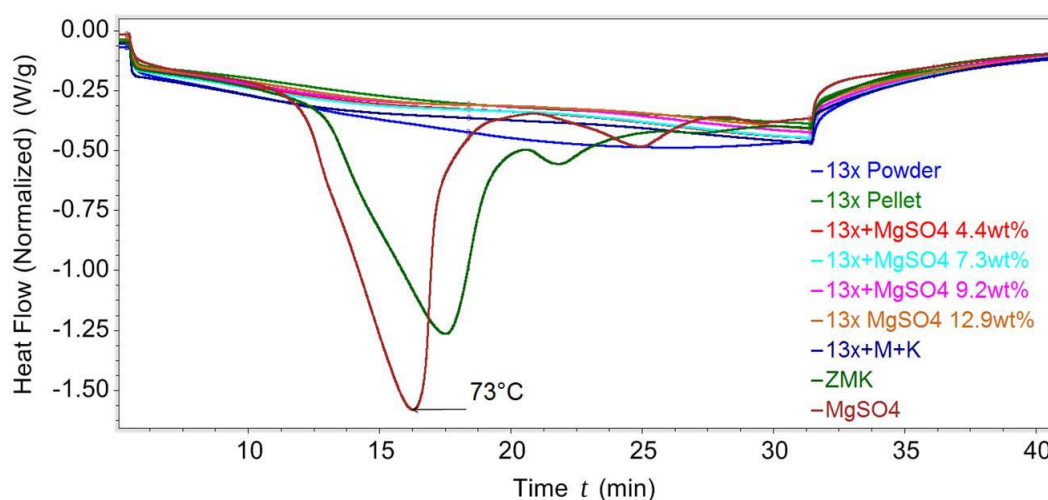


Figure 6-3 DSC plots showing the endothermic dehydration heat flow for 13x samples, ZMK, 13xMK and MgSO_4 .

The absence of the MgSO_4 dehydration peak in the 13x based materials was due to the MgSO_4 which does not hydrate in these samples. Both preparation methods used 13x molecular sieves as a host material and both have an absence of the MgSO_4 dehydration peak. The MgSO_4 dehydration peak was present for the ZMK material suggesting the lack of MgSO_4 dehydration peak was due to the 13x material and to a pore blocking effect which has also been suggested in other work [48]. If MgSO_4 blocks pores in the 13x material it will reduce the available surface area for water adsorption within the 13x material.

When creating the pellets from the powder absorbent material ion exchange can take place between the Mg^{2+} ions in the MgSO_4 solution and the Na^+ ions in the 13x powder. The slurry formed when creating the pellets contains all ions both Mg^{2+} and Na^+ , neither of which

are removed during the process and so will be present in the final produced pellets. This should not prevent the MgSO_4 from recrystallising within the formed pellets, either within the cage structure or on the surface of the 13x material. The ion exchange that occurs is not detrimental to the thermal energy storage potential even if a higher wt% of MgSO_4 is used to create the pellets. Measurements confirm that the ion exchange of Na^+ ions with Mg^{2+} ions actually leads to an increased dehydration enthalpy (see section 6.3).

6.2.4 200g dehydration/hydration cycle testing results of the 13x materials and ZMK

The materials tested on a more practical 200g scale were 13x pellets, 13x+ MgSO_4 (12.9wt%), ZMK and 13xMK. Figure 6-4 presents the hydration results for each 200g experiment. Each material was hydrated and dehydrated for at least 3 times with Figure 6-4 showing the average for each sample. Figure 6-4 shows also the variation of Delta T (between the air inlet and outlet) achieved when hydrating each material with an air flow rate of 10 litres/min of ~56%RH at 20°C after being dehydrated to 150°C using air heated by a hot air gun. The results show that the 13x pellets and the ZMK have the highest hydration enthalpies of 496J/g and 490J/g, respectively. The 13x+ MgSO_4 (12.9wt%) and the 13xMK enthalpies were 407J/g and 385J/g, respectively.

The 13x+ MgSO_4 (12.9wt%) material achieves a higher value of Delta T (i.e. higher peak power output) for the same hydration conditions as the 13x pellets. The DSC data presented in Figure 6-3 shows no sign of the $\text{MgSO}_4 \cdot 6\text{H}_2\text{O}$ dehydration suggesting the MgSO_4 does not produce any heat, indicating that all heat derives from the hydration of the 13x material. The reason for the increased power output of this material relative to the pure 13x pellets will require further investigation. A possible explanation is the dehydration of the 13x+ MgSO_4 (12.9wt%) pellets (formed by immersing 13x pellets in a MgSO_4 solution) within the oven, which drives off all excess water from the solution, results in the recrystallisation of MgSO_4 . This is responsible for cracks and larger vapour channels through the impregnated 13x+ MgSO_4 (12.9wt%) pellets. The larger vapour channels would allow for faster hydration of the 13x material resulting in higher power outputs.

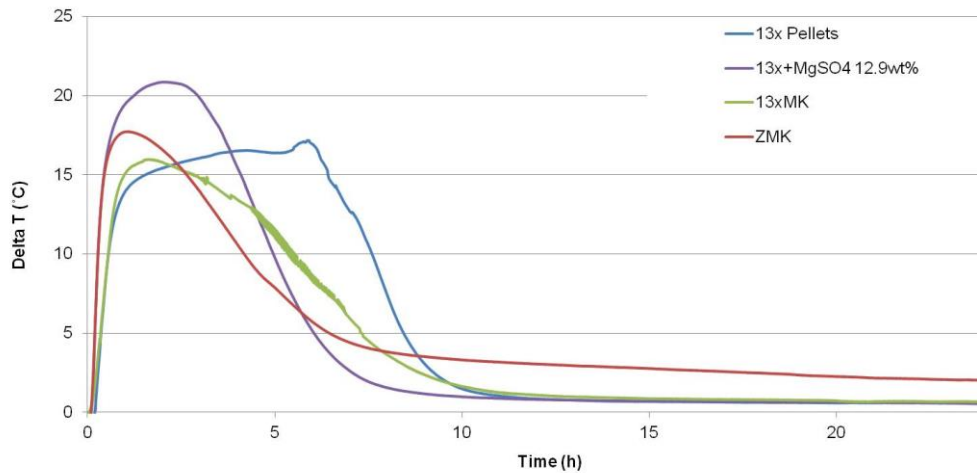


Figure 6-4 200g hydration tests Delta T (outlet air – inlet air temperature) output cycle results for 13x pellets, 13xMK, 13x+MgSO₄(12.9wt%) and ZMK

6.2.5 Comparison of dehydration/hydration cycle results from theory, DSC measurements and 200g sample size measurements

The predicted dehydration enthalpies and the enthalpies measured by DSC and the 200g test equipment are presented in Figure 6-5. The theoretical values are the expected enthalpies for each material, which are calculated using the DSC determined values of each component and their weighted average value. There are two losses in performance calculated: first the percentage of loss between the theoretical values and the measured DSC results and secondly the percentage of loss between the measured DSC and the measured 200g results.

The 13x pellets loss in performance, from the DSC measurements to the 200g results, is negative resulting in negligible performance losses when scaled up to 200g. The two composite materials containing 13x (13x+MgSO₄(12wt%) and 13xMK) suffer reductions in performance from their theoretical values to the DSC measurements. The 13x+MgSO₄(12wt%) suffers a reduction of 6% from the DSC to the 200g measurements, with the 13xMK suffering a reduction of 21%. The laboratory preparation method suffers from a greater loss in performance from DSC to 200g scale compared to the wetness impregnation method.

The ZMK material exhibits no loss in performance from the theoretical to the DSC measurements, from the DSC to 200g measurements the reduction is 31%. The wetness impregnation method suffers from minimal performance losses. The reason for the

performance losses for the wetness impregnation sample (13x+MgSO₄(12.9wt%)) is due to no MgSO₄ hydration in this sample.

The choice of preparation method to achieve the best performance will depend on the amount of binder in the commercially created pellets. The two best candidate materials for testing at a larger scale would be the 13x pellets or the ZMK material as they produce the highest hydration enthalpy. If the laboratory preparation method could be optimised to reduce scaling losses the ZMK material has the potential to achieve much higher hydration heat output increasing by 46%, up to 715 J/g, as achieved in the DSC testing of ZMK.

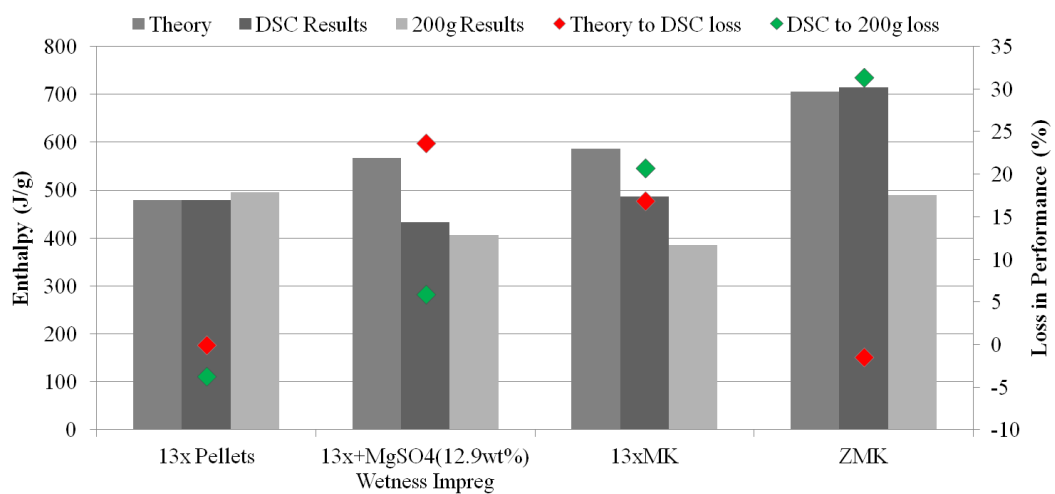


Figure 6-5 Comparison of loss in performance percentage between tested samples at different tested mass.

6.2.6 Theoretical dehydration enthalpy, excluding MgSO₄.xH₂O enthalpy, compared to DSC and 200g sample measured tests

The theoretical dehydration enthalpy for each of the samples tested without the dehydration enthalpy from the MgSO₄.xH₂O has been calculated. Table 6-2 shows the calculated and the experimentally measured values. The calculated theoretical values in Table 6-2 are shown to be within 2% of the measured DSC values for the 13x samples prepared using the wetness impregnation method, suggesting that the dehydration enthalpy from the MgSO₄.xH₂O is not present and the measured dehydration enthalpy is due to the 13x material only. The 13xMK materials percentage difference from the theoretical to the measured DSC value is -10%, which is higher than expected. This is because the 13xMK are produced using the laboratory pellet preparation method which allows the MgSO₄ to

recrystallise within the pellets outside of the 13x lattice. The percentage difference for the ZMK material from theoretical to the measured DSC is -129%, due to the hydration of $MgSO_4$ within the zeolite which has a significant dehydration enthalpy within the ZMK material.

When comparing the theoretical dehydration enthalpy to the 200g sample results the same trend in percentage difference is seen. The percentage difference between the theoretical values and the 200g hydration results are 4%, 13% and -56% for 13x+ $MgSO_4$ (12.9wt %), 13xMK and ZMK, respectively.

Table 6-2 Calculated theoretical dehydration enthalpies for samples, not accounting for the $MgSO_4 \cdot xH_2O$ dehydration enthalpy, compared to the measured DSC and 200g enthalpy results over the temperature range 20-150 °C.

Sample Name	13x pellets	13x + $MgSO_4$ (4.4wt %)	13x + $MgSO_4$ (7.3wt %)	13x + $MgSO_4$ (9.2wt %)	13x+ $MgSO_4$ (12.9wt %) Wetness Impregnation)	13xMK	ZMK
Dehydration enthalpy theory (excluding $MgSO_4$) (J/g)	479	464	450	441	423	442	314
DSC Dehydration enthalpy (J/g)	479	466	445	437	433	487	715
% difference	0%	0%	1%	1%	-2%	-10%	-129%
200g hydration enthalpy (J/g)	496	-	-	-	407	385	490
% difference	-4%	-	-	-	4%	13%	-56%

6.3 13x Mg^{2+} ion exchange pellet testing results

To improve the energy output of the 13x pellets, they were exposed to an ion exchange process where each Mg^{2+} ion replaced two Na^+ ions. Figure 6-6 shows the DSC dehydration enthalpy and TGA mass loss of the 13x Mg ion exchanged pellets and for 13x pellets which have not been put through an ion exchange process. The ion exchanged pellets have a higher dehydration enthalpy and a greater mass loss.

The reason for the increased dehydration enthalpy and the mass loss of the 13x ion exchanged samples is due to the bonding of H_2O to the Mg^{2+} ions within the 13x pellets. Due to the high hydration energy of Mg^{2+} ions the modified 13x pellets have more bonded H_2O

around the Mg^{2+} ion sites and a higher hydration energy [88,94]. Contrastingly the Na^+ ion sites have a lower hydration energy [94]. Other studies have also reported an increase in hydration heat from zeolites after a Mg ion exchange [93,94].

The enthalpy and mass loss for samples prepared for 24, 48 and 72 hours overlaps, with no apparent advantage gained using a 72 hour period for ion exchange compared to a 24 hour period. The 13x pellets have reached their ion exchange capacity, under the exchange conditions used, within 24 hours. The capacity could be increased if the temperature used for the ion exchange process was increased [69]. The increase in mass loss and dehydration enthalpy for the 1 hour ion exchange samples is significantly lower than that of samples prepared with exchange periods of 24, 48 and 72 hours.

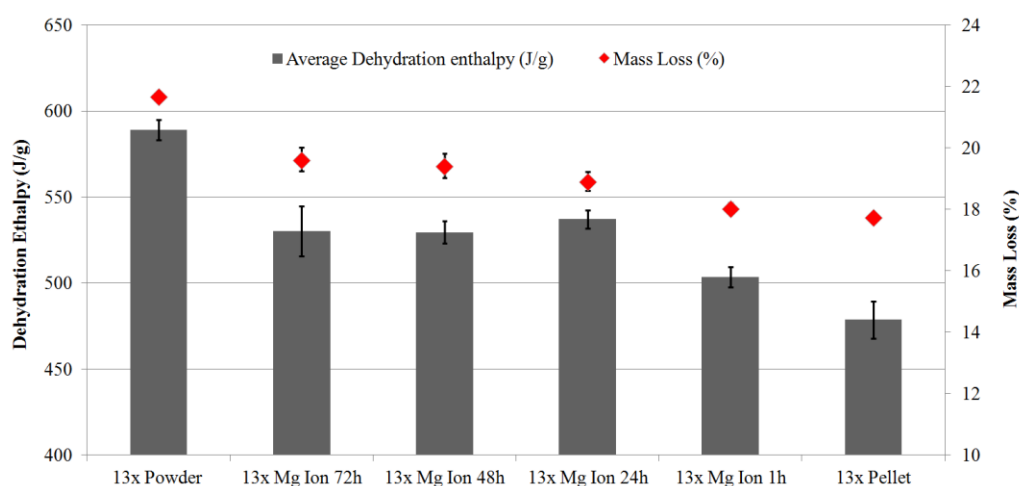


Figure 6-6 DSC dehydration enthalpy and TGA dehydration mass loss results of 13x ion exchanged pellets

Figure 6-7 shows the average sensible enthalpy (J/g) and the performance for each ion exchanged sample. The performance percentage is calculated as the (dehydration enthalpy divided by total enthalpy). The sensible enthalpy is the energy lost prior to the discharge which is due to charging of the material throughout the summer months when there is a small heat load in a domestic environment [18]. The sensible enthalpy for each of the ion exchange samples is 118J/g (+/- 2J/g) and 148J/g for the 13x pellets which have not been put through an ion exchange process.

The performance of each ion exchange sample, neglecting the 1 hour sample, is 81.8% (+/- 0.13%), 5.5% higher than the 13x pellets which have not been put through an ion exchange process. The ion exchanged samples also have a higher performance than the 13x

powder sample. A higher performance is beneficial for materials and will result in higher efficiency if used in a seasonal heat storage system. The increase in performance of the ion exchanged pellets is firstly due to the increased dehydration enthalpy (explained in section 6.3) and also due to a decreased sensible enthalpy.

The performance and the sensible enthalpy for the samples prepared for 24 hours, 48 hours and 72 hours are within 0.13% and 2J/g, respectively which means that the ion exchange reaches its maximum percentage between 1 hour and 24 hours. The quantification of the optimum ion exchange time period will require further investigation.

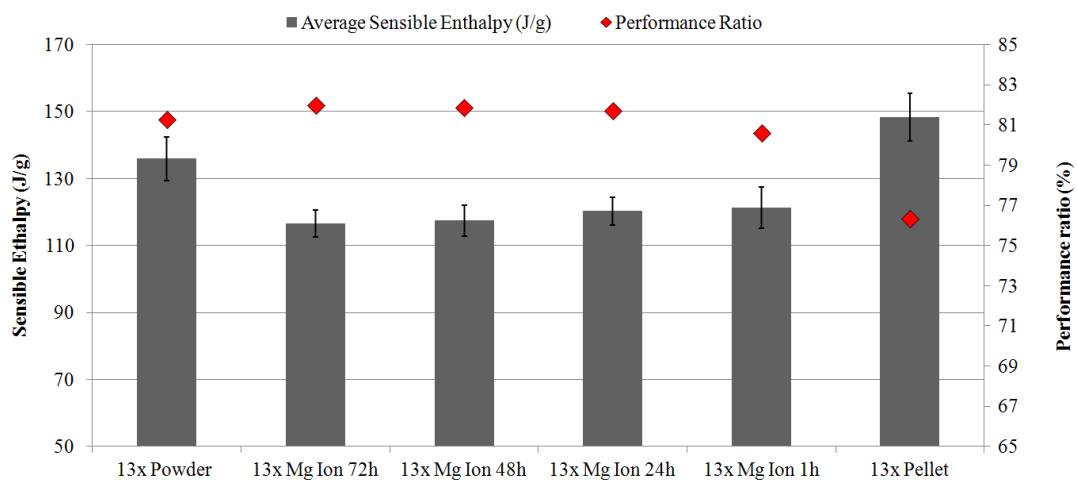


Figure 6-7 Sensible enthalpy and performance (dehydration enthalpy / total enthalpy) of 13x ion exchanged pellets

6.3.1 SEM and EDX analysis of 13x ion exchanged pellets

13x pellets and each ion exchanged sample were analysed using SEM and EDX. To collect the data for the EDX and SEM results presented (Figure 6-8, Figure 6-9 and Figure 6-10) several different samples of each pellet were tested and also data was collected for several locations within each pellet. The EDX composition values obtained were then averaged and normalized for Mg and Na content to determine the changing composition of the pellets. Figure 6-8 shows the EDX determined changing composition of the interior of the 13x pellets before and after different periods of the ion exchange process. After the 24 hour ion exchange process 60% (+/- 4%) of the sodium had been replaced by magnesium. The results show that the ion exchange methodology has successfully replaced Na^+ ions with Mg^{2+} ions within the 13x pellets. Figure 6-8 shows that the Mg^{2+} and Na^+ ion contents of the

24, 48, and 72 hour samples are all within 10% of each other, demonstrating that the ion exchange process is completed in the first 24 hours.

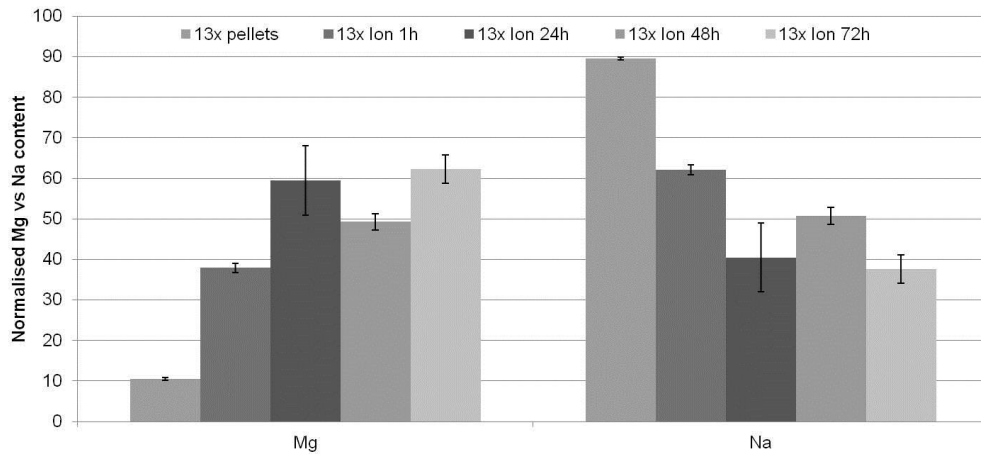


Figure 6-8 EDX analysis of normalised Mg vs Na content of the internal structure of the 13x ion exchanged pellets

Figure 6-9 shows the EDX determined composition values for the external surfaces of the 13x ion exchanged samples. The composition on the external surface is significantly different if compared to the interior of the pellets (presented in Figure 6-8) in terms of Mg versus Na content. The external surfaces of the pellets have a much higher Mg content (average 84%) after the ion exchange process (24 hour, 48 hour and 72 hour samples) compared to the interior (average 57%). The 13x pellets have a much higher ion exchange percentage at the external surface compared to the interior. The internal ion exchange can reach the same percentage as the external surface if a higher temperature is utilised in the ion exchange process (explained in section 6.3). A higher ion exchange percentage in the interior would result in increased hydration heat and performance of the 13x pellets.

A higher ion exchange percentage takes place at the external surface of the pellets because the Mg^{2+} ions can easily exchange with the Na^+ ions. It is more difficult for the Mg^{2+} ions to exchange with the interior Na^+ ions of the pellets.

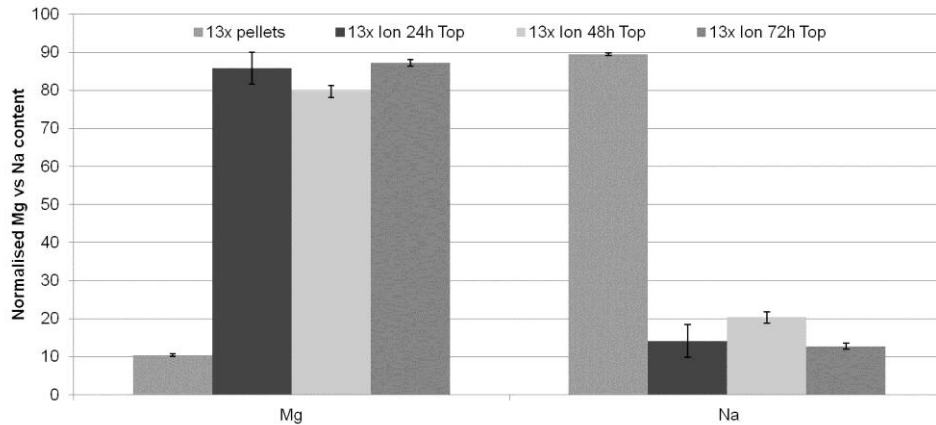


Figure 6-9 EDX external surface analysis of normalised Mg vs Na content of the 13x ion exchanged pellets

EDX data and SEM images of the interior and external surface structure of the pellets were taken. Figure 6-10 shows SEM images of the 13x pellets after a 24 hour ion exchange process. Image 1 shows an image of a pellet fragment, images 2-4 show enlargements of image 1 and images 5 and 6 compare the different structures of the internal and the external surfaces of the pellet. The images show that the external surface of the 13x pellets, after a 24 hour ion exchange process, is very different from the internal surface. The internal surface consists of regular sphere shaped objects (zeolite structures) connected with voids in-between creating a porous structure whereas the external surface is less regular and less porous. There is a reduction in the ion exchange percentage within the interior of the pellets especially if compared with the external surface; this is due to the external surface of the pellets being less porous than the interior. A less porous external surface will reduce the ability of the Mg^{2+} ions to ion exchange with the Na^+ ions in the interior core of the pellets.

The pellet samples were broken into fragments to perform EDX and SEM analysis, to allow the interior structure as well as the exterior surface of the pellets to be analysed.

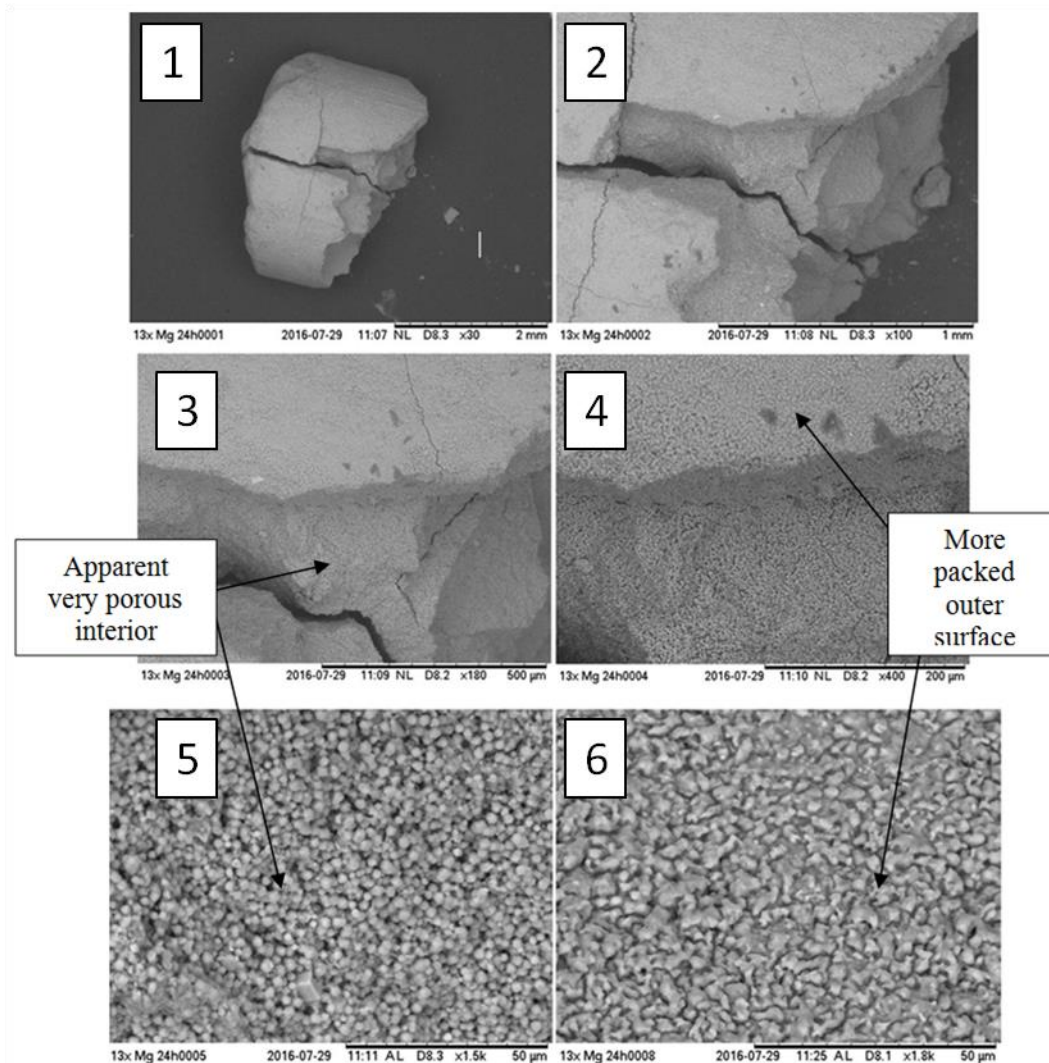


Figure 6-10 SEM images of the 24 hour ion exchanged 13x pellets

6.4 Additional potential host materials for $MgSO_4$

This section of the chapter presents the data from two different potential host materials for $MgSO_4$ impregnation. These materials are Activated Alumina (AA) and Activated Carbon (AC).

This section will present DSC and TGA dehydration plots for each of the host materials before impregnation and then also after the $MgSO_4$ impregnation. For the AA 200g hydration data was collected from the 200g custom built in situ packed bed reactor. The activated carbon showed very poor results on a DSC scale so it was not tested at a 200g scale.

6.4.1 Activated Alumina measurements

6.4.1.1 DSC measurements of activated alumina

Figure 6-11 shows the DSC dehydration of 3 cycles of hydrated activated alumina up to 150°C. It is seen that there is a peak of endothermic heat flow at around 75°C. The endothermic heat flow gradually increases from 20°C up to 75°C then starts to reduce up to 150°C. This suggests that the peak mass loss (i.e. water loss) is at 75°C which gives rise to the potential of using a lower dehydration temperature than 150°C while still achieving the majority of the energy storage potential of the activated alumina.

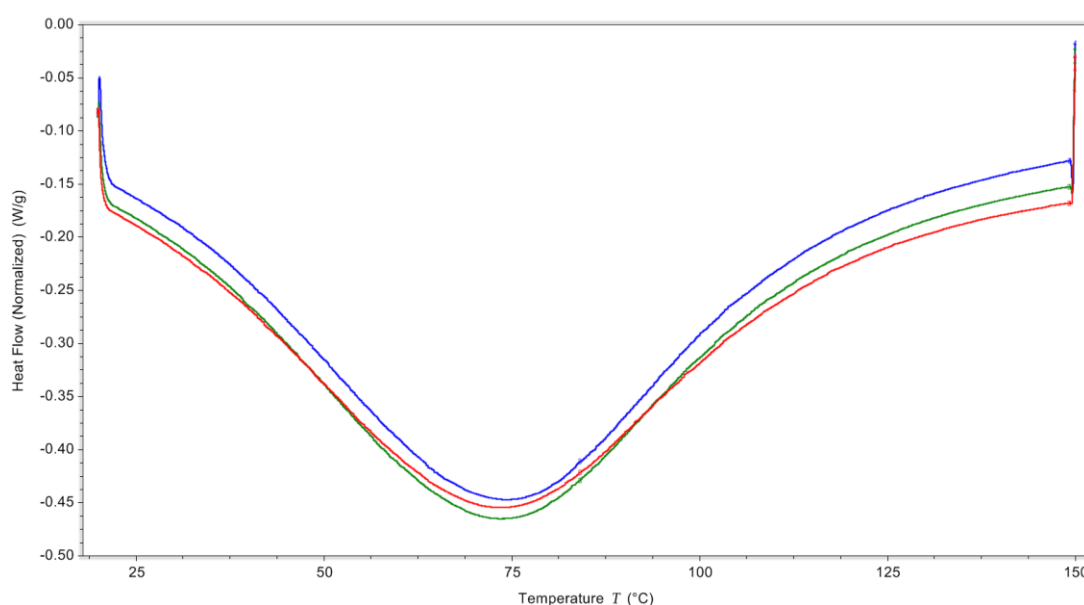


Figure 6-11 DSC dehydration measurements of hydrated activated alumina

Figure 6-12 shows the averaged enthalpies from the DSC dehydration tests. The dehydration enthalpy for the activated alumina was 286J/g and 429J/g for dehydration temperatures of 150°C and 300°C, respectively. The dehydration enthalpy for activated alumina was not as high as zeolite-Y which had a dehydration enthalpy of 615J/g when dehydrated to 150°C and has been used in chapter 4 as a host material for MgSO₄.

Although activated alumina had a higher dehydration enthalpy when dehydrated to 300°C, Figure 6-12 also shows the performance percentage for both dehydration temperatures. The performance percentage when dehydrated to 150°C and 300°C was 76% and 63%, respectively. This means the energy storage is less efficient when dehydrating (charging) the activated alumina to 300°C opposed to 150°C. Also, 150°C is the maximum

temperature which can be used in a domestic environment with a vacuum flat plat collector as the heat source.

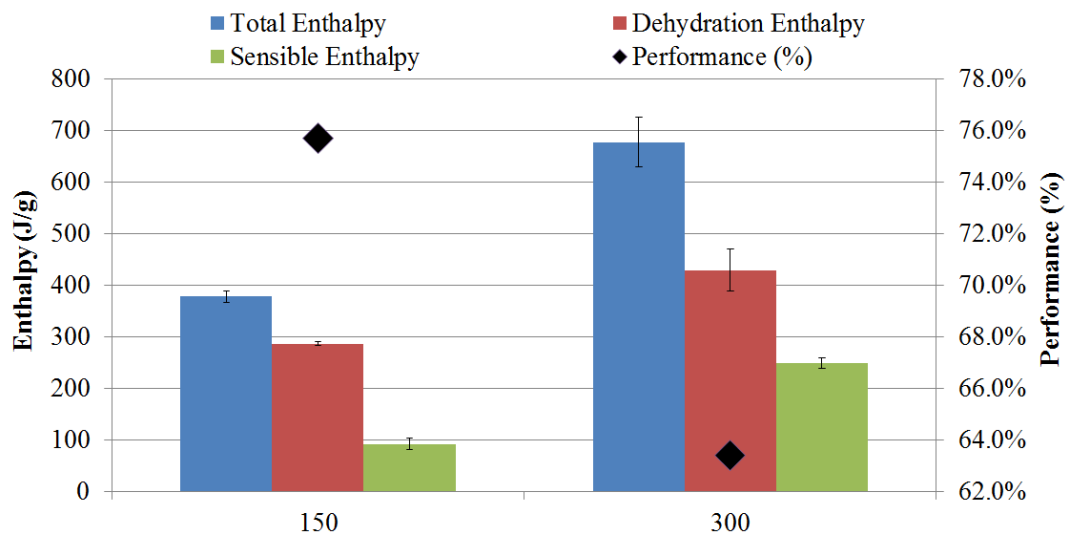


Figure 6-12 Activated alumina DSC results when dehydrated to different temperatures

Figure 6-13 shows the DSC dehydration results of activated alumina and also activated alumina impregnated with $MgSO_4$ ($AA + MgSO_4$). The DSC heat flow profiles are similar with the peak endothermic heat flow at around $75^\circ C$. However, the heat flow of the $AA + MgSO_4$ shifts to a higher temperature (i.e. $\sim 81-87^\circ C$). The heat flow at the peak for the $AA + MgSO_4$ is less than that of the pure AA but it has a higher endothermic heat flow as the temperature approaches $150^\circ C$. Once the AA is impregnated with $MgSO_4$ the DSC dehydration heat flow does not change significantly and there is no prominent $MgSO_4 \cdot xH_2O$ dehydration peak which is seen in the ZMK material (see Figure 6-3). For this reason it is believed that the $MgSO_4$ does not hydrate or dehydrate in the AA similar to the 13x pellets.

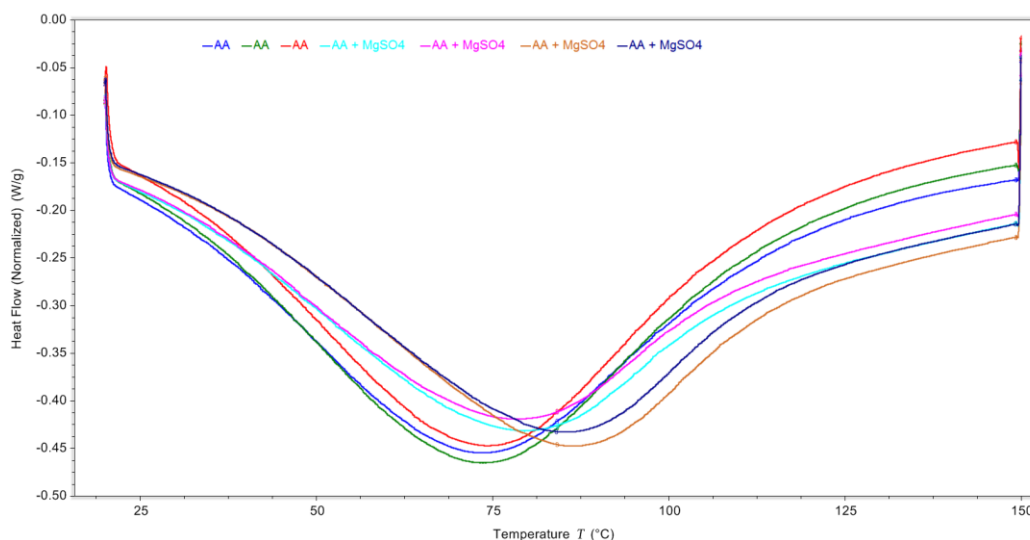


Figure 6-13 DSC dehydration results of activated alumina and activated alumina impregnated with $MgSO_4$

Figure 6-14 shows a comparison of the dehydration enthalpy and performance percentage between the AA and the AA+MgSO₄. The results were similar and when taking into account the error in the data the results for all four values (i.e. total enthalpy, dehydration enthalpy, sensible enthalpy and performance) no difference can be established. This is not the expected result as the AA+MgSO₄ sample had 9.9wt% of MgSO₄ impregnated and the enthalpy of the AA would be expected to rise significantly. If the MgSO₄ was having an adverse impact on the hydration of the AA, possibly through a pore blocking effect, it is expected that a reduction in dehydration enthalpy would be seen due to the AA not being able to absorb as much water.

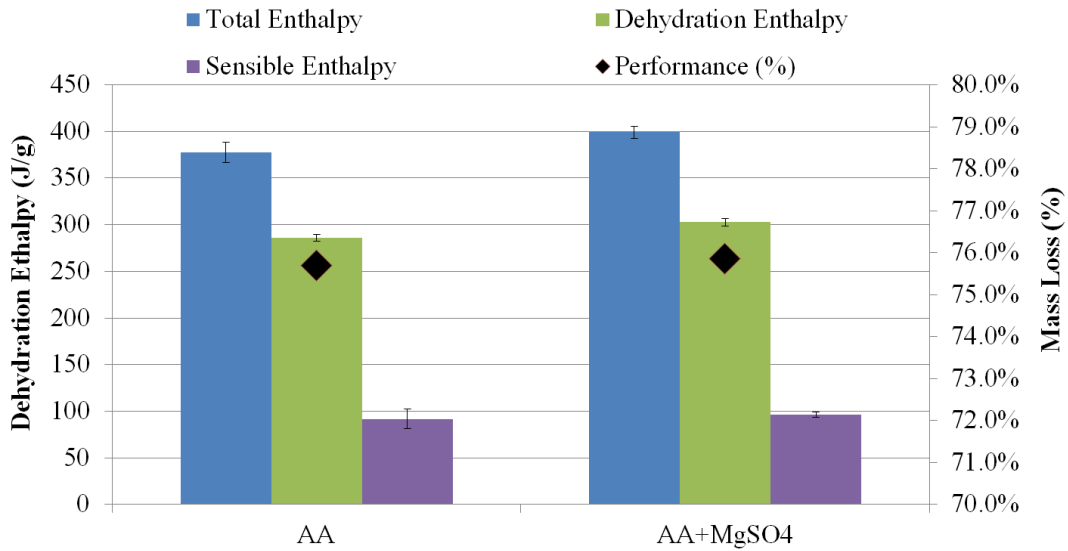


Figure 6-14 Comparison of AA and AA+MgSO4 dehydration enthalpy

6.4.1.2 TGA Tests of activated alumina

TGA tests were conducted to assess the mass loss with temperature of the AA and AA + MgSO₄. Figure 6-15 shows the differential weight with temperature. The peak of the plot is at ~31°C. After 31°C the differential weight loss reduced to a plateau with temperature. As the DSC dehydration of the AA has a large endothermic heat flow at 75°C it was expected that the endothermic heat flow would correspond to a mass loss. Clearly from Figure 6-15 there was no peak mass loss at around 75°C.

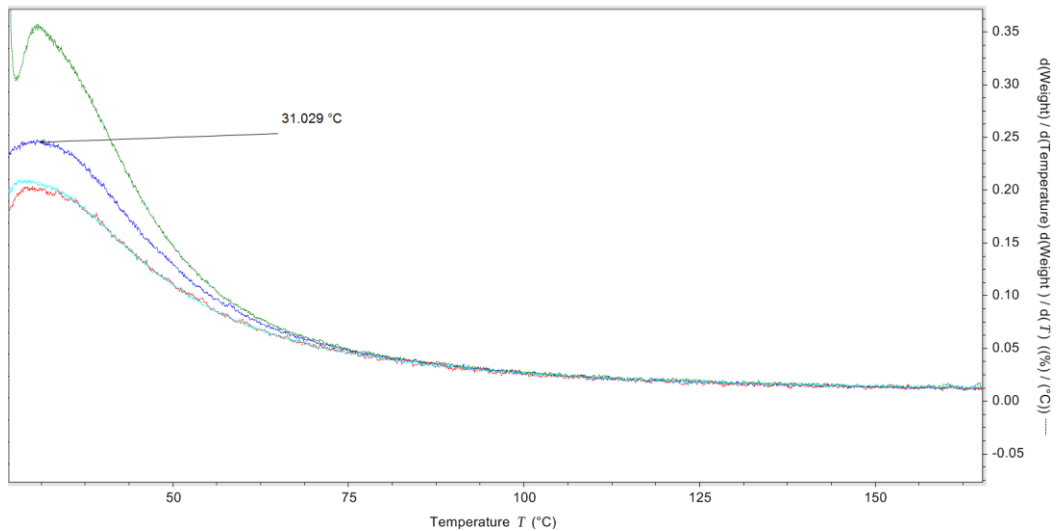


Figure 6-15 TGA dehydration of AA showing differential weight with temperature

Table 6-3 shows a summary of all of the small scale (DSC and TGA testing) results. It is seen that all of the characteristics of the materials are similar; this includes (dehydration enthalpy, Sensible enthalpy, performance, TGA mass loss and Enthalpy/mass loss).

Table 6-3 DSC and TGA Energy output of AA samples

Sample	AA	AA+MgSO ₄
Dehydration Enthalpy (J/g)	287	303
Sensible Enthalpy (J/g)	92	96
Performance (%)	76	76
TGA mass Loss (%)	9	10
Enthalpy/mass loss (J/g.%)	32	31

6.4.1.3 200g tests of activated alumina

200g of AA and AA+MgSO₄ was tested in the in-situ reactor to allow 24h dehydration and hydration testing of the samples and give hydration data at a practical size scale and give an understanding of how the materials react when they are in there pellet form and the form in which they would be used at a large scale.

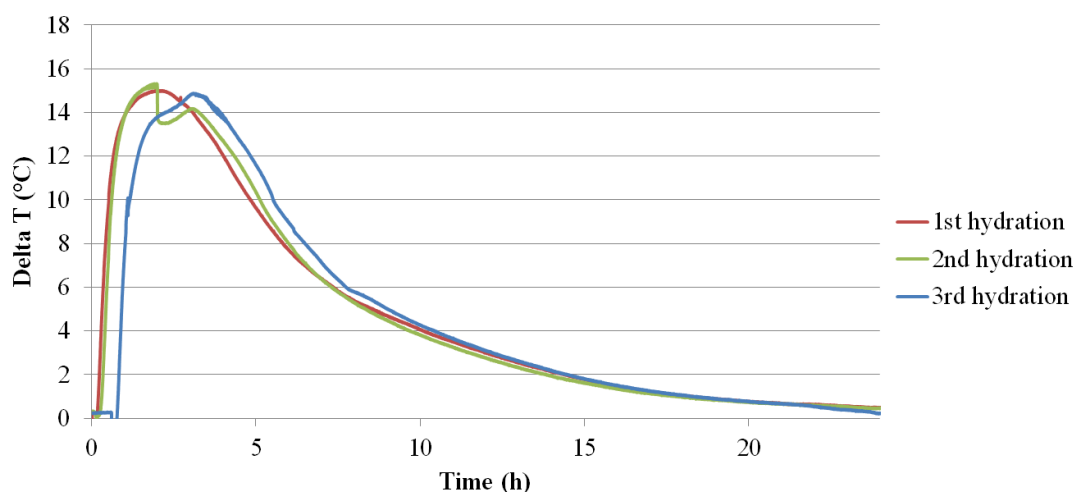


Figure 6-16 24h 200g hydration results of AA

Table 6-4 shows the energy output from 200g of AA and AA+MgSO₄ after a 24h hydration. The results show that the energy output of both samples is similar with a variation of only 11J/g. This is what was expected as the DSC dehydration enthalpy of both samples was also similar (see Figure 6-14). However, the 200g results have a higher hydration

enthalpy of 428J/g and 417J/g opposed to the 286J/g and 303J/g for AA and AA+MgSO₄, respectively. This gives an average difference of 142J/g and 114J/g for the AA and AA+MgSO₄, respectively.

Table 6-4 200g Energy output of AA samples

Sample	200g 24h hydration energy output (kJ/200g)	200g 24h hydration energy output (J/g)
AA	85.5	428
AA+MgSO ₄	83.3	417

6.4.2 Activated Carbon measurements

Figure 6-17 shows the DSC dehydration up to 150°C of the activated carbon after a hydration. It was seen that there was some endothermic heat flow which peaked at around 35°C (i.e. Figure 6-17 has the peaks of some of the plots stamped with temperature for reference). This endothermic heat flow was due to the dehydration of weakly bound water on the activated carbon.

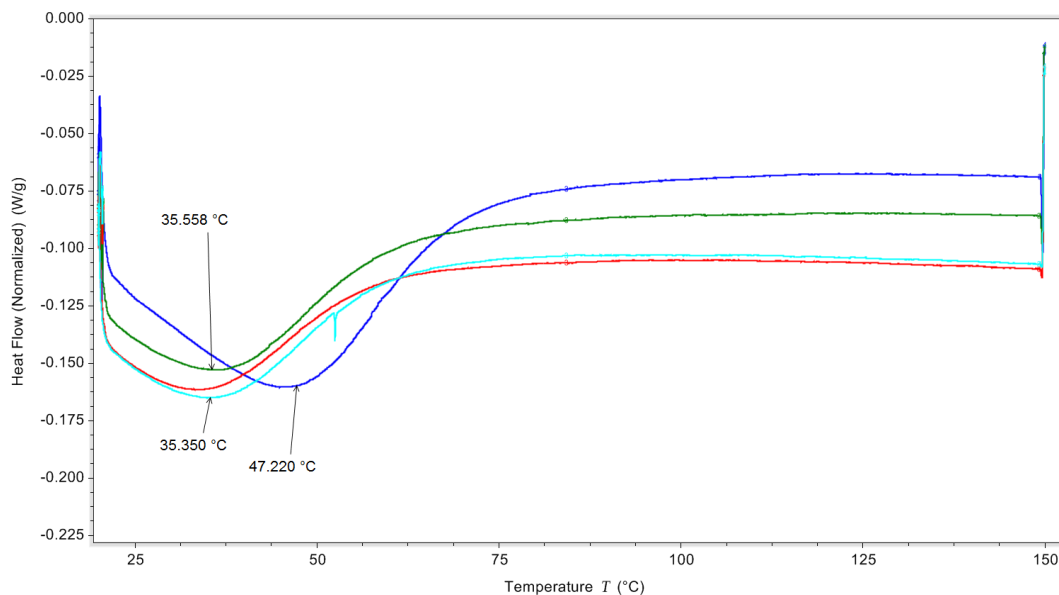


Figure 6-17 DSC dehydration measurements of activated carbon

To confirm the DSC endothermic heat flow is a dehydration the TGA differential weight loss with temperature is shown in Figure 6-18. The differential weight loss with temperature

shows the peaks of mass loss clearer opposed to the mass loss with temperature plots. Figure 6-18 appears quite noisy due to only a small amount of mass loss over a relatively large temperature range. Figure 6-19 is the same data as Figure 6-18 but over a smaller temperature range and it allows for the peak weight loss to be seen more clearly. The peak weight loss has also been stamped with a temperature for two of the samples and it was seen the peak weight loss was around 33°C which confirms that the endothermic heat flow from the DSC plots is due to a dehydration.

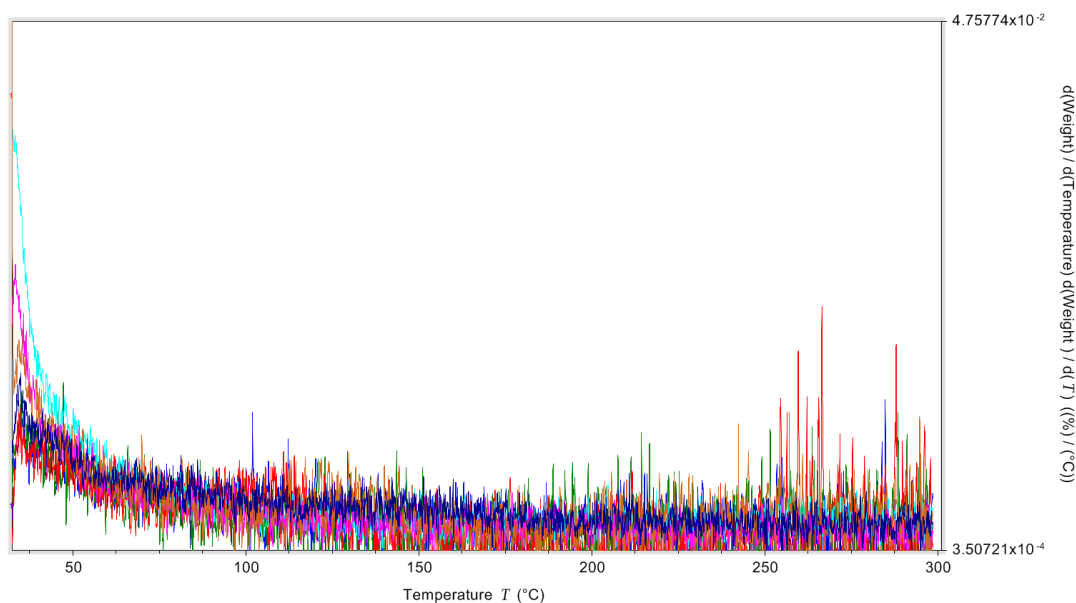


Figure 6-18 TGA differential weight loss showing the dehydration of activated carbon

Although there was some dehydration from the activated carbon and therefore there must have been dehydration enthalpy for this dehydration it was very difficult to evaluate from the DSC data due to the relatively large sensible enthalpy of the material (i.e. the enthalpy is evaluated and shown in Table 6-5).

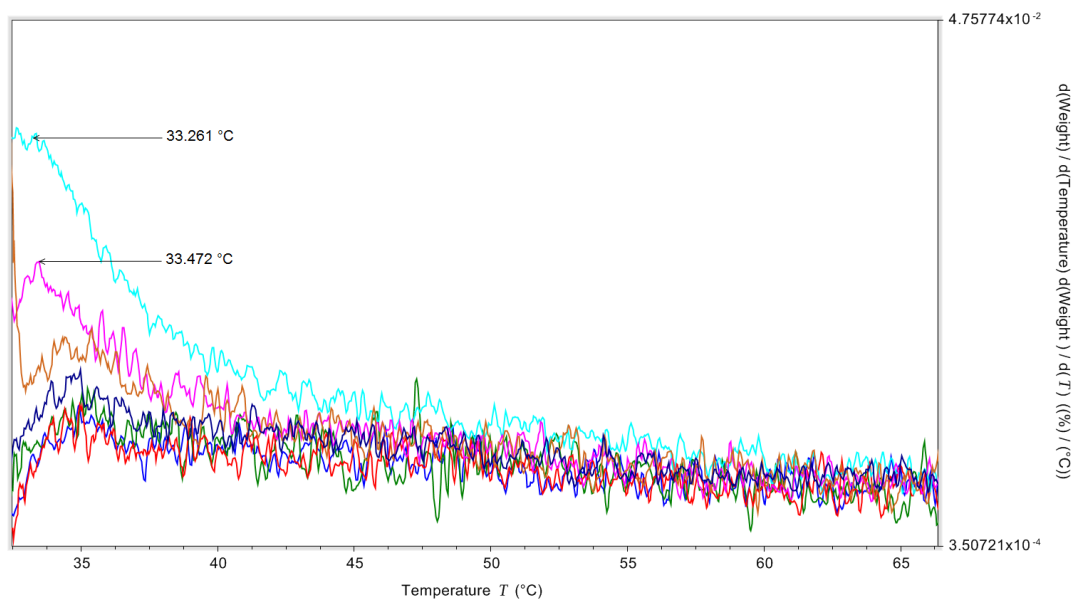


Figure 6-19 TGA differential weight loss showing the dehydration of activated carbon over the temperature range of 30-67.5 °C

Figure 6-20 shows the DSC dehydration of activated carbon and activated carbon with 6.9wt% of impregnated MgSO_4 ($\text{AC}+\text{MgSO}_4$). At around 75°C there was an endothermic peak. This peak was due to the dehydration of the $\text{MgSO}_4 \cdot x\text{H}_2\text{O}$ within the $\text{AC}+\text{MgSO}_4$ sample. This peak was not seen in the pure activated carbon DSC dehydration plots confirming this was due to the impregnated MgSO_4 . The impregnated MgSO_4 in the AC increased the dehydration enthalpy of the AC significantly (see Table 6-5). However, due to the very poor dehydration enthalpy of the AC even with the addition of the MgSO_4 the performance and overall dehydration enthalpy of the $\text{AC}+\text{MgSO}_4$ is low.

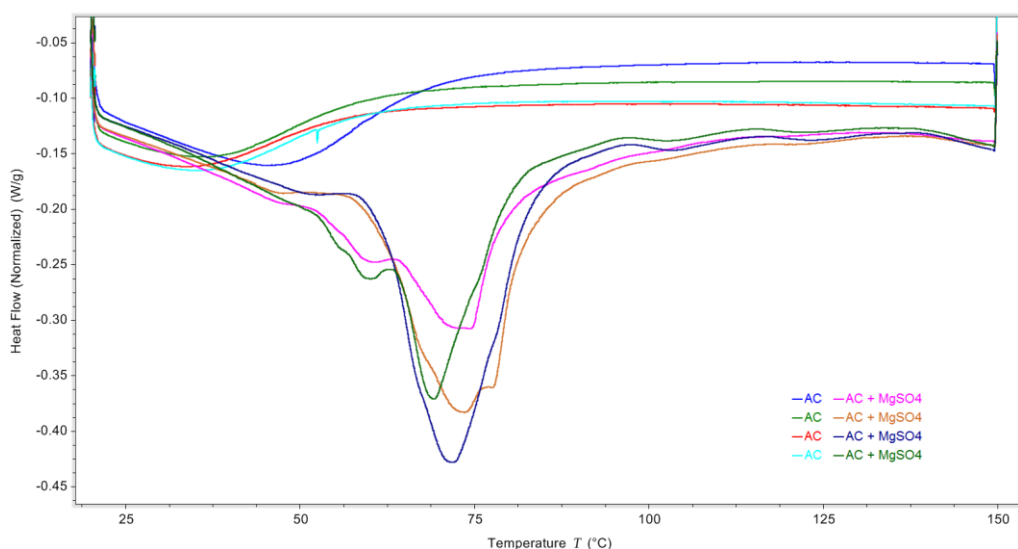


Figure 6-20 DSC dehydration plots of activated carbon and activated carbon with 6.9wt% of impregnated MgSO₄

Table 6-5 shows a summary of the data from the AC and AC+MgSO₄ DSC and TGA testing. The results show how AC did not have any significant dehydration enthalpy (i.e. 3J/g). The 3J/g of dehydration enthalpy could be due water loosely bound to the surface of the AC but it could be likely due to experimental error. After MgSO₄ impregnation the dehydration of the AC+MgSO₄ was 115J/g with a performance of 52%. The enthalpy per mass loss for the AC+MgSO₄ and AC was 30J/g a 4J/g, respectively. This confirmed that the water was bound stronger to the AC+MgSO₄ relative to the AC.

Table 6-5 A summary of the results from the AC and AC+MgSO₄ DSC and TGA analysis

Sample	AC	AC+MgSO ₄
Dehydration Enthalpy (J/g)	3	115
Sensible Enthalpy (J/g)	95	108
Performance (%)	3	52
TGA mass Loss (%)	1	4
Enthalpy/mass loss (J/g.%)	4	30

Due to the poor dehydration enthalpy of the AC and the AC+MgSO₄ it was decided not to carry out any 200g testing of the material.

6.5 Conclusions of chapter 6

Two different absorbents, 13x and zeolite-Y, were shown to exhibit similar dehydration properties through thermal analysis. The 13x material was shown to be a poor host for MgSO_4 as there were no signs of $\text{MgSO}_4 \cdot 6\text{H}_2\text{O}$ dehydration in DSC and 200g tests for any of the 13x materials impregnated with MgSO_4 . Two materials with the same MgSO_4 wt% (13xMK and 13x+ MgSO_4 (12.9wt%)) were created and tested using different pellet preparation methods. Both of them did not show signs of MgSO_4 hydration.

The 200g hydration cycle experiments showed that the 13x pellets and the ZMK pellets have the best properties for use in thermochemical heat storage systems from the materials tested. Zeolite-Y was shown to be a suitable host material for MgSO_4 because of the high energy density reported in the experiments. The pellet preparation method, used to create pellets from absorbent powders, suffered performance losses when moving from DSC measurements to 200g scale system measurements. If this method is optimised the hydration heat of the ZMK could be increased by 46%.

After Mg^{2+} ion exchange with the 13x pellets the properties for heat storage improved. The pellets, after a 24 hour ion exchange period, had a higher DSC dehydration enthalpy and a lower sensible enthalpy component. This resulted in an improved performance by 5.5%.

Two other desiccants AA and AC were characterised and then impregnated with MgSO_4 and characterised again. The results showed that the AC has an average measured dehydration enthalpy of 3J/g. After impregnation the AC+ MgSO_4 material had an averaged measured dehydration enthalpy of 115J/g. However, although the MgSO_4 was able to hydrate and dehydrate in the AC the dehydration enthalpy from the AC was too small and the performance of the AC+ MgSO_4 was very low (52%) relative to the other composite materials characterised in this chapter.

The AA had a measured dehydration enthalpy of 287J/g which was low relative to the 13x and zeolite-Y absorbents. Due to the sensible enthalpy of AA (92J/g) and its low dehydration enthalpy the performance of AA was 76%. After impregnation with MgSO_4 the dehydration of the AA increased to 303J/g however, the performance of the AA+ MgSO_4 was the same as the AA (76%). The hydration energy output, at a 200g scale, from the AA and AA+ MgSO_4 was higher than the DSC results, which was not expected. The AA beads have a

hydration enthalpy output of 428J/g however; this was not as high as the ZMK composite material.

7 Large scale testing of TCES materials

7.1 Introduction and purpose of the custom built modular 40kg rig

To understand the large scale potential of TCESM a custom 8 module automated reactor was designed developed and built which can house ~40kg of TCESM (5kg per module). The system is an open TCES system which serves as a laboratory prototype of a reactor which could be implemented into a domestic environment.

This large scale laboratory rig has been specifically designed in a way which enables flexibility to the charging and discharging of the TCES material. This design has 8 modules which can be opened and closed in any order as required. The connected microcontroller reads the inputs from the modules temperature sensors and can be programmed to open or close any module dependent on module temperature.

The experimental testing using this rig will enable simulation of charging a TCES store with changing weather and irradiances. Currently most TCES reactors use a large packed bed, if this was to be used in a household and charged over the summer months using a STC a packed bed reactor design may result in significant energy losses. For example, if there was a very bright hot period throughout the summer which resulted in significant solar gains from the STC to the TCES material store the TCES material store would increase in temperature. However, assume the TCES material store was heated to 50% of the charging temperature required for complete dehydration (fully charged). After this very bright period if the weather changed to provide minimal solar gains to the TCES material store the TCES material could significantly reduce in temperature. This significant reduction in temperature is wasted thermal energy.

Alternatively, if a modular TCES system was implemented in the household and the same weather patterns were experienced, instead of the whole TCES material store increasing to 50% of the required maximum charge temperature several of the modules could be completely charged and the remaining modules not charged at all throughout the bright weather period. When the weather changes, resulting in minimal solar gains, the charged TCES modules can cool to ambient temperature and not require reheating to complete their charging. This methodology of using a modular system and charging the modules individually could result in saved thermal energy.

Using this novel modular reactor design experimental investigations into the discharge process can be investigated. A modular store allows for segmented discharge. Assume the maximum possible temperature lift (x) from a TCES is required for a short period and a single module could be discharged to supply this temperature lift. As each module is a fraction of the whole TCES there is less thermal energy, supplied through hydration enthalpy, required to bring a single module up to the desired output temperature x and therefore, less wasted thermal energy once the demand for heat has stopped, compared to a packed bed system.

Alternatively, if a packed bed reactor design was used to supply this temperature lift of x for a short period a greater amount of hydration enthalpy would be required to heat the TCES material to the desired output temperature. Once this short demand for heat has stopped all of the sensible enthalpy stored in the TCES material will dissipate to the surroundings potentially resulting in a large amount of wasted thermal energy.

The system presented here will enable experimental research to be conducted into the optimisation of the charging of a TCES material store under unpredictable weather patterns on a large scale.

7.2 Custom built modular 40kg rig system design

An image of the system built can be seen in Figure 7-1. The system used a Huber unistat 510 heat source which pumped oil into a custom built heat exchanger enclosure which houses two oil-air finned heat exchangers. When in dehydration mode the heat source was set to 170°C which allowed for an input air temperature of 150°C. Regulated compressed air would be passed into the system and through one of two gate valves. Gate valve 1 would allow the air to pass directly into the heat exchanger, gate valve 2 would allow the air to pass through the water container first and then into the heat exchanger. The gate valves could be adjusted to change the percentage of air flow that would pass along each path (i.e. either directly into the heat exchanger or through the water container first) this would control the humidity of the air stream. On the input and output of the TCES material modules were gate valves. The gate valves could be opened or closed allowing the air to enter the modules or seal off the modules from the air. The gate valves were controlled by servos which were connected to a microcontroller datalogger and could be programmed to open or close dependant on the output a temperature sensor or other external input.

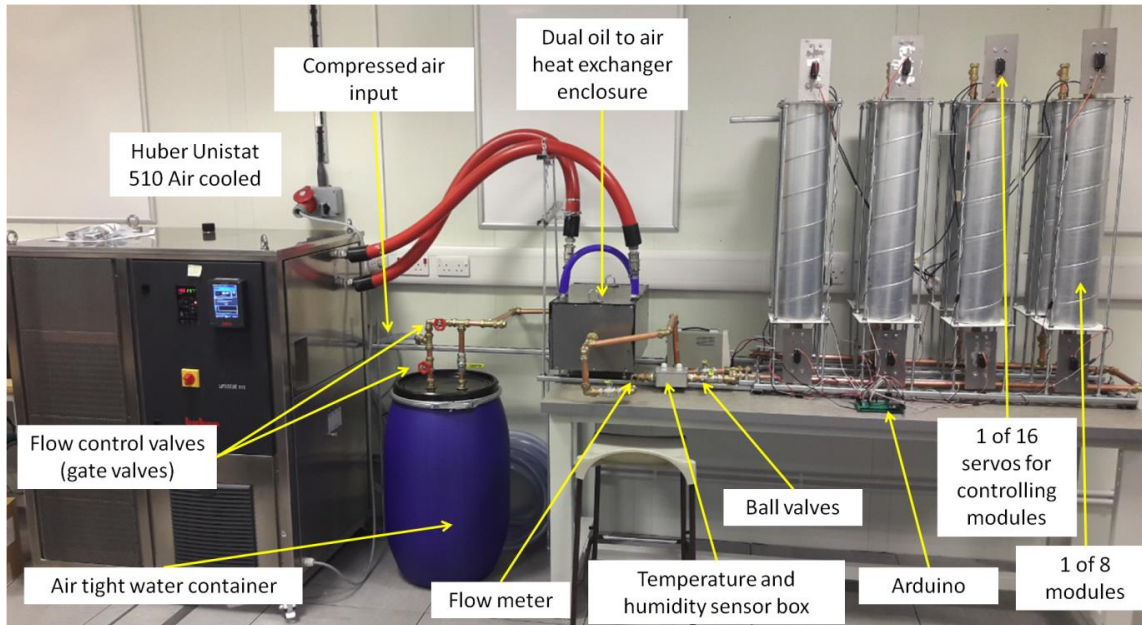


Figure 7-1 Image of the 40kg modular reactor

7.2.1 Arduino microcontroller control of the custom built modular 40kg rig

To automate the opening and closing of each of the TCES material modules a microcontroller datalogger was built and programmed, seen in Figure 7-2. This datalogger was designed to log and store the readings from 8 digital DS18B20 temperature sensors. Connected to the datalogger was a Real Time Clock (RTC) which stored a time stamp of the data recorded from the sensors. The datalogger had an external power supply rail which was used to control 16 high torque servos. These servos were connected to the gate valves at the top and bottom of each module and when in use could draw a high current (+2 amps) per servo and run off 6V. This amount of power could not safely be run through the Arduino microcontroller directly. The microcontroller used on the datalogger was an Arduino Mega. The Arduino Mega was required as it has 16 analogue input pins and 256kb of flash memory which, is more than the more common Arduino UNO, and was required for the developed program to fit on the board's memory.

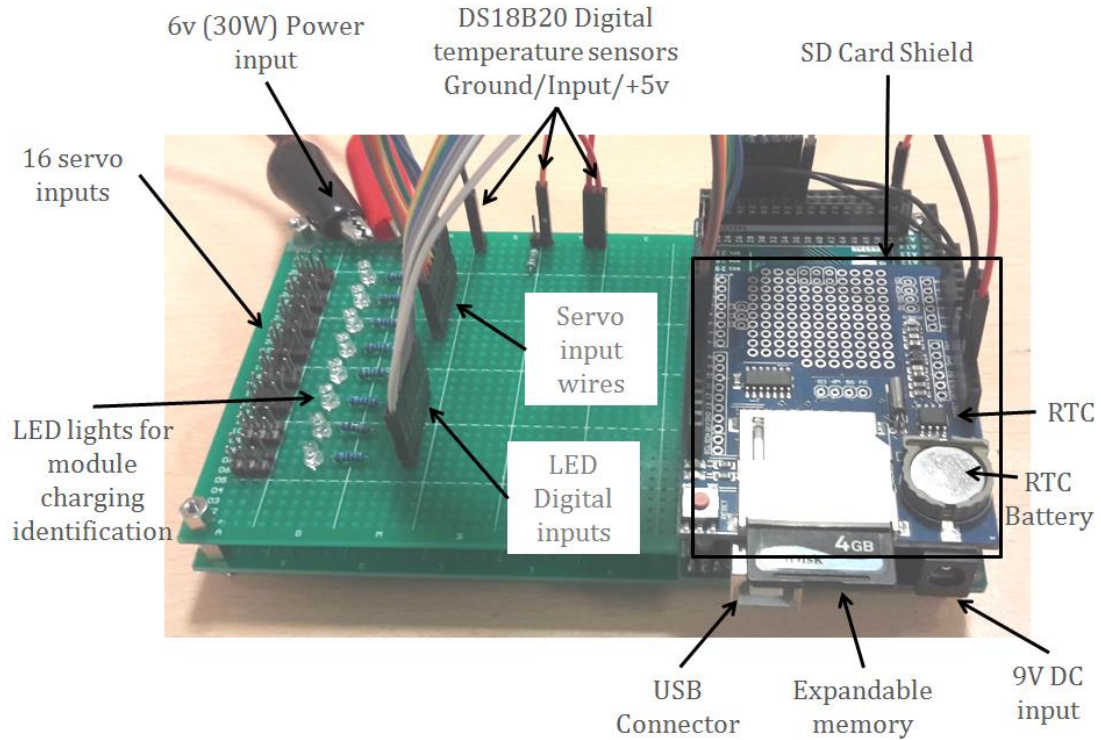


Figure 7-2 Microcontroller data logger

7.3 Experimental operating procedure for the custom built modular 40kg rig methodology

If the system was in hydration mode the air would pass through the water increasing in humidity. Then pass through the heat exchangers at sub ambient temperatures to cool the air. The air would then pass through a ball valve which directed the air through the flow sensor and temperature and humidity sensor box. The humid air would then pass into the TCES modules and start to hydrate the TCESM. The opening and closing of the valves to allow the air to pass into the different modules would be controlled by the microcontroller data logger which is explained in more detail in section 7.2.1.

If the system was in dehydration mode the air path would change. The air would not get humidified by the water tank and pass directly into the heat exchanger where it would be heated to 150°C. The air would then exit the heat exchanger and be diverted so it would not pass through any of the sensors (flow, temperature or humidity) this would happen to prevent the hot air from damaging the sensors. The air would then pass into the TCES modules and start to dehydrate the TCESM.

7.3.1 Default microcontroller data logger program of the custom built modular 40kg rig

The default program set on the microcontroller data logger had two different programs, a dehydration program and a hydration program.

The dehydration program starts by opening the valves on module 1 while the air output temperature was being monitored. Once the air output temperature reached the set point temperature, the microcontroller would open the valves on module 2. Once module 2 was open the valves on module 1 would be sealed. This process would repeat dehydrating each module sequentially. Once all modules had been dehydrated all valves would be shut and the TCES material would be allowed to cool.

The hydration program first opened the valves on reactor 1. The hydration of reactor 1 would then begin. To ensure the hydration was not ended prematurely, there was a delay at this point in the program. The delay allowed enough time for the TCES material to create an air output temperature above the air input temperature. Once the time delay was over the output temperature would be monitored. Once the output air temperature dropped below a set point ΔT the valves on the next module would be opened. Then the module which would have just been hydrated would have its valves closed. This process would be repeated sequentially until all modules were hydrated.

7.3.2 Data collection for the custom built modular 40kg rig

As no experimental data from the 40kg rig containing TCES material was collected in this research project the methodology presented here is an anticipation of what would happen when the 40kg system is used.

The data collected from these experiments would be imported into a spreadsheet. The data collected would include; input air RH%, input air temperature, air flow rate, temperature of air at RH% measurement, output air temperature and time when each valve was opened or closed. This data would be used to calculate the power and energy output of the TCESM for each module. Each material test would be conducted at least 3 times and an average for each module as well as an average for all modules would be calculated. The RH% and temperature measurements would also be used to calculate the partial vapour pressure of the air.

The data collected would give an insight to any performance losses experienced from 200g to 40kg scale and also the overall energy density of the prototype TCES system.

7.4 Conclusions from the custom built 40kg reactor design

This system allows for large scale prototype testing and understanding of the workings of an open TCES system. The modular feature allows for flexibility in the testing of the system. A modular system allows for singular charging and discharging of TCES material stores, opposed to bulk charging and discharging, which could potentially be a more energy efficient way to operate a TCES interseasonal open TES system.

This system was designed and developed for utilisation and testing in future research potentially by other researchers.

8 Thesis conclusions

The conclusions derived from the research conducted for this thesis are described below. The conclusions are split into the conclusions derived from each chapter.

8.1 Conclusions from Chapter 4 – Characterisation of $MgSO_4$, zeolite-Y and composite materials

Chapter 4 investigated the small scale (~10mg) potential of $MgSO_4 \cdot xH_2O$, zeolite-Y and composite materials made from zeolite-Y and $MgSO_4 \cdot xH_2O$. $MgSO_4 \cdot xH_2O$ was tested and shown to have cycle characteristic which make the material an ideal candidate for domestic seasonal heat storage. The materials characteristics improved with successive cycles and the enthalpy of the material remained high (average 1,265J/g).

$MgSO_4 \cdot 7H_2O$ was dehydrated within the DSC and the TGA+RGA using several different heating rates. The measurements showed the dehydration of the $MgSO_4 \cdot 7H_2O$ had more sharp endothermic peaks when using higher dehydration heating rates due to the sudden loss of water from the $MgSO_4$.

$MgSO_4 \cdot 7H_2O$ was dehydrated to a maximum temperature of 110°C and 150°C within the DSC. The results showed that there was only a 7% difference in dehydration enthalpy between the two maximum dehydration temperatures used.

The charging and discharging of $MgSO_4 \cdot xH_2O$ was cycled within the DSC and TGA+RGA using three different dehydration heating rates. The dehydration enthalpy of $MgSO_4$ was not impacted by the dehydration heating rate used and $MgSO_4$ did not have any cycle stability degradation.

$MgSO_4 \cdot xH_2O$ was dehydrated with different heating rates and then imaged within the SEM to inspect the structure of the material after the dehydrations. From the SEM images and the DSC, TGA+ RGA measurements it was shown that higher dehydration heating rates cause more cracks to occur in the $MgSO_4$ which results in improved dehydration kinetics. This is likely to be the same for the hydration kinetics although the DSC setup used would not allow for hydration testing.

Composite materials were created from zeolite-Y with up to 35wt% of impregnated $MgSO_4$. The results have shown that the composite materials did not experience any

degradation with increasing wt% of MgSO_4 with the 35wt% composite material having a dehydration enthalpy of 708J/g.

$\text{MgSO}_4 \cdot x\text{H}_2\text{O}$ was dehydrated within the DSC using different maximum dehydration temperatures and also different dehydration heating rates. It was shown that the length of the dehydration isothermal period is important to “extract” as much of the dehydration enthalpy from MgSO_4 . If the isothermal period used is not sufficiently long enough the dehydration enthalpy of the material is reduced leading to less thermal energy being stored. However, the isothermal stage enthalpy does appear to decrease with successive cycles at the higher heating rates, suggesting the dehydration kinetics improve with successive cycles.

Three different grain sizes of $\text{MgSO}_4 \cdot x\text{H}_2\text{O}$ were dehydrated within the DSC and TGA + RGA. It was shown that the grain size of $\text{MgSO}_4 \cdot x\text{H}_2\text{O}$ used when dehydrating the material had an impact on the temperature at which mass was lost and on the dehydration kinetics of the $\text{MgSO}_4 \cdot x\text{H}_2\text{O}$. The larger grain size had slower dehydration kinetics and lost more mass at a higher temperature relative to the smaller grain size.

8.2 Conclusions from chapter 5 - Understanding the larger scale (100g+) characteristics of MgSO_4 and investigation of sample preparation methods for MgSO_4 for use as a TCES material

Chapter 5 investigated the larger scale (100g+) behaviour of MgSO_4 through hydration and dehydration experiments within custom built experimental configurations.

It was found that the use of pure MgSO_4 at larger scales was problematic due to agglomeration of the material when hydrated and low permeability. Research was undertaken to investigate novel methods to develop composite TCES materials incorporating $\text{MgSO}_4 \cdot x\text{H}_2\text{O}$ to reduce the agglomeration issues and create an energy dense TCES material. Several methodologies were tested and the one which was identified to have the best characteristics was the pellet preparation methodology.

To optimise the pellet preparation methodology two key variables of the methodology were changed and four different batches of pellets were produced. The pellets were created with either a mixture or impregnation composite creation method and then they were initially dehydrated with either a 1°C/min or 5°C/min dehydration heating rate. The names of the four

different pellet batches produced were Mix 1, Mix 5, Impreg 1 and Impreg 5. These four different pellets were tested with a DSC, TGA + RGA, SEM + EDX, nitrogen sorption analyser and cycled in a 200g custom built hydration and dehydration chamber. The results showed that the Impreg 1 pellets synthesized had the highest 200g hydration energy output and also the largest bulk density which resulted in the Impreg 1 pellets having the highest energy density. The Mix 1 pellets had the highest performance ratio.

8.3 Conclusions from chapter 6 - Investigation into potential host materials for impregnating with $MgSO_4$

Chapter 6 investigated several different potential host materials for impregnating with $MgSO_4$. Tests were conducted within the DSC, TGA + RGA, SEM + EDX and the custom built 200g hydration and dehydration chamber. The materials tested were ZMK, 13x, Activated Alumina (AA) and Activated Carbon (AC).

The 13x absorbent was shown to be a poor host for $MgSO_4$ as there were no signs of $MgSO_4 \cdot xH_2O$ dehydration from the 13x material impregnated with $MgSO_4 \cdot xH_2O$. This resulted in significant loss of expected dehydration enthalpy and specific energy density from the composite materials.

To improve the dehydration enthalpy of the 13x pellets they were put through an ion exchange process to replace the Na^+ ions with Mg^{2+} ions. The methodology for the ion exchange process was investigated to find the optimum ion exchange time length. After an Mg^{2+} ion exchange on the 13x pellets their properties for heat storage improved. The ion exchanged 13x pellets had an increased specific energy density and an improved performance ratio.

It was found that the optimal ion exchange time length for the 13x pellets was between 1 and 24 hours. However, after SEM and EDX analysis it was shown that the ion exchange had completed to a higher level on the exterior of the 13x pellets compared to the interior of the pellets. This means that further ion exchange was possible within the 13x pellets which would lead to an increase in dehydration enthalpy and an increase in specific energy density.

Zeolite-Y was shown to be a suitable host material for $MgSO_4$ because of the high energy density reported in the experiments and the $MgSO_4 \cdot xH_2O$ dehydration peaks seen in the DSC

dehydration heat flow measurements indicating the $\text{MgSO}_4 \cdot x\text{H}_2\text{O}$ was charging and discharging within the zeolite-Y composite materials.

The ZMK material was shown to have the highest dehydration enthalpy at DSC scale (715J/g) and a hydration enthalpy of 490J/g at a 200g scale. The ZMK pellets were developed using the novel pellet preparation methodology.

The pellet preparation method, used to create pellets from absorbent powders, suffered significant performance losses when moving from DSC measurements to 200g scale system measurements. The best performing ZMK pellet suffered a 31% loss in performance from DSC scale to 200g scale.

Two other desiccants AA and AC were characterised, within the DSC, TGA + RGA and then impregnated with MgSO_4 . The results showed that AC+ MgSO_4 had a low dehydration enthalpy of 115J/g and a low performance of 52%. The AA beads were better performing than that AC pellets. AA+ MgSO_4 had a DSC dehydration enthalpy of 303J/g and a performance of 76%. The results from both the AA and AC do not make them ideal candidate host materials for MgSO_4 .

ZMK has a specific energy density ~3.8 times higher than water being used to store thermal energy for DSH and DHW (assumed water delta T of 45°C and a dehydration enthalpy of 715J/g for ZMK). If ZMK is used in a large scale TCES system and charged throughout the summer months with a STC, storing typically unutilised thermal energy when demand is low the system has the potential to be financially viable to the user and reduce the CO_2 emissions produced from generating energy for DSH and DHW.

8.4 Conclusions from chapter 7 - Large scale testing of TCES materials

Chapter 7 presents a designed and built large scale TCES modular reactor. This reactor was designed to allow future experimental work to be conducted using a flexible modular reactor. The future experimental work conducted using this reactor will help provide an understanding of how to efficiently charge a modular open TCES reactor.

This reactor has been designed, built and described to give future researchers the opportunity to use a novel large scale TCES test rig.

9 Recommendations for future work

Some of the novel TCES materials developed, throughout this research project, have characteristics (i.e. specific energy density) which should make them a feasible choice to be integrated into a system with a STC to help decarbonise DSH and DHW. However, For TCES + STC systems to be realised in a domestic environment more research is required.

The specific future work identified from each chapter is presented below. However, more broad future work goals have been identified from this research, these future goals are as follows;

1. The methodology used for creating energy dense TCES materials needs to be economically scalable to be viable for mass manufacture. If TCES materials are to be deployed on a large scale in a domestic environment the TCES materials need to be able to be produced quickly and cost effectively on a large scale. For this to be realised research into the manufacturing techniques and a techno-economical evaluation of the cost per J (£/J) needs to be conducted. The methodology used to create the most energy dense TCES materials may not be the most economical method for large scale production. This research should identify which method and materials are most suited for mass manufacture.
2. The TCES materials developed throughout this research project should be tested at a large scale (40kg+) within a system using a STC for charging the TCES materials (a Vacuum Flat Plate Collector (VFPC) would be the best choice). This system would provide valuable data which could be used to develop the charging and discharging management hardware and software of future TCES + STC systems. If successful this work would help progress the large scale deployment of TCES + STC systems within the domestic environment.
3. Once a TCES + STC system has been experimentally tested, developed and optimised the next step should be integration into an occupied test household. This research would highlight any engineering challenges associated with the integration of a TCES + STC system into a household and also the challenges involved in designing management controls for a heating system that is controlled by humans. This research would produce valuable data which would further help the engineering development of a TCES + STC system for domestic integration and also help the development of an effective and intuitive TCES + STC system control interface suitable for human use.

4. Research into other potential different reactor designs for different applications should be considered. It was decided for this research that an open packed bed reactor was the most suitable choice for domestic implementation however; different reactor designs may be more suited to different applications. For example, the use of the TCES materials developed throughout this research project could be used for industrial applications to store heat over a shorter amount of time. For this application the use of a fluidised bed reactor to output higher power from the TCES materials may be the most suitable reactor design. This research would help identify potential sectors where TCES materials could be used to help reduce the CO₂ emissions from that sector.

9.1 Identified future work from chapter 4

Further work is required to confirm if the rate of hydration improves with successive dehydration hydration cycles of MgSO₄ due to higher heating rates causing more cracking within the MgSO₄. This should be tested through DSC/TGA hydration and dehydration testing.

To understand the impact the zeolite-Y has on the hydration of the composite materials containing MgSO₄ hydration and dehydration cycling experiments should be conducted within a TGA/DSC with a humid flow.

To confirm the importance of the dehydration isothermal period length hydration tests should be conducted on MgSO₄.xH₂O after different isothermal periods within a TGA/DSC with a humid flow to quantify the hydration enthalpy.

9.2 Identified future work from chapter 5

More batches of the samples (Mix 1, Mix 5, Impreg 1, Impreg 5) should be synthesised and tested to assess if the sample preparation method produces consistent composition pellets with the same TCES properties.

Hydration and dehydration testing of the different samples (Mix 1, Mix 5, Impreg 1, Impreg 5) would give an understanding of how the changing pore size and surface area affects the speed of hydration and therefore power output. This should be tested through DSC/TGA hydration and dehydration testing.

9.3 Identified future work from chapter 6

The ion exchanged 13x pellets should be tested at a larger scale (200g+) to assess their scaling losses. Optimisation of the ion exchange process should be performed to increase the ion exchange percentage within the 13x pellets to further increase the dehydration enthalpy. Further work should also be conducted investigating the potential of using other ions for the ion exchange process to increase the energy density of 13x pellets.

The pellet preparation method suffered significant scaling losses and work should be conducted to reduce these losses and improve the energy density of the ZMK pellets. The hydration heat from the ZMK pellets could potentially be increased by 46%.

The mechanical strength of the ZMK pellets should be assessed before and after repeated dehydration and hydration cycles to quantify if any mechanical breakdown is apparent.

9.4 Identified future work from chapter 7

Further work should be conducted on the characteristics of the developed TCES materials at larger scales and on the design of the TCES reactors to further verify the potential of the developed TCES materials at a large scale. The 40kg modular reactor built throughout this research project would be an ideal experimental test rig to conduct these larger scale tests as well as investigations into the potential of modular TCES reactors.

10 Research

D Mahon, P Henshall, P C Eames, (2015), MgSO₄ + Zeolite based composite thermo-chemical energy stores integrated with vacuum flat plate solar thermal collectors for seasonal thermal energy storage. Presented at: UKES2015 conference, Birmingham UK.

D. Mahon, G. Claudio, and P. Eames, “An experimental investigation to assess the potential of using MgSO₄ impregnation and Mg²⁺ ion exchange to enhance the performance of 13x molecular sieves for interseasonal domestic thermochemical energy storage,” *Energy Convers. Manag.*, 2017.

D. Mahon, G. Claudio, and P. Eames, “How does MgSO₄ impregnation and Mg²⁺ ion exchange impact the energy storage characteristics of 13x molecular sieves for use in domestic thermochemical energy storage?,” in *SusTEM2017*, 2017.

D. Mahon, G. Claudio, and P. C. Eames, “A study of novel high performance and energy dense zeolite composite materials for domestic inter-seasonal thermochemical energy storage,” *Accepted to ICAE2018 for oral presentation and publication in Energy Procedia*

D. Mahon, P. Henshall, G. Claudio, and P. Eames, “Feasibility study on MgSO₄ + Zeolite based composite thermo-chemical energy stores integrated with vacuum flat plate solar thermal collectors for seasonal thermal energy storage,” *Submitted to Solaris 2018 for oral presentation and publication*

11 References

- [1] UK.GOVERNMENT. Estimates of heat use in the United Kingdom in 2012, 2013, p. 73–80.
- [2] Department of Energy and Climate Change. UK progress towards GHG emissions reduction targets Statistical release: Official Statistics 2015.
- [3] Van den Bergh J, Botzen WJW. Monetary valuation of the social cost of CO 2 emissions: a critical survey. *Ecol Econ* 2015;114:33–46.
- [4] Price R, Thornton S, Nelson S. The social cost of carbon and the shadow price of carbon: what are they, and how to use them in economic appraisal in the UK. 2008.
- [5] Ice2sea.eu. London: A city under threat. Ice2Sea 2014.
<http://www.ice2sea.eu/policy/case-study-london/>.
- [6] Topographic-map.com. Londong topographic map n.d. <http://en-gb.topographic-map.com/places/London-92172/>.
- [7] Defra. Climate Change Risk Assessment for the Floods and Coastal Erosion Sector. 2012.
- [8] CarbonBrief. Q & A : The social cost of carbon. *CarbonBrief* 2017:1–33.
<https://www.carbonbrief.org/qa-social-cost-carbon>.
- [9] Drijfhout S, Bathiany S, Beaulieu C, Brovkin V, Claussen M, Huntingford C, et al. Catalogue of abrupt shifts in Intergovernmental Panel on Climate Change climate models. *Proc Natl Acad Sci* 2015:201511451. doi:10.1073/pnas.1511451112.
- [10] Collins M, Knutt R, Arblaster J, Dufresne J-L, Fichet T, Friedlingstein P, et al. Long-term climate change: projections, commitments, and irreversibility. *Clim Chang* 2013 Phys Sci Basis Contrib Work Gr I to Fifth Assess Rep Intergov Panel Clim Chang 2013. doi:10.1017/CBO9781107415324.024.
- [11] Stocker T, Dahe Q. The WGI contribution to the IPCC 5th Assessment Report. 2013.
- [12] Lontzek T., Cai Y, Judd K., Lenton T. Stochastic integrated assessment of climate tipping points indicates the need for strict climate policy. *Nat Clim Chang* 2015;5:441–4. doi:10.1038/nclimate2570.
- [13] Smith S, Braathen NA. Monetary Carbon Values in Policy Appraisal: An Overview of Current Practice and Key Issues. *OECD Environ Work Pap* 2015.

- [14] Sabihuddin S, Kiprakis A, Mueller M. A Numerical and Graphical Review of Energy Storage Technologies. *Energies* 2014;8:172–216. doi:10.3390/en8010172.
- [15] Eurostat Statistics Explained. Consumption of energy. Eurostat Stat Explain 2018. https://ec.europa.eu/eurostat/statistics-explained/index.php/Consumption_of_energy.
- [16] Eurostat. Energy consumption in households 2018. https://ec.europa.eu/eurostat/statistics-explained/index.php/Energy_consumption_in_households.
- [17] UK.GOVERNMENT. Live tables on dwelling stock 2017. <https://www.gov.uk/government/statistical-data-sets/live-tables-on-dwelling-stock-including-vacants> (accessed February 24, 2017).
- [18] Mette B, Kerskes H, Drück H. Concepts of long-term thermochemical energy storage for solar thermal applications – Selected examples. *Energy Procedia* 2012;30:321–30. doi:10.1016/j.egypro.2012.11.038.
- [19] Weber A, Herzog N, Bergmann T. Numerical simulations of gas-liquid flow in thermal sorption processes. *Comput Chem Eng* 2016;84:171–9. doi:10.1016/j.compchemeng.2015.09.003.
- [20] Pal S, Hajj MR, Wong WP, Puri IK. Thermal energy storage in porous materials with adsorption and desorption of moisture. *Int J Heat Mass Transf* 2014;69:285–92. doi:10.1016/j.ijheatmasstransfer.2013.10.023.
- [21] Kerskes H, Mette B, Bertsch F, Asenbeck S, Drück H. Chemical energy storage using reversible solid/gas-reactions (CWS) - Results of the research project. *Energy Procedia* 2012;30:294–304. doi:10.1016/j.egypro.2012.11.035.
- [22] Abedin AH, Rosen MA. A Critical Review of Thermochemical Energy Storage Systems. *Open Renew Energy J* 2011;4:42–6. doi:10.2174/1876387101004010042.
- [23] Hongois S, Kuznik F, Stevens P, Roux JJ. Development and characterisation of a new MgSO₄-zeolite composite for long-term thermal energy storage. *Sol Energy Mater Sol Cells* 2011;95:1831–7. doi:10.1016/j.solmat.2011.01.050.
- [24] Trausel F, de Jong A-J, Cuypers R. A Review on the Properties of Salt Hydrates for Thermochemical Storage. *Energy Procedia* 2014;48:447–52. doi:10.1016/j.egypro.2014.02.053.
- [25] Opel O, Rammelburg H., Gerard M, Ruck W. THERMOCHEMICAL STORAGE

- [26] Balasubramanian G, Ghommem M, Hajj MR, Wong WP, Tomlin J a., Puri IK. Modeling of thermochemical energy storage by salt hydrates. *Int J Heat Mass Transf* 2010;53:5700–6. doi:10.1016/j.ijheatmasstransfer.2010.08.012.
- [27] Quinnell J a., Davidson JH. Mass transfer during sensible charging of a hybrid absorption/sensible storage tank. *Energy Procedia* 2012;30:353–61. doi:10.1016/j.egypro.2012.11.042.
- [28] van Essen VM, Zondag HA, Gores JC, Bleijendaal LPJ, Bakker M, Schuitema R, et al. Characterization of MgSO₄ Hydrate for Thermochemical Seasonal Heat Storage. *J Sol Energy Eng* 2009;131. doi:10.1115/1.4000275.
- [29] N'Tsoukpoe KE, Liu H, Le Pierrès N, Luo L. A review on long-term sorption solar energy storage. *Renew Sustain Energy Rev* 2009;13:2385–96. doi:10.1016/j.rser.2009.05.008.
- [30] Maciąg K, Olszowka M, Klein A, editors. *Biotechnology Progress – The Polish students' scientific interests*. Cracow: Academic Society of Biotechnology Students; 2014.
- [31] Lin W. *Clean Chemical Energy and Sustainability Module* n.d.
- [32] Yu N, Wang RZ, Wang LW. Sorption thermal storage for solar energy. *Prog Energy Combust Sci* 2013;39:489–514. doi:10.1016/j.pecs.2013.05.004.
- [33] Robert L, Burwell J. Manual of symbol and terminology for physicochemical quantities and units - appendix 2. *Pure Appl Chem* 1976;46:71–90.
- [34] Wang LW, Wang RZ, Oliveira RG. A review on adsorption working pairs for refrigeration. *Renew Sustain Energy Rev* 2009;13:518–34. doi:10.1016/j.rser.2007.12.002.
- [35] Aydin D, Casey SP, Riffat S. The latest advancements on thermochemical heat storage systems. *Renew Sustain Energy Rev* 2015;41:356–67.
- [36] Casey SP, Elvins J, Riffat S, Robinson A. Salt impregnated desiccant matrices for 'open' thermochemical energy storage—Selection, synthesis and characterisation of candidate materials. *Energy Build* 2014;84:412–25. doi:10.1016/j.enbuild.2014.08.028.
- [37] Ding Y, Riffat SB. Thermochemical energy storage technologies for building

- applications: a state-of-the-art review. *Int J Low-Carbon Technol* 2012;8:106–16. doi:10.1093/ijlct/cts004.
- [38] Xu J, Wang RZ, Li Y. A review of available technologies for seasonal thermal energy storage. *Sol Energy* 2014;103:610–38. doi:10.1016/j.solener.2013.06.006.
- [39] Aristov YI. New family of solid sorbents for adsorptive cooling: Material scientist approach. *J Eng Thermophys* 2007;16:63–72. doi:10.1134/S1810232807020026.
- [40] Cuypers R, Maraz N, Eversdijk J, Finck C, Henquet E, Oversloot H, et al. Development of a Seasonal Thermochemical Storage System. *Energy Procedia* 2012;30:207–14. doi:10.1016/j.egypro.2012.11.025.
- [41] Ferchaud J, Zondag A, Rubino A, de Boer R. Seasonal Sorption Heat Storage – Research On Thermochemical Materials And Storage Performance. 2012.
- [42] Wu H, Wang S, Zhu D. Effects of impregnating variables on dynamic sorption characteristics and storage properties of composite sorbent for solar heat storage. *Sol Energy* 2007;81:864–71. doi:10.1016/j.solener.2006.11.013.
- [43] Jänchen J, Herzog TH, Gleichmann K, Unger B, Brandt A, Fischer G, et al. Performance of an open thermal adsorption storage system with Linde type A zeolites: Beads versus honeycombs. *Microporous Mesoporous Mater* 2015;207:179–84. doi:10.1016/j.micromeso.2015.01.018.
- [44] Ferchaud C, Zondag H, Veldhuis J, Boer R De. Study of the reversible water vapour sorption process of $\text{MgSO}_4 \cdot 7\text{H}_2\text{O}$ and $\text{MgCl}_2 \cdot 6\text{H}_2\text{O}$ under the conditions of seasonal solar heat storage. *J Phys Conf Ser* 2012;395. doi:10.1088/1742-6596/395/1/012069.
- [45] N'Tsoukpoe KE, Schmidt T, Rammelberg HU, Watts BA, Ruck WKL. A systematic multi-step screening of numerous salt hydrates for low temperature thermochemical energy storage. *Appl Energy* 2014;124:1–16. doi:10.1016/j.apenergy.2014.02.053.
- [46] Linnow K, Niermann M, Bonatz D, Posern K, Steiger M. Experimental Studies of the Mechanism and Kinetics of Hydration Reactions. *Energy Procedia* 2014;48:394–404. doi:10.1016/j.egypro.2014.02.046.
- [47] Bales C. Thermal Properties of Materials for Thermo-chemical Storage of Solar Heat. 2005.
- [48] Whiting G, Grondin D, Bennici S, Auroux A. Heats of water sorption studies on zeolite- MgSO_4 composites as potential thermochemical heat storage materials. *Sol*

- Energy Mater Sol Cells 2013;112:112–9. doi:10.1016/j.solmat.2013.01.020.
- [49] Posern K, Kaps C. Calorimetric studies of thermochemical heat storage materials based on mixtures of MgSO₄ and MgCl₂. *Thermochim Acta* 2010;502:73–6. doi:10.1016/j.tca.2010.02.009.
- [50] van Essen VM, Gores JC, Bleijendaal LPJ, Zondag HA, Schuitema R, van Helden WGJ. Characterization of salt hydrates for compact seasonal thermochemical storage. 2009.
- [51] Dellerio T, Touzain P. A chemical heat pump using carbon ® bers as additive . Part II : study of constraint parameters 1999;19:1001–11.
- [52] Ferchaud C, Zondag H, Boer R De, Rindt C. Characterization of the sorption process in thermochemical materials for seasonal solar heat storage application. *InnoStock 2012 12th Int. Conf. Energy Storage*, 2012, p. 1–10.
- [53] Zhang H, Iype E, Nedeia S V., Rindt CCM. Molecular dynamics study on thermal dehydration process of epsomite (MgSO₄ · 7H₂O). *Mol Simul* 2013:1–10. doi:10.1080/08927022.2013.854891.
- [54] Bertsch F, Mette B, Asenbeck S, Kerskes H. Low temperature chemical heat storage – an investigation of hydration reactions. *Effstock* 2009, 2010, p. 1–8.
- [55] Ferchaud CJ, Scherpenborg R a. a., Zondag H a., de Boer R. Thermochemical Seasonal Solar Heat Storage in Salt Hydrates for Residential Applications – Influence of the Water Vapor Pressure on the Desorption Kinetics of MgSO₄·7H₂O. *Energy Procedia* 2014;57:2436–40. doi:10.1016/j.egypro.2014.10.252.
- [56] L'vov, Boris V. Chapter 7 - The Topley-smith effect. *Therm. Decompos. solids melts*, 2007, p. 99–109.
- [57] Rammelberg HU, Schmidt T, Ruck W. Hydration and dehydration of salt hydrates and hydroxides for thermal energy storage - kinetics and energy release. *Energy Procedia* 2012;30:362–9. doi:10.1016/j.egypro.2012.11.043.
- [58] N'Tsoukpoe KE, Restuccia G, Schmidt T, Py X. The size of sorbents in low pressure sorption or thermochemical energy storage processes. *Energy* 2014. doi:10.1016/j.energy.2014.10.013.
- [59] Vaniman DT, Bish DL, Chipera SJ, Fialips CI, Carey JW, Feldman WC. Magnesium sulphate salts and the history of water on Mars. *Nature* 2004;431:663–5.

- doi:10.1038/nature02973.
- [60] Cindrella L, Dyer A. Ion-exchanged and salt hydrates-encapsulated zeolites for solar refrigeration. *Sol Energy Mater Sol Cells* 2009;93:161–6.
doi:10.1016/j.solmat.2008.09.057.
- [61] Janchen J, Brosicke W, Ackermann D, Stach H. Studies of the water adsorption on Zeolites and modified mesoporous materials for seasonal storage of solar heat. *Sol Energy* 2004;76:339–44. doi:10.1016/j.solener.2003.07.036.
- [62] Jänchen J, Ackermann D, Weiler E, Stach H, Brösicke W. Calorimetric investigation on zeolites, AlPO₄'s and CaCl₂ impregnated attapulgite for thermochemical storage of heat. *Thermochim Acta* 2005;434:37–41. doi:10.1016/j.tca.2005.01.009.
- [63] Jänchen J, Stach H. Adsorption properties of porous materials for solar thermal energy storage and heat pump applications. *Energy Procedia* 2012;30:289–93.
doi:10.1016/j.egypro.2012.11.034.
- [64] Casey SP, Aydin D, Riffat S, Elvins J. Salt impregnated desiccant matrices for ‘open’ thermochemical energy storage—Hygrothermal cyclic behaviour and energetic analysis by physical experimentation. *Energy Build* 2015;92:128–39.
doi:10.1016/j.enbuild.2015.01.048.
- [65] Bekkum HV, Flanigen E. *Introduction to zeolite science and practice*. 2nd ed. Elsevier; 2001.
- [66] Zheng Y, Li X, Dutta PK. Exploitation of unique properties of zeolites in the development of gas sensors. *Sensors* 2012;12:5170–94. doi:10.3390/s120405170.
- [67] Li X, Narayanan S, Michaelis VK, Ong T-C, Keeler EG, Kim H, et al. Zeolite Y adsorbents with high vapor uptake capacity and robust cycling stability for potential applications in advanced adsorption heat pumps. *Microporous Mesoporous Mater* 2015;201:151–9. doi:10.1016/j.micromeso.2014.09.012.
- [68] Weitkamp J. Zeolites and catalysis. *Solid State Ionics* 2000;131:175–88.
doi:10.1016/S0167-2738(00)00632-9.
- [69] Inglezakis VJ. The concept of “capacity” in zeolite ion-exchange systems. *J Colloid Interface Sci* 2005;281:68–79. doi:10.1016/j.jcis.2004.08.082.
- [70] Schaller C. *Network Solids and Related Materials* 2017.
- [71] Padin J, Munson CL, Yang RT. *Method for selective adsorption of dienes*, 2001.

- [72] Ríos R. CA, Oviedo V. JA, Henao M. JA, Macías L. MA. A NaY zeolite synthesized from Colombian industrial coal by-products: Potential catalytic applications. *Catal Today* 2012;190:61–7. doi:10.1016/j.cattod.2012.02.025.
- [73] Ríos C a, Williams CD, Castellanos OM. Crystallization of low silica Na-A and Na-X zeolites from transformation of kaolin and obsidian by alkaline fusion. *Ing y Compet* 2012;14:125–37.
- [74] de Boer R, Smeding SF, Zondag HA, Krol G. Development of a prototype system for seasonal solar heat storage using an open sorption process. *Eurotherm Semin. #99*, 2014, p. 1–9.
- [75] Pino L, Aristov Y, Cacciola G, Restuccia G. Composite Materials Based on Zeolite 4A for Adsorption Heat Pumps. *Adsorption* 1996;3:33–40.
- [76] Lass-Seyoum A, Blicher M, Borozdenko D, Friedrich T, Langhof T. Transfer of laboratory results on closed sorption thermo-chemical energy storage to a large-scale technical system. *Energy Procedia* 2012;30:310–20. doi:10.1016/j.egypro.2012.11.037.
- [77] Janchen J, Schumann K, Thrun E, Brandt A, Unger B, Hellwig U. Preparation, hydrothermal stability and thermal adsorption storage properties of binderless zeolite beads. *Int J Low-Carbon Technol* 2012;00:1–5. doi:10.1093/ijlct/cts037.
- [78] Johannes K, Kuznik F, Hubert J-L, Durier F, Obrecht C. Design and characterisation of a high powered energy dense zeolite thermal energy storage system for buildings. *Appl Energy* 2015;159:80–6. doi:10.1016/j.apenergy.2015.08.109.
- [79] Zondag HA, Essen VM Van, Bleijendaal LPJ, Kikkert BWJ, Bakker M. Application of $\text{MgCl}_2 \cdot 6\text{H}_2\text{O}$ for thermochemical seasonal solar heat storage. *5th Int. Renew. Energy Storage Conf. IRES 2010*, 2010, p. 22–4.
- [80] Finck C, Henquet E, van Soest C, Oversloot H, de Jong A-J, Cuypers R, et al. Experimental Results of a 3 kWh Thermochemical Heat Storage Module for Space Heating Application. *Energy Procedia* 2014;48:320–6. doi:10.1016/j.egypro.2014.02.037.
- [81] Jabbari-Hichri A, Bennici S, Auroux A. Enhancing the heat storage density of silica–alumina by addition of hygroscopic salts (CaCl_2 , $\text{Ba}(\text{OH})_2$, and LiNO_3). *Sol Energy Mater Sol Cells* 2015;140:351–60. doi:10.1016/j.solmat.2015.04.032.

- [82] Gordeeva LG, Aristov YI. Composites “salt inside porous matrix” for adsorption heat transformation: a current state-of-the-art and new trends. *Int J Low-Carbon Technol* 2012;1–15. doi:10.1093/ijlct/cts050.
- [83] Fakin T, Ristić A, Horvat A, Kaučič V. WATER ADSORPTION STUDY ON THE ZEOLITE LTA GRANULES. 5th Serbian-Croatian-Slovenian Symp. Zeolites, 2013, p. 56–9.
- [84] Allouhi A, Kousksou T, Jamil A, Rha T El, Mourad Y, Zeraouli Y. Optimal working pairs for solar adsorption cooling applications 2014:1–13. doi:10.1016/j.energy.2014.11.010.
- [85] Baowan D, Thamwattana N. Modelling adsorption of a water molecule into various pore structures of silica gel. *J Math Chem* 2011;49:2291–307. doi:10.1007/s10910-011-9887-3.
- [86] Zondag HA, Essen VM Van, Schuitema R, Kalbasenka A, Bakker M, Bleijendaal LPJ, et al. ENGINEERING ASSESSMENT OF REACTOR DESIGNS FOR THERMOCHEMICAL STORAGE OF SOLAR HEAT. 2009.
- [87] Bobonich FM, Forbek G, Voloshina YG. RELATIONSHIP BETWEEN HYDRATION ENERGY OF ZEOLITES AND CATION DISTRIBUTION IN THEIR CRYSTALS. *Theor Exp Chem* 1993;29:120–3.
- [88] Kirov G, Filizova L. Cationic hydration impact on zeolite formation and properties: A review and discussion. *Geochemistry, Mineral Petrol* 2012;49:65–82.
- [89] Tsutsumi K, Mizoe K. Heats of Adsorption of Water on Hydrophobic Zeolites. *Colloids and Surfaces* 1989;37:29–38.
- [90] Da-ming S. The effect of ion exchange on adsorption properties of a 13x molecular sieve. *Vacuum* 1991;42:845–8.
- [91] Benaliouche F, Hidous N, Guerza M, Zouad Y, Boucheffa Y. Microporous and Mesoporous Materials Characterization and water adsorption properties of Ag- and Zn-exchanged A zeolites. *Microporous Mesoporous Mater* 2014. doi:http://dx.doi.org/10.1016/j.micromeso.2014.10.039.
- [92] Stach H, Mugele J, Jänchen J, Weiler E. Influence of cycle temperatures on the thermochemical heat storage densities in the systems water/microporous and water/mesoporous adsorbents. *Adsorption* 2005;11:393–404.

- [93] Mizota T, Matsui K, Kasai T, Nakayama N. Hydration enthalpies of synthetic Na-A, cation-exchanged-A and some natural zeolites for evaluating as heat exchange absorbents. *Thermochim Acta* 1995;266:331–41. doi:10.1016/0040-6031(95)02442-5.
- [94] Petrova N, Mizota T, Fujiwara K. Hydration heats of zeolites for evaluation of heat exchangers. *J Therm Anal Calorim* 2001;64:157–66. doi:10.1023/A:1011537029569.
- [95] RSC: Advancing the Chemical Sciences : Hydration Enthalpies of Selected Ions n.d.
- [96] Dorai F, Rolland M, Wachs a., Marcoux M, Climent E. Packing fixed bed reactors with cylinders: Influence of particle length distribution. *Procedia Eng* 2012;42:1335–45. doi:10.1016/j.proeng.2012.07.525.
- [97] Haden WL. Attapulgite: properties and uses. *Proc. 10th Conf. Clays Clay Miner.*, 1963, p. 284–90.
- [98] Aidoun Z, Ternan M. Salt impregnated carbon fibres as the reactive medium in a chemical heat pump : the NH₃ – CoCl₂ system. *Appl Therm Eng* 2002;22:1163–73.
- [99] Druske M, Fopah-lele A, Korhammer K, Rammelberg HU, Wegscheider N, Ruck W, et al. Developed materials for thermal energy storage : synthesis and characterization. *Energy Procedia* 2014.
- [100] Dellerio T, Sarneo D, Touzain P. A chemical heat pump using carbon ® bers as additive . Part I : enhancement of thermal conduction 1999;19.
- [101] Pandey P, Lobo NF, Kumar P. Optimization of Disc Parameters Producing More Suitable Size Range of Green Pellets 2012;1:48–59. doi:10.5923/j.ijmee.20120104.02.
- [102] Gu A. Utilization of fly ash by pelletization process ; theory , application areas and research results 2000;30:59–77.
- [103] Liu H, Nagano K, Sugiyama D, Togawa J, Nakamura M. Honeycomb filters made from mesoporous composite material for an open sorption thermal energy storage system to store low-temperature industrial waste heat. *Int J Heat Mass Transf* 2013;65:471–80. doi:10.1016/j.ijheatmasstransfer.2013.06.021.
- [104] Liu H, Nagano K. Numerical simulation of an open sorption thermal energy storage system using composite sorbents built into a honeycomb structure. *Int J Heat Mass Transf* 2014;78:648–61. doi:10.1016/j.ijheatmasstransfer.2014.07.034.
- [105] Liu H, Nagano K, Togawa J. A composite material made of mesoporous siliceous shale impregnated with lithium chloride for an open sorption thermal energy storage

- system. *Sol Energy* 2015;111:186–200. doi:10.1016/j.solener.2014.10.044.
- [106] Zondag H, Essen M Van, He Z, Schuitema R, Helden W Van. CHARACTERISATION OF MgSO₄ FOR THERMOCHEMICAL STORAGE 2007.
- [107] Subramanian R. *Flow through Packed Beds and Fluidized Beds*. 2004.
- [108] Rovero G, Curti M, Cavaglià G. Optimization of Spouted Bed Scale-Up by Square-Based Multiple Unit Design. *Adv Chem Eng* 2012. doi:10.5772/33395.
- [109] Geldart D. Types of gas fluidization. *Powder Technol* 1973;7:285–92. doi:10.1016/0032-5910(73)80037-3.
- [110] Abedin AH, Rosen MA. Energy and Exergy Analyses of an Open Thermochemical Energy Storage System : Methodology and Illustrative Application 2012:41–8.
- [111] Mette B, Kerskes H. PROCESS AND REACTOR DESIGN FOR THERMOCHEMICAL ENERGY STORES. *ISES Sol. World Congr.*, Kassel: 2011, p. 1–12.
- [112] de Jong A-J, Trausel F, Finck C, van Vliet L, Cuypers R. Thermochemical Heat Storage – System Design Issues. *Energy Procedia* 2014;48:309–19. doi:10.1016/j.egypro.2014.02.036.
- [113] Michel B, Mazet N, Neveu P. Experimental investigation of an innovative thermochemical process operating with a hydrate salt and moist air for thermal storage of solar energy: Global performance. *Appl Energy* 2014;129:177–86. doi:10.1016/j.apenergy.2014.04.073.
- [114] Zettl B, Englmaier G, Steinmaurer G. Development of a revolving drum reactor for open-sorption heat storage processes. *Appl Therm Eng* 2014;70:42–9. doi:10.1016/j.applthermaleng.2014.04.069.
- [115] TA Instruments Discovery DSC 2011.
- [116] PerkinElmer. Thermogravimetric Analysis (TGA) A Beginner ’ s Guide. PerkinElmer 2015. http://www.perkinelmer.co.uk/CMSResources/Images/44-74556GDE_TGABeginnersGuide.pdf (accessed February 26, 2015).
- [117] Genius nitrogen generator 2016.
- [118] Verdonck E. Strategies for Better DSC Data 2016.
- [119] Henshall P, Eames P, Arya F, Hyde T, Moss R, Shire S. Constant temperature induced stresses in evacuated enclosures for high performance flat plate solar thermal

- collectors. *Sol Energy* 2016;127:250–61.
- [120] MKS. MKS Cirrus 2 Data Sheet 2011.
- [121] TA instruments TGA 2010:2500.
- [122] TA Instruments. TA Instruments Discovery TGA n.d.
<http://www.tainstruments.com/the-powerful-discovery-tga/> (accessed November 14, 2017).
- [123] Texus U of. Lab 7 : Residual Gas Analyzers 2002:1–15.
- [124] Zondag HA, Essen VM Van, Bakker M. Application of $\text{MgCl}_2 \cdot 6\text{H}_2\text{O}$ for thermochemical seasonal solar heat storage. *IRES* 2010, 2010, p. 22–4.
- [125] Ruiz-Agudo E, Martín-Ramos JD, Rodriguez-Navarro C. Mechanism and kinetics of dehydration of epsomite crystals formed in the presence of organic additives. *J Phys Chem B* 2007;111:41–52. doi:10.1021/jp064460b.
- [126] Yu N, Wang RZ, Lu ZS, Wang LW. Study on consolidated composite sorbents impregnated with LiCl for thermal energy storage. *Int J Heat Mass Transf* 2015;84:660–70. doi:10.1016/j.ijheatmasstransfer.2015.01.065.
- [127] Heath J. Energy Dispersive Spectroscopy. *Essent Knowl Briefings* 2015;Second Edi:32. doi:10.1007/978-1-4615-4919-2_12.
- [128] University of California Riverside. Introduction to Energy Dispersive X-ray Spectrometry (EDS). *Cent Facil Adv Microsc Microanal Manuals* 2011;2013:1–12.
- [129] Alothman Z a. A review: Fundamental aspects of silicate mesoporous materials. *Materials (Basel)* 2012;5:2874–902. doi:10.3390/ma5122874.
- [130] Jänchen J, Ackermann D, Weiler E, Stach H, Brösicke W. Calorimetric investigation on zeolites, AlPO_4 's and CaCl_2 impregnated attapulgite for thermochemical storage of heat. *Thermochim Acta* 2005;434:37–41. doi:10.1016/j.tca.2005.01.009.
- [131] Linnow K, Niermann M, Kaps C, Steiger M, Posern K, Talreja T. Calorimetric Investigation of Magnesium Sulfate Hydration in Porous Glasses. *Proc. EuroSun 2014 Conf.*, 2015, p. 1–7. doi:10.18086/eurosun.2014.10.15.